Theoretical study of electronic and phononic properties of systems containing kagome-like lattice

Surajit Basak

A thesis presented for the degree of
Doctor of Philosophy

Supervisor: dr. hab. Przemyslaw Piekarz, prof. IFJ PAN
Co-supervisor: dr. hab. Andrzej Ptok, prof. IFJ PAN

THE HENRYK NIEWODNICZAŃSKI
INSTITUTE OF NUCLEAR PHYSICS
POLISH ACADEMY OF SCIENCES

Department of Computational Materials Research
Kraków, Poland
2024

Contents

Acknowledgements

Firstly, I would like to thank my supervisor dr. hab. Przemyslaw Piekarz and co-supervisor dr. hab. Andrzej Ptok for introducing me to the world of Condensed Matter Physics (CMP), teaching both numerical tight-binding analysis and DFT techniques from scratch, providing thorough guidance throughout all phases of my Ph.D., giving me the opportunity and freedom to explore several branches of CMP and many more.

I would also like to thank Prof. Dominik Legut (IT4Innovations, VSB-Technical University Ostrava) for emphasizing on focusing the nuances of all computations and for playing a big role in helping me gain professional fluency in working with Linux.

The Ph.D. would have been incomplete without the immense influence of Prof. Jean-Nöel FUCHS and Prof. Julien Vidal (LPTMC, Sorbonne University) during the final year of Ph.D., which is indescribable in words.

I want to express my gratitude towards dr. David Alspaugh for his immense help in my effort to learn the Kitaev honeycomb model and dr. Svitlana Pastukh for her help with the references for lattice dynamical calculations and for always providing a step-by-step guide to almost every official work.

In the end, a big shout-out to Arpan Ghosal and, especially to Mateusz Gala for their comments after a thorough reading of the manuscript with exceptional typo-spotting abilities.

English abstract

Materials containing kagome lattice act as a platform to study condensed matter phenomena which are interesting from both fundamental and application perspectives. The lattice, which contains an array of corner-sharing triangles, is known to host many intriguing electronic properties with their roots in the strong electron-electron correlation and topological properties arising from symmetry-protected degenerate points in the band structure. In this thesis, I discuss the possibility of realizing kagome and kagome-like lattices in real materials. It will be shown in some works that the perfect kagome structure is found in only a few materials. In all the other cases the compounds stabilize in symmetries containing distorted kagome layers. For example, I explicitly study this phenomenon for different symmetry groups of CoGe, under ambient and applied pressure. The analysis of the phonon soft modes leads to the conclusion that CoGe does not stabilize in the symmetry group containing the perfect kagome layer (Cmmm, P6/mmm), rather it stabilizes in the symmetry group containing distorted kagome layer ($P\bar{6}2m$). Similar studies are also presented for Pt_3Pb_2Sn and FeGe. I will show that this has a significant impact on the properties of materials. Such as, for FeGe it leads to a charge density wave instability, and the reason behind the distortion in this case turns out to be the strong electron-electron correlation amongst the Fe atoms forming the kagome lattice. While immensely studied in the context of electronic band structure, the largely unexplored area of symmetry-protected degenerate points, degenerate lines, and flat bands in the context of phonon band structure will be explored too. For T_3Pb_2Ch (T = Pd, Pt and Ch = S, Se) and RhPb, I observe nodal lines in the phonon band structure and for RhPb, phonon drumhead states extending between two such nodal lines in the phonon surface state spectrum are observed. For T_3Pb_2Ch (T = Pd, Pt and Ch = S, Se) and ABi_2 (A = K, Rb, Cs), I discuss the possibility of finding chiral phonons, phonons with finite handedness. In that direction, I theoretically predict two new materials with broken bulk inversion symmetry ($KRbBi_4$, $RbCsBi_4$), which can be synthesized in the experiment and used to study the phonon Hall effect. I also describe some interesting electronic properties of kagome lattice-based superconductors. In particular, it is shown that the presence of van Hove singularity and flat band singularity in the density of states can drastically impact the coupling strength and the decay length of the impurity-induced in-gap bound states of the superconductor (known as the Shiba states), making them more useful for application purposes. This thesis is a collection of papers that resulted from my works performed during my PhD study. The papers are stacked up in Chapter 4. Chapter 3 gives a short guide to the Sections of Chapter 4. In Chapter 2, I describe the theoretical methods used to obtain the results.

Abstrakt w języku polskim

Materiały zawierające sieć kagome stanowią platformę do badania różnego rodzaju zjawisk fizycznych (podstawowych i aplikacyjnych) w fizyce ciała stałego. Sieć powstająca z połączonych wierzchołkami trójkątów posiada wiele intrygujących własności elektronowych, które stanowią podstawę silnych korelacji elektronowych oraz własności topologicznych, wynikających z istnienia w strukturze pasmowej punktów o zdegenerowanych energiach. W tej rozprawie dyskutuję możliwość realizacji sieci kagome oraz podobnej do kagome w układach rzeczywistych. W niektórych pracach pokazano, że idealna sieć kagome jest realizowana w kilku materiałach. W pozostałych przypadkach, układ jest stabilny w fazie, która zawiera zdeformowaną sieć kagome. Dla przykładu, dokładnie badam to zachowanie w CoGe z różnymi symetriami, w obecności ciśnienia. Analiza miękkiego modu prowadzi do wniosku, że CoGe nie jest stabilny w symetrii z idealną siecią kagome (np. Cmmm lub P6/mmm), i jest stabilny w obecności dystorsji tej sieci (w symetrii P$\bar{6}$2m). Podobne badania przeprowadzono dla Pt_3Pb_2Sn i FeGe. Pokażemy, że również taka sieć posiada istotny wpływ na własności materiałów. Podobnie jak w przypadku FeGe, może to prowadzić do niestabilności CDW (fali gęstości ładunku). O ile w tym kontekście struktura elektronowa była intensywnie badana, o tyle w przypadku relacji dyspersyjnych fononów badanie punktów zdegenerowanych, linii nodalnych, czy płaskich pasm stanowi otwarty temat. Dla T_3Pb_2Ch (T = Pd, Pt and Ch = S, Se) i RhPb, obserwujemy linie nodalne w pasmach fononowych, a w przypadku RhPb stany powierzchniowe pomiędzy tymi liniami. Dla T_3Pb_2Ch (T = Pd, Pt and Ch = S, Se) i ABi_2 (A = K, Rb, Cs) dyskutuję możliwość znalezienia fononów chiralnych (o skończonej skrętności). W tym kontekście, teoretycznie przewiduję istnienie dwóch nowych materiałów ze złamaną symetrią inwersji ($KRbBi_4$, $RbCsBi_4$), które mogą być wykorzystane do eksperymentalnego badnia fononowego efektu Halla. Opisuję również niektóre interesujące własności elektronów nadprzewodników z siecą kagome. Dokładniej, jak magnetyczna domieszka indukuje stan wewnątrzszczelinowy (wewnątrz przerwy nadprzewodzącej), nazywany stanem Shiby, oraz jak może on być "sterowany" poprzez istnienie płaskiego pasma w układzie. Rozprawa ta stanowi zbiór prac naukowych prezentujących wyniki uzyskane w czasie studiów doktoranckich. Prace naukowe stanowiące ten zbiór zebrane są w Rozdziale 4. Rozdział 3 stanowi krótkie wprowadzenie do tematyki omawianej w pracach naukowych. W Rozdziale 2 opisuję metody zastosowane w prowadzonych badaniach.

List of publications

This thesis is based on the papers

1. S. Basak and A. Ptok, "Shiba states in systems with density of states singularities", Phys. Rev. B **105**, 094204 (2022).

2. S. Basak, P. Piekarz, and A. Ptok, "Chiral phonon in the cubic system based on the Laves phase of $A\mathrm{Bi}_2$ (A = K, Rb, Cs)", Comput. Mater. Sci **230**, 112545 (2023).

3. S. Basak and A. Ptok. "Theoretical Study of Dynamical and Electronic Properties of Noncentrosymmetric Superconductor NbReSi", Materials **16**, 78 (2023).

4. S. Basak, A. Kobiałka, and A. Ptok, "Dynamical Properties of $T_3\mathrm{Pb}_2Ch_2$ (T = Pd, Pt and Ch = S, Se) with Transition Metal Kagome Net", Adv. Phys. Res. **2**, 2300025 (2023).

5. A. Ptok, W. R. Meier, A. Kobiałka, S. Basak, M. Sternik, J. Łażewski, P. T. Jochym, M. A. McGuire, B. C. Sales, H. Miao, P. Piekarz, and A. M. Oleś, "Phononic drumhead surface state in the distorted kagome compound RhPb", Phys. Rev. Research **5**, 043231 (2023).

6. S. Basak, A. Kobiałka, M. Sternik, J. Łażewski, P. T. Jochym, A. M. Oleś, P. Piekarz, and A. Ptok, "Electronic and dynamical properties of cobalt monogermanide CoGe phases under pressure", arXiv:2403.07580, submitted to Phys. Rev. B.

7. A. Ptok, S. Basak, A. Kobiałka, M. Sternik, J. Łażewski, P. T. Jochym, A. M. Oleś, and P. Piekarz, "Lattice dynamics study of electron-correlation-induced charge density wave in antiferromagnetic kagome metal FeGe", arXiv:2403.00297, submitted to Phys. Rev. Materials.

Beyond the scope of this thesis

1. S. Basak, P. D. Roy, S. Kar, "A new model with solitary waves: solution, stability and quasinormal modes", Eur. Phys. J. Plus **136**, 618 (2021).

2. S. Basak, A. Ptok, "Ab Initio Study of Chiral Phonons in Ternary YAlSi Compound", Crystals **12**, 436 (2022).

3. S. Basak, P. Piekarz, A. Ptok, "Electronic properties and surface states of $\mathrm{RbNi}_2\mathrm{Se}_2$", Phys. B **654**, 414697 (2023).

4. A. Ptok, S. Basak, P. Piekarz, A. M. Oleś, 'Influence of f Electrons on the Electronic Band Structure of Rare-Earth Nickelates", Condens. Matter **8**, 19 (2023).

5. S. Basak, A. Ptok, "Termination Dependence of the Surface States in Pb_2Pd", Acta Phys. Pol. A **143**, 195 (2023).

6. S. Basak A. Ptok. "Majorana Bound States in the Presence of Half-Smeared Potential", Acta Phys. Pol. A **143**, 164 (2023).

7. S. Basak and A. Ptok, "Lattice dynamics of altermagnetic ruthenium oxide RuO_2", Acta Phys. Pol. A **145**, 93 (2024).

Chapter 1

Introduction

The properties of a condensed matter system can be understood in terms of the interaction between its constituents, i.e. the atoms forming a regular pattern, and the charge carrier electrons. At room temperature, the interactions between electrons usually get suppressed due to their thermal energy. However, in certain materials, due to special geometry, one can find localized electronic states [1–3]. These localized states, in the momentum space, manifest themselves as a flat dispersionless band (Fig. 1.1), for which the electron energy becomes independent of its momentum. As we shall see later, these states are not localization at specific points in space, rather they are the localization of electronic wave function inside hexagonal plaquettes. Due to the quenching of kinetic energy, the electron-electron correlation gets enhanced, and systems with flat bands become an ideal platform to study the properties of the system which arises from a strong correlation between the carriers.

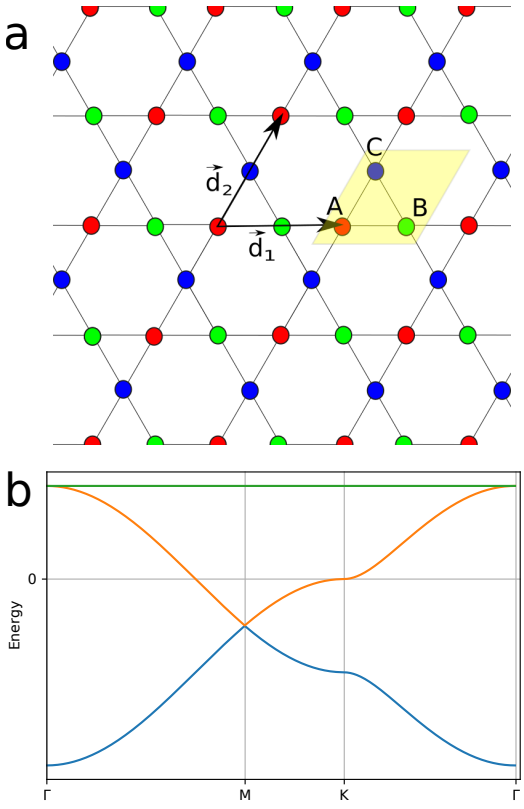

Figure 1.1: a) kagome lattice and b) its electronic dispersion relation, characterized by the presence of a flat band and a Dirac point.

Using simple tight binding calculation, one can see that a flat band can occur naturally if, due to the geometry, the classical trajectory of the charge carriers interfere destructively, forming electronic states localized at certain regions of space (more on this in Chapter 2). The presence of a flat band is related to the vanishing group velocity of the carriers, so in practice, a perfect flat band can never be present in a three-dimensional system. But almost flat bands with a finite curvature and a small but non-zero bandwidth were observed in CoSn [4], FeSn [5], Fe_3Sn_2 [6], Nb_3Cl_8 [7], photonic Lieb lattice [8]. Due to the vanishing group velocity, and subsequent quenching of energy, these materials become ideal platforms to study strongly correlated physics. In the above-mentioned

structures, CoSn, FeSn, Nb_3Cl_8 contains layers of kagome lattice, while Lieb lattice is found in the high-temperature superconductors. *This thesis is about performing comprehensive research on electronic and lattice dynamic properties of materials containing kagome lattice.*

Kagome lattice consists of a network of corner-sharing triangles (Fig. 1.1), resembling the traditional Japanese basket-weaving pattern. Along with a flat band, the kagome lattice's band structure also contains a symmetry-protected Dirac band crossing point. At this point, two bands cross each other linearly. This signifies the presence of a massless fermion in the system. This is one of the few systems whose band structure contains both an infinitely massive excitation (manifesting as a flat band) and also a massless Dirac fermion. Along with that, the density of states contains a van Hove singularity (VHS) at M point. This VHS, if present close to the Fermi surface, can often drive a system towards charge density wave (CDW) instability [9, 10]. The geometry of the kagome lattice system makes it naturally frustrated, the presence of a symmetry-protected Dirac cone supports the presence of topological excitation and the presence of a flat band resulting in increased Coulomb interaction amongst the electrons resulting in a plethora of quantum many-body phenomena, namely, many-body spin-orbit tunability [11], correlations and topology [12], fractional quantum Hall effect [13], giant quantum Hall effect [14], topological superconductivity [15] have been observed in system containing kagome lattice. But it is not only the electronic properties that make kagome materials interesting. Certain materials containing kagome lattice are also known to host topological magnons [16], bosonic edge and surface states [17], valence bond solids arising from the hard core bosons [18] etc.

On the other hand, the presence of a flat band can affect the superconducting properties of the system too. In twisted bilayer graphene, it was observed that, at magic angle flat band turns up in the band structure of the system [3, 19–21], and it is accompanied by strong many-body interaction and the resulting occurrence of superconductivity. Also, some basic analysis of the Bogoliubov–de Gennes (BdG) equations suggests that an increased value of the density of states (DOS) at the Fermi level can enhance the critical temperature (T_c) of the system. Similar phenomena were reported for d-wave superconductors too. Not only that, the presence of flat bands affects the impurity-driven quantum phase transition of the superconductor. When a magnetic impurity is placed on top of a s-wave superconductor, for a critical value of coupling between the superconductor and the impurity, a quantum phase transition takes place, and the total spin of the system changes. From analytical models of tight binding analysis, it is known that the value of critical coupling (J_c) is suppressed when a VHS appears in the band structure [22]. *It will be interesting to ask how this situation will change when we have a flat band singularity in the band structure. Moreover, for systems containing Lieb lattice, this phenomenon can be even more interesting, since in Lieb lattice, the spectral weight of the flat band is unevenly distributed among the inequivalent sublattices of the unit cell.*

1.1 Flat band in real materials

In Fig. 1.2, I present the electronic band structures of CoSn, RhPb, NiLn, and PtTi calculated within the density functional theory (DFT) [23]. The band structures were obtained for symmetry group P6/mmm. This symmetry group is characterized by the presence of an exact kagome layer formed by Co/Rh/Ni/Pt atom, while the other atom of the chemical symbol forms a hexagonal structure. In the electronic band structure (Fig 1.2), one can locate several flat-like bands. In practice, due to many-body effects we always observe bands with a finite bandwidth. The widths of the bands are proportional to the contribution of the d-orbitals. The green color marks the contribution of d_{xz} and d_{yz} orbitals, whereas the red color marks the contribution of $d_{x^2-y^2}$ and d_{xy}. The vertical panels presented on the right of each plot denote the density of states (DOS) of the d-orbitals. Those flat bands that lie close to the Fermi level are the most useful ones for application purposes. Although we don't see any flat band exactly at the Fermi level for any of the compounds, at least two flat bands, with small bandwidths (0.2 and 0.3 eV) are observed close to the Fermi level in CoSn, along high symmetry path A-L-H-A. For other compounds, the flat-like bands arising from the $d_{x^2-y^2}$ and d_{xy} orbitals are more dispersive, evident from their large values of bandwidths. In all the situations, the presence of flat bands is

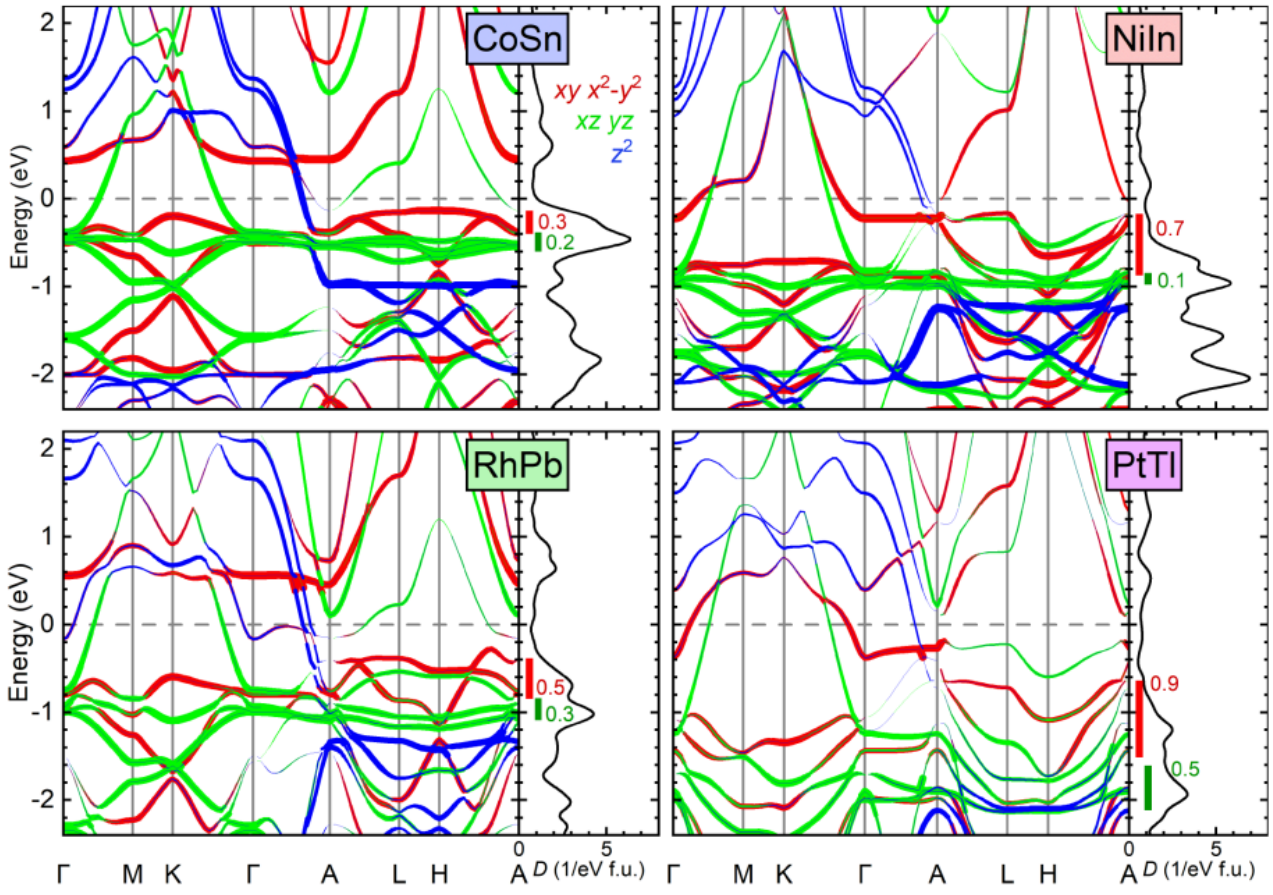

Figure 1.2: Flat-like bands in kagome systems. In the vertical panels on the right, the density of states (DOS) of the d orbitals are shown. Within the DOS spectrum, the bandwidths of the flat bands are shown in red and green colors. Adapted from [23].

justified by the presence of sharp peaks in the DOS. The bandwidth of a flat band can be used as a measure of the strength of electron correlation. Although the compounds with P6/mmm symmetry are promising places to find exact kagome lattices and hence perfect places to study kagome physics, the lattices with P6/mmm symmetry are often unstable in nature. It was shown in some previous works that RhPb is also unstable in symmetry group P6/mmm group and stabilizes in P$\bar{6}$2m symmetry, with distorted kagome lattice structure. This prediction was verified in one of the works the author was involved in and is presented in Chapter 4.2.1.

Fig. 1.3 shows an experimentally observed flat band and Dirac point in the electronic band structure of CoSn, measured using ARPES [4]. Results are shown for different fixed values of k_y (Figure 1.3(b-f)). For all the cases, almost non-dispersive bands are observed throughout the Brillouin zone. The width of the flat band over the entire Brillouin zone is a maximum of 150 meV. Only at $\bar{\mathbf{K}}$ point the band becomes slightly dispersive. The presence of a flat band is further confirmed by the sharp peak in the DOS shown in Fig. 1.3(h). Another characteristic of the electronic band structure of the kagome lattice is the presence of the Dirac point, which is shown in Figure 1.3(g). In Fig. 1.3(i), the dispersion is plotted along the out-of-the-plane momentum. It can be noticed that the flat band still exists in the band structure even if we move away from the kagome plane. In case (b-f), the flat band arises due to the kinetic energy quenching of the electrons in the kagome plane. However, the flat-like band is maintained even in out-of-the-plane direction due to the quasi-2D nature of the system. A quasi-2D system

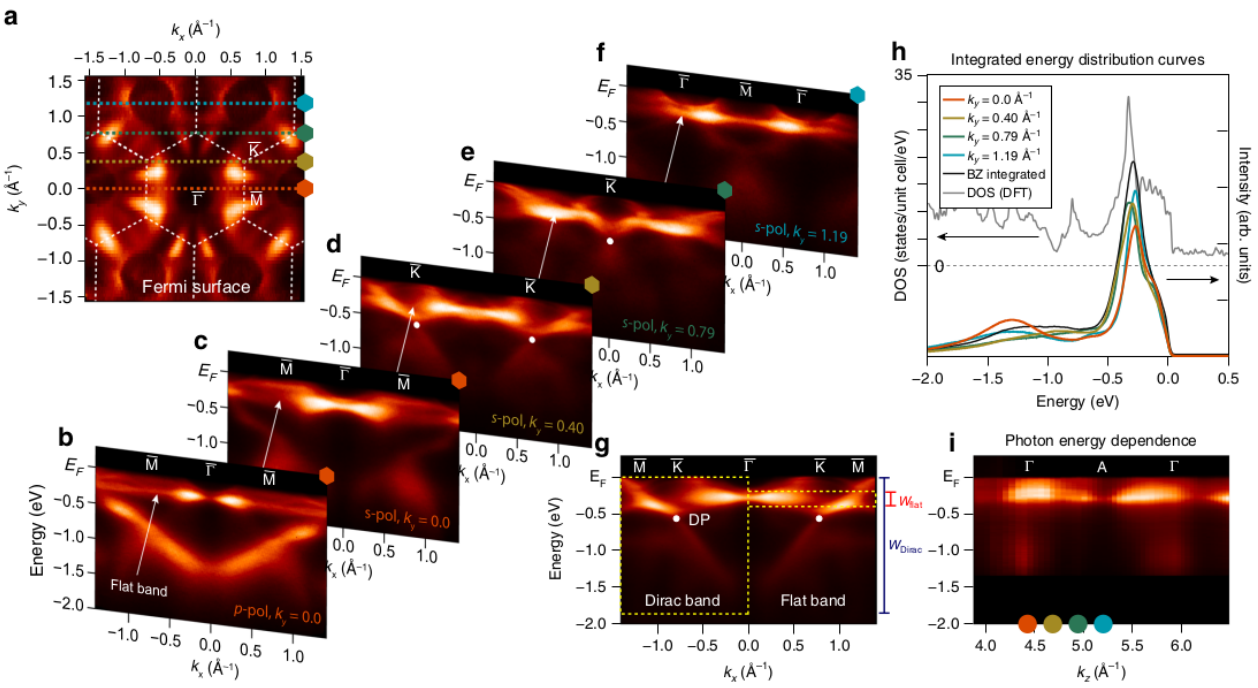

Figure 1.3: a) Fermi surface of CoSn. Electronic dispersions for fixed values of k_y=0.0 Å^{-1} (b, c), 0.40 Å^{-1} (d), 0.79 Å^{-1} (e), and 1.19 Å^{-1} (f). The flat band is visible with little dispersion at $\bar{\text{K}}$ point. g) clearly shows the existence of Dirac point and flat band. h) shows the density of states with flat band peak and i) presents out-of-the-plane dispersion, which shows that the flat band exists even along a direction perpendicular to the kagome plane. Figures are taken from [4].

containing the kagome layer will be the subject of discussion in Chapter. 4.2.2.

1.2 Electronic properties

Here I give some examples of materials containing kagome lattice and shortly discuss their noble properties. We start our discussion with ferromagnetic $Co_3Sn_2S_2$. The kagome layers of $Co_3Sn_2S_2$ give rise to interesting transporting properties in the form of anomalous Hall effect. $Co_3Sn_2S_2$ crystalizes in the rhombohedral structure with space group R-3m (No. 166), with the kagome layers of Co_3Sn stacked between layers of S atoms. The kagome layers of ferromagnetic $Co_3Sn_2S_2$ give rise to a pair of Weyl points in the electronic band structure (Fig. 1.4) close to ($\sim$ 60 meV) the Fermi level. The band structure also reveals that spin-up states cross the Fermi level suggesting a metallic character. The Fermi surface shows a mixed contribution containing both electron and hole characters. Spin-orbit coupling makes the Weyl cones gapped. All these properties make $Co_3Sn_2S_2$ an ideal Weyl semimetal. What makes it more interesting is the fact that the material is intrinsically magnetic due to the magnetization of Co atoms. The Weyl semimetal phase, intrinsically broken time-reversal symmetry, together with the highly entangled Bloch bands makes it a promising platform to study the giant anomalous Hall effect. This was in fact the first material that was found to host the Hall effect even in the absence of

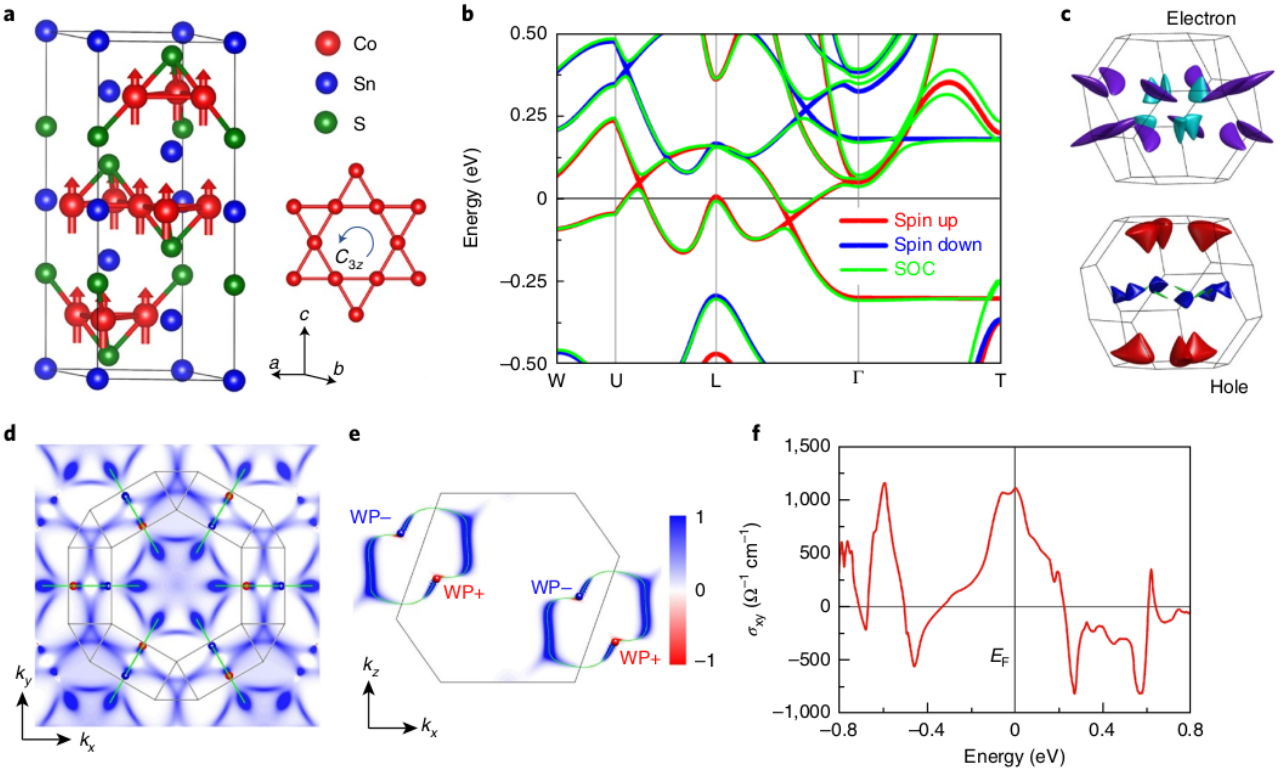

Figure 1.4: a) Crystal structure of $Co_3Sn_2S_2$. The out-of-the-plane magnetic moments of Co atoms are shown in arrow, b) band structure. The pair of Weyl points become gapped in the presence of spin-orbit coupling, c) the Fermi surface split into electron and hole parts, d) distribution of Berry curvature over the Brillouin zone, projected on the k_x, k_y plane, e) Berry curvature on the k_y plane, f) finite Hall conductivity. Figures are taken from [24].

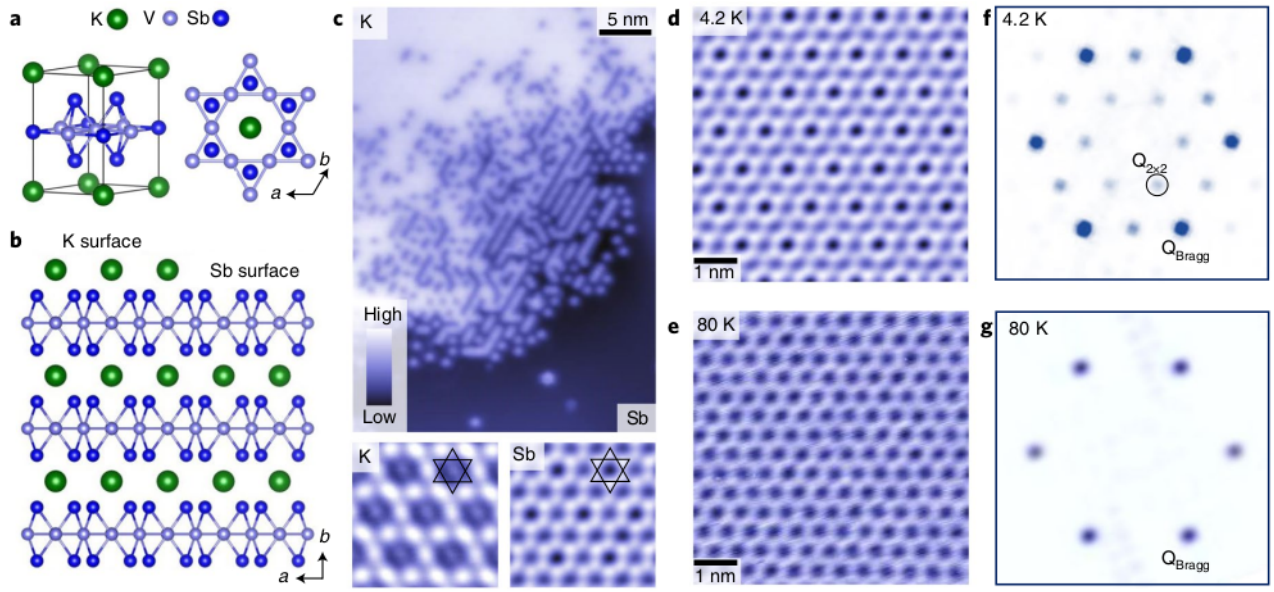

Figure 1.5: a) Crystal structure of KV_3Sb_5 and the top view of a kagome plaquette, b) side view, c) topographic image of a step edge which shows a clear separation between the layer containing K atom and the layer containing Sb atom. The bottom panel shows the topographic image of the layer containing a hexagonal plaquette of K atoms and that containing a Sb hexagon. d) image showing 2×2 modulation at 4.2 K, and e) the absence of 2×2 modulation at 80 K. f) The Fourier transform of the topographic image of the modulation at 4.2 K with the modulation peak $Q_{2\times2}$, Bragg peak Q_{Bragg} shown in circle. g) The modulation peaks disappear at 80 K. Figures are taken from [25].

an external magnetic field [24]. The large Berry curvature that exists throughout the Brillouin zone and the resulting finite Hall current are presented in Fig. 1.4 d, e, and f. The layers of kagome lattice with out-of-the-plane magnetization give rise to a giant intrinsic anomalous quantum Hall conductivity (1130 $\Omega^{-1}\ cm^{-1}$).

The presence of Weyl points in the band structure has topological significance too. Symmetry-protected degenerate points, such as the Weyl (Dirac) points are characteristic features of the topological Weyl (Dirac) semimetals. Due to the robust stability of these points under perturbations, the host materials attract a lot of applications. We also look for these symmetry-protected degenerate points but in phonon dispersions. For both RhPb (Chapter 4.2.1) and $T_3Pb_2Ch_2$ (T = Pd, Pt and Ch = S, Se) (Chapter 4.2.5), we observe not only degenerate Dirac points but nodal lines (lines along which the energy is degenerate). In RhPb, we even observe flat drumhead states which extend between two such nodal lines.

My second example is about a phase transition which results from the kagome lattice distortion. There is a certain class of materials, which at low temperatures deviates from an ideal kagome structure and makes a phase transition to a less symmetric distorted kagome-like structure, and the final state is characterized by the presence of novel phases. The members of the AV_3Sb_5 (A = K, Rb, and Cs) family show this kind of behaviour [26]. As the temperature is lowered, the displaced atoms drive these materials towards a transition from P6/mmm to C2/m symmetry and this is accompanied by an onset of CDW [25, 27, 28]. One such example

is presented in Fig. 1.5.

The V atoms form the kagome structure here whereas both the K and Sb atoms form hexagonal layers separately. As the temperature is lowered (∼4.2 K), we observe that the material is driven towards the CDW phase. The emergent 2×2 modulation is well visible in Fig. 1.5(f). This disappears once the temperature is raised to 80 K (Fig.1.5(g)). Along with the images, the static standing wave nature of the CDW was confirmed by the presence of non-dispersive states at the modulation vector, which is not shown here for the sake of brevity. Although the result is shown only for the Sb layer, CDW is observed in the kagome layer too. The reason for the occurrence of CDW is the electron-phonon mediated Jahn-Teller effect which arises from the distortion of the trimeric and hexameric V atoms [26]. The kagome lattice structure after the onset of CDW is shown in Fig. 1.6. We can compare the lengths of bonds forming the kagome lattice with the bond length before the onset of CDW, which is 2.718 Å.

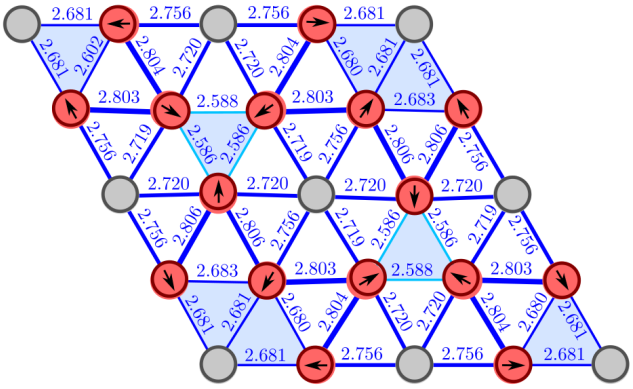

Figure 1.6: The kagome layer after distortion. The bond length should be compared with the bond length before distortion, which is 2.718 Å. Figure adapted from [26]

There are other mechanisms for the onset of CDW too. The most famous one is the Fermi surface nesting, and a less well-known one is CDW driven by electron-electron correlations. This possibility is explored in 4.2.4, where we investigated the mechanism behind the CDW transition in FeGe and proved that it indeed is driven by a strong correlation in the Fe-d orbital.

If a magnetic impurity is placed on top of a superconductor, it interacts with the Cooper pairs and leads to Cooper pair breaking. This destroys the superconductivity locally, at the position of the impurity, and creates a pair of bound states within the superconducting gap, known as the Shiba states (Fig. 1.7). Extensively studied from a theoretical standpoint during the second half of the last century [29–34], they have attracted a lot of experimental attention recently too due to the advancement of Scanning Tunneling Spectroscopy (STS) [35–39] and as the proposed building blocks to host topological superconductivity [40–50], including noble excitations like Majorana zero modes [51–60] to build a fault-tolerant quantum computer. For application purposes, those states are more attractive and have both coupling strength (which determines how strongly the impurity interacts with the superconductor) and a long coherence length/ decay length (a short coherence length means the bound states are strongly localized at the position of the impurity). As shown in Fig. (1.8), the localization of the in-gap states depends largely on the system dimension. For three-dimensional systems, they are highly localized at the position of the impurity. Whereas for two dimensions, their spatial extent is much larger. However, there are ways to manipulate both the decay length and the coupling strength to the substrate. It is known that if a van Hove singularity (VHS) [22] is present in the DOS, and it can be tuned to

the position of the Fermi level, then the coupling between the magnetic impurity and the parent material can be enhanced drastically. In Chapter. 4.1.1 we extend this to the case when along with a VHS, a flat band singularity (in kagome and Lieb lattices) is also present in the system.

The above examples prove that materials containing kagome lattice act as an ideal playground for many body correlations and give rise to an array of intriguing phenomena. Thus, it will be interesting to look for materials containing kagome lattice and study the noble properties arising from strong electron correlations.

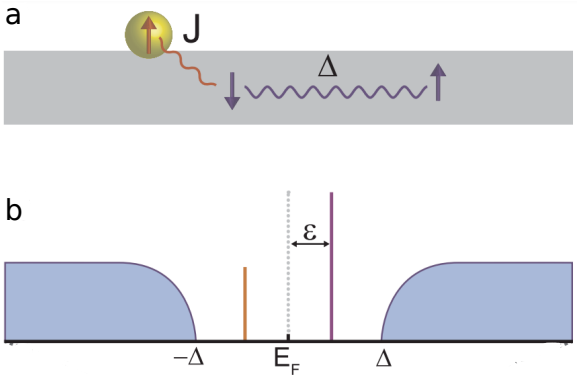

Figure 1.7: a) Magnetic impurity interacts with the Cooper pair and breaks it, destroying the superconductivity locally and creating a pair of in-gap states known as Shiba states. b) A cartoon plot for the local density of states. The bound in-gap states are presented as vertical lines. Different colors represent the electron and hole nature of the states. Different spectral weights on electron-like and hole-like states are indicated by different heights. Figure adapted from [35]

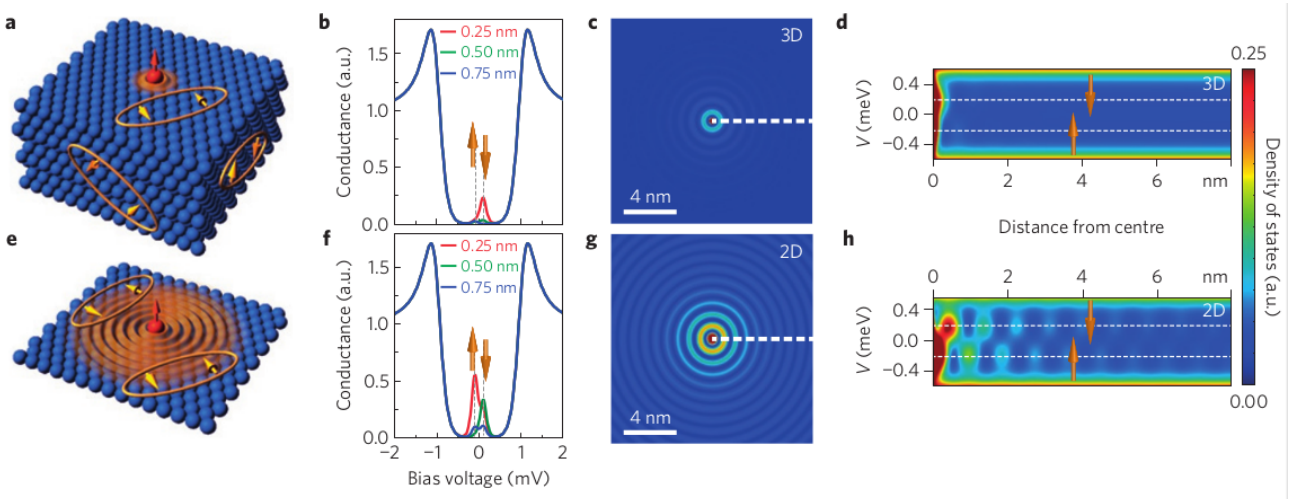

Figure 1.8: The upper and lower panel shows STM results for magnetic impurity placed on 2D and 3D materials respectively. b) and f) show the conductance spectra, which is a measure of the local density of states, at different distances from the impurity, showing the spin-polarized in-gap states. c) and g) show the simulated conductance map, at a particular distance from the impurity (4 nm), around the impurity. d) and h) show the computed plot for the local density of states as a function of distance, obtained between -0.6 to 0.6 meV, along the dotted line of c) and g). Figure courtesy [61].

1.3 Lattice dynamical properties

Unlike the electronic properties, the lattice dynamical properties of systems containing kagome lattices have remained largely unexplored. We seek to fill this void in one part of this thesis. *The question we ask is whether flat band and Dirac point, characteristic of kagome electronic band structure, can be found in the phonon dispersion relation too.* In some photonic lattices, both phonon flat bands and Dirac crossings were observed [63, 64]. We seek to add more materials to the literature on phonon flat bands. In the presence of both electron and phonon flat bands, one can expect strong correlations between the flat band phonons and the electrons of the kagome lattice. Let us take, for example, the case of CoSn, which crystalizes in the space group P6/mmm with the d-block elements (Co) forming the kagome lattice. Due to the presence of a kagome lattice, the electronic band structure contains a flat band. To study the presence of phonon flat band and the interaction between the flat band phonons with the kagome lattice electrons, Yin *et. al.* [65] studied the differential conductance of the system, which is shown in Fig. 1.10.

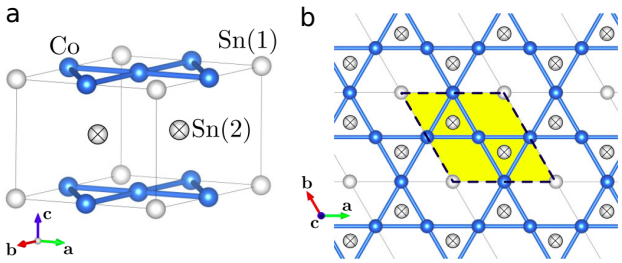

Figure 1.9: a) The lattice structure of CoSn, containing kagome layers of Co_3Sn separated by the hexagonal layer of Sn_2. b) Top view showing the kagome layer formed by Co_3Sn. Figures taken from [62].

One can notice from Fig. 1.10 a, b, and c that there is strong low energy modulation of the conduction spectra for the level containing Co_3Sn kagome layer. However, these modulations are missing in the hexagonal Sn_2 layer. These kinds of peaks are the signature of strong fermion-boson interactions [66, 67]. The bosonic excitation can be either phonon or spin resonance. However, the invariance of the conduction spectra under different magnetic fields shown in Fig. 1.10(c) indicates that phonons must be involved in this process. But to further investigate the involvement of phonons, the authors computed the double derivative of conductance, which is closely related to the Eliashberg function $\alpha^2F(\omega)$, where α is the coupling matrix element and $F(\omega)$ is the phonon DOS. The shape of the double derivative of conductance fits well in the Eliashberg function with a Gaussian peak at $E \simeq 15$ meV. This peak is in agreement with the phonon flat band found exactly at $E \simeq 15$ meV. Fig. 1.11 shows the calculated phonon dispersion relation, which has a phonon flat band that touches a neighbor band quadratically. The DOS also confirms that the phonon flat band arises from the vibration of Co atoms in the kagome plane. Looking at Fig 1.11(c), we notice that the displacement of the Co atoms in the hexagonal unit cell is such that they do not exert any force on the atoms that are outside. And this confined vibration gives rise to the phonon flat bands.

Unlike electrons, phonons do not obey the Pauli exclusion principle and do not have a Fermi level in the phonon band structure. So, the entire phonon dispersion spectrum is practically

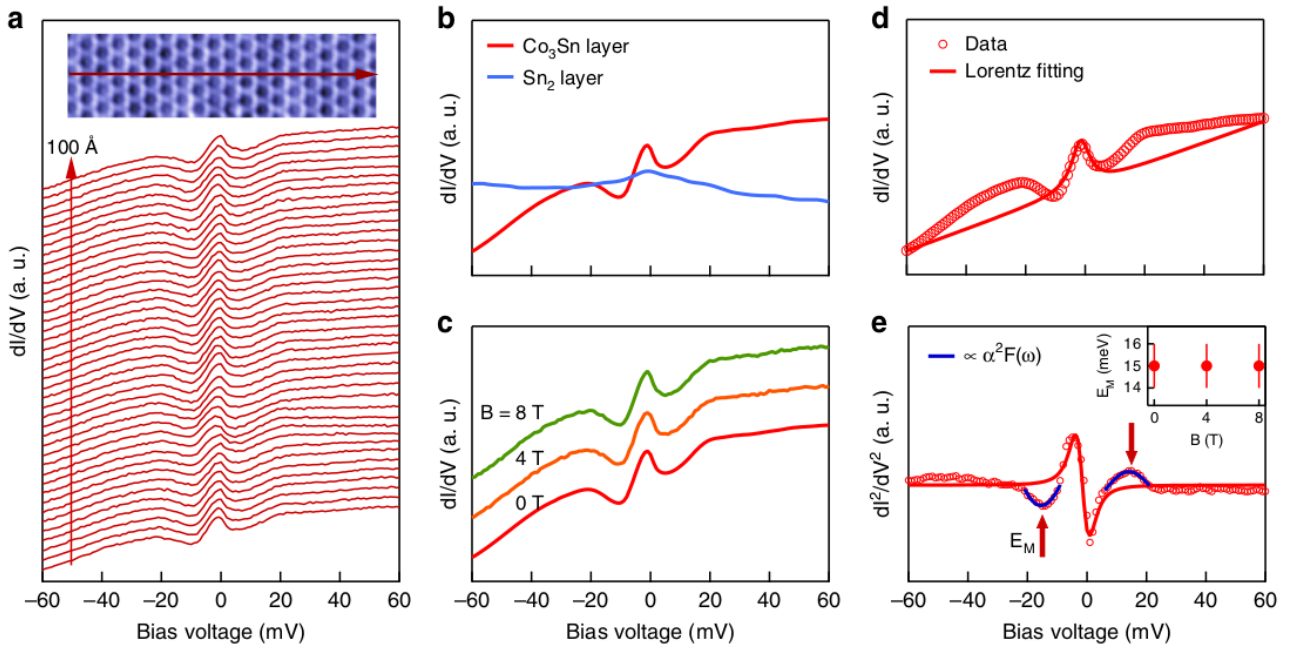

Figure 1.10: a) Differential conductance obtained along the direction shown in the inset, b) differential conductance for the kagome layer Co_3Sn and hexagonal layer Sn_2, c) differential conductance for different values of applied magnetic fields, d) fitted with a Lorentzian. e) The double derivative of conductance compared with Eliashberg function shows a Gaussian-like peak at $E_M = 15$ meV. Figures are taken from [65].

accessible in the experiment. Hence, if present, Dirac phonons can be more conveniently accessed in the experiment and harnessed for application purposes. That is why it is so important to study the phonon properties of kagome lattice as intensively as it was done with electronic properties. Like in the electronic case, the presence of a Dirac crossing point indicates the topological nature of the phonons. Hence, to unravel their topological nature, we need to look for the presence of nodal lines and non-trivial phonon surface states. These studies are compiled

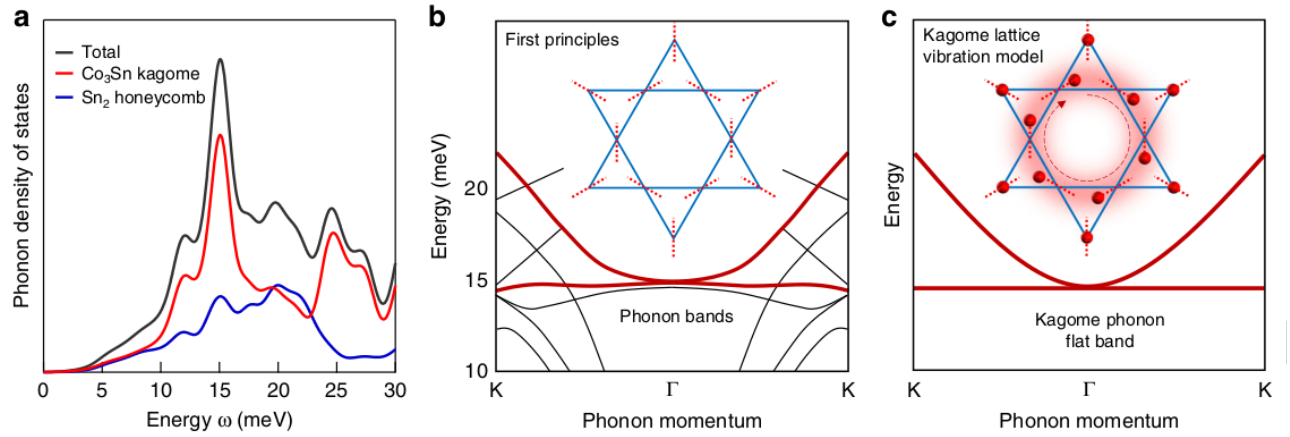

Figure 1.11: a) Phonon density of states (DOS), total, and atom projected. The peak in the phonon DOS is an indicator of a phonon flat band, b) the phonon flat band touching a neighbor band quadratically and the Co vibration responsible for this flat band is shown in red lines on the kagome plaquette, c) the Co atoms vibrate in such a way that it does not insert any force on the atoms residing outside the hexagonal plaquette. Figures taken from [65].

in Chapter. 4.2.1, 4.2.2 and 4.2.5.

There are more reasons to study the phonon dispersion relations of a solid. The frequencies of the phonon modes are the normal mode frequencies of vibration of lattice atoms around their equilibrium positions (more on this in the next Chapter). So an imaginary frequency is regarded as unphysical. Consequently, the structure having imaginary phonon modes, known as the soft modes, is not stable in considered thermodynamic conditions. They usually stabilize in a structure with lower energy and lower symmetry. Consider RbV_3Sb_5 for example. In Fig. 1.12 (a), the phonon dispersion relations obtained for P6/mmm symmetry are shown. This symmetry group is characterized by the presence of exact kagome layers in the lattice. But as the phonon dispersion shows, the structure contains soft modes (plotted with negative values). The eigenvectors corresponding to this soft mode can be analyzed to find out which atomic vibrations are responsible for this soft mode. Later if one plots the energy of the structure for different displacements of the responsible atoms around their position in the parent structure, then for a certain set of values of displacements one can find a structure with lower energy. For this particular case, the structure stabilizes into C2/m symmetry with distorted kagome lattice and the phonon dispersion shown in Fig. 1.12 (b) has no soft modes [26]. Thus the study of phonon soft modes can give us information about structural phase transition. Lattice dynamical study of structural phase transition will be performed in Chapter. 4.2.3 and Chapter. 4.2.4 for CoGe and FeGe, respectively.

Like the topological properties, another of the heavily studied properties of phonons in modern times is the property of chirality. In certain lattices, the symmetry of the system often allows the atoms to rotate around their equilibrium position in perfectly circular or elliptical orbits. The collective excitations, the phonons, arising from these special kinds of vibrations

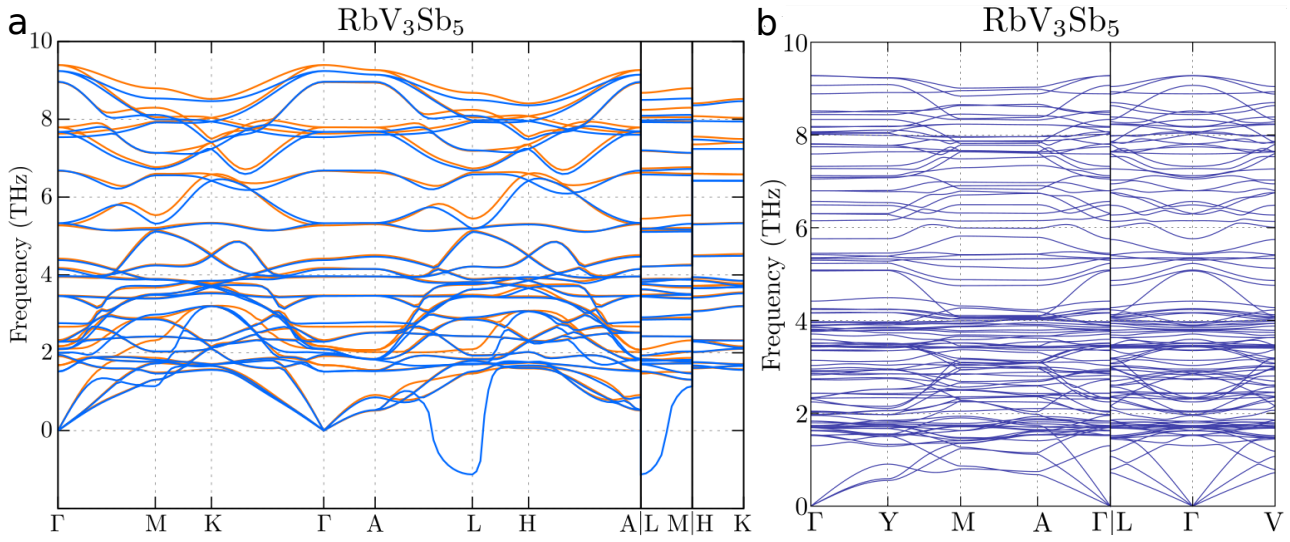

Figure 1.12: a) Phonon dispersions of RbV_3Sb_5 in P6/mmm symmetry. Blue and orange curves represent the band structures obtained for 50 K and 150 K, respectively. b) The dynamically stable C2/m symmetry contains no phonon soft modes. The congested dispersion is a result of Brillouin zone folding. Figures adapted from [26].

inherit the property of the parent system and have a sense of handedness associated with these vibrations. Phonons with a particular value of handedness are known as chiral phonons. Chiral phonons were predicted to be present in the high symmetry **K**, **K′** and **Γ** points of hexagonal lattice [68]. The chirality of phonons is considered as a polarization of the phonon eigenmodes and is treated in the same way as the circularly polarized light is theoretically studied. However, it can be shown that the operator defining the chirality has the same form as the angular momentum operator. Hence a finite value of chirality also means a finite value of pseudo-angular momentum (pseudo- due to the discrete rotational symmetry). In Fig. (1.13 a), we show a plot of the phonon band structure of a hexagonal lattice. The 2D lattice, with 2 atoms per unit cell gives rise to four bands. In the inset, it is shown that the phonons at both **K** and **K′** points appear due to the circular vibration of both A and B sublattices. The radius of the circles is proportional to the amplitudes of vibrations. For band 2, only the B atom performs the circulation, while for band 3, it's the A atom that circulates. For band 1, both A and B atoms perform circulations, but in opposite directions and with equal amplitudes. Whereas for band 4, the amplitudes of vibration are different for A and B.

Following the years after its prediction, chiral phonons were widely studied in a string of materials containing kagome lattice [69], Kekulé lattice [70], lattice with C_4 symmetry [71], Moiré superlattices [72], Weyl semimetals [73] and in various three-dimensional materials, like pseudo-gap phase of the cuprates [74, 75], transition metal dichalcogenides [76]. Due to the finite handedness, chiral phonons interact selectively with other chiral objects, like polarized light. In fact, this property of chiral phonons was exploited in the lab to detect them experimentally for the first time in the hexagonal layers of WSe_2 in 2018 [77]. Despite of the intensive research on chiral phonons, the study of the same in 3D materials remains still very much open. *Study of chiral phonons in materials containing kagome layer will be the subject of study in Chapter 4.2.5 and 4.2.6.*

Phonons with a non-zero value of chirality also possesses a non-zero value of angular momentum [68]. These phonons with angular momentum lead to a bunch of fundamentally interesting novel quantum phenomena, e.g., phonon quantum Hall effect [74], phonon Einstein-de Haas effect [78], phonon Zeeman effect [79], while finding a place in the pseudo gap phase of the cuprates too [75]. Like the electrons, the presence of a transverse magnetic field can give rise to the accumulation of opposite charges on opposite sides of a sample, known as the electron Hall effect, phonons can give rise to the phonon Hall effect in the presence of externally applied magnetic field. In fact, phonons with intrinsic angular momentum can produce the phonon Hall effect even in the absence of magnetic field [80]. This effect leads to heating one side of the material while cooling up the other side. Let's consider our previous example with chiral phonons in a hexagonal lattice again. From Fig. 1.13(a), it is clear that the phonons at **K** and **K′** valley arise from atoms that circulate in opposite directions. Hence the phonon excited at valley K has the value of chirality opposite to that of a phonon excited at valley **K′**. As mentioned earlier, due to the finite value of PAM, chiral phonons interact selectively with

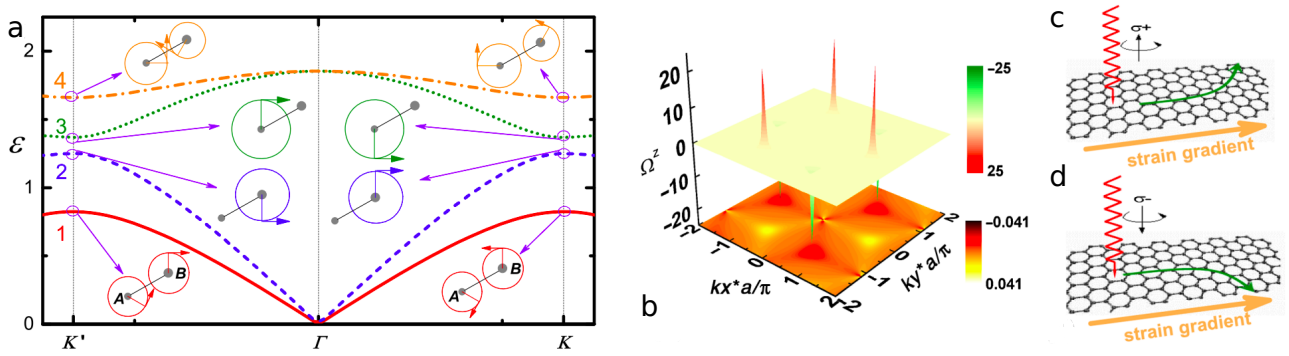

Figure 1.13: a) Phonon dispersion relations of the hexagonal lattice. Inset shows the circulation of atoms generating the phonons. The radius of the orbit is proportional to the amplitude of vibration. b) Finite Berry curvature created by broken inversion symmetry. The top panel shows the 3D plot for the Berry curvature of band 2, and the bottom one shows the contour plot of the same for band 1. As visible, Band 2 has a large value of Berry curvature. c) and d) show the motion of phonons in green arrow when left or right circularly polarized light is used to excite them. Picture adapted from [68].

.

circularly polarized light. Hence if a right circularly polarized light can excite a phonon from valley **K**, then it will require a left circularly polarized light to excite a phonon at valley **K′** (since they have opposite values of PAM). Another point to notice is that the main reason behind the electron Hall effect is the finite value of Berry curvature of the electrons. In this system with hexagonal lattice too the phonons can acquire finite Berry curvature (Ω) if the inversion symmetry of the system is broken. So, if an electric strain gradient $\mathbf{E_s}$ is applied in a system with broken inversion symmetry, then the phonons at two different valleys will travel in two different directions since the Hall coefficient $\nu_{Hall} = -\mathbf{E}_s \times \Omega$ (Figure 1.13). In this case, a temperature gradient can be observed across two opposite sides of the material. *Materials with broken inversion symmetry and hosting phonons with finite PAM will be the subject of Chapter 4.2.6.*

1.4 Aim

The general aim of this thesis can be briefly divided into the following parts:

- Study the role of the main features of the density of states (like van Hove singularity and flat band) on the physical properties of the ideal two-dimensional kagome lattice. In this case, we use tight-binding model on Lieb and kagome lattices (both contain the ideal flat electronic band) to calculate the energy of the in-gap states induced by magnetic impurity (called Shiba states). Results published in Ref. [81] are presented in Sec. 4.1.1.

- Perform a comprehensive electronic and lattice dynamical study of real materials containing (ideal or distorted) kagome lattice. In this case, I will focus on the layered materials with CoSn-like structure: RhPb [82], CoGe [83], and FeGe [84]. Initially, all of them

were recognized to possess P6/mmm symmetry, but our calculations show some phonon instability. Results are presented in Sec. 4.2.1, 4.2.3, and 4.2.4.

- Look for the presence of flat bands, Dirac point, and nodal lines in the phonon dispersion relations and study their topological properties. The phonon dispersion curves can exhibit similar topological features like electronic band structure. We focus on this issue in the context of RhPb [82] and $T_3Pb_2Ch_2$ (T = Pd, Pt and Ch = S, Se) [85] – results are presented in Sec. 4.2.1 and 4.2.5, respectively.

- Theoretically predict the presence of chiral phonons (related to the circular motion of atoms around equilibrium positions) in materials containing kagome net and most importantly search for, or harness new materials that host phonons with a non-zero value of total angular momentum. In this context, we investigate $T_3Pb_2Ch_2$ (T = Pd, Pt and Ch = S, Se) [85] and ABi_2 (A = K, Rb, Cs) [86] and the results are presented in Sec. 4.2.5 and Sec. 4.2.6.

The theoretical details of the used methods can be found in Chapter 2. In Chapter 3, I present a short description of my cumulative contribution to the discussed papers, which are presented separately in Chapter 4.

Chapter 2

Theoretical background

2.1 Tight binding formulation

In this Section, we will apply tight-binding model to see how a flat band can occur in a generic tight-binding model. A general tight-binding Hamiltonian can be written as

$$H = -t \sum c_{ia}^{\dagger} c_{jb}, \tag{2.1}$$

where $c_{ia}^{\dagger}$ creates a particle of type a at site i, and c_{jb} annihilates a particle of type b at site j, t is the hopping parameter. To keep things simple, we take into account only the hopping between neighboring sites. The way to solve this Hamiltonian is to go to the momentum space through the Fourier transform, and the Hamiltonian in the Fourier space looks like

$$H = \sum_{\mathbf{k},a,b} c_a^{\dagger}(\mathbf{k}) h_{ab}(\mathbf{k}) c_b(\mathbf{k}), \tag{2.2}$$

here the sum is implied over the whole Brillouin Zone (BZ), and over all types of atoms (a,b). Now, we are seeking an eigenvalue of the Hamiltonian $h(\mathbf{k})$ which is independent of the momentum ($\mathbf{k}$). One trivial way to do this is to set the hopping parameter $t = 0$. It gives a flat band at zero energy. It just means that the electrons are sitting at the positions of their atoms and moving nowhere. This happens for systems with heavy fermions or in systems with large unit cells, with well-separated atoms. In these cases, the overlap between the wavefunctions of two electrons from neighboring sites vanishes. But this is a rather boring solution. Another route towards finding a flat band is to notice that the eigenfunction of the Hamiltonian h($\mathbf{k}$) can be expressed as a function of momentum as $\epsilon(\mathbf{k})$. So, if we perform a transformation which takes the Hamiltonian h($\mathbf{k}$) to $\dfrac{h(\mathbf{k})}{\epsilon(\mathbf{k})}$, and provided that $\epsilon(\mathbf{k})$ is separated from rest of the band structure, this particular band can be made flat. But when we translate the Hamiltonian transformation in real space, it gives an exponentially decaying hopping term and requires that $\epsilon(\mathbf{k})$ is separated from the rest of the bands by a band gap. So, in principle, any band that is separated from the other bands by a gap can be made flat with the introduction of an exponentially

decaying hopping parameter [87]. But in certain lattices, like the kagome lattice, a flat band arises naturally in the band structure, and also it touches the neighboring band at a certain point in the Brillouin zone. Hence, it does not necessarily have to be separated from the rest of the spectrum by a gap. To theoretically show how a flat band and Dirac point appear in the band structure of the kagome lattice, I give here a short description of the tight binding band structure of the kagome lattice.

Kagome lattice (shown in Fig. 1.1) contains three equivalent sites per unit cell. The lattice vectors are shown by vectors $\vec{d_1} = a(1,0)$ and $\vec{d_2} = a\left(\frac{1}{2}, \frac{\sqrt{3}}{2}\right)$. We consider a general tight binding Hamiltonian given by Eq. (2.1), where a,b $\in$ {A, B, C}. In the following description, we will consider only nearest-neighbor hopping. The best way to solve this is to Fourier transform to the momentum space. However, the translational symmetry is present in the kagome lattice due to the presence of more than one atom in the unit cell. But the atoms of one particular type (say A) form a translationally invariant triangular lattice system amongst the atoms of the same kind. So to go to the momentum space, we need to define the Fourier transform separately for each type of atom in the unit cell

$$c_{is}^{\dagger} = \frac{1}{N} \sum_{\mathbf{k}} \exp(i\mathbf{k} \cdot \mathbf{R}_i) c_{\mathbf{k}s}^{\dagger}, \tag{2.3}$$

where $s \in \{A, B, C\}$. After taking the Fourier transform, one can obtain

$$H = \sum_{\mathbf{k},a,b} c_{\mathbf{k}a}^{\dagger}\ h_{\mathbf{k},ab}\ c_{\mathbf{k}b} = \sum_{\mathbf{k}} \mathbf{c}_{\mathbf{k}}^{\dagger}\ \mathbf{h}_{\mathbf{k}}\ \mathbf{c}_{\mathbf{k}}, \tag{2.4}$$

where $\mathbf{c}_{\mathbf{k}}^{\dagger} = \left(c_{\mathbf{k}A}^{\dagger}\ c_{\mathbf{k}B}^{\dagger}\ c_{\mathbf{k}C}^{\dagger}\right)$, and

$$\mathbf{h}_{\mathbf{k}} = \begin{pmatrix} 0 & -2t\cos(\frac{k_x a}{2}) & -2t\cos((k_x + \sqrt{3}k_y)\frac{a}{4}) \\ -2t\cos(\frac{k_x a}{2}) & 0 & -2t\cos((k_x - \sqrt{3}k_y)\frac{a}{4}) \\ -2t\cos((k_x + \sqrt{3}k_y)\frac{a}{4}) & -2t\cos((k_x - \sqrt{3}k_y)\frac{a}{4}) & 0 \end{pmatrix}. \tag{2.5}$$

The eigenvalues can be obtained by diagonalizing $\mathbf{h}(\mathbf{k})$, which are

$$\varepsilon_{\mathbf{k}}/t = +2, -1 \mp \sqrt{1 + \cos\left(\frac{k_x a}{2}\right) \cos\left((k_x + \sqrt{3}k_y)\frac{a}{4}\right) \cos\left((k_x - \sqrt{3}k_y)\frac{a}{4}\right)}. \tag{2.6}$$

The flat conduction band occurs due to the constant, positive eigenvalue. We also notice that the two dispersive bands meet each other at a linear band crossing point below the Fermi level. However, note that an exactly flat band throughout the Brillouin Zone (BZ) exists in the tight binding description only when we consider the nearest neighbor interaction. The moment we switch on the next-nearest neighbor term, the band becomes dispersive [88]. However, it remains dispersionless along some paths of the BZ.

2.2 Mean field description of superconductivity

In a metal, if the temperature is lowered, the interacting electrons of the system stabilize in a highly degenerate ground state and give rise to a resistanceless flow of current known as superconductivity. The theory of superconductivity is well understood within the framework of Bardeen–Cooper–Schrieffer (BCS) theory. The type of superconductivity this theory explains very well is known as s-wave superconductivity. One part of the thesis deals with the scenario where a magnetic impurity is placed on top of an s-wave superconductor. The details of this particular work are presented in Chapter 4. In this Section, we talk about some basics of BCS theory.

According to the BCS theory of superconductivity, as the temperature of the system is lowered below the critical temperature, electrons with opposite spin and momentum pair up and form a 'Cooper pair'. These Cooper pairs, being bosons, then condense into the ground state of the material, giving rise to superconductivity. Once the superconductivity kicks in, the Hamiltonian describing the BCS superconductivity can be written as

$$H = -t\sum_{ij\sigma} c^{\dagger}_{i\sigma}c_{j\sigma} + \sum_{i}\Delta_i\left(c^{\dagger}_{i\uparrow}c^{\dagger}_{i\downarrow} + h.c.\right), \tag{2.7}$$

where $c^{\dagger}_{i\sigma}$ creates an electron with spin σ at site i, t is the hopping parameter and $\Delta_i = \langle c_{i\downarrow}c_{i\uparrow}\rangle$ is a mean-field parameter describing the correlation between electrons forming the Cooper pair. We will diagonalize this Hamiltonian in real space, keeping in mind that our main goal is to put an impurity on the system that breaks the translational symmetry. And, for a system with broken translational invariance, transforming to momentum space does not make the problem any simpler. To diagonalize the Hamiltonian we perform the Bogoliubov-de-Gennes (BdG) transformation:

$$c_{i\sigma} = \sum_{n}\left(u_{in\sigma}\gamma_{n\sigma} - \sigma v^{*}_{in\sigma}\gamma^{\dagger}_{n\bar{\sigma}}\right). \tag{2.8}$$

I wish to make the Hamiltonian diagonal in the new transformed basis γ:

$$H' = \sum_{n\sigma} E_{n\sigma}\gamma^{\dagger}_{n\sigma}\gamma_{n\sigma}. \tag{2.9}$$

In the next step, we compute $[c_{i\sigma}, H]$ and express the results in terms of γ and $\gamma^{\dagger}$. Equating this with $[c_{i\sigma}, H']$, we can obtain

$$E_{n\sigma}\begin{pmatrix} u_{in\sigma} \\ v_{in\bar{\sigma}} \end{pmatrix} = \sum_{j}\begin{pmatrix} H_{ij\sigma} & D_{ij} \\ D^{*}_{ij} & -H^{*}_{ij\bar{\sigma}} \end{pmatrix}\begin{pmatrix} u_{jn\sigma} \\ v_{jn\bar{\sigma}} \end{pmatrix}, \tag{2.10}$$

with $D_{ij} = \Delta_i\delta_{ij}$ (superconducting term), and $H_{ij\sigma} = -t\delta_{\langle i,j\rangle}$ (kinetic term), where $\langle i,j\rangle$

denotes neighbouring sites. This is the celebrated BDG equation. If we have a system with N lattice sites, then the eigenspectrum of the Hamiltonian can be obtained by diagonalizing the $N \times N$ matrix on the right-hand side. Once we have the eigenvalues $E_{n\sigma}$, a very important quantity called the local density of states can be obtained by using

$$\rho_i(\omega) = \sum_{n\sigma} \left[|u_{in\sigma}|^2 \delta(\omega - E_{n\sigma}) + |v_{in\sigma}|^2 \delta(\omega + E_{n\bar{\sigma}}) \right]. \tag{2.11}$$

2.3 Density functional theory

A solid consists of a periodic array of atoms, more precisely it consists of almost immobile nuclei and charge carrier electrons that revolve around the nuclei. So, in general, if we want to discuss the properties of a solid, we should start by writing a many-body Schrödinger equation which contains both electronic and nuclear degrees of freedom. The first approximation made towards solving this equation is called the Born-Oppenheimer approximation. Under this approximation, all nuclei are assumed to be frozen at particular positions of the solid. So, under this approximation, the only degrees of freedom that remain necessary to describe the properties of a solid are the electronic degrees of freedom. And the many-body Schrödinger equation looks like

$$\hat{H}\mathbf{\Psi} = \left[-\sum_i \frac{\hbar^2}{2m} \nabla_i^2 + \sum_i \mathbf{V}(\mathbf{r}_i) + \sum_{i<j} \mathbf{U}(|\mathbf{r}_i - \mathbf{r}_j|) \right] \mathbf{\Psi} = E\mathbf{\Psi}. \tag{2.12}$$

$\mathbf{V}$ contains all the information about the influence of the nuclei on the electrons, and this is a system-dependent term, whereas $\mathbf{U}$ is the Coulomb interaction between the electrons, which is the same for all the systems. For a system containing N particles, $\mathbf{\Psi}$ is a 3N component wavefunction. To get an idea of the complexity of this problem, let's think of a simple scenario of one dimension, with N interacting electrons. In general, for an interacting system, an electron can interact with any other (N-1) number of electrons present in the system. If we want to solve this problem on a computer, we need to store one e-e interaction in one bit. So, for N electrons, to store just the information of all possible interactions, we will need $N^{(N-1)}$ bits. For a single sodium atom (Na), this means 11^{10}. This is a gigantic number and at first sight, the problem seems unsolvable for real material! This is where the density functional theory (DFT) comes to the rescue, thanks to Hohenberg, Kohn, and Sham. The foundation of DFT lies in two fundamental theorems:

- All the physical quantities of a system can be unequivocally determined by the density of electrons in the ground state. Equivalently, there exists a one-to-one mapping between the density of the ground state and the ground state wavefunction [89].
- The ground state density is the one that minimizes the energy functional [90].

So, to solve the many-particle interacting system, we need to consider all the measurable quantities, in particular, energy as a function of the density of the electrons. Symbolically, the

energy of the system, in terms of the density $n(\mathbf{r})$ can be written as

$$E[n(\mathbf{r})] = T[n(\mathbf{r})] + V[n(\mathbf{r})] + U[n(\mathbf{r})], \tag{2.13}$$

where the first term is the kinetic energy, the second term represents the external potential (this includes the attractive Coulomb interaction by the nuclei too), and the third term represents the Coulomb interaction between the electrons. This can be rearranged as

$$\begin{aligned} E[n(\mathbf{r})] &= T[n(\mathbf{r})] + V[n(\mathbf{r})] + U[n(\mathbf{r})] && (2.14)\\ &= T_s + V + V_H + \{(T - T_s) + (U - V_H))\} && (2.15)\\ &= T_s + V + V_H + E_{xc}. && (2.16) \end{aligned}$$

The term V_H denotes the direct Coulomb interaction amongst electrons, T_s represents the kinetic energy of the free electrons, and E_{xc} contains all the exchange and correlation interactions. The very essence of the Kohn-Sham (KS) theorem is that a many-body problem of interacting electrons can be brought into a problem of a single particle moving in an effective potential $V + V_H + E_{xc}$. So that, in terms of the single particle wavefunctions ϕ_i and density $n(\mathbf{r})$, we can write

$$T_s = -\frac{1}{2}\sum_{i=1}^{N}\int \phi_i^*(\mathbf{r})\nabla^2\phi_i(\mathbf{r})d\mathbf{r},\ V_H = \frac{1}{2}\int\left[\frac{n(\mathbf{r})n(\mathbf{r}')}{|\mathbf{r}-\mathbf{r}'|}\right]d\mathbf{r}d\mathbf{r}',\ V[n(\mathbf{r})] = \int v(\mathbf{r})n(\mathbf{r})d\mathbf{r} \tag{2.17}$$

once we vary the energy $E[n(\mathbf{r})]$ with respect to the density n($\mathbf{r}$), we can obtain the celebrated Kohn-Sham equation

$$\left[-\frac{\hbar^2}{2m}\nabla^2 + v_{eff}(\mathbf{r})\right]\phi_i(\mathbf{r}) = \epsilon_i\phi_i(\mathbf{r}) \equiv H_{eff}(\mathbf{r})\phi_i(\mathbf{r}) = \epsilon_i\phi_i(\mathbf{r}), \tag{2.18}$$

where the effective potential v_{eff} is given by

$$v_{eff}(\mathbf{r}) = v(\mathbf{r}) + \int\frac{n(\mathbf{r}')}{|\mathbf{r}-\mathbf{r}'|}d\mathbf{r}' + v_{xc}(\mathbf{r}), \tag{2.19}$$

with $v_{xc}(\mathbf{r}) = \dfrac{\partial E_{xc}}{\partial n(\mathbf{r})}$. Once we have solved the KS equation, we can obtain the electron density as

$$n(\mathbf{r}) = \sum_{i}^{N}|\phi_i(\mathbf{r})|^2, \tag{2.20}$$

and once we know $n(\mathbf{r})$, we can compute all the measurable quantities from it. However, we notice that the effective potential v_{eff} is itself a function of density, $n(\mathbf{r})$. So, in practice, the KS equation is solved iteratively. We take an initial guess for the density $n(\mathbf{r})$, this gives us v_{eff}, and this in turn gives the orbitals, $\phi_i(\mathbf{r})$ from the KS equation. We then use these $\phi_i(\mathbf{r})$ to build the density through 2.20 and continue the same process again until a desired limit of

accuracy is reached.

The only remaining problem now is to fix an expression for the highly non-local exchange-correlation energy E_{xc}. There are two most widely known ways of fixing them. One is called local density approximation (LDA). The second one is called generalized gradient approximation (GGA). Under LDA, one approximates E_{xc} with the exchange-correlation energy of a homogeneous electron gas:

$$E_{xc} = \int d\mathbf{r}\ n(\mathbf{r})\epsilon_{xc}^{hom}[n(\mathbf{r})], \tag{2.21}$$

where ϵ_{xc}^{hom} is the exchange-correlation energy of a homogeneous electron gas with this particular density $n = n(\mathbf{r})$. To obtain a more realistic situation, in GGA, the exchange-correlation energy is thought as a function of the gradient of $n(\mathbf{r})$ too, to better account for the variation of density over space. So in GGA,

$$E_{xc} = \int d\mathbf{r}\ n(\mathbf{r})\epsilon_{xc}^{hom}[n(\mathbf{r}), \nabla n(\mathbf{r})]. \tag{2.22}$$

In practice, $\epsilon_{xc}^{hom}[n(\mathbf{r}), \nabla n(\mathbf{r})]$ can be parameterized in several ways. The most famous one, and the parametrization used in this thesis is called Perdew–Burke–Ernzerhof (PBE) parametrization [91].

2.3.1 Electronic band structure calculation

I now briefly discuss how using the KS equation (2.18) one can get the band structure of a solid. The first step is to write the wavefunction $\phi_n(\mathbf{r})$ in the Fourier basis:

$$\phi_n(\mathbf{r}) = \frac{1}{\sqrt{V}} \sum_{\mathbf{q}} c_{n,\mathbf{q}} \exp(i\mathbf{q}\cdot\mathbf{r}) \equiv |\phi_n\rangle = \sum_{\mathbf{q}} c_{n,\mathbf{q}} |\mathbf{q}\rangle, \tag{2.23}$$

where V is the volume of the material and $|\mathbf{q}\rangle$ are the orthonormal set of basis. Applying this transformation, one can rewrite the KS equation (2.18) as

$$\sum_{\mathbf{q}} \langle \mathbf{q}'|H_{eff}(\mathbf{r})|\mathbf{q}\rangle c_{n,\mathbf{q}} = \epsilon_n\ c_{n,\mathbf{q}'}. \tag{2.24}$$

The potential $v_{eff}(\mathbf{r})$ has the periodicity of the lattice, so it can be written as

$$v_{eff}(\mathbf{r}) = \sum_m v_{eff}(\mathbf{G}_m) \exp(i\mathbf{G}_m\cdot\mathbf{r}), \tag{2.25}$$

where $\mathbf{G}_m$ are the reciprocal lattice vectors. Defining $\mathbf{q} = \mathbf{k} + \mathbf{G}_m$ and $\mathbf{q}' = \mathbf{k} + \mathbf{G}'_m$, from Eq. (2.24) and (2.25) one can easily derive

$$\sum_m H_{m,m'}(\mathbf{k}) c_{n,m'}(\mathbf{k}) = \epsilon_n(\mathbf{k}) c_{n,m'}(\mathbf{k}), \tag{2.26}$$

where $H_{m,m'}(\mathbf{k}) = \langle \mathbf{k}+\mathbf{G}_m | H_{eff} | \mathbf{k}+\mathbf{G}'_m \rangle = \frac{\hbar^2}{2m}|\mathbf{k}+\mathbf{G}_m|^2\delta_{m,m'} + v_{eff}(\mathbf{G}_{m'}-\mathbf{G}_m)$. We wrote ϵ_n as a function of $\mathbf{k}$ just to emphasize the fact that the KS equation in the momentum space (2.26) should be solved for one particular value of momentum $\mathbf{k}$, giving the value of energy for that particular momentum. Thus to get the value of energy over the entire Brillouin zone, one must form a $\mathbf{k}$ grid and numerically solve equation (2.26) for different values of $\mathbf{k}$.

2.3.2 Pseudopotential

The problem that we need to take care of right now is the problem of valence electrons. There are two types of electrons present in the system: 1) the core electrons, bound to the core nuclei; 2) the valence electrons living in the outer shells. As we approach the atomic core, the valence electron wave function oscillates very rapidly, hence we require a lot of Fourier components for the expansion of the wavefunction in Eq. (2.23). One way to circumvent this problem is to notice that, the role of the core electrons is to screen the atomic nucleus so that the outer shell electrons see the (nucleus + core electron) system as a core with a 'screened charge'. Hence, to correctly treat these core electrons, we replace the potential that diverges at the core, with another potential that varies very slowly as we approach the nucleus (Fig. 2.1). This also replaces the highly oscillating electronic wavefunction with a smoothly varying wavefunction. In the final step, we demand that both the original and final potential have the same form outside some cutoff radius. The potential so obtained is called a pseudo-potential and the wavefunction is called a pseudo wavefunction. The pseudo-potentials used in this thesis are ones obtained using the so-called projector augmented-wave (PAW) method. In this particular method [92], both the valence and core electrons are expressed in the partial wave basis and smooth valence electron wavefunction as shown in Fig. 2.1 can be obtained.

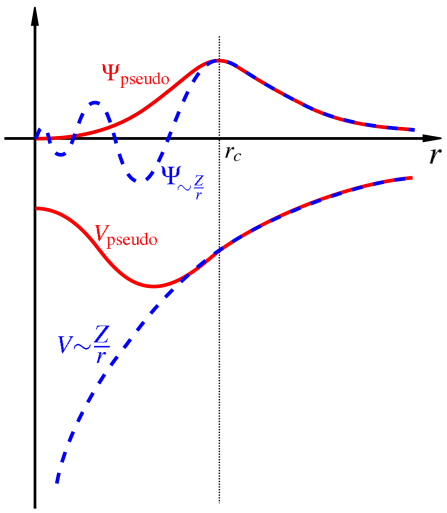

Figure 2.1: The actual potential and wavefunction are shown in blue dashed lines and the affected pseudo-potential and pseudo-wavefunction are shown in red lines. Picture courtesy Wikipedia.

2.3.3 Surface states

In this Section, I will briefly discuss how using the results of *ab initio* calculations one can compute the surface states of a material. This, in practice, is done through the combination of softwares WANNIER90 [93] and WANNIERTOOLS [94]. As a starting point we notice that, due to the lattice periodicity, one can write the KS wavefunctions $\phi_n(\mathbf{r})$ as

$$\phi_n(\mathbf{r}+\mathbf{R}) = \exp(\mathbf{k}\cdot\mathbf{R})\ \phi_n(\mathbf{r}). \tag{2.27}$$

To make this $\mathbf{k}$ dependence explicit, we now write $\phi_n(\mathbf{r})$ as the Bloch bands $\phi_{n\mathbf{k}}(\mathbf{r})$. These Bloch bands are then expressed in terms of the Wannier orbitals

$$\omega_{n\mathbf{R}}(\mathbf{r}) = \frac{V}{(2\pi)^3}\int_{BZ}\sum_m U^{\mathbf{k}}_{mn}\phi_{m\mathbf{k}}(\mathbf{r})e^{-i\mathbf{k}\cdot\mathbf{R}}d\mathbf{r}, \tag{2.28}$$

where V is, as usual, the system volume. Wannier orbitals $\omega_{n\mathbf{R}}(\mathbf{r})$ are molecular orbitals, localized in space at the lattice position. Different orbitals localized at different lattice points are orthogonal to each other. The Bloch orbitals $\phi_n(\mathbf{r})$ are not unique. They are undetermined upto a phase factor $e^{i\phi_n(\mathbf{k})}$. Due to this indeterminacy, there is huge freedom in the choice of the unitary matrix $U^{\mathbf{k}}_{mn}$ which leads to different expressions for Wannier orbitals $\omega_{n\mathbf{R}}(\mathbf{r})$. Thus the value of this mixing matrix $U^{\mathbf{k}}_{mn}$ is chosen in such a way that it minimizes the spread of the Wannier function and makes it as localized as possible. Defining the spread of the Wannier Function (WF) as

$$\Omega = \sum_n \left[\langle\omega_{n0}(\mathbf{r})|r^2|\omega_{n0}(\mathbf{r})\rangle - |\langle\omega_{n0}(\mathbf{r})|\mathbf{r}|\omega_{n0}(\mathbf{r})\rangle|^2\right] = \sum_n \left[\langle r^2\rangle_n - |\bar{\mathbf{r}}_n|^2\right]. \tag{2.29}$$

The integral is solved numerically, and for that, a dense k-point mesh is chosen. With a chosen k-point mesh, the expression for Ω (2.29) is written in terms of the matrix elements

$$M^{(\mathbf{k},\mathbf{b})}_{mn} = \langle u_{m,\mathbf{k}}|u_{n,\mathbf{k}+\mathbf{b}}\rangle, \tag{2.30}$$

where $\mathbf{b}$ is a vector connecting two neighbouring $\mathbf{k}$ points in the $\mathbf{k}$ mesh. Once it is done, we choose the following matrix as the initial guess for $U^{\mathbf{k}}_{mn}$:

$$A^{(\mathbf{k})}_{mn} = \langle\psi_{m\mathbf{k}}|g_n\rangle, \tag{2.31}$$

where $|g_n\rangle$ are some trial localised orbitals. The matrices $\mathbf{M}$ and $\mathbf{A}$ are found from *ab initio* calculations. For example, in VASP, they can be generated using the tag 'LWANNIER90' in the INCAR file. $\mathbf{A}$ is then used as the initial guess for U. Then after finding the Wannier orbitals using (2.28), the spread Ω is then minimized numerically to find the value of U and consequently the Wannier orbitals $\omega_{n\mathbf{R}}(\mathbf{r})$. But in practice, the Wannier orbitals are not required to calculate the surface states. We need the tight-binding Hamiltonian, the Hamiltonian written in the Wannier basis, $\omega_{n\mathbf{R}}$. That can be done easily once we have the matrix $\mathbf{U}^{\mathbf{k}}$. Using this, we can rotate the Hamiltonian to the Wannier basis, from the Bloch basis:

$$H^W(\mathbf{k}) = (U^{\mathbf{k}})^\dagger H(\mathbf{k})(U^{(\mathbf{k})}), \tag{2.32}$$

where $H_{mn}(\mathbf{k}) = \epsilon_m(\mathbf{k})\delta_{mn}$. Next, we bring it to the real space using the Fourier transform:

$$H^W_{nm}(\mathbf{R}) = \frac{1}{N_0}\sum_{\mathbf{k}} e^{-i\mathbf{k}\cdot\mathbf{R}} H^W_{nm}(\mathbf{k}), \tag{2.33}$$

where N_0 is the number of real space lattice vectors, conjugate to the chosen $\mathbf{k}$-point grid. This is the tight binding Hamiltonian, which is used as an input to the software WannierTools in the next step.

The method WannierTools uses to calculate the surface states is called surface Green's function method for a semi-infinite system. In this description, a solid with a surface is thought of as a semi-infinite stack of layers called principal layers. A principle layer consists of a bunch of atomic layers in a way that only the principle layers, neighbor to each other can interact [95]. If we denote the m'th atomic orbital of l'th atomic layer, belonging to the n'th principle layer as $\phi^{lm}_n(\mathbf{k})$, then the Bloch state for the n'th principle layer can be written as

$$\mathbf{\Psi}_n(\mathbf{k}_\parallel) = \begin{pmatrix} \phi^{11}_n(\mathbf{k}_\parallel) \\ \vdots \\ \phi^{lm}_n(\mathbf{k}_\parallel) \end{pmatrix}, \tag{2.34}$$

where

$$\phi^{lm}_n(\mathbf{k}_\parallel) = \frac{1}{\sqrt{N_\parallel}}\sum_{\mathbf{R}_\parallel} \exp(i\mathbf{k}_\parallel\cdot\mathbf{R}_\parallel)\phi^{lm}_n(\mathbf{R}_\parallel), \tag{2.35}$$

and $N_\parallel$ is the number of atoms and $\mathbf{R}_\parallel$ denotes the lattice vector in the plane. To find the surface states, we first find the surface Green's function and its imaginary part gives us the spectral function of the corresponding surface states. So, in principle, we need to solve Green's equation $(\omega - H^W)G(\omega) = \mathbb{1}$, where H^W is the Hamiltonian in the maximally localized Wannier function basis. Taking the matrix elements of this equation in the Bloch state (2.34) gives rise to a chain of equations [96]

$$(\omega - H^W_{00})G_{00} = 1 + H^W_{01}G_{10} \tag{2.36}$$

$$(\omega - H^W_{00})G_{10} = H^{W\dagger}_{10}G_{00} + H^W_{01}G_{20} \tag{2.37}$$

$$\vdots$$

$$(\omega - H^W_{00})G_{n0} = H^{W\dagger}_{10}G_{n-1,0} + H^W_{01}G_{n+1,0}, \tag{2.38}$$

where $n = 0$ denotes the principal layer of the surface, and

$$H^W_{nn'}(\mathbf{k}_\parallel) = \langle \mathbf{\Psi_n}(\mathbf{k}_\parallel)|H^W|\mathbf{\Psi_{n'}}(\mathbf{k}_\parallel)\rangle \tag{2.39}$$

$$, G_{nn'}(\omega, \mathbf{k}_\parallel) = \langle \mathbf{\Psi_n}(\mathbf{k}_\parallel)|G(\omega)|\mathbf{\Psi_{n'}}(\mathbf{k}_\parallel)\rangle. \tag{2.40}$$

These equations need to be solved iteratively. But in practice, this is a very computationally expensive process. To go around this difficulty, one introduces a pair of effective principal layers, with some interaction between them, in place of the original layer. This results in the doubling of the lattice vector. This process of doubling is continued until the interaction between two layers almost vanishes. So at the end of n iterations, one has a system whose lattice constant is 2^n times the lattice constant of the original system and the number of layers replacing the original layer is also 2^n. This process of introducing extra layers, after i iterations, reduces Eq. (2.38) to

$$\alpha_i = \alpha_{i-1}(\omega - \epsilon_{i-1})^{-1}\alpha_{i-1} \tag{2.41}$$

$$\beta_i = \beta_{i-1}(\omega - \epsilon_{i-1})^{-1}\beta_{i-1} \tag{2.42}$$

$$\epsilon_i = \epsilon_{i-1} + \alpha_{i-1}(\omega - \epsilon_{i-1})^{-1}\beta_{i-1} + \beta_{i-1}(\omega - \epsilon_{i-1})^{-1}\alpha_{i-1} \tag{2.43}$$

$$\epsilon_i^s = \epsilon_{i-1}^s + \alpha_{i-1}(\omega - \epsilon_{i-1})^{-1}\beta_{i-1}, \tag{2.44}$$

with the initial values $\epsilon_0 = \epsilon_0^s = H_{00}^W$, $\alpha_0 = H_{01}^W$ and $\beta_0 = H_{01}^{W\dagger}$. The iteration is repeated until $\epsilon_i^s \simeq \epsilon_{i-1}^s$. In the end, the surface Green's function ($G_s(\mathbf{k}_\parallel, \omega)$) and the bulk Green's function ($G_b(\mathbf{k}_\parallel, \omega)$) can be obtained as:

$$G_s(\mathbf{k}_\parallel, \omega) \simeq (\omega - \epsilon_i^s)^{-1} \tag{2.45}$$

$$G_b(\mathbf{k}_\parallel, \omega) \simeq (\omega - \epsilon_i)^{-1}. \tag{2.46}$$

Finally, the surface spectral function can be obtained as the imaginary part of the Green's function

$$\mathbf{A}(\mathbf{k}_\parallel, \omega) = -\frac{1}{\pi}\lim_{\eta\to 0} Im\ Tr\ G_s(\mathbf{k}_\parallel, \omega + i\eta). \tag{2.47}$$

2.4 Lattice dynamics

The lattice dynamical properties of a solid are described in terms of a bunch of quasiparticles named phonons. Phonons are the collective excitation of a periodic solid medium. Any properties of a solid arising from the vibration of lattice, such as thermal properties, phase stabilization, and structural phase transition, can be studied via an analysis of phonons. In the following paragraphs, I will discuss how the theoretical properties of phonons are studied.

The total energy of a solid can be expressed as a function of lattice positions of the constituent atoms $\mathbf{R}_m^\mu$, where μ represents the type of atom in the m'th unit cell. The dynamical properties of a lattice arise due to the vibration of atoms around their equilibrium positions. So in general, an atom is displaced from its initial position $\mathbf{R}_m^{0\mu}$ to a final position $\mathbf{R}_m^\mu$, then the total energy of the system E can be expanded in a Taylor series in the lattice displacement

$U^{\mu}_{m} = \mathbf{R}^{\mu}_{m} - \mathbf{R}^{0\mu}_{m}$:

$$E = E_0 + \sum_{N=2}^{\infty} \frac{1}{N!} \sum_{m_1 \ldots m_N} \sum_{\mu_1 \ldots \mu_N} \sum_{\alpha_1 \ldots \alpha_N} \Phi^{\mu_1 \ldots \mu_N}_{m_1\alpha_1 \ldots m_N\alpha_N} U^{\mu_1}_{m_1\alpha_1} \ldots U^{\mu_N}_{m_N\alpha_N}, \tag{2.48}$$

where $\alpha_N = x, y, z$. E_0 is the energy of the system when all the atoms are at equilibrium positions and Φ is the N'th order derivative of total energy with respect to the lattice displacements, known as the interatomic force constants (IFC):

$$\Phi^{\mu_1 \ldots \mu_N}_{m_1\alpha_1 \ldots m_N\alpha_N} = \frac{\partial^N E}{\partial U^{\mu_1}_{m_1\alpha_1} \ldots \partial U^{\mu_N}_{m_N\alpha_N}}\Big|_{U^{\mu_1}_{m_1\alpha_1} = \ldots = U^{\mu_N}_{m_N\alpha_N} = 0}. \tag{2.49}$$

The Taylor sum is started from $N = 2$, because the expansion was carried out around the equilibrium lattice distribution, and at equilibrium, the first derivative of the function (E) with respect to its arguments (U) vanishes. The force on atoms, when they are displaced from the equilibrium position can be calculated using the Hellmann-Feynman theorem [97, 98] and Eq. (2.48)

$$F^{\mu}_{m\alpha} = -\frac{\partial E}{\partial U^{\mu}_{m\alpha}}. \tag{2.50}$$

If the temperature is sufficiently low, then we can keep only the lowest order term in Eq. (2.48) which is proportional to U^2. Given that the atomic displacement $U^{\mu_N}_{m_N\alpha_N}$ is way smaller than the lattice constant, we can neglect all the higher-order terms. An approximation of this kind is known as the harmonic approximation. Under this approximation, the Hellmann-Feynman force in the system (2.50) is linear in displacement $U^{\mu_N}_{m_N\alpha_N}$, and the equation governing the displacement of atoms from their equilibrium positions looks similar to the equation of a harmonic oscillator:

$$M_{\mu} \frac{\partial^2 U^{\mu}_{m\alpha}}{\partial t^2} = -\sum_{\beta,n,\nu} \Phi^{\mu\nu}_{m\alpha,n\beta} U^{\nu}_{n\beta}. \tag{2.51}$$

So similar to the harmonic oscillator, one can find normal modes with a specific energy and momentum as a solution of the above equation for the displacement, $U^{\mu}_{m\alpha}$. These normal modes are called phonons. And when we assume a plane wave with a particular momentum $\mathbf{k}$ and frequency ω as the solution to Eq. (2.51), one arrives at the equation defining the energy of different phonon modes

$$\omega^2(\mathbf{k}, j)\varepsilon(\mathbf{k}, j) = \mathbf{D}(\mathbf{k})\varepsilon(\mathbf{k}, j), \tag{2.52}$$

where $D(\mathbf{k})$ is the Fourier transform of the force constant matrix $\mathbf{\Phi}$, known as the dynamical

matrix

$$D(\mathbf{k}) = \frac{1}{\sqrt{M_\mu M_\nu}} \sum_m \Phi^{\mu,\nu}_{0,m} \exp[-2\pi i \mathbf{k} \cdot (\mathbf{R}^\mu_0 - \mathbf{R}^\nu_m)], \tag{2.53}$$

and $\varepsilon^\mu_\alpha(\mathbf{k}, j)$ is the polarization vector, denoting the displacement of μ'th atom along α direction. M_μ is the mass of the μ'th atom. So in the end diagonalizing the dynamical matrix $D(\mathbf{k})$ gives us an expression for the frequency of a phonon, $\omega(\mathbf{k}, j)$ with momentum $\mathbf{k}$ and branch number j. Given that, one can also obtain the phonon density of states as

$$g(\omega) = \sum_{\mathbf{k},j} \delta(\omega - \omega(\mathbf{k}, j)). \tag{2.54}$$

The force constant matrix is usually generated by *ab initio* packages like VASP and the dynamical matrix and the consequent frequency of phonon modes and the density of states are obtained using software like ALAMODE [99] and PHONOPY [100].

2.4.1 Chiral phonons

Chiral phonons are phonons with definite handedness, arising from the circular or elliptical vibrations of atoms around their equilibrium positions. Due to the handedness, to study the chirality of the phonons, the eigenvectors $\varepsilon^\mu_\alpha(\mathbf{k}, j)$ are treated in the same way as the eigenvectors of circularly polarized light. A circular polarization occurs when two oscillations, which are out of phase with each other, superimpose. So as a first step, we introduce the Jones vectors $\frac{1}{\sqrt{2}}(1, \pm i)^T$, where the upper sign denotes left circular polarization (LCP) and the bottom sign denotes the right circular polarization (RCP). In fact we can introduce the Jones vector for each atom and introduce the new basis $|R_1\rangle \equiv (1\ i\ 0 \dots\ 0)^T$, $|L_1\rangle \equiv (1\ -i\ 0 \dots\ 0)^T$, $|Z_1\rangle = (0\ 0\ 1 \dots\ 0)^T$. Here, I introduced the Jones vector in the x-y plane of the first atom and kept the z-direction intact. The phonon eigenvectors $\varepsilon^\mu_\alpha(\mathbf{k}, j) \equiv \varepsilon$ can then be expressed in this new basis:

$$\varepsilon = \sum_j (\alpha^R_j |R_j\rangle + \alpha^L_j |L_j\rangle + \alpha^Z_j |Z_j\rangle), \tag{2.55}$$

where $\alpha^P_j = \langle P_j | \mathbf{e} \rangle$ and $j \in [1 \dots N]$, and N being the number of atoms in the primitive cell. We then define the phonon circular polarization operator as

$$\hat{\mathbf{S}}^z_{ph} = \sum_j \hat{S}^z_j = \sum_j (|R_j\rangle\langle R_j| - |L_j\rangle\langle L_j|), \tag{2.56}$$

and we compute the polarization or the chirality of the j'th atom as the expectation value of this polarization operator

$$s^z_j = \hbar \mathbf{e}^\dagger \hat{\mathbf{S}}^z_{ph} \mathbf{e} = \hbar(|\alpha^R_j|^2 - |\alpha^L_j|^2). \tag{2.57}$$

Here, I assumed that the system is polarized in the z-direction. If $s_j^z = 0$, we say that the system is linearly polarized. If $s_j^z = \hbar$, then the atoms responsible for the generation of these phonons rotate in a perfectly circular orbit around their equilibrium positions, and if $|s_j^z| < \hbar$, then the orbit is elliptical. Hence, once the eigenvectors of the dynamical matrix are known through ALAMODE or PHONOPY, phonon chirality can be obtained using the procedure described above.

2.5 Numerical implementation

The method I used using the *ab initio* calculations to determine the phonon dispersions is called the direct method. There are ways in which the direct method is implemented. The first approach is called the frozen phonon approximation [101]. In this scheme, the lattice is distorted from its equilibrium position, and the phonon energy is derived as the difference between the original and the distorted structure, as a function of the lattice displacement. In the second approach [102], the Hellmann-Feynman forces on the atoms are calculated as the derivative of energy with respect to the displacement of the atoms (2.50). In our work, we use a variation of the direct method using the second scheme, introduced by Parlinski, Li, and Kawazoe [103]. In this method, at first, a supercell is built from the primitive cell. Usually, a cell or supercell with lattice constant ~ 10 Å is enough to get a bulk dispersion relation. After relaxing the supercell, a single atom is displaced from its equilibrium position. Then, following (2.51), this displaced atom exerts force on all the other atoms in the supercell. The number of required displacements is determined by the number of atoms in the unit cell and the lattice space group symmetry. In the next step, for each such displaced structure, using *ab initio* codes, the forces on each atom are determined using the Hellmann-Feynman theorem, and the force constant matrix is built afterward using PHONOPY or ALAMODE exploiting the linear dependence of the force on the displacement (2.51). Using a k-point grid and Fourier transform, the dynamical matrix is then built (2.53) and its eigenvalues give us the phonon dispersion relations (Eq. 2.52), and the eigenvectors can be used to determine the chirality (cf. 2.57).

Chapter 3

Cumulative contribution by the author

The next chapter contains an accumulation of all the original works, which align with the main theme of the topic of the thesis, done by the author during the period of PhD study. Depending on the used methodology, the works can be divided into two categories. Numerical tight binding calculations were used in Section 4.1, whereas density functional theory was used in the studies of Section 4.2.

In Section 4.1, we will see how the van Hove singularity (VHS) of hexagonal lattice, VHS and flat band singularity of kagome and Lieb lattice can be tuned to harness the coupling strength and localization of the Yu–Shiba–Russinov (YSR) bound state, to make them viable for application purposes [81]. Section 4.2.1 starts with experimentally verifying the space group symmetry of RhPb and goes on to theoretically find Dirac nodal lines and drumhead surface states connecting these degenerate lines [82]. Section 4.2.2 is about a quasi-2D system containing a kagome lattice. The main themes of this paper [104] are to theoretically investigate and confirm the space group symmetry of this material and reveal its quasi-2D nature. In Section 4.2.3, we study the pressure dependence ground state symmetry of CoGe [83]. We look for the mechanism behind the recently discovered charge density wave (CDW) in FeGe in Section 4.2.4 and reveal the role played by electron-electron correlation [84]. Both Section 4.2.5 and Section 4.2.6 investigate the presence of chiral phonons in materials containing kagome layer [85, 86]. In Section 4.2.6 we further propose new materials which can be used as a platform to study phonon quantum Hall effect [86].

Chapter 4

Collection of papers

4.1 Calculations based on tight binding model

4.1.1 Shiba states in systems with density of states singularities

S. Basak and A. Ptok, Phys. Rev. B **105**, 094204 (2022)

A single magnetic impurity, when coupled with a superconductor, creates a pair of bound in-gap states known as the Shiba states, localized at the position of the impurity. The crossing point of two such Shiba states is related to a quantum phase transition, at which the ground state spin of the system changes its value. The value of coupling strength for which this transition occurs is known as the critical coupling strength (J_c). In this paper, we investigate the role of various density of states (DOS) singularities on this phase transition point. An earlier study [22] had shown that the presence of van-Hove singularity can suppress the value of J_c. In this work, we go beyond this and study what happens in the presence of a flat band singularity, observed in the band structure of kagome and Lieb lattice. We further investigate how the result changes when we place the impurity at two nonequivalent lattice positions of the unit cell. Due to the unequal distribution of the spectral weight of the flat band, one can expect to find some interesting behaviors. To demonstrate the strong localization of these bound states, we compute the local density of states (LDOS) and plot them close to and away from the quantum phase transition point. In application, impurities with strong coupling to superconductor and long localization length are highly desired. Our work thus acts as a valuable guiding article for harnessing Shiba states for various application purposes.

Author's contribution: Writing numerical code to perform the calculations (band structures and density of states for non-interacting states, in-gap energy state energy, critical J_c, the local density of states of in-gap state, fitting the data, and finding the coherence length), analysis and discussion of the obtained results, preparation of the figures, preparation of the initial version of the manuscript, and participation in preparing the response for Referees.

Shiba states in systems with density of states singularities

Surajit Basak [*] and Andrzej Ptok [†]

Institute of Nuclear Physics, Polish Academy of Sciences, W. E. Radzikowskiego 152, PL-31342 Kraków, Poland

(Received 6 December 2021; revised 7 February 2022; accepted 23 March 2022; published 31 March 2022)

Magnetic impurities placed in the superconductor can lead to the emergence of Yu-Shiba-Rusinov bound states. Coupling between the impurity and the substrate depends on the density of states (DOS) at the Fermi level and can be tuned by DOS singularities. In this paper, we study the role of DOS singularities using the real space Bogoliubov–de Gennes equations for chosen lattice models. To uncover the role of these singularities (Dirac point, van Hove singularity, or the flat band), we study honeycomb, kagome, and Lieb lattices. We show that the properties of the Shiba state strongly depend on the type of lattice. Nevertheless some behaviors are generic, e.g., dependence of the critical magnetic coupling on the DOS at the Fermi level. However, the Shiba states realized in the Lieb lattice exhibit extraordinary properties, which can be explained by the presence of a few nonequivalent sublattices. Depending on the location of the magnetic impurity in the chosen sublattice, the value of critical magnetic coupling J_c can be reduced or enhanced when the flat band is located at the Fermi level. In this context, we also present differences in the local DOS and coherence lengths for different sublattices in the Lieb lattice.

DOI: 10.1103/PhysRevB.105.094204

I. INTRODUCTION

The interplay between a superconducting system and magnetic impurity can lead to the emergence of Yu-Shiba-Rusinov (YSR) bound states [1–3] (the Shiba states for short), due to local breaking of the Cooper pairs by the magnetic moment of the impurity [Fig. 1(a)]. This leads to the formation of in-gap states inside the superconducting gap, with spatially oscillating wave function [4]. Recent progress in the experimental techniques has resulted in increased experimental [5] as well as theoretical [6] attention in this field.

Dimensionality of the system plays a critical role in the formation of the Shiba state. The three-dimensional conventional superconductor shows a fast decay of the YSR states away from the magnetic impurity. Contrary to this, in the case of two-dimensional systems the YSR states are characterized by the long-range coherence length [7,8].

The YSR states can be observed experimentally within the topographic scanning tunneling microscopic (STM) imaging of the surface. It was first reported in the presence of Mn and Gd adatoms on the surface of a single-crystal Nb sample [9]. Increased resolution allows mapping of the YSR states occurring from individual orbitals of the atom. Such cases have been reported in transition metal atoms deposited on conventional superconductors (Pb [10–14] or Nb [15–18]). YSR states were also realized by depositing Fe on the $NbSe_2$ surface [7,19–21]. Similar observations can be made in the presence of magnetic molecules, such as (Mn, Cu, V, or Co) phthalocyanine [14,22–28] or (Fe or Mn) porphyrin [29–31]. Also, recently the fabrication of YSR states in the iron-based unconventional superconductor attracted a lot of attention [32–34].

The presence of artificial structures of magnetic atoms can lead to the emergence of in-gap Shiba bands. If the nontrivial topological phase is realized [35], the Majorana end modes can occur [36]. Recently this type of structures were realized in many experiments [37–43].

Motivation. In the simplest case, the magnetic impurity gives rise to a pair of in-gap states, symmetric in energy with respect to the Fermi level, characterized as YSR states. For the classical spin, the energies of the in-gap YSR states are given as

$$E_{\mathrm{YSR}} = \pm\Delta\frac{1-\alpha^2}{1+\alpha^2}, \tag{1}$$

where $\alpha^2 = \pi N(E_{\mathrm{F}})J$ is the dimensionless impurity coupling (neglecting Coulomb scattering), Δ is the superconducting gap, $N(E_{\mathrm{F}})$ denotes the density of states (DOS) at the Fermi level E_{F}, while J describes coupling between magnetic moment and electrons. At $J = J_c$ the YSR states cross the Fermi level [$E_{\mathrm{YSR}}(J_c) = 0$]. That point is related to the quantum phase transition (QPT), also known as the 0-π transition. During the QPT, the ground state is changed from the BCS-type spinless state (for the weak coupling $J < J_c$) to the singly occupied (spinful configuration (for strong coupling $J > J_c$) [44]. As we can see from Eq. (1), the value of J_c is proportional to $1/N(E_{\mathrm{F}})$. Indeed, previous study of the YSR states in the presence of the van Hove singularity (VHS) show that the tuning of $N(E_{\mathrm{F}})$ by the VHS can lead to enhanced J_c [45]. A similar observation was reported in the case of the critical temperature of the *s-wave* and *d-wave* superconductors on a square lattice, where it was shown that T_c can be tuned by increasing $N(E_{\mathrm{F}})$ [46]. Similarly for the hexagonal lattice,

[*] surajit.basak@ifj.edu.pl
[†] aptok@mmj.pl

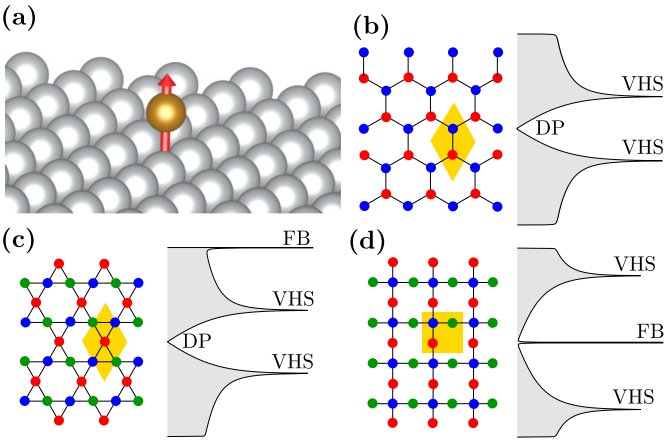

FIG. 1. (a) Schematic representation of the magnetic atom (brown ball) deposited on the superconducting surface (silver balls). Studies performed on two-dimensional lattices and their density of states: (b) hexagonal, (c) kagome, and (d) Lieb lattices. The colors of the dots (red, green, or blue) denote nonequivalent sites, while the yellow quadrangle marks the primitive unit cell. In the case of a hexagonal and a kagome lattice, the Dirac point (DP) is realized. The flat bands (FBs) are observed in the Lieb and kagome lattices. The saddle points in the band structures give rise to van Hove singularities (VHSs) in all lattices.

in the presence of the magnetic field, the VHS can lead to superconductivity reentrant behavior [47].

General behavior of the in-gap energies is well known from the milestone works of Yu, Shiba, and Rusinov [1–3]. The general J dependence of the bound state (in-gap) energies is given by Eq. (1). Similar behavior is observed also in the presence of several atoms, e.g., monoatomic chains [48,49], where in-gap states cross the Fermi level a few times. Moreover, this type of behavior of the in-gap state energies was observed experimentally in the case of a magnetic molecule of manganese phthalocyanine (MnPc) on a Pb(111) surface [23].

Another aspect of the Shiba states is strongly associated with the Fermi surface of the studied system [50]. Interestingly, the pattern of the localized state induced by the magnetic impurity reflects some properties of the Fermi surface of the system [51]. This is well visible in the star-shaped localization of the Shiba states around the magnetic impurity on a $NbSe_2$ [7] or La [8] surface, which is associated with a sixfold symmetry of the Fermi surface of these systems.

In this paper we study the role of DOS singularities on the YSR states using exact lattice models [Figs. 1(b)–1(d)]. These techniques allow us to study not only VHS [realized, e.g., in the honeycomb lattice [Fig. 1(b)], but also the role of flat bands [realized, e.g., in a kagome or Lieb lattice [52], presented in Figs. 1(c) and 1(d), respectively]. The flat bands can play an important role in the context of the recently discovered superconducting kagome systems (such as AV_3Sb_5 [53] or $LaRu_3Si_2$ [54]), artificial structures (like twisted bilayer graphene [55,56], or some type of heterostructures and interfaces [57]). Also, recent progress in the realization of artificial lattices [58] opens up a new opportunity to study the YSR states in the flat-band systems.

However, the DOS does not contain full information about the lattice, which can be important in the context of correct description of the Shiba states in real systems. As an example, this can be important in the context of the recent study of the Shiba states based on the Green's function approach [45,50]. In our study we analyze this problem, based on the real space tight-binding formulation. Our finding shows the important role played by the sublattices present in the system. Depending on the position of the magnetic impurity, the Shiba states can exhibit "extreme" behaviors, even within one specific lattice.

The paper is organized as follows. The theoretical background is presented in Sec. II. In Sec. III we present the numerical results and discussions. We conclude our study in Sec. IV.

II. THEORETICAL BACKGROUND

The system is described by the Hamiltonian

$$H = H_0 + H_{\mathrm{SC}} + H_{\mathrm{imp}}. \tag{2}$$

The first term describes the tight-binding model of the lattice (cf. Fig. 1):

$$H_0 = -t \sum_{\langle ij\rangle\sigma} \hat{c}^{\dagger}_{i\sigma}\hat{c}_{j\sigma} - \mu \sum_{i\sigma} \hat{c}^{\dagger}_{i\sigma}\hat{c}_{i\sigma}, \tag{3}$$

where $\hat{c}^{\dagger}_{i\sigma}$ ($\hat{c}_{i\sigma}$) denotes the creation (annihilation) operator an electron with spin σ at site i, t is the hopping integral between nearest neighbors $\langle i, j\rangle$, and μ is the chemical potential. The second term is responsible for superconductivity:

$$H_{\mathrm{SC}} = \sum_i (\Delta \hat{c}^{\dagger}_{i\uparrow}\hat{c}^{\dagger}_{i\downarrow} + \mathrm{H.c.}), \tag{4}$$

where Δ is the superconducting gap. The third term describes coupling of the magnetic impurity with the underlying lattice. In our investigation, we describe the magnetic impurity captured by H_{imp} as a classical spin aligned out of plane and only present on site [i.e., term proportional to $\delta(r_0 - r_i)$, where the subscript "0" denotes the impurity site]. In this case, the scattering potential at the position of the impurity is given as

$$H_{\mathrm{imp}} = K(\hat{c}^{\dagger}_{0\uparrow}\hat{c}_{0\uparrow} + \hat{c}^{\dagger}_{0\downarrow}\hat{c}_{0\downarrow}) - J(\hat{c}^{\dagger}_{0\uparrow}\hat{c}_{0\uparrow} - \hat{c}^{\dagger}_{0\downarrow}\hat{c}_{0\downarrow}), \tag{5}$$

where K denotes the nonmagnetic scattering potential, while J denotes the coupling strength between the electrons and the magnetic impurity. The classical magnetic impurity limit is technically achieved by taking $S \to \infty$ (large spin), while simultaneously letting $J \to 0$ so that $JS = \mathrm{const}$ [6]. Effectively, the classical magnetic impurity acts on the system in two ways: (i) by shifting the chemical potential (K term), which effectively leads to a modification of the number of electrons at site "0"; and (ii) by an on-site Zeeman-like magnetic field ($J \equiv JS$ term, where S is magnetic moment) [6].

The Hamiltonian (2) describing the inhomogeneous problem, can be diagonalized via the following unitary transformation:

$$\hat{c}_{i\sigma} = \sum_n (u_{in\sigma}\hat{\gamma}_{n\sigma} - \sigma v^{*}_{in\sigma}\hat{\gamma}^{\dagger}_{n\bar{\sigma}}), \tag{6}$$

where $\hat{\gamma}_n$ and $\hat{\gamma}^{\dagger}_n$ are quasiparticle fermionic operators, and $u_{in\sigma}$ and $v_{in\sigma}$ are the eigenvector coefficients. This leads to the

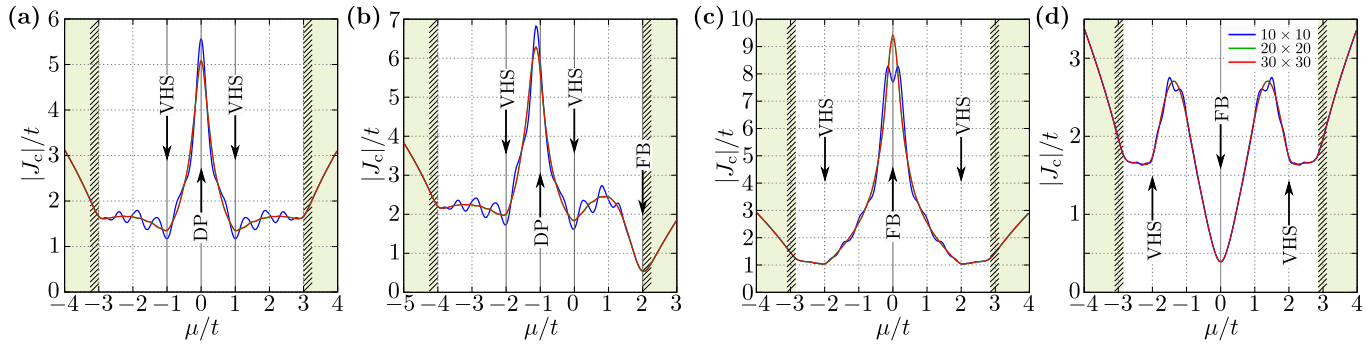

FIG. 2. Critical value of the magnetic coupling J, denoting phase transition, for different size lattices (as labeled). Results are shown for (a) hexagonal, (b) kagome, and (c),(d) Lieb lattices. For the Lieb lattice, the impurity is located at (c) the corner site or at (d) the edge site [i.e., blue and green/red sites in Fig. 1(d), respectively]. The chemical potentials for flat bands, van Hove singularities, and Dirac points, are marked as FB, VHS, and DP, respectively. Ranges of chemical potential which are out of range of the bands for given lattices are marked by green areas.

Bogoliubov–de Gennes (BdG) equations [59]:

$$\mathcal{E}_{n\sigma}\begin{pmatrix} u_{in\sigma} \\ v_{in\bar{\sigma}} \end{pmatrix} = \sum_j \begin{pmatrix} H_{ij\sigma} & D_{ij} \\ D^*_{ij} & -H^*_{ij\bar{\sigma}} \end{pmatrix}\begin{pmatrix} u_{in\sigma} \\ v_{in\bar{\sigma}} \end{pmatrix}, \tag{7}$$

where $H_{ij\sigma} = -t\delta_{\langle i,j\rangle} - [\mu + (K - \sigma J)\delta_{i0}]\delta_{ij}$ and $D_{ij} = \Delta_i\delta_{ij}$ denotes the kinetic and superconducting part of the Hamiltonian, respectively [60–62].

From the solution of the BdG equation (7) we can extract the local density of states (LDOS) for specified parameters of the system as [63]

$$\rho_i(\omega) = \sum_{n\sigma}\left[|u_{in\sigma}|^2\delta(\omega - \mathcal{E}_{n\sigma}) + |v_{in\sigma}|^2\delta(\omega + \mathcal{E}_{n\bar{\sigma}})\right], \tag{8}$$

while the total DOS is given as $N(\omega) = \sum_i \rho_i(\omega)$. The LDOS for $\omega = \pm E_{\mathrm{YSR}}$ denotes the localization of the YSR state in real space [64], and can be useful in coherence length study. In this case $\langle\rho_i(E_{\mathrm{YSR}})\rangle \propto \exp(-r/\zeta_c)$ denotes the wave function of the YSR states and can be used to estimate the coherence length ζ_c for a given lattice and Fermi level.

Numerical computations have been done at zero temperature $T = 0$ for the lattices with the periodic boundary conditions, containing $N_a \times N_b = 30 \times 30$ primitive unit cells. In the case of the honeycomb lattice this corresponds to 1800 sites, while for the kagome and Lieb lattices, we have 2700 sites. For simplicity and without loss of generality, we assume a constant value of $\Delta/t = 0.2$. Additionally, to study only the role of the DOS of the underlying system on the YSR states, we take $K = 0$. In numerical determination, we have replaced the Dirac δ function by the Lorentzian $\delta(\omega) = \eta/[\pi(\omega^2 + \eta^2)]$ with a small broadening $\eta = 0.05t$.

III. NUMERICAL RESULTS AND DISCUSSION

In our analysis, we consider honeycomb, kagome, and Lieb lattices. Each of them is formed by the unit cells containing more than one site, and as a consequence in the DOS a few bands can be distinguished. The honeycomb (kagome) lattice is formed by unit cells containing two (three) equivalent sites (in Fig. 1 represented by dots with different colors). In this case, one of the sublattices can be transformed to another by the combination of a few translation, rotation, or reflection operations. Contrary to this, the Lieb lattice is formed by unit cells containing two different types of sites. Two edge sites [green/red dots in Fig. 1(c)] are equivalent to each other, but nonequivalent to the corner site (blue dots). As a result, the Lieb lattice is characterized by two nonequivalent sublattices; the sublattice of the edge site cannot be transformed to the corner site sublattice, and vice versa. We will show that this characteristic feature of the Lieb lattice plays an important role in the realization of the Shiba states.

Depending on the lattice, in the DOS we can find a few interesting features. For example, honeycomb and kagome lattices contain Dirac points (DPs) at band touching points. Similarly, in the DOS of the kagome and Lieb lattices the flat-band (FB) feature can be distinguished. Additionally, the VHSs in the form of characteristic peaks in the DOS are visible for all lattices. As we can see, the DOSs exhibit similar behaviors regardless of the chosen lattice. However, the DOS do not contain the full information about the lattice (e.g., symmetry of the system, number of neighboring sites, existence of eventual sublattices, etc.). Despite the similarities in DOSs, the strong differences are well visible in the chemical potential dependence of the critical magnetic coupling J_c (Fig. 2) and the Shiba state energies $\pm E_{\mathrm{YSR}}$ (Fig. 3).

First, we notice that the J_c vs μ plot follows the same symmetry as the DOS (cf. Fig. 2 and Fig. 1). For honeycomb and Lieb lattices, the DOS is symmetric with respect to the center of the bandwidth (related to $\mu/t = 0$) and the same character is reflected in $J_c(\mu)$. Similarly, the asymmetric DOS of the kagome lattice is reflected in Fig. 2(b).

$J_c(\mu)$ exhibits a strong dependence on the position of the Fermi level which is related to μ (Fig. 2). However, the dependence of J_c on $N(E_F)$ is highly unexpected. In the case of honeycomb and kagome lattices [presented in Figs. 2(a) and 2(b), respectively], the presence of the DP with $N(E_F) = 0$ leads to the occurrence of a peak in J_c. Contrary to this, the presence of VHS leads to a relatively small reduction of J_c. The most important modification of J_c is introduced by the FB (theoretically with infinite DOS) in the kagome lattice. In this case, J_c decreases dramatically to its minimum value with respect to rest of the plot. Nevertheless, the most surprising results can be found in the Lieb lattice [Figs. 2(c) and 2(d)]. When impurity is located at the corner site, $J_c(\mu)$ exhibits

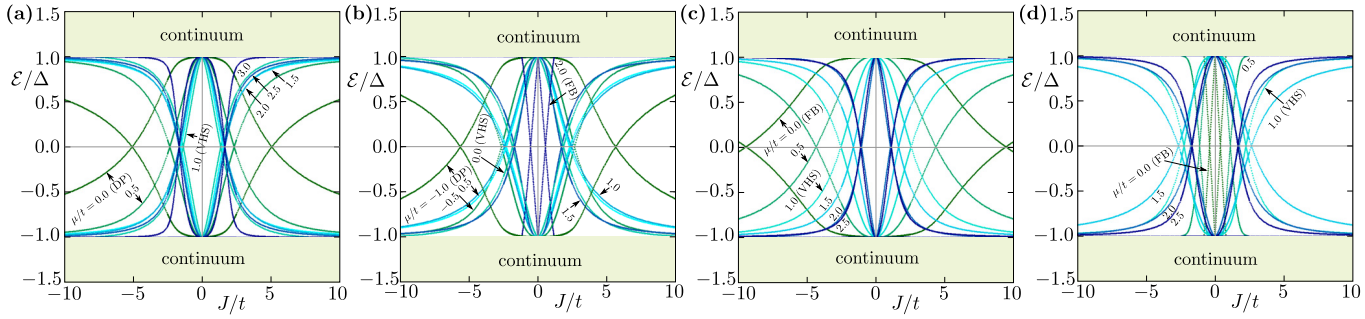

FIG. 3. In-gap spectrum of the Shiba states for different values of the chemical potential (as labeled) in the case of (a) hexagonal, (b) kagome, and (c),(d) Lieb lattices. For the Lieb lattice, the impurity was located in (c) the corner site or (d) the edge site [i.e., blue and green/red sites in Fig. 1(c), respectively]. The chemical potentials for flat bands, van Hove singularities, and Dirac points are marked as FB, VHS, and DP, respectively. Additionally, the green areas mark the ranges of energies for (out-gap) continuum states.

features similar to the honeycomb lattice [cf. Fig. 2(a) and Fig. 2(c)]. J_c reaches the maximum value when μ is located at the FB. Contrary to this, the impurity located at the edge site leads to opposite (expected) behaviors, i.e., a dramatic decrease of J_c for $\mu/t = 0$ (corresponding to the FB).

The results presented here are sensitive to the number of sites of the discussed system (cf. lines with different color in Fig. 2). Nevertheless, $J_c(\mu)$ has the same (qualitative) behavior independent of the size of the system, and describes the thermodynamic limit ($N_a \times N_b \to \infty$) relatively well for lattice with 30×30 unit cells. Similar effects can be observed with decreasing Δ, when the emergence of the superconducting phase (i.e., when Δ is comparable to the gap between states) strongly modifies states in the system.

The value of $J_c(\mu)$ is related to the Shiba state energy $\pm E_{\mathrm{YSR}}$ (Fig. 3). The reduced value of J_c induced by VHS or FB leads to a nearly linear dependence of E_{YSR} on coupling strength J. Similar features of the Shiba states in the presence of VHS were discussed by Uldemolins *et al.* in Ref. [45]. The authors found a strong reduction of J_c when the Fermi level was located at the VHS. In this case, the linearity of $E_{\mathrm{YSR}}(J)$ was also reported around J_c. In our case, the presence of a FB allows the existence of the Shiba state with exactly linear $E_{\mathrm{YSR}}(J)$ dependence [cf. Fig. 3(b) or Fig. 3(d)]. For a system with small DOS (e.g., μ corresponding to the DP) or approximately constant value of DOS, the Shiba state energy has expected features, given by the general formula (1).

Extraordinary properties of the Shiba states in the Lieb lattice can be directly connected with the presence of two sublattices, formed by the corner sites or the edge sites. The partial DOS projected on the corner or edge sites, which clearly show the impact of each sublattice [58,65,66] could be a proof of this hypothesis. In particular, the whole spectral weight of the FB peak in the DOS corresponds to the edge site sublattice [giving vanishing PDOS for the corner site sublattice and opposite J_c tuning for $\mu/t = 0$; cf. Figs. 2(c) and 2(d)]. Contrary to the FB peak, the DOS at the VHS has contributions from both sublattices [66]. This very well explains the $J_c(\mu)$ dependence the for corner site sublattice [Fig. 2(c)] and the edge site sublattice [Fig. 2(d)]. A second direct proof can be given by the LDOS of the Shiba states induced by the magnetic impurities located at a given sublattice (Fig. 4). As we can see, the pattern of the LDOS corresponding to the Shiba state strongly depends on the position of the impurity (cf. top and bottom panels in Fig. 4). Similarly, the coherence length depends on the parameters of the systems (cf. left and right panels in Fig. 4). From these numerical studies we can find that the Shiba state is mostly localized at the same sublattice as the magnetic impurity site (marked by a black circle). Only in the sites which are neighbors to the impurity's location, is some modification of LDOS observed. Interestingly, similar behavior was observed experimentally within the STM measurements of the Zn impurity in the copper-dioxide Lieb lattice of the high temperature superconductor $Bi_2Sr_2CaCu_2O_{8+\delta}$ [67]. In this case, for the impurity located at the corner site, the LDOS of bound states was observed

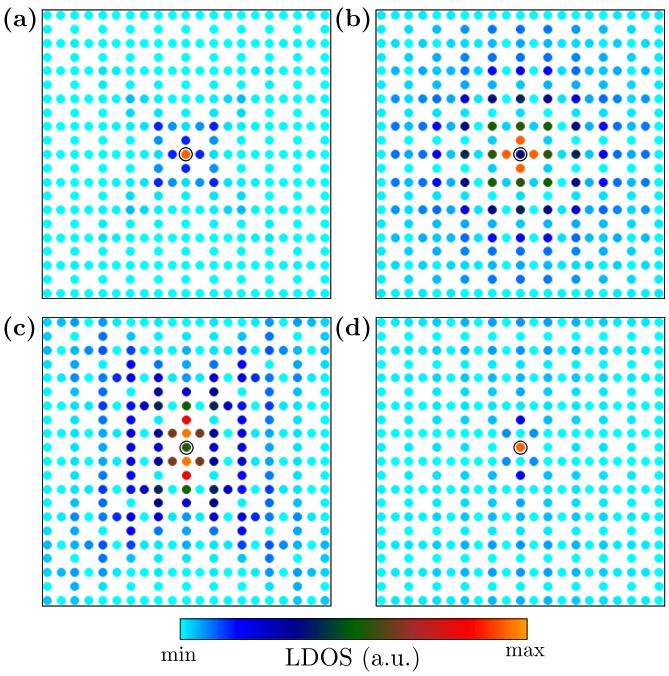

FIG. 4. Local density of states (LDOS) for the Lieb lattice. The position of the impurity is marked by a black circle. In panels (a) and (b) the impurity is located at the corner site [blue site in Fig. 1(d)], while in (c) and (d) it is located at the edge site [green or red site in Fig. 1(d)]. Results are shown for the following values of parameters $(\mu/t; J/t)$: $(2.0; 0.5)$, $(0.5; 7.5)$, $(2.0; 5.0)$, and $(0.5; 0.5)$ for panel (a), (b), (c), and (d), respectively.

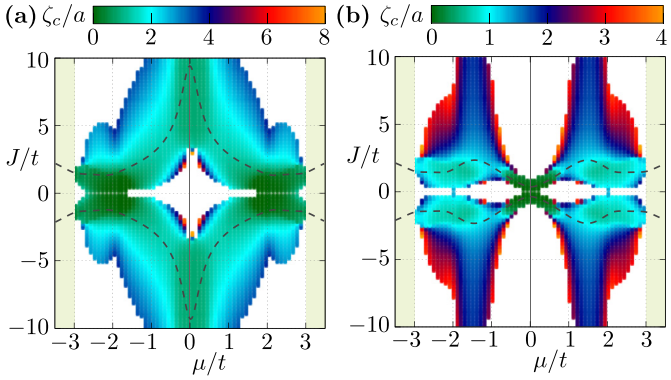

FIG. 5. Coherence length ζ_c as a function of chemical potential μ and magnetic coupling J for the Lieb lattice when the impurity is located at (a) the corner site or (b) the edge site [i.e., blue and green/red site in Fig. 1(c), respectively]. Dashed black line denotes the value of critical J for a given μ (cf. Fig. 2). Results are presented for Shiba states with energies $|E_{\mathrm{YSR}}| < 0.95\Delta$. a is the distance between neighboring sites (i.e., distance between the corner and edge state), taken as a unit of distance.

in diagonal directions (rotated 45° to the x-y axis), i.e., a situation similar to Fig. 4(a).

Exponential decay of the Shiba states as a function of distance from the impurity gives information about the coherence length ζ_c (Fig. 5). Similar to J_c for the Lieb lattice, the coherence length depends on the sublattice in which the magnetic impurity is located. Moreover, around $J_c(\mu)$ (represented by the black dashed line) the coherence length is relatively small (in range $\sim 2a$ or $\sim 1a$ for impurity in the corner site or edge site, respectively). For $J \gg J_c$ the coherence length can be much bigger—this behavior is also visible in the LDOS discussed earlier (Fig. 4).

IV. SUMMARY

In this paper we discuss the effect of density of states singularities on the Shiba states. In particular, we investigated the role of Dirac point, van Hove singularity, and flat band in honeycomb, kagome, and Lieb lattices. In its simplest form, the energy of the Shiba states strongly depends on the density of states at the Fermi level. For example, the presence of a flat band leads to strong suppression of the critical magnetic coupling J_c, while the existence of the Dirac point leads to an enhanced J_c. We examined the tuning of the parameters (e.g., energy or critical magnetic coupling) describing the Shiba states in the aforementioned lattices.

The Shiba states realized in the honeycomb and the kagome lattices exhibit typical behaviors. For the Fermi level at the Dirac point we observed a maximum of J_c, while the flat band strongly suppresses J_c. Similarly, the van Hove singularity leads to a decrease in J_c. Contrary to this, the Lieb lattice containing two sublattices (of the corner and edge sites), exhibits extraordinary behavior. In this case, the properties of the Shiba states strongly depend on the position of the magnetic impurity (in a specific sublattice). The atypical behavior is observed in J_c, the local density of states, and coherence length studies. (i) The magnetic coupling exhibits dependence similar to the density of states projected on the specific sublattice. (ii) The majority of the spectral weight in the local density of states of the Shiba states is observed in the sublattice containing the magnetic impurity. (iii) The coherence length strongly depends on the sublattice in which the magnetic impurity is located. These findings should be generic for systems with a few sublattices, and can explain some experimental data observed in systems where a Lieb lattice is realized (like high temperature superconductors).

ACKNOWLEDGMENTS

We kindly thank Szczepan Głodzik, Przemysław Piekarz, and Pascal Simon for insightful discussions. This work was supported by National Science Centre (NCN, Poland) under Projects No. 2017/25/B/ST3/02586 (S.B.) and No. 2017/24/C/ST3/00276 (A.P.). In addition, A.P. appreciates funding in the frame of scholarships of the Minister of Science and Higher Education (Poland) for outstanding young scientists (2019 edition, No. 818/STYP/14/2019).

[1] L. Yu, Bound state in superconductors with paramagnetic impurities, Acta Phys. Sin. **21**, 75 (1965).
[2] H. Shiba, Classical spins in superconductors, Prog. Theor. Exp. Phys. **40**, 435 (1968).
[3] A. I. Rusinov, Theory of gapless superconductivity in alloys with paramagnetic impurities, Zh. Eksp. Theor. Fiz. **57**, 2047 (1969).
[4] A. L. Fetter, Spherical Impurity in an Infinite Superconductor, Phys. Rev. **140**, A1921 (1965).
[5] B. W. Heinrich, J. I. Pascual, and K. J. Franke, Single magnetic adsorbates on s-wave superconductors, Prog. Surf. Sci. **93**, 1 (2018).
[6] A. V. Balatsky, I. Vekhter, and J.-X. Zhu, Impurity-induced states in conventional and unconventional superconductors, Rev. Mod. Phys. **78**, 373 (2006).
[7] G. C. Ménard, S. Guissart, C. Brun, S. Pons, V. S. Stolyarov, F. Debontridder, M. V. Leclerc, E. Janod, L. Cario, D. Roditchev, P. Simon, and T. Cren, Coherent long-range magnetic bound states in a superconductor, Nat. Phys. **11**, 1013 (2015).
[8] H. Kim, L. Rózsa, D. Schreyer, E. Simon, and R. Wiesendanger, Long-range focusing of magnetic bound states in superconducting lanthanum, Nat. Commun. **11**, 4573 (2020).
[9] A. Yazdani, B. A. Jones, C. P. Lutz, M. F. Crommie, and D. M. Eigler, Probing the local effects of magnetic impurities on superconductivity, Science **275**, 1767 (1997).
[10] S.-H. Ji, T. Zhang, Y.-S. Fu, X. Chen, X.-C. Ma, J. Li, W.-H. Duan, J.-F. Jia, and Q.-K. Xue, High-Resolution Scanning Tunneling Spectroscopy of Magnetic Impurity Induced Bound States in the Superconducting Gap of Pb Thin Films, Phys. Rev. Lett. **100**, 226801 (2008).
[11] M. Ruby, F. Pientka, Y. Peng, F. von Oppen, B. W. Heinrich, and K. J. Franke, Tunneling Processes Into Localized Subgap States in Superconductors, Phys. Rev. Lett. **115**, 087001 (2015).

[12] M. Ruby, Y. Peng, F. von Oppen, B. W. Heinrich, and K. J. Franke, Orbital Picture of Yu-Shiba-Rusinov Multiplets, Phys. Rev. Lett. **117**, 186801 (2016).

[13] D.-J. Choi, C. Rubio-Verdú, J. de Bruijckere, M. M. Ugeda, N. Lorente, and J. I. Pascual, Mapping the orbital structure of impurity bound states in a superconductor, Nat. Commun. **8**, 15175 (2017).

[14] S. Y. Song, Y. S. Park, Y. Jeong, M.-S. Kim, K.-S. Kim, and J. Seo, Yu-Shiba-Rusinov bound states studied by tuning the electron density at the fermi energy, Phys. Rev. B **103**, 214509 (2021).

[15] A. Odobesko, D. Di Sante, A. Kowalski, S. Wilfert, F. Friedrich, R. Thomale, G. Sangiovanni, and M. Bode, Observation of tunable single-atom Yu-Shiba-Rusinov states, Phys. Rev. B **102**, 174504 (2020).

[16] F. Küster, S. Brinker, S. Lounis, S. S. P. Parkin, and P. Sessi, Long range and highly tunable interaction between local spins coupled to a superconducting condensate, Nat. Commun. **12**, 6722 (2021).

[17] F. Friedrich, R. Boshuis, M. Bode, and A. Odobesko, Coupling of Yu-Shiba-Rusinov states in one-dimensional chains of Fe atoms on Nb(110), Phys. Rev. B **103**, 235437 (2021).

[18] P. Beck, L. Schneider, L. Rózsa, K. Palotás, A. Lászlóffy, L. Szunyogh, J. Wiebe, and R. Wiesendanger, Spin-orbit coupling induced splitting of Yu-Shiba-Rusinov states in antiferromagnetic dimers, Nat. Commun. **12**, 2040 (2021).

[19] J. Senkpiel, C. Rubio-Verdú, M. Etzkorn, R. Drost, L. M. Schoop, S. Dambach, C. Padurariu, B. Kubala, J. Ankerhold, C. R. Ast, and K. Kern, Robustness of Yu-shiba-Rusinov resonances in the presence of a complex superconducting order parameter, Phys. Rev. B **100**, 014502 (2019).

[20] E. Liebhaber, S. Acero González, R. Baba, G. Reecht, B. W. Heinrich, S. Rohlf, K. Rossnagel, F. von Oppen, and K. J. Franke, Yu–Shiba–Rusinov states in the charge-density modulated superconductor $NbSe_2$, Nano Lett. **20**, 339 (2020).

[21] X. Yang, Y. Yuan, Y. Peng, E. Minamitani, L. Peng, J.-J. Xian, W.-H. Zhang, and Y.-S. Fu, Observation of short-range Yu–Shiba–Rusinov states with threefold symmetry in layered superconductor 2H-$NbSe_2$, Nanoscale **12**, 8174 (2020).

[22] K. J. Franke, G. Schulze, and J. I. Pascual, Competition of superconducting phenomena and Kondo screening at the nanoscale, Science **332**, 940 (2011).

[23] N. Hatter, B. W. Heinrich, M. Ruby, J. I. Pascual, and K. J. Franke, Magnetic anisotropy in Shiba bound states across a quantum phase transition, Nat. Commun. **6**, 8988 (2015).

[24] M. Etzkorn, M. Eltschka, B. Jäck, C. R. Ast, and K. Kern, Mapping of Yu-Shiba-Rusinov states from an extended scatterer, arXiv:1807.00646.

[25] L. Malavolti, M. Briganti, M. Hänze, G. Serrano, I. Cimatti, G. McMurtrie, E. Otero, P. Ohresser, F. Totti, M. Mannini, R. Sessoli, and S. Loth, Tunable spin–superconductor coupling of spin 1/2 vanadyl phthalocyanine molecules, Nano Lett. **18**, 7955 (2018).

[26] J. Brand, S. Gozdzik, N. Néel, J. L. Lado, J. Fernández-Rossier, and J. Kröger, Electron and Cooper-pair transport across a single magnetic molecule explored with a scanning tunneling microscope, Phys. Rev. B **97**, 195429 (2018).

[27] S. Kezilebieke, M. Dvorak, T. Ojanen, and P. Liljeroth, Coupled Yu–Shiba–Rusinov states in molecular dimers on $NbSe_2$, Nano Lett. **18**, 2311 (2018).

[28] S. Kezilebieke, R. Žitko, M. Dvorak, T. Ojanen, and P. Liljeroth, Observation of coexistence of Yu-Shiba-Rusinov states and spin-flip excitations, Nano Lett. **19**, 4614 (2019).

[29] N. Hatter, B. W. Heinrich, D. Rolf, and K. J. Franke, Scaling of Yu-Shiba-Rusinov energies in the weak-coupling Kondo regime, Nat. Commun. **8**, 2016 (2017).

[30] L. Farinacci, G. Ahmadi, M. Ruby, G. Reecht, B. W. Heinrich, C. Czekelius, F. von Oppen, and K. J. Franke, Interfering Tunneling Paths Through Magnetic Molecules on Superconductors: Asymmetries of Kondo and Yu-Shiba-Rusinov Resonances, Phys. Rev. Lett. **125**, 256805 (2020).

[31] C. Rubio-Verdú, J. Zaldívar, R. Žitko, and J. I. Pascual, Coupled Yu-Shiba-Rusinov States Induced by a Many-Body Molecular Spin on a Superconductor, Phys. Rev. Lett. **126**, 017001 (2021).

[32] D. Wang, J. Wiebe, R. Zhong, G. Gu, and R. Wiesendanger, Spin-Polarized Yu-Shiba-Rusinov States in an Iron-Based Superconductor, Phys. Rev. Lett. **126**, 076802 (2021).

[33] D. Chatzopoulos, D. Cho, K. M. Bastiaans, G. O. Steffensen, D. Bouwmeester, A. Akbari, G. Gu, J. Paaske, B. M. Andersen, and M. P. Allan, Spatially dispersing Yu-Shiba-Rusinov states in the unconventional superconductor $FeTe_{0.55}Se_{0.45}$, Nat. Commun. **12**, 298 (2021).

[34] S. Y. Song, J. H. J. Martiny, A. Kreisel, B. M. Andersen, and J. Seo, Visualization of Local Magnetic Moments Emerging from Impurities in Hund's Metal States of FeSe, Phys. Rev. Lett. **124**, 117001 (2020).

[35] A. Kobiałka, P. Piekarz, A. M. Oleś, and A. Ptok, First-principles study of the nontrivial topological phase in chains of 3*d* transition metals, Phys. Rev. B **101**, 205143 (2020).

[36] A. Y. Kitaev, Unpaired Majorana fermions in quantum wires, Phys.-Usp. **44**, 131 (2001).

[37] A. Kamlapure, L. Cornils, J. Wiebe, and R. Wiesendanger, Engineering the spin couplings in atomically crafted spin chains on an elemental superconductor, Nat. Commun. **9**, 3253 (2018).

[38] A. Kamlapure, L. Cornils, R. Žitko, M. Valentyuk, R. Mozara, S. Pradhan, J. Fransson, A. I. Lichtenstein, J. Wiebe, and R. Wiesendanger, Correlation of Yu–Shiba–Rusinov states and Kondo resonances in artificial spin arrays on an *s*-wave superconductor, Nano Lett. **21**, 6748 (2021).

[39] H. Ding, Y. Hu, M. T. Randeria, S. Hoffman, O. Deb, J. Klinovaja, D. Loss, and A. Yazdani, Tuning interactions between spins in a superconductor, Proc. Natl. Acad. Sci. USA **118**, e2024837118 (2021).

[40] E. Liebhaber, L. M. Rütten, G. Reecht, J. F. Steiner, S. Rohlf, K. Rossnagel, F. von Oppen, and K. J. Franke, Quantum spins and hybridization in artificially-constructed chains of magnetic adatoms on a superconductor, arXiv:2107.06361.

[41] L. Schneider, P. Beck, J. Neuhaus-Steinmetz, T. Posske, J. Wiebe, and R. Wiesendanger, Controlled length-dependent interaction of Majorana modes in Yu-Shiba-Rusinov chains, arXiv:2104.11503.

[42] C. Mier, J. Hwang, J. Kim, Y. Bae, F. Nabeshima, Y. Imai, A. Maeda, N. Lorente, A. Heinrich, and D.-J. Choi, Atomic manipulation of in-gap states in the β-Bi_2Pd superconductor, Phys. Rev. B **104**, 045406 (2021).

[43] L. Schneider, P. Beck, T. Posske, D. Crawford, E. Mascot, S. Rachel, R. Wiesendanger, and J. Wiebe, Topological Shiba bands in artificial spin chains on superconductors, Nat. Phys. **17**, 943 (2021).

[44] S. Głodzik and A. Ptok, Quantum phase transition induced by magnetic impurity, J. Supercond. Nov. Magn. **31**, 647 (2018).

[45] M. Uldemolins, A. Mesaros, and P. Simon, Effect of van Hove singularities on Shiba states in two-dimensional *s*-wave superconductors, Phys. Rev. B **103**, 214514 (2021).

[46] A. Ptok, K. Rodríguez, and K. J. Kapcia, Superconducting monolayer deposited on substrate: Effects of the spin-orbit coupling induced by proximity effects, Phys. Rev. Materials **2**, 024801 (2018).

[47] A. Cichy and A. Ptok, Reentrant Fulde-Ferrell-Larkin-Ovchinnikov superfluidity in the honeycomb lattice, Phys. Rev. A **97**, 053619 (2018).

[48] K. Björnson, A. V. Balatsky, and A. M. Black-Schaffer, Superconducting order parameter π-phase shift in magnetic impurity wires, Phys. Rev. B **95**, 104521 (2017).

[49] N. Mohanta, A. P. Kampf, and T. Kopp, Supercurrent as a probe for topological superconductivity in magnetic adatom chains, Phys. Rev. B **97**, 214507 (2018).

[50] J. Ortuzar, S. Trivini, M. Rouco, J. Zaldivar, J. I. Pascual, and F. S. Bergeret, Yu-Shiba-Rusinov states in 2D superconductors with arbitrary Fermi contours, arXiv:2111.02473.

[51] A. Weismann, M. Wenderoth, S. Lounis, P. Zahn, N. Quaas, R. G. Ulbrich, P. H. Dederichs, and S. Blügel, Seeing the Fermi surface in real space by nanoscale electron focusing, Science **323**, 1190 (2009).

[52] E. H. Lieb, Two Theorems on the Hubbard Model, Phys. Rev. Lett. **62**, 1201 (1989).

[53] B. R. Ortiz, L. C. Gomes, J. R. Morey, M. Winiarski, M. Bordelon, J. S. Mangum, I. W. H. Oswald, J. A. Rodriguez-Rivera, J. R. Neilson, S. D. Wilson, E. Ertekin, T. M. McQueen, and E. S. Toberer, New kagome prototype materials: Discovery of KV_3Sb_5, RbV_3Sb_5, and CsV_3Sb_5, Phys. Rev. Materials **3**, 094407 (2019).

[54] C. Mielke, Y. Qin, J.-X. Yin, H. Nakamura, D. Das, K. Guo, R. Khasanov, J. Chang, Z. Q. Wang, S. Jia, S. Nakatsuji, A. Amato, H. Luetkens, G. Xu, M. Z. Hasan, and Z. Guguchia, Nodeless kagome superconductivity in $LaRu_3Si_2$, Phys. Rev. Materials **5**, 034803 (2021).

[55] Y. Cao, V. Fatemi, S. Fang, K. Watanabe, T. Taniguchi, E. Kaxiras, and P. Jarillo-Herrero, Unconventional superconductivity in magic-angle graphene superlattices, Nature (London) **556**, 43 (2018).

[56] M. Yankowitz, S. Chen, H. Polshyn, Y. Zhang, K. Watanabe, T. Taniguchi, D. Graf, A. F. Young, and C. R. Dean, Tuning superconductivity in twisted bilayer graphene, Science **363**, 1059 (2019).

[57] T. Yilmaz, X. Tong, Z. Dai, J. T. Sadowski, E. F. Schwier, K. Shimada, S. Hwang, K. Kisslinger, K. Kaznatcheev, E. Vescovo, and B. Sinkovic, Emergent flat band electronic structure in a VSe_2/Bi_2Se_3 heterostructure, Commun. Mater. **2**, 11 (2021).

[58] M. R. Slot, T. S. Gardenier, P. H. Jacobse, G. C. P. van Miert, S. N. Kempkes, S. J. M. Zevenhuizen, C. M. Smith, D. Vanmaekelbergh, and I. Swart, Experimental realization and characterization of an electronic Lieb lattice, Nat. Phys. **13**, 672 (2017).

[59] P. G. de Gennes, *Superconductivity of Metals and Alloys* (Addison-Wesley, Reading, MA, 1989).

[60] A. Ptok, The Fulde–Ferrell–Larkin–Ovchinnikov superconductivity in disordered systems, Acta Phys. Pol. A **118**, 420 (2010).

[61] A. Ptok, The Fulde–Ferrell–Larkin–Ovchinnikov state in quantum rings, J. Supercond. Novel Magn. **25**, 1843 (2012).

[62] A. Ptok and K. J. Kapcia, Probe-type of superconductivity by impurity in materials with short coherence length: the *s*-wave and η-wave phases study, Supercond. Sci. Technol. **28**, 045022 (2015).

[63] H. Matsui, T. Sato, T. Takahashi, S.-C. Wang, H.-B. Yang, H. Ding, T. Fujii, T. Watanabe, and A. Matsuda, BCS-Like Bogoliubov Quasiparticles in High-T_c Superconductors Observed by Angle-Resolved Photoemission Spectroscopy, Phys. Rev. Lett. **90**, 217002 (2003).

[64] A. Ptok, S. Głodzik, and T. Domański, Yu–Shiba–Rusinov states of impurities in a triangular lattice of $NbSe_2$ with spin-orbit coupling, Phys. Rev. B **96**, 184425 (2017).

[65] W. Jiang, H. Huang, and F. Liu, A Lieb-like lattice in a covalent-organic framework and its Stoner ferromagnetism, Nat. Commun. **10**, 2207 (2019).

[66] B. Cui, X. Zheng, J. Wang, D. Liu, S. Xie, and B. Huang, Realization of Lieb lattice in covalent-organic frameworks with tunable topology and magnetism, Nat. Commun. **11**, 66 (2020).

[67] S. H. Pan, E. W. Hudson, K. M. Lang, H. Eisaki, S. Uchida, and J. C. Davis, Imaging the effects of individual zinc impurity atoms on superconductivity in $Bi_2Sr_2CaCu_2O_{8+\delta}$, Nature (London) **403**, 746 (2000).

4.2 Studies based on density functional theory

4.2.1 Phononic drumhead surface state in the distorted kagome compound RhPb

A. Ptok, W. R. Meier, A. Kobiałka, S. Basak, M. Sternik, J. Łażewski, P. T. Jochym, M. A. McGuire, B. C. Sales, H. Miao, P. Piekarz, and A. M. Oleś, Phys. Rev. Research **5**, 043231 (2023).

CoSn-like compounds (FeSn, FeGe, etc.) contain alternating layers of kagome lattice formed by Co atoms, separated from each other by layers of hexagonal lattice formed by Sn. This group of materials is famous for having a clean electronic band structure, with well visible flat band and Dirac point. From a previous theoretical calculation by our group [62] it is known that RhPb, a member from apparently the same family, cannot stabilize in the same symmetry group (P6/mmm) as the other members. More precisely, it cannot stabilize with layers of exact kagome lattice, rather it stabilizes in symmetry group P$\bar{6}$2m with distorted kagome structure formed by Rh atoms. This manuscript starts with the experimental verification of this claim through single-crystal X-ray diffraction. Then we move on to study the phonon dispersion relations of both symmetries. Both of them contain a flat band in the phonon band structure, with P$\bar{6}$2m containing a slightly more dispersive band due to distortion of the ideal kagome lattice. We also observe several degenerate Dirac points and Dirac nodal lines. The presence of these nodal lines led us to look for phonon surface states connecting these lines. Indeed when we investigated the termination dependence surface states, we observed drumhead-like surface states connecting these nodal lines.

Author's contribution: Numerical evaluations (phonon dispersion curves and phonon density of states), participation in theoretical analysis, discussion of obtained results, partial preparation of the manuscript, correspondence with other research groups during the prepublication period, participation in preparing the response for Referees.

Phononic drumhead surface state in the distorted kagome compound RhPb

Andrzej Ptok [1,*] William R. Meier [2,†] Aksel Kobiałka [3] Surajit Basak [1] Małgorzata Sternik [1] Jan Łażewski [1] Paweł T. Jochym [1] Michael A. McGuire [2] Brian C. Sales [2] Hu Miao [2] Przemysław Piekarz [1] and Andrzej M. Oleś [4,5,‡]

[1]*Institute of Nuclear Physics, Polish Academy of Sciences, W. E. Radzikowskiego 152, PL-31342 Kraków, Poland*
[2]*Material Science & Technology Division, Oak Ridge National Laboratory, Oak Ridge, Tennessee 37831, USA*
[3]*Department of Physics, University of Basel, Klingelbergstrasse 82, CH-4056 Basel, Switzerland*
[4]*Max Planck Institute for Solid State Research, Heisenbergstrasse 1, D-70569 Stuttgart, Germany*
[5]*Institute of Theoretical Physics, Jagiellonian University, Prof. Stanisława Łojasiewicza 11, PL-30348 Kraków, Poland*

(Received 16 July 2023; revised 19 October 2023; accepted 14 November 2023; published 11 December 2023)

RhPb was initially recognized as one of CoSn-like compounds with $P6/mmm$ symmetry, containing an ideal kagome lattice of d-block atoms. However, theoretical calculations predict the realization of the phonon soft mode, which leads to the kagome lattice distortion and stabilization of the structure with $P\bar{6}2m$ symmetry [A. Ptok *et al.*, Phys. Rev. B **104**, 054305 (2021)]. Here, we present the single crystal x-ray diffraction results supporting this prediction. Furthermore, we discuss the main dynamical properties of RhPb with $P\bar{6}2m$ symmetry, i.e. phonon dispersions and surface Green's functions using the modern theoretical methods based on density functional theory. The bulk phononic dispersion curves contain several flattened bands, Dirac nodal lines, and triple degenerate Dirac points. As a consequence, the phononic drumhead surface state is realized for the (100) surface, terminated by the zigzaglike edge of Pb honeycomb sublattice.

DOI: 10.1103/PhysRevResearch.5.043231

I. INTRODUCTION

Discovery of the topological insulators with conducting surface states in the form of the Dirac cone [1–4] opened a period of intensive studies in the subject of fermionic topological systems [5–7]. However, a realization of the nontrivial topological states is not limited only to fermionic systems, but can be also expected in bosonic ones as well [8–12]. We can find several examples of the occurrence of phonon Dirac/Weyl points [13–27], nodal lines [28–33], nodal rings [33–38], and nodal nets [39–42]. Topological properties are also manifested by the emergence of phonon surface states [15–19,32,35,36,43–49] or phonon Hall effect [50–56]. As a result, existence of the topological phonons with nonzero Berry curvature [57] can give rise to the development of nanodevices based on the heat transfer manipulation, i.e., in phononics [58].

In the context of the topological properties, the kagome-supported systems have been of great interest recently. The basic property of the system with the kagome lattice is the formation of flat electronic bands [59–61]. One such example of the kagome systems are CoSn-like compounds, which combine kagome and honeycomb layers [62–65]. The electronic band structure exhibits a flat band and Dirac fermions [62–70]. Some CoSn-like compounds exhibit frustrated magnetism with an important role for itinerant electrons [71], like magnetically ordered FeGe [72], or FeSn [62,70,73,74]. However, most commonly, these compounds are paramagnets, such as CoSn [73].

Motivation: Typically, the kagome net CoSn-like compounds crystallize with the $P6/mmm$ symmetry [62,63]. In such a structure, the d-block element (e.g., Fe, Co, Ni, Rh, or Pt) forms an ideal kagome sublattice, while the p-block element (e.g., Ge, In, Sn, Tl, or Pb) has two nonequivalent positions: one of the p-block elements is located in the plane of the kagome sublattice when the second's position forms honeycomb sublattice intercalated between two kagome-sublattice planes. RhPb satisfies the mentioned conditions, and therefore it should behave as an ideal kagome metal [63]. However, theoretical investigations of the lattice dynamics of RhPb show that this compound should be unstable with the $P6/mmm$ symmetry [75]. Stabilization of RhPb can be achieved by distorting the kagome lattice, resulting in the $P\bar{6}2m$ symmetry (see Fig. 1). In this paper, we present experimental evidence for the distorted kagome structure in the RhPb system. Furthermore, we investigate the dynamic properties of RhPb with a distorted kagome lattice. We show that this compound is an excellent candidate for the study of the phonon drumhead surface state.

The paper is organized as follows. First, we discuss the results indicating formation of the distorted kagome lattice in RhPb with the $P\bar{6}2m$ symmetry (Sec. II). Next, we present

*aptok@mmj.pl
†javamocham@gmail.com; Present address: Materials Science & Engineering Department, University of Tennessee Knoxville, Knoxville, Tennessee 37996, USA.
‡a.m.oles@fkf.mpg.de

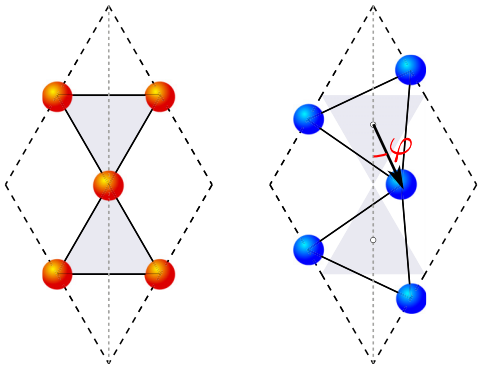

FIG. 1. Schematic representation of the ideal (left panel) and distorted (right panel) kagome lattices, realized in the system with symmetries $P6/mmm$ and $P\bar{6}2m$, respectively. In the ideal kagome lattice, the system is centrosymmetric. The rotation of perfectly ordered triangles by angle φ transforms the system into the noncentrosymmetric structure.

the theoretical study of the dynamical properties of this compound (Sec. III). Finally, we summarize the paper with the main conclusions in Sec. IV.

II. CRYSTAL STRUCTURE

Crystals of RhPb were grown from a high-temperature Pb-rich melt [63]. A 1:3 atomic ratio of rhodium sponge (Alfa Aesar 99.95%) and lead slugs (Alfa Aesar Puratronic 99.999%) were loaded into one side of a 2 mL alumina Canfield crucible set [76] and then sealed in a fused silica ampule under vacuum with a hydrogen-oxygen torch. The ampule was placed in a box furnace and heated to 1000 °C or 1100 °C over 6 h. This temperature was held for 2 h to dissolve the rhodium in lead and homogenize the fluid. The furnace was quickly cooled to 900 °C over 3.5 h and held for 0.5 h before cooling to 750 °C over 320 h (−0.47 °C/h) to slowly precipitate the crystal. The hot ampule was removed from the furnace and inverted into a centrifuge to fling the remaining liquid of the crystals. In the batch used for single crystal diffraction, 5.4 g of reactants yielded a single 4 × 7 mm crystal weighing about 1.2 g. It had a slightly skeletal hexagonal-prismatic shape with a shiny metallic cluster [see Fig. 2(a)]. Other batches of crystals yielded faceted euhedral blocky hexagonal prisms. Crystals of RhPb are brittle with a conchoidal fracture and have weak (001)-cleavage. Broken surfaces sometimes reveal

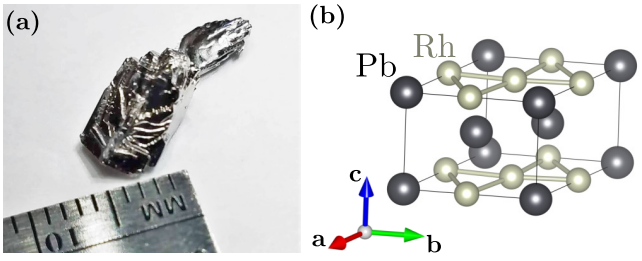

FIG. 2. Single crystal of RhPb grown from lead melt (a), and crystal structure of RhPb with $P\bar{6}2m$ symmetry (b).

TABLE I. An important characteristic of refined structures of RhPb at 293 K from single crystal x-ray diffraction. Note the significant improvement of fit quality in the $P\bar{6}2m$ refinement.

Space group	$P6/mmm$	$P\bar{6}2m$
x_{Rh}	1/2	0.4775(2)
Twin fraction	N/A	0.568(25)
Triangle rotation, φ in Fig. 1	0°	4.45(3)°
R(obs) (%)	6.01	2.83
Goodness of fit obs	4.91	1.65

inclusions of bluish metallic Pb metal that contrast with the silver metallic RhPb surfaces.

To determine the crystal structure of RhPb, fragments of the 1.2 g crystal were selected for single crystal x-ray diffraction (XRD). The crystal, approximately 60 × 40 × 10 μm^3, was mounted on the end of a Kapton loop with Locktite glue for data collection at room temperature using a Bruker D8 Quest diffractometer (0.71073 Å Mo K_α radiation). Data were collected, reduced, and analyzed using APEX3 software, including a semiempirical absorption correction based on equivalent reflections. Structure refinement was performed using JANA 2020 [77] for both $P6/mmm$ (space group No. 191) and $P\bar{6}2m$ (space group No. 189) symmetries.

The first-principles density functional theory (DFT) calculations were performed using the projector augmented-wave (PAW) potentials [78] implemented in the Vienna *ab initio* simulation package (VASP) code [79–81]. Calculations were made within the generalized gradient approximation (GGA) in the Perdew, Burke, and Ernzerhof (PBE) parametrization [82]. The energy cutoff for the plane-wave expansion was set to 350 eV. Optimizations of structural parameters (lattice constants and atomic positions) were performed in the primitive unit cell using the 10 × 10 × 6$\boldsymbol{k}$-point grid in the Monkhorst-Pack scheme [83]. As a break condition of the optimization loop, we took the energy difference of 10^{-6} eV and 10^{-8} eV for ionic and electronic degrees of freedom, respectively.

Structure: Initially, the RhPb structure was assumed to possess the $P6/mmm$ symmetry [63]. However, theoretical analysis of the RhPb dynamical properties shows that such a system is unstable [75]. Our single crystal refinement does indeed reveal that RhPb adopts the distorted $P\bar{6}2m$ structure based on a distinctly better fit quality over the $P6/mmm$ solution (Table I). DFT calculations estimate very subtle differences in the lattice parameters for both structures (Table II), but more stable phonons in the $P\bar{6}2m$ structure (detailed discussion in Sec. III A).

In the case of the $P6/mmm$ symmetry, the Rh atoms are located in the Wyckoff position $3f$ $(1/2, 1/2, 0)$, while the Pb atoms in two nonequivalent Wyckoff positions $2d$

TABLE II. Comparison of the experimental and theoretical (DFT) lattice constants for RhPb with different symmetries.

	a (Å)	c (Å)
Exp. 293(2) K	5.6794(4)	4.4311(3)
Exp. 15 K (Ref. [63])	5.66601(2)	4.41267(1)
DFT $P6/mmm$	5.740	4.487
DFT $P\bar{6}2m$	5.762	4.466

(1/3, 2/3, 1/2) and 1*a* (0,0,0). In the case of the $P\bar{6}2m$ symmetry [see Fig. 2(b)], the 3*f* position of the Rh atom is calculated to lie at (0.467,0.467,0). Experimentally, the position of the Rh atom was estimated as (0.4775(2),0.4775(2),0). The distortion present in the system corresponds to the rotation of the triangles that form an ideal kagome lattice (see Fig. 1) with angle $\varphi = 6.5^\circ$ determined by DFT, while the experimentally obtained value is 4.46°. The rotation of the kagome triangles in RhPb reflects the modified kagome pattern seen in the ZrNiAl-type materials [84–92]. The $P\bar{6}2m$ space group does not alter the translational symmetry for the lattice and therefore can only be distinguished from $P6/mmm$ by fitting the diffracted intensities. The smaller *R* and goodness of fit values reported in Table I demonstrate that the lower symmetry structure better models the experimentally observed intensities. More crystallographic data (e.g., CIF files as well as XRD refinements) can be found in the Supplemental Material (SM) [93].

Regardless of the symmetry, RhPb exhibits a metallic band structure (see Fig. S2 in the SM [93]). The electronic band structure obtained for both symmetries is very similar, and in correspondence to other CoSn-like compounds, it contains several flattened bands (detailed discussion can be found in Sec. S2 in the SM [93]).

III. DYNAMICAL PROPERTIES

The dynamical properties were calculated using the direct Parlinski-Li-Kawazoe method [94], implemented in the PHONOPY package [95]. Within this method, the interatomic force constants (IFC) are calculated from the Hellmann-Feynman (HF) forces acting on the atoms after displacements of individual atoms inside the supercell. We performed these calculations using the $2 \times 2 \times 2$ supercell with 48 atoms, and the reduced $\boldsymbol{k}$-point grid $3 \times 3 \times 3$. Next, the IFC were used to study the surface states, by calculations of the surface Green's function for the semiinfinite system [96], using WANNIERTOOLS [97]. Additionally, we also calculate the phonon dispersion curves for a finite temperature. In this case, the calculations were performed for the thermal distribution of multidisplacement of atoms [98], generated within the HECSS procedure [99]. The total energy and HF forces acting on all atoms are calculated with VASP for 100 different configurations of atomic displacements in the supercell. In dynamical properties calculations, we include second- and third-order phonon contributions, which correspond to the harmonic and cubic IFC, respectively.

A. Phonon dispersion curves

The phonon dispersion relations and the phonon density of states (DOS) for RhPb with both symmetries are presented in Fig. 3. In the case of the $P6/mmm$ symmetry, there exists the imaginary soft mode (presented as negative frequencies) [see Fig. 3(a)]. This soft mode, with the frequency of −2.59 THz at the Γ point, is characterized by the B_{1u} symmetry. Atomic displacements induced by this mode lead to the rotation of the triangles forming the ideal kagome lattice [75] (see Fig. 1). As a consequence, the $P\bar{6}2m$ symmetry is stabilized—after the transformation, the phonon dispersion does not exhibit any imaginary modes, so all frequencies are real [Fig. 3(c)]. The analysis of the zone-center mode frequencies and symmetries shows that in the distorted structure, the mode corresponding to the soft mode has a frequency of 3.2 THz and an *A*-like symmetry.

Soft modes observed in the $P6/mmm$ symmetry are associated only with the Rh atoms' vibration, which is reflected in the phonon density of states. In practice, all spectral weights at DOS related to the soft mode [negative frequencies in Fig. 3(b)] correspond to the Rh atoms contribution. For negative frequencies, the contribution of Pb atoms is negligible. Indeed, stabilization of RhPb with the $P\bar{6}2m$ symmetry mainly modified the Rh contribution [cf. Figs. 3(b) and 3(d)]. As expected, independently of the system symmetry, the vibrations of the heavy Pb atoms are located mostly in the lower frequency range. The vibrations of lighter Rh atoms exist in the higher frequency range.

Here, we should point out that the spontaneous kagome rotation can also be achieved in other compounds, like $MgCo_6Ge_6$ [100], at $T = 100$ K. Nevertheless, in the case of RhPb, the theoretical investigation of temperature-dependent phonon dispersion for $P6/mmm$ always shows soft mode at the Γ point (even up to 1500 K). From this, we can conclude that the RhPb compound crystallizes only with the $P\bar{6}2m$ symmetry, while the structure with the $P6/mmm$ symmetry is unstable even at high temperatures.

Symmetry realized by RhPb has an impact on the irreducible representation of phonons at the Γ point. Indeed, the exact analysis presented in Sec. S3 in the SM [93] clearly shows differences between these two phases. In fact, due to the different number of active modes in both symmetries, e.g., visible in the Raman spectroscopy, we can gain additional evidence for the formation of the $P\bar{6}2m$ crystal symmetry.

B. Flat phonon bands

Typically, the kagome lattice allows the creation of flat bands—this property is observed in the electronic band structure of CoSn-like compounds [63–66] as well as in their phonon dispersion curves. For both symmetries, there are several flat bands with a weak dispersion along the Γ-K-M-Γ and A-H-L-A paths [e.g., the branch marked in yellow in Figs. 3(a) and 3(c)]. A previous study on the similar CoSn system, suggests that the flat bands are related to the collective vibrations of *d*-block atoms (i.e., Co) [101]. However, as we have shown for CoSn-like compounds in Ref. [75], phonon bands order results rather from the mass sequence, and the flat bands correspond to the vibrations of the heaviest (*p*-block) atoms. Also, analysis of the polarization vectors of RhPb phonons, presented here, clearly shows that dispersionless modes are related to the vibrations of Pb atoms [marked with blue arrows in Figs. 3(b) and 3(d)]. Moreover, the flat low-frequency mode corresponds to the vibration of the Pb atom in the Rh kagome net plane (see also partial DOS presented in Fig. S6 in the SM [93]). The separation of Pb phonon modes can be understood by taking into account the significant Pb:Rh mass ratio (207.2:102.9), which is responsible for the relatively weak coupling of Pb vibrations with those of neighboring Rh atoms and justifies the existence of separated and mostly dispersionless mode. Furthermore, in the frequency range of

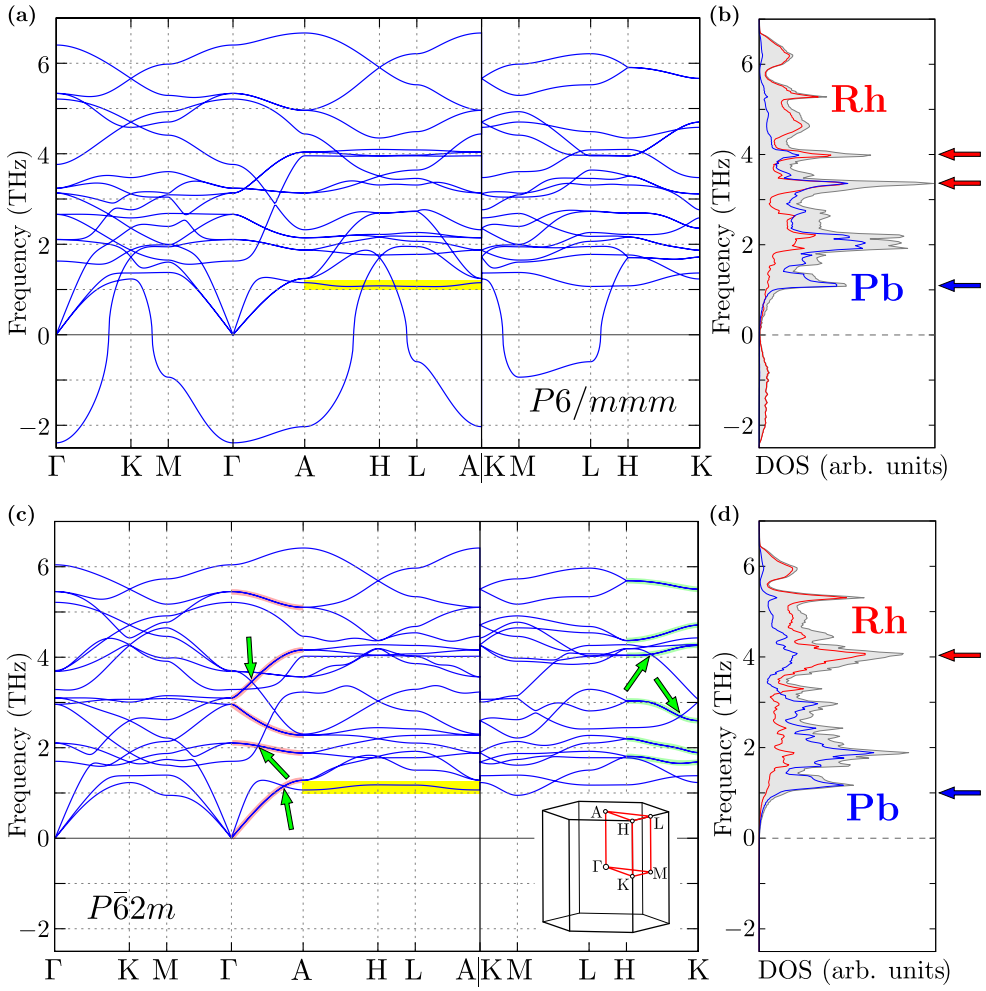

FIG. 3. Phonon dispersion relations (left column) and phonon density of states (right column) for RhPb with $P6/mmm$ (top row) and $P\bar{6}2m$ (bottom row) symmetry. The branches marked with solid light red or light green lines corresponding to the doubly degenerate band along the Γ-A and K-H directions, respectively. Similarly, the green arrows indicate triple degenerate Dirac points resulting from the intersection of the doubly degenerate band with the nondegenerate band. Color lines in the right panels are related to the total DOS (gray) or partial DOS (red and blue for lighter Rh and heavier Pb atoms, respectively). The inset in panel (c) represents the Brillouin zone and its high symmetry points.

flat bands, the chiral phonons (i.e., circulations of the atoms around the equilibrium position) were predicted within the Pb honeycomb sublattice [75].

The occurrence of the mentioned flat bands is reflected in phonon DOS, by the relatively sharp peaks [marked with red arrows in Figs. 3(b) and 3(d)]. Moreover, the phonon DOS describes the frequency distribution of normal modes inside the whole Brillouin zone, in contrast to the phonon dispersion curves which only represent the modes along high symmetry directions. Therefore, the truly flat bands (separated from others' contributions) are represented in DOS for $P6/mmm$ symmetry by very sharp peaks [see Fig. 3(b)]. In the case of $P\bar{6}2m$ symmetry, however, a stronger k dependence of phonon dispersion relations should be noticed, resulting in much broader peaks of phonon DOS [see Fig. 3(d)]. It means, that the phonon bands for the $P\bar{6}2m$ symmetry are more dispersive than in the case of the $P6/mmm$ symmetry.

C. Bands degeneracy and Dirac points/lines

The presence of three and sixfolded rotational symmetry results in preserving band degeneracy of the Γ point also along so-called high-symmetry directions. Indeed, the degeneracy preservation is well visible along the Γ-A path (i.e., for the z direction, perpendicular to the honeycomb and kagome layers) [branches marked with the red solid line in Fig. 3(c)]. Additionally, the hexagonal symmetry affects the band structure along the K-H path, where some bands are double degenerate and form the Dirac nodal lines. Irreducible representations at the K (H) point allow for the realization of double degenerate points. However, the symmetry of this state is preserved for any point P with coordinates $(1/3,1/3,u)$ within the double degenerate state. Finally, the Dirac point at the K (H) point [visible, e.g., in the form of characteristic band crossing around 5.6 THz for both symmetries in Figs. 3(a) and 3(c)], exists along the whole K-H path, forming the Dirac nodal line.

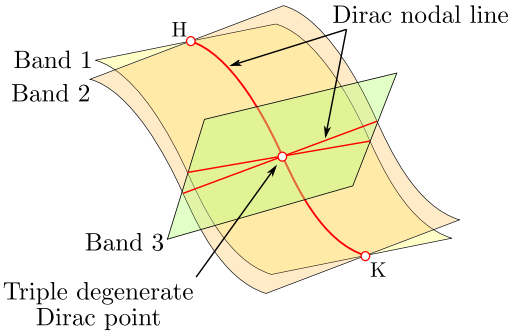

FIG. 4. Schematic representation of triple degenerate Dirac point forming along the K-H path.

The intersections of doubly degenerate and non-degenerate bands occurring along the Γ-A and K-H directions [pointed out by green arrows in Fig. 3(c)] determine Dirac points with a triple degeneracy. Figure 4 schematically illustrates how the Dirac nodal line and triply degenerate Dirac point are defined. Two bands (band 1 and 2) intersecting along the K-H path form a nodal line, and another band (band 3) crossing this line marks a triply degenerate point. Two additional Dirac nodal lines are created where band 3 intersects bands 1 and 2. Here we would like to stress that the realization of (bulk) Dirac point and nodal lines strongly affects the surface states character. In the next paragraph, we will focus on this aspect.

D. Phonon surface states

Some hexagonal lattices, like honeycomb [102–104] and kagome [105,106] nets, can form the electronic surface states at the zigzaglike edge of the lattice. This is also true in the case of the bosonic systems [43,107–110]. Indeed, the phonon zigzag edge modes could be realized in RhPb at the (100) surface [Fig. 5(a)]. Similar behavior was also earlier reported for NbReSi, which possesses the same symmetry [111].

The calculated phonon surface states of RhPb for the (100) surface are presented in Fig. 5. In our calculations, we consider two types of terminations. The zigzag edge of the Pb honeycomb lattice is realized in both of them. The "top" surface also contains a chain of Rh atoms from the kagome lattice. Similarly, the "bottom" surface contains a chain of Rh-Pb atoms from the triangular lattice formed by the Rh kagome net decorated by Pb atoms represented by nonbonded black atoms in Fig. 5(a). Slablike calculations (for ten layers of RhPb) clearly show the existence of surface states, independently of the termination [blue and red lines in Fig. 5(c)]. The phonon dispersion curves, in this case, contain many more branches than the dispersion curves for the bulk [Fig. 3(c)], what is the consequence of projection of all phonon states from the bulk (3D) Brillouin zone onto the 2D Brillouin zone of the surface [see Fig. 5(b)]. It is interesting that, in the case of the surface directly terminated by the zigzag edge of the Pb honeycomb lattice (i.e., top surface), the phonon surface states at the highest frequencies exhibit behavior similar to this observed in electronic surface states at the zigzag edge in

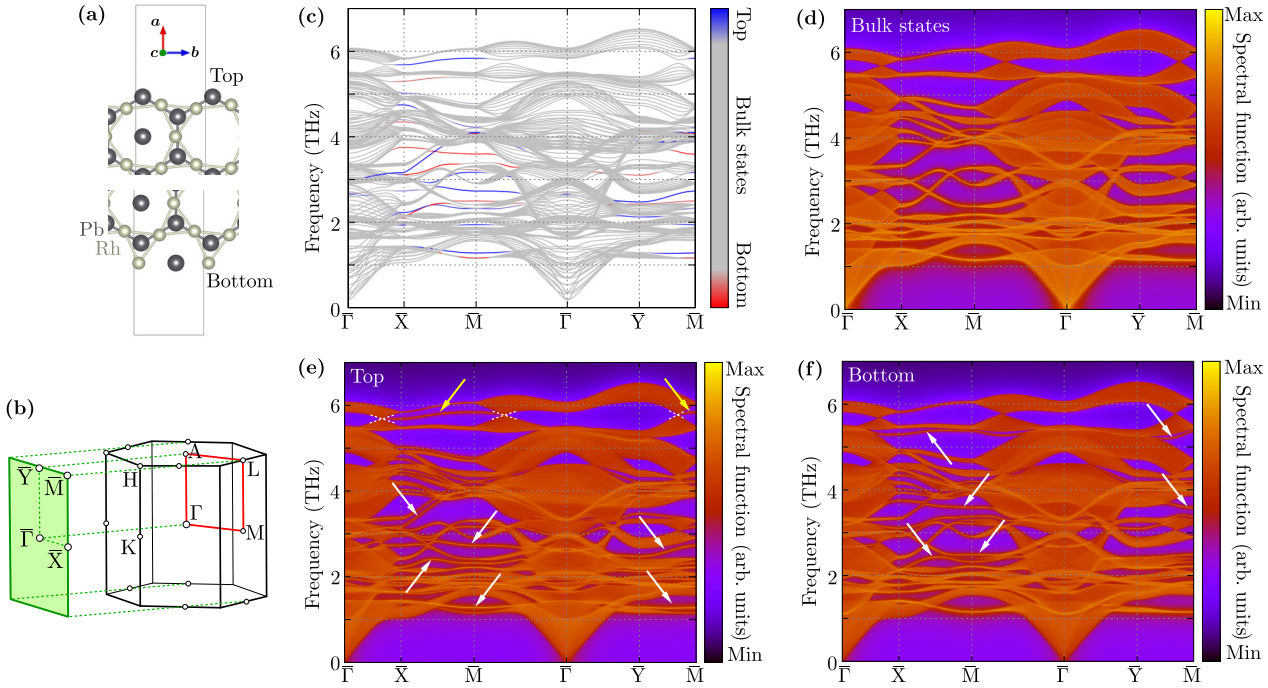

FIG. 5. The phonon surface states realized at the edge of the (100) surfaces of RhPb with $P\bar{6}2m$ symmetry. Surface terminations are presented in panel (a). For simplification, we show only bonding between Rh atoms forming a distorted kagome lattice and Pb atoms forming a honeycomb lattice. The Pb atom in the center of hexagons is placed in the plane of a distorted kagome lattice. (b) Relation between the bulk (3D) and surface (2D) Brillouin zone. Phonon band structure calculated for slablike structure (c), containing ten layers. The colors correspond to the states related to vibrations of the atoms at the top surface (blue), central bulklike part (gray), or bottom surface (red). The panels from (d) to (f) present the spectral function calculated for the central bulklike part, the top surface, and the bottom surface part of the slab, respectively. The arrows in (e) and (f) show the locations of the soft modes of the phonons realized on the top or bottom surfaces, respectively.

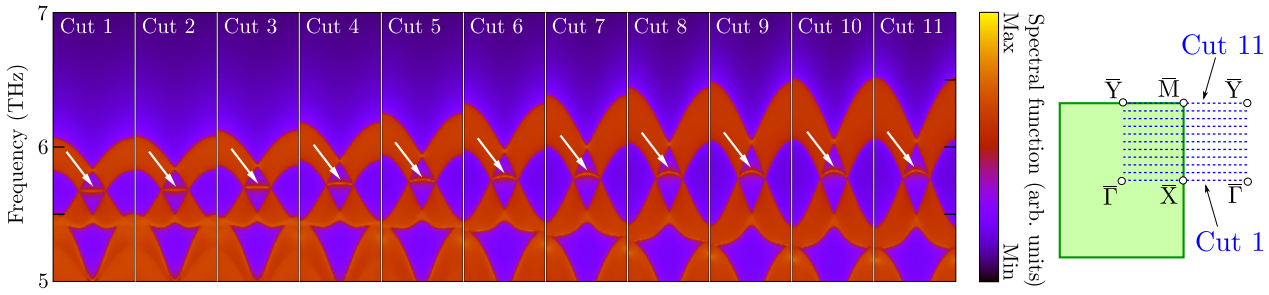

FIG. 6. The surface spectral function for different cuts of the surface (2D) Brillouin zone (right panel), presenting $\boldsymbol{k}$-point dependence of the phonon drumhead surface state (marked with white arrows).

the graphene nanoribbon [102] [see the states with frequencies around 5.75 THz, marked with yellow arrows in Fig. 5(e)].

Direct calculations of the spectral functions for the bulk and surface regions are presented in Figs. 5(d)–5(f). The phonon surface states can be, in a relatively simple way, extracted from the bulk spectra, by comparing the spectral function related to the bulk states [see Fig. 5(d)] with the adequate spectral function for a specific surface [Fig. 5(e) or 5(f)]. Additional states, i.e., surface states, are marked with arrows. Comparing the frequencies of surface states with the bulk phonon DOS [Fig. 3(d)], we see that the surface states in the low (high) frequency range are realized mostly by Pb (Rh) atoms.

Probably, the most interesting properties of the slablike structure can be observed for the highest branches of the spectrum. First, the signature of the bulk Dirac "point" [i.e., Dirac lines from the K-H direction in the 3D bulk Brillouin zone are projected on the 2D surface Brillouin zone, see Fig. 5(b)] can be well recognized in the spectrum [white dashed crosses in Fig. 5(e)]. Between these points, the previously mentioned zigzaglike edge mode is formed.

However, a more precise analysis of this latter state uncovers the realization of the drumhead phononic surface state. Indeed, as one can recognize in Fig. 6, these surface states exists independently of momentum $\boldsymbol{k}$, forming a 2D surface state between the two bulk Dirac lines mentioned earlier. Formation of the drumhead phonon surface state is presented schematically in Fig. 7. Remarkably, the projected bulk phonon surface state creates a graphenelike spectrum, independently of momentum $\boldsymbol{k}$. Note that the band crossing discussed earlier (red line in Fig. 7) is visible as a Dirac "point" for any value of $\boldsymbol{k}$. Finally, the drumhead surface state is realized between the Dirac nodal lines. It is remarkable that the frequency of the phonon drumhead surface state strongly depends on momentum $\boldsymbol{k}$ (see Fig. 6).

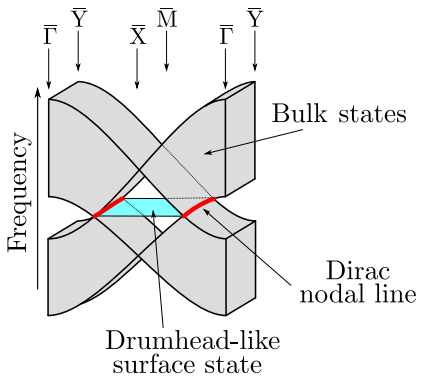

FIG. 7. Schematic representation of the phonon drumhead surface state.

IV. SUMMARY

In this paper, we discuss the basic properties of RhPb with the distorted kagome lattice of Rh atoms. Initially presented theoretical calculations [75] predict the realization of the distorted kagome lattice in RhPb. Indeed, our single crystal diffraction results confirm the predicted distortion of the kagome net in RhPb.

We presented a study of the dynamical properties of the bulk RhPb compound. In such a system, the emergence of several flattened phonon bands is possible. However, a more precise analysis shows that phonons in this band have even broader dispersion than for an ideal kagome lattice. This behavior is clearly recognized in the phonon density of states.

The phonon dispersion curves exhibit several interesting features, namely the (bulk) Dirac nodal lines and triple degenerated Dirac points. Such structures have consequences for the observed surface states. The most prominent example is the phonon drumhead surface state, between two (bulk) Dirac nodal lines projected on the surface Brillouin zone. In this context, the RhPb crystal with the distorted kagome lattice is an excellent platform to study the interplay between topological phonon surface states and flat electronic bands.

ACKNOWLEDGMENTS

We kindly thank Mark O. Goerbig for insightful discussions. Some figures in this work were rendered using VESTA [112] and XCRYSDEN [113] software. A.P. is grateful to Laboratoire de Physique des Solides in Orsay (CNRS, University Paris Saclay) for hospitality during a part of his work on this project. Work by W.R.M., M.A.M., B.C.S., and H.M. was funded by the U.S. Department of Energy, Office of Science, Basic Energy Sciences, Materials Sciences and Engineering Division. A.M.O. is grateful for support via the Alexander von Humboldt Foundation Fellowship (Humboldt-Forschungspreis) [117].

[1] H. Zhang, C.-X. Liu, X.-L. Qi, X. Dai, Z. Fang, and S.-C. Zhang, Topological insulators in Bi_2Se_3, Bi_2Te_3 and Sb_2Te_3 with a single Dirac cone on the surface, Nat. Phys. **5**, 438 (2009).

[2] Y. Xia, D. Qian, D. Hsieh, L. Wray, A. Pal, H. Lin, A. Bansil, D. Grauer, Y. S. Hor, R. J. Cava, and M. Z. Hasan, Observation of a large-gap topological-insulator class with a single Dirac cone on the surface, Nat. Phys. **5**, 398 (2009).

[3] D. Hsieh, Y. Xia, D. Qian, L. Wray, F. Meier, J. H. Dil, J. Osterwalder, L. Patthey, A. V. Fedorov, H. Lin, A. Bansil, D. Grauer, Y. S. Hor, R. J. Cava, and M. Z. Hasan, Observation of time-reversal-protected single-Dirac-cone topological-insulator states in Bi_2Te_3 and Sb_2Te_3, Phys. Rev. Lett. **103**, 146401 (2009).

[4] Z. Alpichshev, J. G. Analytis, J.-H. Chu, I. R. Fisher, Y. L. Chen, Z. X. Shen, A. Fang, and A. Kapitulnik, Stm imaging of electronic waves on the surface of Bi_2Te_3: Topologically protected surface states and hexagonal warping effects, Phys. Rev. Lett. **104**, 016401 (2010).

[5] M. Z. Hasan and C. L. Kane, Colloquium: Topological insulators, Rev. Mod. Phys. **82**, 3045 (2010).

[6] X.-L. Qi and S.-C. Zhang, Topological insulators and superconductors, Rev. Mod. Phys. **83**, 1057 (2011).

[7] N. P. Armitage, E. J. Mele, and A. Vishwanath, Weyl and Dirac semimetals in three-dimensional solids, Rev. Mod. Phys. **90**, 015001 (2018).

[8] L. Lu, J. D. Joannopoulos, and M. Soljačić, Topological photonics, Nat. Photonics **8**, 821 (2014).

[9] Z. Yang, F. Gao, X. Shi, X. Lin, Z. Gao, Y. Chong, and B. Zhang, Topological acoustics, Phys. Rev. Lett. **114**, 114301 (2015).

[10] T. Ozawa, H. M. Price, A. Amo, N. Goldman, M. Hafezi, L. Lu, M. C. Rechtsman, D. Schuster, J. Simon, O. Zilberberg, and I. Carusotto, Topological photonics, Rev. Mod. Phys. **91**, 015006 (2019).

[11] Y. Liu, X. Chen, and Y. Xu, Topological phononics: From fundamental models to real materials, Adv. Funct. Mater. **30**, 1904784 (2020).

[12] P. A. McClarty, Topological magnons: A review, Annu. Rev. Condens. Matter Phys. **13**, 171 (2022).

[13] H. Miao, T. T. Zhang, L. Wang, D. Meyers, A. H. Said, Y. L. Wang, Y. G. Shi, H. M. Weng, Z. Fang, and M. P. M. Dean, Observation of double Weyl phonons in parity-breaking FeSi, Phys. Rev. Lett. **121**, 035302 (2018).

[14] J. Li, Q. Xie, J. Liu, R. Li, M. Liu, L. Wang, D. Li, Y. Li, and X.-Q. Chen, Phononic Weyl nodal straight lines in MgB_2, Phys. Rev. B **101**, 024301 (2020).

[15] J. Li, Q. Xie, S. Ullah, R. Li, H. Ma, D. Li, Y. Li, and X.-Q. Chen, Coexistent three-component and two-component Weyl phonons in TiS, ZrSe, and HfTe, Phys. Rev. B **97**, 054305 (2018).

[16] R. Wang, B. W. Xia, Z. J. Chen, B. B. Zheng, Y. J. Zhao, and H. Xu, Symmetry-protected topological triangular Weyl complex, Phys. Rev. Lett. **124**, 105303 (2020).

[17] Z. J. Chen, R. Wang, B. W. Xia, B. B. Zheng, Y. J. Jin, Y.-J. Zhao, and H. Xu, Three-dimensional Dirac phonons with inversion symmetry, Phys. Rev. Lett. **126**, 185301 (2021).

[18] T. Zhang, Z. Song, A. Alexandradinata, H. Weng, C. Fang, L. Lu, and Z. Fang, Double-Weyl phonons in transition-metal monosilicides, Phys. Rev. Lett. **120**, 016401 (2018).

[19] M. Zhong, Y. Liu, F. Zhou, M. Kuang, T. Yang, X. Wang, and G. Zhang, Coexistence of phononic sixfold, fourfold, and threefold excitations in the ternary antimonide $Zr_3Ni_3Sb_4$, Phys. Rev. B **104**, 085118 (2021).

[20] C. Xie, Y. Liu, Z. Zhang, F. Zhou, T. Yang, M. Kuang, X. Wang, and G. Zhang, Sixfold degenerate nodal-point phonons: Symmetry analysis and materials realization, Phys. Rev. B **104**, 045148 (2021).

[21] P.-F. Liu, J. Li, X.-H. Tu, H. Li, J. Zhang, P. Zhang, Q. Gao, and B.-T. Wang, First-principles prediction of ideal type-II Weyl phonons in wurtzite ZnSe, Phys. Rev. B **103**, 094306 (2021).

[22] J. Liu, W. Hou, E. Wang, S. Zhang, J.-T. Sun, and S. Meng, Ideal type-II Weyl phonons in wurtzite CuI, Phys. Rev. B **100**, 081204(R) (2019).

[23] Q.-B. Liu, Y. Qian, H.-H. Fu, and Z. Wang, Symmetry-enforced Weyl phonons, npj Comput. Mater. **6**, 95 (2020).

[24] Q.-B. Liu, Z. Wang, and H.-H. Fu, Charge-four Weyl phonons, Phys. Rev. B **103**, L161303 (2021).

[25] J. Wang, H. Yuan, Y. Liu, F. Zhou, X. Wang, and G. Zhang, Hourglass Weyl and Dirac nodal line phonons, and drumhead-like and torus phonon surface states in orthorhombic-type KCuS, Phys. Chem. Chem. Phys. **24**, 2752 (2022).

[26] G. Ding, J. Wang, Z.-M. Yu, Z. Zhang, W. Wang, and X. Wang, Single pair of type-III Weyl points half-metals: $BaNiIO_6$ as an example, Phys. Rev. Mater. **7**, 014202 (2023).

[27] Y. Yang, C. Xie, Y. Cui, X. Wang, and W. Wu, Maximally charged single-pair multi-Weyl point phonons in $P23$-type BeH_2, Phys. Rev. B **107**, 054310 (2023).

[28] X. Wang, T. Yang, Z. Cheng, G. Surucu, J. Wang, F. Zhou, Z. Zhang, and G. Zhang, Topological nodal line phonons: Recent advances in materials realization, Appl. Phys. Rev. **9**, 041304 (2022).

[29] G. Liu, Y. Jin, Z. Chen, and H. Xu, Symmetry-enforced straight nodal-line phonons, Phys. Rev. B **104**, 024304 (2021).

[30] C. Xie, H. Yuan, Y. Liu, X. Wang, and G. Zhang, Three-nodal surface phonons in solid-state materials: Theory and material realization, Phys. Rev. B **104**, 134303 (2021).

[31] M. Wang, Y. Wang, Z. Yang, J. Fan, B. Zheng, R. Wang, and X. Wu, Symmetry-enforced nodal cage phonons in Th_2BC_2, Phys. Rev. B **105**, 174309 (2022).

[32] S. Basak, A. Kobiałka, and A. Ptok, Dynamical properties of $T_3Pb_2Ch_2$ (T = Pd, Pt and Ch = S, Se) with transition metal kagome net, Adv. Phys. Res. **2**, 2300025 (2023).

[33] F. Zhou, Z. Zhang, H. Chen, M. Kuang, T. Yang, and X. Wang, Hybrid-type nodal ring phonons and coexistence of higher-order quadratic nodal line phonons in an AgZr alloy, Phys. Rev. B **104**, 174108 (2021).

[34] B. Zheng, B. Xia, R. Wang, Z. Chen, J. Zhao, Y. Zhao, and H. Xu, Ideal type-III nodal-ring phonons, Phys. Rev. B **101**, 100303(R) (2020).

[35] Y. J. Jin, Z. J. Chen, B. W. Xia, Y. J. Zhao, R. Wang, and H. Xu, Ideal intersecting nodal-ring phonons in bcc C_8, Phys. Rev. B **98**, 220103(R) (2018).

[36] B. Zheng, F. Zhan, X. Wu, R. Wang, and J. Fan, Hourglass phonons jointly protected by symmorphic and nonsymmorphic symmetries, Phys. Rev. B **104**, L060301 (2021).

[37] R. Y. Wang, Z. J. Chen, Z. Q. Huang, B. W. Xia, and H. Xu, Classification and materials realization of topologically robust nodal ring phonons, Phys. Rev. Mater. **5**, 084202 (2021).

[38] Z. J. Chen, Z. J. Xie, Y. J. Jin, G. Liu, and H. Xu, Hybrid nodal-ring phonons with hourglass dispersion in $AgAlO_2$, Phys. Rev. Mater. **6**, 034202 (2022).

[39] Y. S. Chen, F. F. Huang, P. Zhou, Z. S. Ma, and L. Z. Sun, Ideal topological phononic nodal chain in K_2O materials class, New J. Phys. **23**, 103043 (2021).

[40] F. Zhou, H. Chen, Z.-M. Yu, Z. Zhang, and X. Wang, Realistic cesium fluogermanate: An ideal platform to realize the topologically nodal-box and nodal-chain phonons, Phys. Rev. B **104**, 214310 (2021).

[41] G. Ding, T. Sun, and X. Wang, Ideal nodal-net, nodal-chain, and nodal-cage phonons in some realistic materials, Phys. Chem. Chem. Phys. **24**, 11175 (2022).

[42] J. Zhu, W. Wu, J. Zhao, H. Chen, L. Zhang, and S. A. Yang, Symmetry-enforced nodal chain phonons, npj Quantum Mater. **7**, 52 (2022).

[43] J. Li, L. Wang, J. Liu, R. Li, Z. Zhang, and X.-Q. Chen, Topological phonons in graphene, Phys. Rev. B **101**, 081403(R) (2020).

[44] J. Wang, H. Yuan, Z.-M. Yu, Z. Zhang, and X. Wang, Coexistence of symmetry-enforced phononic Dirac nodal-line net and three-nodal surfaces phonons in solid-state materials: Theory and materials realization, Phys. Rev. Mater. **5**, 124203 (2021).

[45] Q.-B. Liu, Z.-Q. Wang, and H.-H. Fu, Ideal topological nodal-surface phonons in RbTeAu-family materials, Phys. Rev. B **104**, L041405 (2021).

[46] J. Wang, H. Yuan, M. Kuang, T. Yang, Z.-M. Yu, Z. Zhang, and X. Wang, Coexistence of zero-, one-, and two-dimensional degeneracy in tetragonal SnO_2 phonons, Phys. Rev. B **104**, L041107 (2021).

[47] Q.-B. Liu, H.-H. Fu, and R. Wu, Topological phononic nodal hexahedron net and nodal links in the high-pressure phase of the semiconductor CuCl, Phys. Rev. B **104**, 045409 (2021).

[48] Z. Wang, W. Zhou, A. N. Rudenko, and S. Yuan, Lattice dynamics and topological surface phonon states in cuprous oxide Cu_2O, Phys. Rev. B **103**, 195137 (2021).

[49] Y. Yang, J. Wang, Y. Liu, Y. Cui, G. Ding, and X. Wang, Topological phonons in Cs-Te binary systems, Phys. Rev. B **107**, 024304 (2023).

[50] C. Strohm, G. L. J. A. Rikken, and P. Wyder, Phenomenological evidence for the phonon Hall effect, Phys. Rev. Lett. **95**, 155901 (2005).

[51] L. Sheng, D. N. Sheng, and C. S. Ting, Theory of the phonon Hall effect in paramagnetic dielectrics, Phys. Rev. Lett. **96**, 155901 (2006).

[52] Y. Kagan and L. A. Maksimov, Anomalous Hall effect for the phonon heat conductivity in paramagnetic dielectrics, Phys. Rev. Lett. **100**, 145902 (2008).

[53] L. Zhang, J. Ren, J.-S. Wang, and B. Li, Topological nature of the phonon Hall effect, Phys. Rev. Lett. **105**, 225901 (2010).

[54] T. Qin, J. Zhou, and J. Shi, Berry curvature and the phonon Hall effect, Phys. Rev. B **86**, 104305 (2012).

[55] T. Saito, K. Misaki, H. Ishizuka, and N. Nagaosa, Berry phase of phonons and thermal Hall effect in nonmagnetic insulators, Phys. Rev. Lett. **123**, 255901 (2019).

[56] X. Zhang, Y. Zhang, S. Okamoto, and D. Xiao, Thermal Hall effect induced by magnon-phonon interactions, Phys. Rev. Lett. **123**, 167202 (2019).

[57] L. Zhang and Q. Niu, Chiral phonons at high-symmetry points in monolayer hexagonal lattices, Phys. Rev. Lett. **115**, 115502 (2015).

[58] N. Li, J. Ren, L. Wang, G. Zhang, P. Hänggi, and B. Li, Colloquium: Phononics: Manipulating heat flow with electronic analogs and beyond, Rev. Mod. Phys. **84**, 1045 (2012).

[59] Z. Lin, J.-H. Choi, Q. Zhang, W. Qin, S. Yi, P. Wang, L. Li, Y. Wang, H. Zhang, Z. Sun, L. Wei, S. Zhang, T. Guo, Q. Lu, J.-H. Cho, C. Zeng, and Z. Zhang, Flatbands and emergent ferromagnetic ordering in Fe_3Sn_2 kagome lattices, Phys. Rev. Lett. **121**, 096401 (2018).

[60] J.-X. Yin, S. S. Zhang, G. Chang, Q. Wang, S. S. Tsirkin, Z. Guguchia, B. Lian, H. Zhou, K. Jiang, I. Belopolski, N. Shumiya, D. Multer, M. Litskevich, T. A. Cochran, H. Lin, Z. Wang, T. Neupert, S. Jia, H. Lei, and M. Z. Hasan, Negative flat band magnetism in a spin–orbit-coupled correlated kagome magnet, Nat. Phys. **15**, 443 (2019).

[61] M. Li, Q. Wang, G. Wang, Z. Yuan, W. Song, R. Lou, Z. Liu, Y. Huang, Z. Liu, H. Lei, Z. Yin, and S. Wang, Dirac cone, flat band and saddle point in kagome magnet YMn_6Sn_6, Nat. Commun. **12**, 3129 (2021).

[62] B. C. Sales, J. Yan, W. R. Meier, A. D. Christianson, S. Okamoto, and M. A. McGuire, Electronic, magnetic, and thermodynamic properties of the kagome layer compound FeSn, Phys. Rev. Mater. **3**, 114203 (2019).

[63] W. R. Meier, M.-H. Du, S. Okamoto, N. Mohanta, A. F. May, M. A. McGuire, C. A. Bridges, G. D. Samolyuk, and B. C. Sales, Flat bands in the CoSn-type compounds, Phys. Rev. B **102**, 075148 (2020).

[64] Z. Liu, M. Li, Q. Wang, G. Wang, C. Wen, K. Jiang, X. Lu, S. Yan, Y. Huang, D. Shen, J.-X. Yin, Z. Wang, Z. Yin, H. Lei, and S. Wang, Orbital-selective Dirac fermions and extremely flat bands in frustrated kagome-lattice metal CoSn, Nat. Commun. **11**, 4002 (2020).

[65] H. Huang, L. Zheng, Z. Lin, X. Guo, S. Wang, S. Zhang, C. Zhang, Z. Sun, Z. Wang, H. Weng, L. Li, T. Wu, X. Chen, and C. Zeng, Flat-band-induced anomalous anisotropic charge transport and orbital magnetism in kagome metal CoSn, Phys. Rev. Lett. **128**, 096601 (2022).

[66] M. Kang, S. Fang, L. Ye, H. C. Po, J. Denlinger, C. Jozwiak, A. Bostwick, E. Rotenberg, E. Kaxiras, J. G. Checkelsky, and R. Comin, Topological flat bands in frustrated kagome lattice CoSn, Nat. Commun. **11**, 4004 (2020).

[67] M. Kang, L. Ye, S. Fang, J.-S. You, A. Levitan, M. Han, J. I. Facio, C. Jozwiak, A. Bostwick, E. Rotenberg, M. K. Chan, R. D. McDonald, D. Graf, K. Kaznatcheev, E. Vescovo, D. C. Bell, E. Kaxiras, J. van den Brink, M. Richter, M. Prasad Ghimire *et al.*, Dirac fermions and flat bands in the ideal kagome metal FeSn, Nat. Mater. **19**, 163 (2020).

[68] Z. Lin, C. Wang, P. Wang, S. Yi, L. Li, Q. Zhang, Y. Wang, Z. Wang, H. Huang, Y. Sun, Y. Huang, D. Shen, D. Feng, Z. Sun, J.-H. Cho, C. Zeng, and Z. Zhang, Dirac fermions in antiferromagnetic FeSn kagome lattices with combined space inversion and time-reversal symmetry, Phys. Rev. B **102**, 155103 (2020).

[69] M. Han, H. Inoue, S. Fang, C. John, L. Ye, M. K. Chan, D. Graf, T. Suzuki, M. P. Ghimire, W. J. Cho, E. Kaxiras, and J. G. Checkelsky, Evidence of two-dimensional flat band at the surface of antiferromagnetic kagome metal FeSn, Nat. Commun. **12**, 5345 (2021).

[70] B. C. Sales, W. R. Meier, A. F. May, J. Xing, J.-Q. Yan, S. Gao, Y. H. Liu, M. B. Stone, A. D. Christianson, Q. Zhang, and M. A. McGuire, Tuning the flat bands of the kagome metal CoSn with Fe, In, or Ni doping, Phys. Rev. Mater. **5**, 044202 (2021).

[71] Y. Xie, L. Chen, T. Chen, Q. Wang, Q. Yin, J. R. Stewart, M. B. Stone, L. L. Daemen, E. Feng, H. Cao, H. Lei, Z. Yin, A. H. MacDonald, and P. Dai, Spin excitations in metallic kagome lattice FeSn and CoSn, Commun. Phys. **4**, 240 (2021).

[72] C. Zeng, P. R. C. Kent, M. Varela, M. Eisenbach, G. M. Stocks, M. Torija, J. Shen, and H. H. Weitering, Epitaxial stabilization of ferromagnetism in the nanophase of FeGe, Phys. Rev. Lett. **96**, 127201 (2006).

[73] M. Kakihana, K. Nishimura, D. Aoki, A. Nakamura, M. Nakashima, Y. Amako, T. Takeuchi, T. Kida, T. Tahara, M. Hagiwara, H. Harima, M. Hedo, T. Nakama, and Y. Onuki, Electronic states of antiferromagnet FeSn and Pauli paramagnet CoSn, J. Phys. Soc. Jpn. **88**, 014705 (2019).

[74] D. Khadka, T. R. Thapaliya, J. Wen, R. F. Need, and S. X. Huang, High quality epitaxial thin films and exchange bias of antiferromagnetic dirac semimetal FeSn, Appl. Phys. Lett. **117**, 032403 (2020).

[75] A. Ptok, A. Kobiałka, M. Sternik, J. Łażewski, P. T. Jochym, A. M. Oleś, S. Stankov, and P. Piekarz, Chiral phonons in the honeycomb sublattice of layered CoSn-like compounds, Phys. Rev. B **104**, 054305 (2021).

[76] P. C. Canfield, T. Kong, U. S. Kaluarachchi, and N. H. Jo, Use of frit-disc crucibles for routine and exploratory solution growth of single crystalline samples, Philos. Mag. **96**, 84 (2016).

[77] V. Petříček, M. Dušek, and L. Palatinus, Crystallographic computing system JANA2006: General features, Z. Kristallogr. - Cryst. Mater. **229**, 345 (2014).

[78] P. E. Blöchl, Projector augmented-wave method, Phys. Rev. B **50**, 17953 (1994).

[79] G. Kresse and J. Hafner, *Ab initio* molecular-dynamics simulation of the liquid-metal–amorphous-semiconductor transition in germanium, Phys. Rev. B **49**, 14251 (1994).

[80] G. Kresse and J. Furthmüller, Efficient iterative schemes for *ab initio* total-energy calculations using a plane-wave basis set, Phys. Rev. B **54**, 11169 (1996).

[81] G. Kresse and D. Joubert, From ultrasoft pseudopotentials to the projector augmented-wave method, Phys. Rev. B **59**, 1758 (1999).

[82] J. P. Perdew, K. Burke, and M. Ernzerhof, Generalized gradient approximation made simple, Phys. Rev. Lett. **77**, 3865 (1996).

[83] H. J. Monkhorst and J. D. Pack, Special points for Brillouin-zone integrations, Phys. Rev. B **13**, 5188 (1976).

[84] R. Pott, R. Schefzyk, D. Wohlleben, and A. Junod, Thermal expansion and specific heat of intermediate valent YbCuAl, Z. Phys. B **44**, 17 (1981).

[85] M. S. Kim, Y. Echizen, K. Umeo, S. Kobayashi, M. Sera, P. S. Salamkha, O. L. Sologub, T. Takabatake, X. Chen, T. Tayama, T. Sakakibara, M. H. Jung, and M. B. Maple, Low-temperature anomalies in magnetic, transport, and thermal properties of single-crystal CeRhSn with valence fluctuations, Phys. Rev. B **68**, 054416 (2003).

[86] E. Morosan, S. Bud'ko, P. Canfield, M. Torikachvili, and A. Lacerda, Thermodynamic and transport properties of *R*AgGe (R = Tb–Lu) single crystals, J. Magn. Magn. Mater. **277**, 298 (2004).

[87] S. F. Matar, J. F. Riecken, B. Chevalier, R. Pöttgen, A. F. Al Alam, and V. Eyert, Electronic and magnetic properties and chemical bonding of CeMSn (M = Rh, Ru) from first principles, Phys. Rev. B **76**, 174434 (2007).

[88] F. R. de Boer, R. A. Elenbaas, and W. C. M. Mattens, Abstract: Mixed valence behaviour in the intermetallic compound YbCuAl, J. Appl. Phys. **49**, 2100 (1978).

[89] Y. Qian, S. Nie, C. Yi, L. Kong, C. Fang, T. Qian, H. Ding, Y. Shi, Z. Wang, H. Weng, and Z. Fang, Topological electronic states in HfRuP family superconductors, npj Comput. Mater. **5**, 121 (2019).

[90] H. Su, T. Shang, F. Du, C. F. Chen, H. Q. Ye, X. Lu, C. Cao, M. Smidman, and H. Q. Yuan, NbReSi: A noncentrosymetric superconductor with large upper critical field, Phys. Rev. Mater. **5**, 114802 (2021).

[91] T. Asaba, V. Ivanov, S. M. Thomas, S. Y. Savrasov, J. D. Thompson, E. D. Bauer, and F. Ronning, Colossal anomalous Nernst effect in a correlated noncentrosymmetric kagome ferromagnet, Sci. Adv. **7**, eabf1467 (2021).

[92] R. Kumar, S.-S. Luo, F. Du, H. Su, J. Zhang, C. Cao, and H. Q. Yuan, Superconductivity in non-centrosymmetric ZrNiAl and HfRhSn-type compounds, J. Phys.: Condens. Matter **34**, 435701 (2022).

[93] See the Supplemental Material at http://link.aps.org/supplemental/10.1103/PhysRevResearch.5.043231 for more details on the crystallographic data, XRD refinements, and additional numerical results. This Supplemental Material contains Ref. [62–66,70,72–74,114–116].

[94] K. Parlinski, Z. Q. Li, and Y. Kawazoe, First-principles determination of the soft mode in cubic ZrO_2, Phys. Rev. Lett. **78**, 4063 (1997).

[95] A. Togo and I. Tanaka, First principles phonon calculations in materials science, Scr. Mater. **108**, 1 (2015).

[96] M. P. L. Sancho, J. M. L. Sancho, J. M. L. Sancho, and J. Rubio, Highly convergent schemes for the calculation of bulk and surface Green functions, J. Phys. F: Met. Phys. **15**, 851 (1985).

[97] Q. S. Wu, S. N. Zhang, H.-F. Song, M. Troyer, and A. A. Soluyanov, WannierTools: An open-source software package for novel topological materials, Comput. Phys. Commun. **224**, 405 (2018).

[98] O. Hellman, I. A. Abrikosov, and S. I. Simak, Lattice dynamics of anharmonic solids from first principles, Phys. Rev. B **84**, 180301(R) (2011).

[99] P. T. Jochym and J. Łażewski, High Efficiency Configuration Space Sampling–probing the distribution of available states, SciPost Phys. **10**, 129 (2021).

[100] M. Sinha, H. K. Vivanco, C. Wan, M. A. Siegler, V. J. Stewart, E. A. Pogue, L. A. Pressley, T. Berry, Z. Wang, I. Johnson, M. Chen, T. T. Tran, W. A. Phelan, and T. M. McQueen, Twisting of 2D kagome sheets in layered intermetallics, ACS Cent. Sci. **7**, 1381 (2021).

[101] J.-X. Yin, N. Shumiya, S. Mardanya, Q. Wang, S. S. Zhang, H.-J. Tien, D. Multer, Y. Jiang, G. Cheng, N. Yao, S. Wu, D. Wu, L. Deng, Z. Ye, R. He, G. Chang, Z. Liu, K. Jiang, Z. Wang, T. Neupert *et al.*, Fermion–boson many-body interplay in a frustrated kagome paramagnet, Nat. Commun. **11**, 4003 (2020).

[102] L. Brey and H. A. Fertig, Electronic states of graphene nanoribbons studied with the Dirac equation, Phys. Rev. B **73**, 235411 (2006).

[103] K. Wakabayashi, Y. Takane, and M. Sigrist, Perfectly conducting channel and universality crossover in disordered graphene nanoribbons, Phys. Rev. Lett. **99**, 036601 (2007).

[104] W. Yao, S. A. Yang, and Q. Niu, Edge states in graphene: From gapped flat-band to gapless chiral modes, Phys. Rev. Lett. **102**, 096801 (2009).

[105] B.-J. Yang and N. Nagaosa, Emergent topological phenomena in thin films of pyrochlore iridates, Phys. Rev. Lett. **112**, 246402 (2014).

[106] Z. Li, J. Zhuang, L. Wang, H. Feng, Q. Gao, X. Xu, W. Hao, X. Wang, C. Zhang, K. Wu, S. X. Dou, L. Chen, Z. Hu, and Y. Du, Realization of flat band with possible nontrivial topology in electronic kagome lattice, Sci. Adv. **4**, eaau4511 (2018).

[107] A. Mook, J. Henk, and I. Mertig, Edge states in topological magnon insulators, Phys. Rev. B **90**, 024412 (2014).

[108] D. Malz, J. Knolle, and A. Nunnenkamp, Topological magnon amplification, Nat. Commun. **10**, 3937 (2019).

[109] H. Zhong, R. Wang, F. Ye, J. Zhang, L. Zhang, Y. Zhang, M. R. Belić, and Y. Zhang, Topological insulator properties of photonic kagome helical waveguide arrays, Results Phys. **12**, 996 (2019).

[110] X. Xi, J. Ma, S. Wan, C.-H. Dong, and X. Sun, Observation of chiral edge states in gapped nanomechanical graphene, Sci. Adv. **7**, eabe1398 (2021).

[111] S. Basak and A. Ptok, Theoretical study of dynamical and electronic properties of noncentrosymmetric superconductor NbReSi, Materials **16**, 78 (2023).

[112] K. Momma and F. Izumi, VESTA3 for three-dimensional visualization of crystal, volumetric and morphology data, J. Appl. Crystallogr. **44**, 1272 (2011).

[113] A. Kokalj, Xcrysden–a new program for displaying crystalline structures and electron densities, J. Mol. Graphics Modell. **17**, 176 (1999).

[114] M. Jovanovic and L. M. Schoop, Simple chemical rules for predicting band structures of kagome materials, J. Am. Chem. Soc. **144**, 10978 (2022).

[115] F. Herman, C. D. Kuglin, K. F. Cuff, and R. L. Kortum, Relativistic corrections to the band structure of tetrahedrally bonded semiconductors, Phys. Rev. Lett. **11**, 541 (1963).

[116] K. V. Shanavas, Z. S. Popović, and S. Satpathy, Theoretical model for Rashba spin-orbit interaction in *d* electrons, Phys. Rev. B **90**, 165108 (2014).

[117] https://www.humboldt-foundation.de/web/humboldt-preis.html.

4.2.2 Theoretical Study of Dynamical and Electronic Properties of Noncentrosymmetric Superconductor NbReSi

S. Basak and A. Ptok, Materials **16**, 78 (2023).

Noncentrosymmetric superconductors provide an attractive platform to study unconventional superconductivity. The antisymmetric spin-orbit coupling has suggested the mixture of spin-singlet and spin-triplet states as the superconducting pairing mechanism. In this family, the Re-based superconductors are especially important due to the high upper critical magnetic field (> 8 T) and, in some cases, broken time-reversal symmetry. In this paper, we study the electronic and lattice dynamical properties of non-centrosymmetric superconductor NbReSi. We start by analyzing the dynamical stability of two symmetry groups, P$\bar{6}$2m and Ima2, and conclude that P$\bar{6}$2m is stable while the other one is not. We then study the stability of both the symmetries under external hydrostatic pressure and comment on their ground state energies. NbReSi is very similar in electronic structure to $A_2Cr_3As_3$ (A =K, Rb, Cs). Similar to $A_2Cr_3As_3$, we observe a quasi-one-dimensional behavior in this compound, highly dispersive in the direction perpendicular to the kagome-like plane reflected in the plot of Fermi surface. We also observe phonon surface states depending on the type of surface terminations, concentrated in the low-frequency range, coming from the vibration of Nb and Re atoms forming the distorted kagome structure.

Author's contribution: Performing the lattice dynamic calculations (phonon dispersion curves and phonon density of states), analysis and discussion of obtained results, partial preparation of figures, partial preparation of the manuscript, participation in preparing the response for Referees.

materials

MDPI

Article

Theoretical Study of Dynamical and Electronic Properties of Noncentrosymmetric Superconductor NbReSi

Surajit Basak and Andrzej Ptok *

Institute of Nuclear Physics, Polish Academy of Sciences, W. E. Radzikowskiego 152, PL-31342 Kraków, Poland
* Correspondence: aptok@mmj.pl

Abstract: The noncentrosymmetric NbReSi superconductor with $T_c \simeq 6.5$ K is characterized by the relatively large upper critical magnetic field. Its multigap features were observed experimentally. Recent studies suggested the realization of P$\bar{6}$2m or Ima2 symmetry. We discuss the dynamical properties of both symmetries (e.g., phonon spectra). In this paper, using the ab initio techniques, we clarify this ambiguity, and conclude that the Ima2 symmetry is unstable, and P$\bar{6}$2m should be realized. The P$\bar{6}$2m symmetry is also stable in the presence of external hydrostatic pressure. We show that NbReSi with the P$\bar{6}$2m symmetry should host phonon surface states for (100) and (110) surfaces. Additionally, we discuss the main electronic properties of the system with the stable symmetry.

Keywords: noncentrosymmetric superconductor; phonons; surface states; spin–orbit coupling

1. Introduction

Noncentrosymmetric superconductors are characterized by antisymmetric spin–orbit coupling (SOC) [1–3], which gives rise to the topological superconducting pairing as a result of a mixture of spin-singlet and spin-triplet components [3–5]. This behavior was first discovered in the heavy fermion compound $CePt_3Si$ [6]. Recently, a large group of noncentrosymmetric superconductors have been discovered, e.g., $Li_2(Pt_{1-x}Pd_x)_3B$ [7,8], $BaPtSi_3$ [9], $LaNiC_2$ [10], $SrPtAs_2$ [11], RPtSi (R = La, Ce, Pr, Nd, Sm, Gd) [12,13], $A_2Cr_3As_3$ (A = K, Rb, Cs) [14–16], $K_2Mo_3As_3$ [17], (Ta,Nb)Rh_2B_2 [18], ThTSi (T = Co, Ir, Ni, Pt) [19–21], or $CeRh_2As_2$ [22,23].

Recently, many ternary noncentrosymmetric superconductors were discovered and studied. Typically, the MM'Si class of materials (where M and M' are transition metals or rare earth metals) crystallise in several distinct structural symmetries, such as tetragonal PbClF-type (P4/nmm symmetry) [24], orthorhombic TiNiSi-type (Pnma symmetry) [25], hexagonal ZrNiAl-type (P$\bar{6}$2m symmetry) [26], or orthorhombic TiFeSi-type (Ima2 symmetry) [26]. Among the mentioned symmetries, two are noncentrosymmetric (P$\bar{6}$2m and Ima2) and can give rise to unconventional triplet superconductivity. These types of features were discussed in the case of TaTSi (T = Re, Ru) [27,28] or TRuSi (T = Ti, Nb, Hf, Ta) [29], both with Ima2 symmetry.

In our paper, we focus on the recently studied noncentrosymmetric NbReSi superconductor [30], which exhibits superconducting properties below $T_c \simeq 6.5$ K [30–32]. A relatively large upper critical magnetic filed was reported experimentally (around 12.5 T [31], 13.5 T [30], or 8.1 T [32]). The absence of spontaneous magnetic fields below T_c from muon-spin relaxation (μSR) was observed [30]. The superfuild density and the spin-lattice relaxation rate suggest nodeless superconductivity [30]. The signatures of multigap superconductivity, evidenced by the field-dependent μSR rate and the electronic specific heat coefficient [30] can be related to the multiband Fermi level [31].

However, the characterization of the studied samples suggest the realization of the P$\bar{6}$2m symmetry (cf. Refs. [30,31]) or Ima2 (cf. Ref. [32])—structures presented in Figure 1. We clarify this ambiguity using the ab initio techniques. From the study of dynamical

check for updates

Citation: Basak, S.; Ptok, A. Theoretical Study of Dynamical and Electronic Properties of Noncentrosymmetric Superconductor NbReSi. *Materials* **2023**, *16*, 78. https://doi.org/10.3390/ma16010078

Academic Editor: Tim Coombs

Received: 18 November 2022
Revised: 11 December 2022
Accepted: 16 December 2022
Published: 21 December 2022

properties, we claim that the P$\bar{6}$2m symmetry is stable in this system. We also discuss the dynamical and electronic properties of the system with stable symmetry.

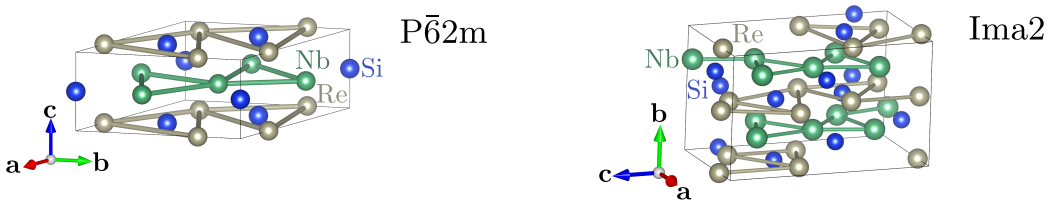

Figure 1. Schematic representation of NbReSi conventional cell with P$\bar{6}$2m and Ima2 symmetries (as labeled). In both structures, the Re and Nb atoms form distorted kagome-like sublattices.

The paper is organized as follows. Details of the techniques used are provided in Section 2. Next, in Section 3 we present and discuss our theoretical results. Finally, a summary is provided in Section 4.

2. Calculation Details

First-principle (DFT) calculations are performed using the projector augmented-wave (PAW) potentials [33] implemented in the Vienna Ab initio Simulation Package (VASP) code [34–36]. Calculations are made within the generalized gradient approximation (GGA) in the Perdew, Burke, and Ernzerhof (PBE) parameterization [37]. The calculations, including SOC, were performed with the energy cut-off set to 600 eV.

Initially, the crystal structure and atom positions were optimised. In the case of the P$\bar{6}$2m symmetry, the primitive cell containing three formula units was optimized, with the $6 \times 6 \times 12$ **k**-point grid in the Monkhorst–Pack scheme [38]. Similarly, for the Ima2 symmetry, we used a conventional unit cell with $6 \times 6 \times 3$ **k**-point grid. As the convergence condition of an optimization loop, we take the energy difference of 10^{-5} eV and 10^{-7} eV for ionic and electronic degrees of freedom, respectively. Optimized structure parameters are collected in Section 3.1

The interatomic force constants (IFC) are calculated within the Parlinski-Li-Kawazoe method [39] implemented in PHONOPY package [40]. Force constants were obtained from first-principles calculations of the Hellmann–Feynman forces by VASP and used to build a dynamical matrix of the crystal. Phonon frequencies were obtained by diagonalization of the dynamical matrix. Calculations were performed using the supercell technique. In the case of the P$\bar{6}$2m symmetry, the supercell based on $2 \times 2 \times 3$ primitive cells was used. For the Ima2 symmetry, we used a supercell based on $2 \times 1 \times 2$ conventional cells. In both cases, the reduced $3 \times 3 \times 3$ **k**-grid was used. Furthermore, dynamical properties were evaluated withing ALAMODE software [41], using the multidisplacement method. Finally, to study the surface states of phonons, the surface Green's function for a semi-infinite system [42] was calculated using WANNIERTOOLS [43].

3. Results and Discussion

3.1. Crystal Structure

After optimizing the crystal structures, we found:

- for the P$\bar{6}$2m symmetry (space group No. 189): $a = b = 6.872$ Å, and $c = 3.310$ Å, while experimental values are $a = b = 6.719$ Å, and $c = 3.485$ Å [31]; Nb atoms are in Wyckoff positions 3*g*: (0.4020, 0, 1/2), Re atoms in Wyckoff positions 3*f*: (0.7411, 0, 0), while Si atoms in the two non-equivalent Wyckoff positions 2*c*: (1/3, 2/3, 0) and 1*b*: (0, 0, 1/2).
- for the Ima2 symmetry (space group No. 46): $a = 6.990$ Å, $b = 11.618$ Å, $c = 6.726$ Å, while the reported values are $a = 6.925$ Å, $b = 11.671$ Å, and $c = 6.694$ Å [32]; Nb atoms are in three non-equivalent Wyckoff positions 4*b*: (1/4, 0.1959, 0.7093), 4*b*: (1/4, 0.7873, 0.7130) and 4*a*: (1/4, −0.0033, 0.0919), Re atoms in the two non-equivalent

Wyckoff positions 4*a* (0, 0, 0.7547) and 8*c*: (0.5344, 0.8732, 0.3776), while Si atoms in two non-equivalent positions 4*b*: (1/4, −0.0259, 0.4920) and 8*c*: (0.0037, 0.1677, 0.0064).

In the case of the P$\bar{6}$2m symmetry, the primitive unit cell is equivalent to the conventional cell and contains three formula units. Contrary to this, for the Ima2 symmetry, the primitive cell contains six formula units, while the conventional one is twice as big. The obtained crystal parameters are used in the next part of the paper as reference ones.

3.2. Dynamical Properties

The phonon dispersions for both symmetries are presented in Figure 2. Regardless of the symmetry, the phonon branches are collected into several groups separated by gaps. In the case of P$\bar{6}$2m symmetry, acoustic modes exhibit a linear behavior around the Γ point. For the Ima2 symmetry, one of the acoustic modes along the Γ–Λ_0 path (continuing along the G_0-X path) poses the soft mode. However, this soft mode is also visible around the S-point. From the dynamical point of view, NbReSi is unstable with the Ima2 symmetry.

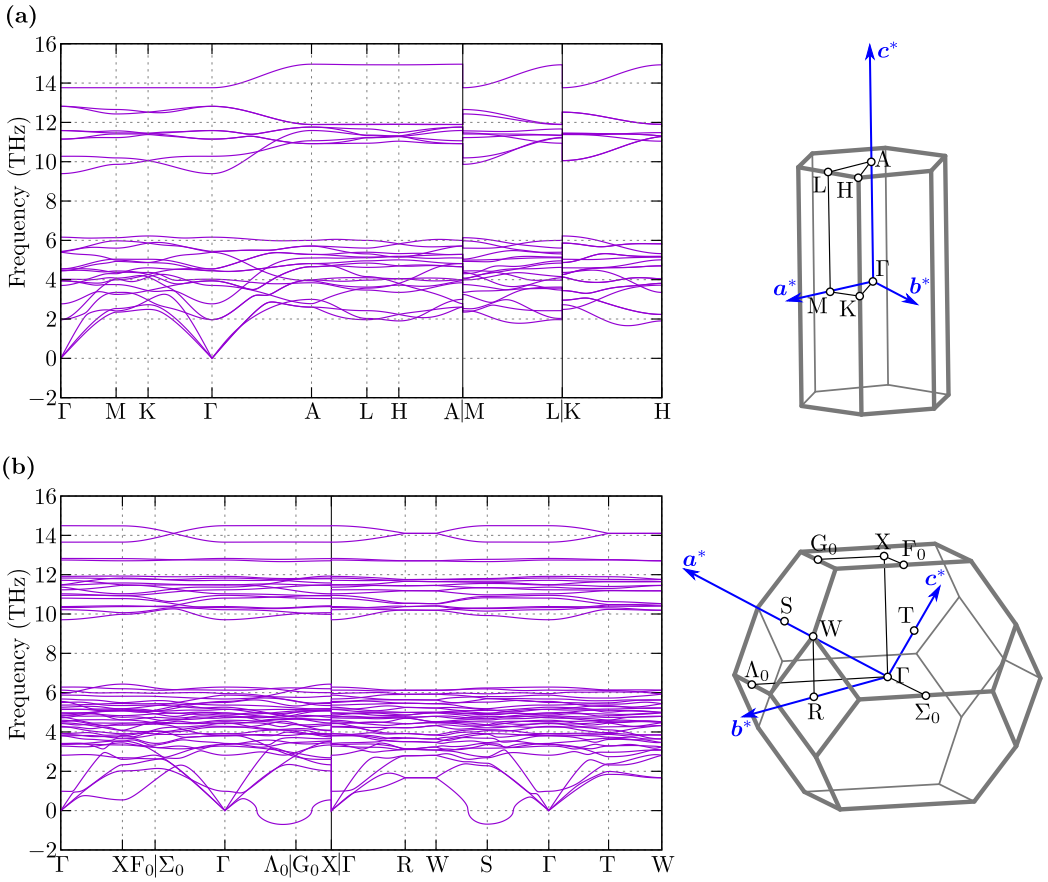

Figure 2. The phonon dispersion along high symmetry directions (left panels) and the Brillouin zone (right panels) for P$\bar{6}$2m (**a**) and Ima2 (**b**).

In both symmetries, Re and Nb atoms form distorted kagome-like sublattices (see Figure 1), and should exist a relation between these two structures. In fact, there is a group-subgroup relationship between the discussed symmetries [44], which is, P$\bar{6}$2m→Amm2→Ima2. This allows Ima2 to emerge from P$\bar{6}$2m as a consequence of atom displacements. Nevertheless, P$\bar{6}$2m is stable and does not exhibit any soft modes that can lead to Amm2 or Ima2 symmetries.

The above mentioned properties are also reflected in the phonon density of states (PDOS), presented in Figure 3. A more precise analysis uncovers the contribution of separate atoms in vibration modes. The lower-frequency modes are realized by Re and Nb atoms (relatively heavy atoms). As can be expected, high-frequency modes are realized by

lighter atoms, i.e., Si. The PDOS are qualitatively comparable for both symmetries. As we can see, the soft mode in the Ima2 structure is realized by vibrations of Nb atoms.

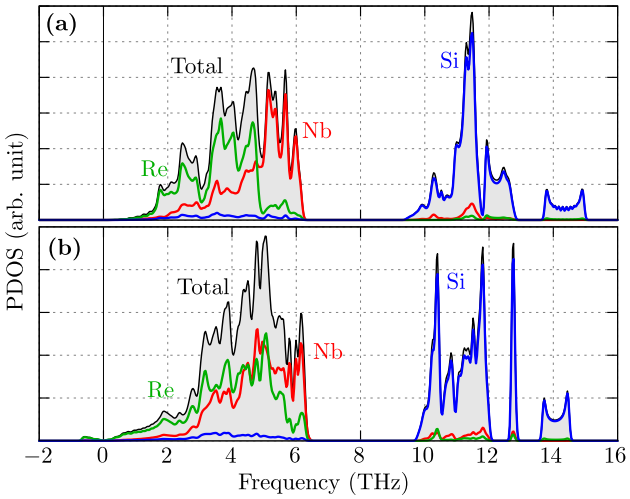

Figure 3. The phonon density of states (PDOS) for P$\bar{6}$2m (**a**) and Ima2 (**b**).

The irreducible representations of the phonon modes at the Γ point are given as [45]:

- for the P$\bar{6}$2m symmetry:

$$\begin{aligned} \Gamma_{\text{acoustic}} &= A_2'' + E' \\ \Gamma_{\text{optic}} &= 2A_1' + 2A_2' + A_1'' + 3A_2'' + 6E' + 2E'', \end{aligned} \tag{1}$$

where $A_2'' + E'$ modes are infra-red active, while $E' + E''$ modes are Raman active.

- for the Ima2 symmetry:

$$\begin{aligned} \Gamma_{\text{acoustic}} &= A_1 + B_1 + B_2 \\ \Gamma_{\text{optic}} &= 14A_1 + 11A_2 + 11B_1 + 15B_2, \end{aligned} \tag{2}$$

where $A_1 + B_1 + B_2$ modes are infra-red active, while $A_1 + A_2 + B_1 + B_2$ modes are Raman active.

For lower symmetry (i.e., Ima2), in practice all modes are Raman active. Here we should note that in both symmetries primitive cells contain different numbers of atoms. As a consequence, the Raman spectra can be used as a tool to confirm the symmetry realized by NbReSi.

3.2.1. Phonon Surface States

Realization of hexagonal symmetry by NbReSi can give rise to phonon surface states [46]. The calculated surface Green functions are presented in Figure 4. The phonon dispersion (Figure 2) is very complex and concentrated in the low frequency range (below 7.5 THz). However, for surfaces (100) and (110), the phonon edge states are clearly visible at several places. For example, at the $\bar{\text{L}}$ point, where the phonon surface states are realized by separated modes with relatively large intensity (marked by blue arrows in Figure 4). Interestingly, for some terminations, this mode is not realized, see Figure 4c)

The relatively small frequencies of the mentioned phonon surface modes suggest their strong connection with Nb or Re atoms on the surface. For the surface (100), where the bulk M and Γ points are projected on the surface $\bar{\Gamma}$ point, we observed a Dirac-like structure (Figure 4b). A more precise analysis of the surface band structure uncovers avoided crossing of two edge states. Contrary to this, for the (110) surface, where bulk K and M points are projected on the surface $\bar{\text{M}}$ point, while bulk K and Γ points are projected on surface $\bar{\Gamma}$ point, we observed only one separated surface state (Figure 4c,d).

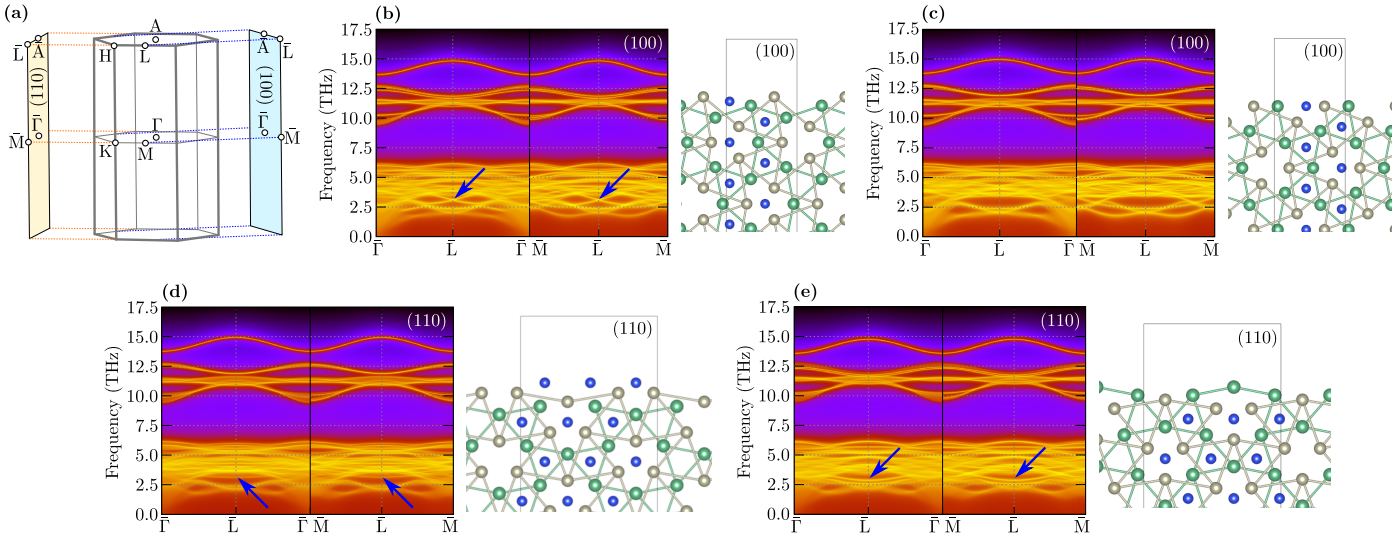

Figure 4. Projection of the 3D bulk Brillouin zone on the 2D surface Brillouin zones for (100) and (110) surfaces (**a**). Panels (**b**–**e**) present surface Green functions for different surfaces (as labeled) and corresponding terminations (right schemats). Blue arrows show phonon surface states at $\bar{\Gamma}$ point.

3.2.2. Role of Hydrostatic Pressure

Now, we briefly discuss the impact of external hydrostatic pressure on NbReSi. Under external pressure, the volume of the system decreases monotonically (Figure 5a). In the absence of pressure, the energy for both symmetries is comparable. However, comparison of their volumes (per formula unit, see Figure 5a) clearly show that the unit cell of P$\bar{6}$2m is always more dense. This feature has an important impact under external pressure and indicates a smaller enthalpy (i.e., the sum of the ground states energy and pV terms) of the system with P$\bar{6}$2m than Ima2. Furthermore, above some pressure (around 20 GPa), the system with the Ima2 symmetry was impossible to optimize, and the structure goes to the P$\bar{6}$2m symmetry. This suggests instability of the NbReSi system with the Ima2 symmetry even under pressure.

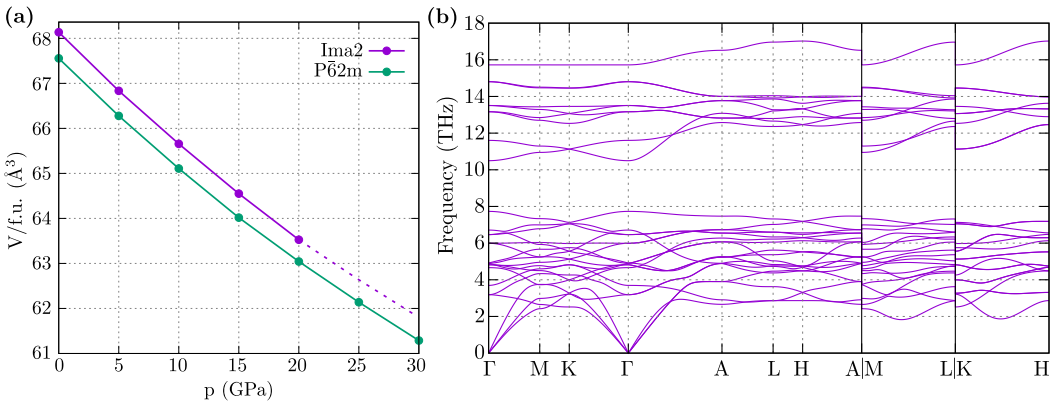

Figure 5. Influence of external hydrostatic pressure on NbReSi. (**a**) Pressure dependence of the unit cell volume (per formula unit) for system with P$\bar{6}$2m and Ima2 symmetries (as labeled). (**b**) Phonon dispersion curves for system with P$\bar{6}$2m under pressure 30 GPa.

Figure 5b shows the dispersion cerves for the P$\bar{6}$2m symmetry under pressure 30 GPa, which are comparable with the one obtained in the ambient pressure (i.e., Figure 2a). The range of realized phonon frequencies increase under pressure, as a result of the decreased volume of the system. Nevertheless, the system is stable and does not exhibit phonon softening.

3.3. Electronic Properties

Now, we briefly describe the electronic properties of the NbReSi system with stable the P$\bar{6}$2m symmetry. The obtained electronic band structure (Figure 6) is in agreement with the initial one presented in Ref. [31].

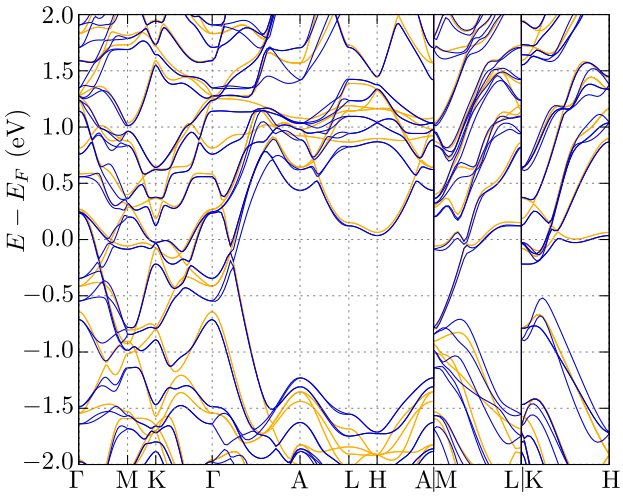

Figure 6. The electronic band structure along high symmetry directions for the P$\bar{6}$2m symmetry in the absence and presence of spin–orbit coupling (orange and blue lines, respectively).

The SOC band splitting near the Fermi level is estimated to be 180 meV. This is a relatively high value of the SOC in comparison to the other noncentrosymmetric superconductors [3], suggesting the realization of topological superconductivity in NbReSi. A significant role of the antisymmetric SOC is well visible along the c direction (e.g., the M–L or K–H paths in Figure 6). A large SOC is observed in the $k_z = 0$ plane (e.g., along the Γ–M–K–Γ path), in contrast to a relatively suppressed value of the SOC for $k_z = \pi/c$ (e.g., along the A–L–H–A)

The Fermi surface is presented in Figure 7. In the absence of SOC, the Fermi surface is composed of three pockets. Introduction of the SOC leads to band decoupling, whereas the Fermi surface preserves the shape unchanged qualitatively. Surprisingly, the Fermi surface exhibits quasi-one-dimensional features (i.e., the Fermi surface pocket are given by relatively flat pieces for k_z = const., see Figure 7b).

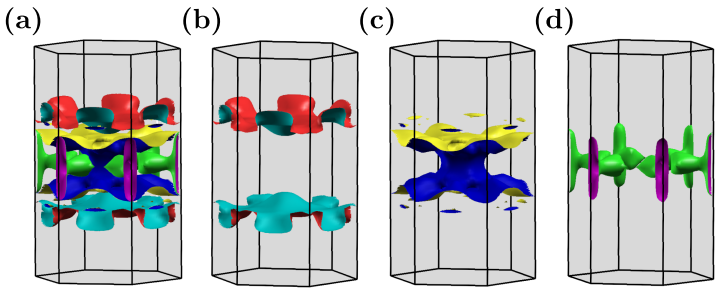

Figure 7. The Fermi surface for the P$\bar{6}$2m symmetry (in the absence of spin–orbit coupling). Panel (**a**) presents the total Fermi surface, while panels (**b**–**d**) show separated pockets.

The features of the electronic band structure, as well as the Fermi surface topology, make NbReSi very similar to the $A_2Cr_3As_3$ (A = K, Rb, Cs) [47–50] and $K_2Mo_3As_3$ [50,51] compounds. NbReSi does not exhibit any magnetic order features (the ground state is nonmagnetic), while mentioned $A_2Cr_3As_3$ poses magnetic order [52]. Regardless of this, the electronic band structure at $k_z = \pi/c$ is characterized by a relatively large gap, which was observed in both cases. For NbReSi, the states around the Fermi level are mostly

composed of Re-5*d* and Nb-4*d* orbitals [31], while for $A_2Cr_3As_3$, Cr-3*d* orbitals have the greatest contribution [47]. The Fermi surface of NbReSi is very similar to $A_2Cr_3As_3$ [47–50] or $K_2Mo_3As_3$ [50,51] (both cases with P$\bar{6}$2m symmetry).

Here, we should mention that despite having the same symmetry, the two structures possess different intrinsic features: e.g., $A_2Cr_3As_3$ contains quasi-one-dimensional chain of Cr atoms along the *c* direction, while NbReSi has layers of distorted kagome-like sublattice of Nb and Re atoms in the *ab* plane (see Figure 1). This causes detailed differences in the electronic band structure. Quasi-one-dimensional chains in $A_2Cr_3As_3$ are related to the nearly flat bands within the *ab* plane and a strong k_z dependence of the electron dispersion. In NbReSi, too, we observe strong k_z-dependence of the electron dispersion. Additionally, the absence of characteristic band structure features for the kagome-like structure is observed (i.e., absence of the flat bands). This can be related to the relatively large distances between atoms in the distorted kagome-like planes (3.63 Å and 4.47 Å for Nb–Nb and Re–Re pairs, respectively; cf. Figure 1).

The smaller distance between the atoms is related to the bonding between Re and Si (distance around 2.43 Å), and can have a relatively strong impact on the electronic properties. Indeed, the charge density distribution analyses (not presented) provide a signature of a strong bonding within these pairs. Such a structure with a strong bonding between the atoms along *c* can be responsible for the quasi-one-dimensional character of NbReSi visible on the Fermi surface.

4. Summary and Conclusions

We discussed the basic properties of the recently experimentally studied noncentrosymmetric superconductor, NbReSi. The experiments suggest the realization of the P$\bar{6}$2m symmetry (cf. Refs. [30,31]) or Ima2 (cf. Ref. [32]) symmetry. Using the ab initio technique, we demonstrate that NbReSi is stable with the P$\bar{6}$2m symmetry, while the Ima2 phase exhibits (imaginary) phonon soft modes. This can be verified in a relatively simple way by the Raman scattering measurements. The NbReSi with the P$\bar{6}$2m symmetry is stable also under hydrostatic pressure. We also found that the phonon surface states can be realized by NbReSi with the P$\bar{6}$2m symmetry, for (100) and (110) surfaces.

NbReSi with stable the P$\bar{6}$2m symmetry exhibits the electronic band structure and the Fermi surface very similar to quasi-one-dimensional $A_2Cr_3As_3$ [53]. Surprisingly, the Fermi surface of NbReSi uncovers quasi-one-dimensional features, which can be associated with the realization of the quasi-one-dimensional chains of Re–Si, with a strong bonding between the atoms. Additionally, the relatively large value of spin–orbit coupling, as well as similarities to $A_2Cr_3As_3$ promote this compound as a good candidate for the realization of unconventional superconductivity.

Author Contributions: A.P. initialized this project; S.B. and A.P. realized theoretical calculations; A.P. prepared the first version of the manuscript. All authors have read and agreed to the published version of the manuscript.

Funding: This work was supported by National Science Centre (NCN, Poland) under Projects No. 2021/43/B/ST3/02166 (A.P.).

Institutional Review Board Statement: Not applicable.

Informed Consent Statement: Not applicable.

Data Availability Statement: Not applicable.

Acknowledgments: Some figures in this work were rendered using VESTA [54] and XCRYSDEN [55]. A.P. appreciates funding in the framework of scholarships of the Minister of Science and Higher Education (Poland) for outstanding young scientists (2019 edition, No. 818/STYP/14/2019).

Conflicts of Interest: The authors declare no conflict of interest.

References

1. Yip, S. Noncentrosymmetric Superconductors. *Annu. Rev. Condens. Matter Phys.* **2014**, *5*, 15–33 . [CrossRef]
2. Zhang, X.; Liu, J.; Liu, F. Topological Superconductivity Based on Antisymmetric Spin–Orbit Coupling. *Nano Lett.* **2022**, *22*, 9000–9005. [CrossRef] [PubMed]
3. Smidman, M.; Salamon, M.B.; Yuan, H.Q.; Agterberg, D.F. Superconductivity and spin–orbit coupling in non-centrosymmetric materials: A review. *Rep. Prog. Phys.* **2017**, *80*, 036501. [CrossRef] [PubMed]
4. Gor'kov, L.P.; Rashba, E.I. Superconducting 2D System with Lifted Spin Degeneracy: Mixed Singlet-Triplet State. *Phys. Rev. Lett.* **2001**, *87*, 037004. [CrossRef] [PubMed]
5. Ptok, A.; Rodríguez, K.; Kapcia, K.J. Superconducting monolayer deposited on substrate: Effects of the spin-orbit coupling induced by proximity effects. *Phys. Rev. Mater.* **2018**, *2*, 024801. [CrossRef]
6. Bauer, E.; Hilscher, G.; Michor, H.; Paul, C.; Scheidt, E.W.; Gribanov, A.; Seropegin, Y.; Noël, H.; Sigrist, M.; Rogl, P. Heavy Fermion Superconductivity and Magnetic Order in Noncentrosymmetric $CePt_3Si$. *Phys. Rev. Lett.* **2004**, *92*, 027003. [CrossRef] [PubMed]
7. Togano, K.; Badica, P.; Nakamori, Y.; Orimo, S.; Takeya, H.; Hirata, K. Superconductivity in the Metal Rich Li-Pd-B Ternary Boride. *Phys. Rev. Lett.* **2004**, *93*, 247004. [CrossRef]
8. Yuan, H.Q.; Agterberg, D.F.; Hayashi, N.; Badica, P.; Vandervelde, D.; Togano, K.; Sigrist, M.; Salamon, M.B. *S*-Wave Spin-Triplet Order in Superconductors without Inversion Symmetry: Li_2Pd_3B and Li_2Pt_3B. *Phys. Rev. Lett.* **2006**, *97*, 017006. [CrossRef]
9. Bauer, E.; Khan, R.T.; Michor, H.; Royanian, E.; Grytsiv, A.; Melnychenko-Koblyuk, N.; Rogl, P.; Reith, D.; Podloucky, R.; Scheidt, E.W.; et al. $BaPtSi_3$: A noncentrosymmetric BCS-like superconductor. *Phys. Rev. B* **2009**, *80*, 064504. [CrossRef]
10. Bonalde, I.; Ribeiro, R.L.; Syu, K.J.; Sung, H.H.; Lee, W.H. Nodal gap structure in the noncentrosymmetric superconductor $LaNiC_2$ from magnetic-penetration-depth measurements. *New J. Phys.* **2011**, *13*, 123022. [CrossRef]
11. Nishikubo, Y.; Kudo, K.; Nohara, M. Superconductivity in the Honeycomb-Lattice Pnictide SrPtAs. *J. Phys. Soc. Jpn.* **2011**, *80*, 055002. [CrossRef]
12. Klepp, K.; Parthé, E. *R*PtSi phases (*R* = La, Ce, Pr, Nd, Sm and Gd) with an ordered $ThSi_2$ derivative structure. *Acta Crystallogr. B* **1982**, *38*, 1105–1108. [CrossRef]
13. Kneidinger, F.; Michor, H.; Sidorenko, A.; Bauer, E.; Zeiringer, I.; Rogl, P.; Blaas-Schenner, C.; Reith, D.; Podloucky, R. Synthesis, characterization, electronic structure, and phonon properties of the noncentrosymmetric superconductor LaPtSi. *Phys. Rev. B* **2013**, *88*, 104508. [CrossRef]
14. Bao, J.K.; Liu, J.Y.; Ma, C.W.; Meng, Z.H.; Tang, Z.T.; Sun, Y.L.; Zhai, H.F.; Jiang, H.; Bai, H.; Feng, C.M.; et al. Superconductivity in Quasi-One-Dimensional $K_2Cr_3As_3$ with Significant Electron Correlations. *Phys. Rev. X* **2015**, *5*, 011013. [CrossRef]
15. Tang, Z.T.; Bao, J.K.; Liu, Y.; Sun, Y.L.; Ablimit, A.; Zhai, H.F.; Jiang, H.; Feng, C.M.; Xu, Z.A.; Cao, G.H. Unconventional superconductivity in quasi-one-dimensional $Rb_2Cr_3As_3$. *Phys. Rev. B* **2015**, *91*, 020506. [CrossRef]
16. Tang, Z.T.; Bao, J.K.; Wang, Z.; Bai, H.; Jiang, H.; Liu, Y.; Zhai, H.F.; Feng, C.M.; Xu, Z.A.; Cao, G.H. Superconductivity in quasi-one-dimensional $Cs_2Cr_3As_3$ with large interchain distance. *Sci. China Mater.* **2015**, *58*, 16–20. [CrossRef]
17. Mu, Q.G.; Ruan, B.B.; Zhao, K.; Pan, B.J.; Liu, T.; Shan, L.; Chen, G.F.; Ren, Z.A. Superconductivity at 10.4 K in a novel quasi-one-dimensional ternary molybdenum pnictide $K_2Mo_3As_3$. *Sci. Bull.* **2018**, *63*, 952–956. [CrossRef]
18. Carnicom, E.M.; Xie, W.; Klimczuk, T.; Lin, J.; Górnicka, K.; Sobczak, Z.; Ong, N.P.; Cava, R.J. $TaRh_2B_2$ and $NbRh_2B_2$: Superconductors with a chiral noncentrosymmetric crystal structure. *Sci. Adv.* **2018**, *4*, eaar7969. [CrossRef] [PubMed]
19. Domieracki, K.; Kaczorowski, D. Superconductivity in a non-centrosymmetric compound ThCoSi. *J. Alloys Compd.* **2016**, *688*, 206–210. [CrossRef]
20. Domieracki, K.; Kaczorowski, D. Superconductivity in non-centrosymmetric ThNiSi. *J. Alloys Compd.* **2018**, *731*, 64–69. [CrossRef]
21. Ptok, A.; Domieracki, K.; Kapcia, K.J.; Łażewski, J.; Jochym, P.T.; Sternik, M.; Piekarz, P.; Kaczorowski, D. Electronic and lattice properties of noncentrosymmetric superconductors Th*T*Si (*T* = Co, Ir, Ni, and Pt). *Phys. Rev. B* **2019**, *100*, 165130. [CrossRef]
22. Khim, S.; Landaeta, J.F.; Banda, J.; Bannor, N.; Brando, M.; Brydon, P.M.R.; Hafner, D.; Küchler, R.; Cardoso-Gil, R.; Stockert, U.; et al. Field-induced transition within the superconducting state of $CeRh_2As_2$. *Science* **2021**, *373*, 1012–1016. [CrossRef]
23. Ptok, A.; Kapcia, K.J.; Jochym, P.T.; Łażewski, J.; Oleś, A.M.; Piekarz, P. Electronic and dynamical properties of $CeRh_2As_2$: Role of Rh_2As_2 layers and expected orbital order. *Phys. Rev. B* **2021**, *104*, L041109. [CrossRef]
24. Welter, R.; Venturini, G.; Malaman, B.; Ressouche, E. Crystallographic data and magnetic properties of new RTX compounds (R=La-Sm, Gd; T=Ru, Os; X=Si, Ge). Magnetic structure of NdRuSi. *J. Alloys Compd.* **1993**, *202*, 165–172. [CrossRef]
25. Morozkin, A.; Seropegin, Y.; Sviridov, I.; Riabinkin, I. Crystallographic data of new ternary Co_2Si-type *RT*Si (R = Y, Tb-Tm, T = Mn, Ru) compounds. *J. Alloys Compd.* **1999**, *282*, L4–L5. [CrossRef]
26. Subba Rao, G.V.; Wagner, K.; Balakrishnan, G.; Janaki, J.; Paulus, W.; Schöllhorn, R.; Subramanian, V.S.; Poppe, U. Structure and superconductivity studies on ternary equiatomic silicides, MM'Si. *Bull. Mater. Sci.* **1985**, *7*, 215–228. [CrossRef]
27. Sajilesh, K. P.; Singh, R.P. Superconducting properties of the non-centrosymmetric superconductors Ta*X*Si (*X* = Re, Ru). *Supercond. Sci. Technol.* **2021**, *34*, 055003. [CrossRef]
28. Sharma, S.; Sajilesh, K.P.; Richards, A.D.S.; Gautreau, J.; Pula, M.; Beare, J.; Kojima, K.M.; Yoon, S.; Cai, Y.; Kushwaha, R.K.; et al. Role of spin orbital coupling in unconventional superconductivity. *arXiv* **2022**, arXiv:2209.09852.
29. Shang, T.; Zhao, J.; Hu, L.H.; Ma, J.; Gawryluk, D.J.; Zhu, X.; Zhang, H.; Zhen, Z.; Yu, B.; Xu, Y.; et al. Unconventional superconductivity in topological Kramers nodal-line semimetals. *Sci. Adv.* **2022**, *8*, eabq6589. [CrossRef]

30. Shang, T.; Tay, D.; Su, H.; Yuan, H.Q.; Shiroka, T. Evidence of fully gapped superconductivity in NbReSi: A combined μSR and NMR study. *Phys. Rev. B* **2022**, *105*, 144506. [CrossRef]
31. Su, H.; Shang, T.; Du, F.; Chen, C.F.; Ye, H.Q.; Lu, X.; Cao, C.; Smidman, M.; Yuan, H.Q. NbReSi: A noncentrosymetric superconductor with large upper critical field. *Phys. Rev. Mater.* **2021**, *5*, 114802. [CrossRef]
32. Sajilesh, K.P.; Motla, K.; Meena, P.K.; Kataria, A.; Patra, C.; Somesh, K.; Hillier, A.D.; Singh, R.P. Superconductivity in noncentrosymmetric NbReSi investigated by muon spin rotation and relaxation. *Phys. Rev. B* **2022**, *105*, 094523. [CrossRef]
33. Blöchl, P.E. Projector augmented-wave method. *Phys. Rev. B* **1994**, *50*, 17953. [CrossRef]
34. Kresse, G.; Hafner, J. *Ab initio* molecular-dynamics simulation of the liquid-metal–amorphous-semiconductor transition in germanium. *Phys. Rev. B* **1994**, *49*, 14251. [CrossRef] [PubMed]
35. Kresse, G.; Furthmüller, J. Efficient iterative schemes for ab initio total-energy calculations using a plane-wave basis set. *Phys. Rev. B* **1996**, *54*, 11169. [CrossRef]
36. Kresse, G.; Joubert, D. From ultrasoft pseudopotentials to the projector augmented-wave method. *Phys. Rev. B* **1999**, *59*, 1758. [CrossRef]
37. Perdew, J.P.; Burke, K.; Ernzerhof, M. Generalized Gradient Approximation Made Simple. *Phys. Rev. Lett.* **1996**, *77*, 3865. [CrossRef]
38. Monkhorst, H.J.; Pack, J.D. Special points for Brillouin-zone integrations. *Phys. Rev. B* **1976**, *13*, 5188. [CrossRef]
39. Parlinski, K.; Li, Z.Q.; Kawazoe, Y. First-Principles Determination of the Soft Mode in Cubic ZrO_2. *Phys. Rev. Lett.* **1997**, *78*, 4063. [CrossRef]
40. Togo, A.; Tanaka, I. First principles phonon calculations in materials science. *Scr. Mater.* **2015**, *108*, 1–5. [CrossRef]
41. Tadano, T.; Gohda, Y.; Tsuneyuki, S. Anharmonic force constants extracted from first-principles molecular dynamics: Applications to heat transfer simulations. *J. Phys. Condens. Matter* **2014**, *26*, 225402. [CrossRef]
42. Sancho, M.P.L.; Sancho, J.M.L.; Sancho, J.M.L.; Rubio, J. Highly convergent schemes for the calculation of bulk and surface Green functions. *J. Phys. F Met. Phys.* **1985**, *15*, 851. [CrossRef]
43. Wu, Q.S.; Zhang, S.N.; Song, H.F.; Troyer, M.; Soluyanov, A.A. WannierTools: An open-source software package for novel topological materials. *Comput. Phys. Commun.* **2018**, *224*, 405–416. [CrossRef]
44. Ivantchev, S.; Kroumova, E.; Madariaga, G.; Pérez-Mato, J.M.; Aroyo, M.I. *SUBGROUPGRAPH*: a computer program for analysis of group–subgroup relations between space groups. *J. Appl. Cryst.* **2000**, *33*, 1190–1191. [CrossRef]
45. Kroumova, E.; Aroyo, M.I.; Perez-Mato, J.M.; Kirov, A.; Capillas, C.; Ivantchev, S.; Wondratschek, H. Bilbao Crystallographic Server: Useful Databases and Tools for Phase-Transition Studies. *Phase Transitions* **2003**, *76*, 155–170. [CrossRef]
46. Li, J.; Wang, L.; Liu, J.; Li, R.; Zhang, Z.; Chen, X.Q. Topological phonons in graphene. *Phys. Rev. B* **2020**, *101*, 081403. [CrossRef]
47. Jiang, H.; Cao, G.; Cao, C. Electronic structure of quasi-one-dimensional superconductor $K_2Cr_3As_3$ from first-principles calculations. *Sci. Rep.* **2015**, *5*, 16054. [CrossRef]
48. Cuono, G.; Autieri, C.; Forte, F.; Mercaldo, M.T.; Romano, A.; Avella, A.; Noce, C. A minimal tight-binding model for the quasi-one-dimensional superconductor $K_2Cr_3As_3$. *New J. Phys.* **2019**, *21*, 063027. [CrossRef]
49. Xu, C.; Wu, N.; Zhi, G.X.; Lei, B.H.; Duan, X.; Ning, F.; Cao, C.; Chen, Q. Coexistence of nontrivial topological properties and strong ferromagnetic fluctuations in quasi-one-dimensional $A_2Cr_3As_3$. *npj Comput. Mater.* **2020**, *6*, 30. [CrossRef]
50. Taddei, K.M.; Lei, B.H.; Susner, M.A.; Zhai, H.F.; Bullard, T.J.; Sanjeewa, L.D.; Zheng, Q.; Sefat, A.S.; Chi, S.; dela Cruz, C.; et al. Gapless spin-excitations in the superconducting state of a quasi-one-dimensional spin-triplet superconductor. *arXiv* **2022**, arXiv:2206.11757.
51. Yang, Y.; Feng, S.Q.; Lu, H.Y.; Wang, W.S.; Chen, Z.P. Electronic Structures of Newly Discovered Quasi-One-Dimensional Superconductors $A_2Mo_3As_3$ (A = K, Rb, Cs). *J. Supercond. Nov. Magn.* **2019**, *32*, 2421–2426. [CrossRef]
52. Wu, X.X.; Le, C.C.; Yuan, J.; Fan, H.; Hu, J.P. Magnetism in Quasi-One-Dimensional $A_2Cr_3As_3$ (A = K, Rb) Superconductors. *Chin. Phys. Lett.* **2015**, *32*, 057401. [CrossRef]
53. Wu, X.; Yang, F.; Le, C.; Fan, H.; Hu, J. Triplet p_z-wave pairing in quasi-one-dimensional $A_2Cr_3As_3$ superconductors (A = K, Rb, Cs). *Phys. Rev. B* **2015**, *92*, 104511. [CrossRef]
54. Momma, K.; Izumi, F. VESTA3 for three-dimensional visualization of crystal, volumetric and morphology data. *J. Appl. Crystallogr.* **2011**, *44*, 1272–1276. [CrossRef]
55. Kokalj, A. XCrySDen—A new program for displaying crystalline structures and electron densities. *J. Mol. Graphics Modelling* **1999**, *17*, 176–179. [CrossRef] [PubMed]

4.2.3 Pressure dependence of electronic and dynamical properties of CoGe with different symmetries

S. Basak, A. Kobiałka, M. Sternik, J. Łażewski, P. T. Jochym, A. M. Oleś, P. Piekarz, and A. Ptok, arXiv:2403.07580, *submitted* to Phys. Rev. B as a Regular Article.

CoGe is a transition metal monogermanide, known to be a non-centrosymmetric crystal which makes the structure intrinsically chiral, giving rise to fascinating magnetic and electronic properties. It can exist in several symmetry groups, e.g. cubic $P2_13$ (B20 type structure), hexagonal P6/mmm, orthorhombic Cmmm etc. Depending on the symmetry group, it can contain layers of perfect kagome lattice (Cmmm, P6/mmm), or layers of distorted kagome lattice ($P\bar{6}2m$). In this paper, we present a comprehensive study of the structural stability of CoGe in different symmetry groups. Analyzing the phonon dispersion relation, we conclude in which structure can CoGe exist and which structures are not realizable in nature, both at ambient conditions and at different values of pressure. We compare the enthalpies to comment on which structure is more favorable energetically. We also found small values of bulk modulus for all the structures, which led us to believe that external pressure should not have a huge impact on the structures. Drawing similarities with FeGe, and due to the small but finite change in the band structure, we estimated that CoGe should also make a transition from P6/mmm to $P2_13$ symmetry under pressure close to 3 GPa. The electronic band structure of $P2_13$ symmetry shows interesting features, e.g. presence of spin-1 fermion and doubly-degenerate Weyl points. We end this manuscript by studying the pressure-induced Lifshitz transition in the symmetry groups $P\bar{6}2m$ and $P2_13$.

Author's contribution: Performing the numerical calculations (phonon dispersion curves, system energies in the absence and presence of pressure, electronic band structure), analysis and discussion of the obtained results, correspondence with other research groups during the pre-publication period, partial preparation of the figures.

Electronic and dynamical properties of cobalt monogermanide CoGe phases under pressure

Surajit Basak,[1,*] Aksel Kobiałka,[2] Małgorzata Sternik,[1] Jan Łażewski,[1]
Paweł T. Jochym,[1] Andrzej M. Oleś,[3] Przemysław Piekarz,[1] and Andrzej Ptok[1,†]

[1] *Institute of Nuclear Physics, Polish Academy of Sciences, W. E. Radzikowskiego 152, PL-31342 Kraków, Poland*
[2] *Department of Physics and Astronomy, Uppsala University, Uppsala SE-75120, Sweden*
[3] *Institute of Theoretical Physics, Jagiellonian University, Prof. Stanisława Łojasiewicza 11, PL-30348 Kraków, Poland*

(Dated: March 13, 2024)

We present the pressure dependence of the electronic and dynamical properties of six different CoGe phases: orthorhombic Cmmm, hexagonal P6/mmm and P$\bar{6}$2m, monoclinic C2/m, cubic P2_13, and orthorhombic Pnma. Using first-principles DFT calculations and the direct force-constants method, we study the dynamical stability of individual phases under external pressure. We show that the orthorombic Cmmm and hexagonal P6/mmm structures are unstable over a broad pressure range and most pronounced imaginary phonon soft mode in both cases leads to a stable hexagonal P$\bar{6}$2m structure of the lowest ground-state energy of all studied phases at ambient and low (below ~ 3 GPa) external pressure. Under these conditions, the cubic P2_13 phase has the highest energy, however, together with monoclinic C2/m and orthorombic Pnma it is dynamically stable and all these three structures can potentially coexist as meta-stable phases. Above ~ 3 GPa, the cubic P2_13 phase becomes the most energetically favorable. Fitting the Birch–Murnaghan equation of state we derive bulk modulus for all mentioned phases, which indicate relatively high resistance of CoGe to compression. Such conclusions are confirmed by band structure calculations. Additionally, we show that electronic bands of the hexagonal P$\bar{6}$2m phase reveal characteristic features of the kagome-like structure, while in the cubic P2_13 phase spectrum, one can locate spin-1 and double Weyl fermions. In both cases, the external pressure induces the Lifshitz transition, related to the modification of the Fermi surface topology.

I. INTRODUCTION

Exploring the structure of materials is a fundamental first research step in physics, chemistry, and material science. The crystal structure as well as its other properties are inherently determined by bonds between atoms, molecules, or ions. However, a structure exposed to changing external conditions, such as temperature or pressure, may undergo a structural phase transition between different arrangements of atoms, causing the crystal symmetry change. Inspired by the recent discovery of several distinct structures of cobalt monogermanide, we performed an extensive study of stability and pressure dependence of different CoGe crystalline phases.

The CoGe binary compounds are an example of transition metal (TM) monogermanides [1–15]. TM monogermanides are isostructural to TM monosilicides [16–21], but they are more difficult to grow and study [12]. Nevertheless, such compounds have attracted a lot of attention because of the interesting properties observed in different phases. Contrary to MnGe [5, 22, 23] and similarly to FeGe, CoGe does not exhibit magnetic order [5], but can possess intrinsic spin Hall and spin Nernst effects [24]. The surface of CoGe is strongly active and shows bulk oxygen incorporation [25]. Similarly to RhGe [12] or FeGe [8], one can expect that the external conditions can cause a formation of various crystal structures.

Typically, the single crystal of CoGe is grown using a chemical vapor transport method [14]. CoGe can also be synthesized in the cubic FeSi-type structure (B20) at high pressures and temperatures [1, 2]. The cubic phase is a simple, low carrier density, metal, similar to CoSi [5]. Furthermore, the B20 phase was investigated by measuring the specific heat, resistivity, and ^{59}Co nuclear magnetic resonance, which uncovered a phase transition at 13.7 K [11]. FeGe also crystallizes with the B20 structure and monoclinic phase. At 893 K, the cubic B20 phase transforms into the CoSn-type structure, which in turn undergoes a transition at 1013 K to the high-temperature monoclinic polymorph, isostructural with CoGe [14]. Furthermore, FeGe exhibits a hexagonal high-temperature P6/mmm structure, while decreasing temperature leads to the cubic P2_13 structure [8, 26]. High-pressure conditions should favor the cubic B20 structure which has the highest density of all monogermanides polymorphs [2, 14]. Nevertheless, the question of CoGe structure under pressure still remains open. In this work we discuss the crystal stability of CoGe under pressure and its structural, electronic, and dynamical properties.

The paper is organized as follows. Our results are presented and discussed in Sec. II: First, we analyze the investigated crystal structures (Sec. II A). Next, we describe lattice dynamics and system stability at zero pressure (Sec. II B) and under external hydrostatic pressure (Sec. II C). Afterwards, the electronic band structures of the most favorable crystal structures are presented (Sec. III). Finally, we summarize and conclude our findings in Sec. IV. Details of the numerical calculation can

* e-mail: surajit.basak@ifj.edu.pl
† e-mail: aptok@mmj.pl

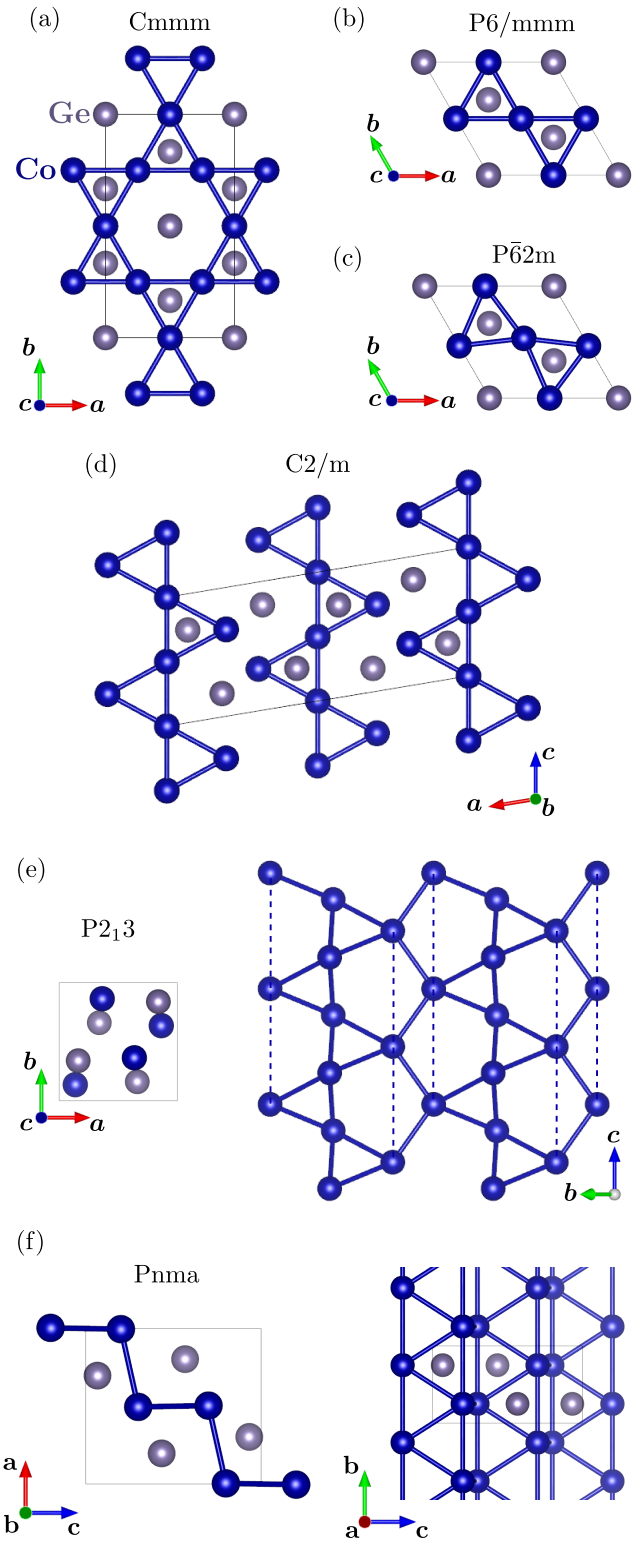

FIG. 1. Overview of CoGe structures: orthorhombic Cmmm (a), hexagonal P6/mmm (b) and P$\bar{6}$2m (c), monoclinic C2/m (d), cubic P2$_1$3 (e), and orthorhombic Pnma (f).

be found in App. A

II. SYSTEM STABILITY

A. Crystal structures

As we mentioned in the Introduction, TM monogermanides [1–11] and TM monosilicides [16–21] crystallize within several structures. Early stage study of CoGe suggests existence of monoclinic C2/m [13–15] and cubic P2$_1$3 (B20) structures [1]. Recently, theoretical studies have also predicted the hexagonal P$\bar{6}$2m structure [27]. Additionally, one should expect a strong impact of external conditions, such as temperature or pressure, on structure and stability of the material. For example, the crystal structure of FeGe undergoes transformation from the hexagonal P6/mmm to cubic P2$_1$3 phase with decreasing temperature, around 625 K [8, 26]. Motivated by this, we take up here the topic of stability under pressure of a few plausible structures of CoGe.

Beyond the reported structures (C2/m, P2$_1$3, and P$\bar{6}$2m), we also examine following cases:

- Cmmm symmetry, which in OQMD database [28, 29] carries the lowest formation energy [30];
- P6/mmm symmetry – hexagonal (B35) structure, well known from the FeGe system [31], but also reported for CoSn [32] and FeSn [33];
- Pnma symmetry – MnP-like (B31) structure reported for TGe (with T = Ni, Pd, Ir, Pt) [34] and RhGe [35].

The last two symmetries were taken into account due to the chemical affinity of CoGe with other similar systems [36].

All discussed structures of CoGe with different symmetries are presented in Fig. 1. In this group, we can find several similarities. The orthorhombic Cmmm structure [Fig. 1(a)], akin to the hexagonal P6/mmm and P$\bar{3}$2m symmetries [Fig. 1(b) and 1(c), respectively], contains two-dimensional (2D) kagome(-like) net of Co atoms. The geometry of these structures implies the existence of exotic electronic dispersion relation, containing a flat band, characteristic for a 2D kagome lattice and reported e.g., for CoSn-like compounds [37–45]. The monoclinic C2/m and cubic P2$_1$3 structures [Figs 1(d) and 1(e), respectively] contain chains of apex-connected Co triangles. A similar structure can also be found in the orthorhombic Pnma symmetry [Fig. 1(f)] with a ladder formed of Co triangles. In those cases, a quasi-one-dimensional (1D) structure should be reflected in the electronic band structure, in form of characteristic for 1D chains electronic bands. Such feature was reported, e.g., in $A_2Cr_3As_3$ [46–49] or $A_2Mo_3As_3$ [50–52], where A =K, Rb, and Cs.

After optimization, we found the following lattice parameters:

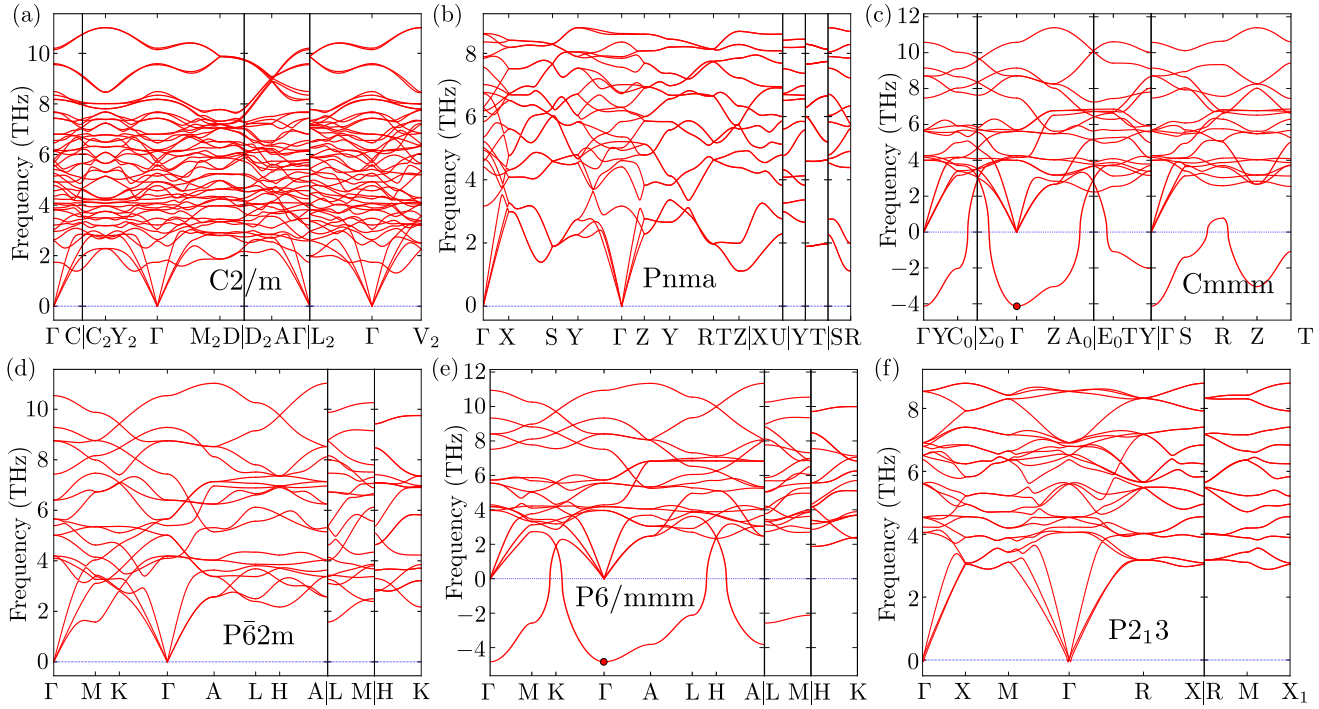

FIG. 2. The phonon dispersion curves of CoGe along the high symmetry directions of considered structures at zero pressure. Corresponding symmetry groups are indicated in the graphs.

The monoclinic C2/m symmetry (space group No. 12): $a = 11.722$ Å, $b = 3.763$ Å, and $c = 4.930$ Å ($\beta = 99.436°$). The Wyckoff positions are: 2a (0,0,0), 4i (0.1964,0,0.3260), and 2c (0,0,1/2) for Co, and 4i (0.8169,0,0.1821) and 4i (0.5693,0,0.2807) for Ge. The lattice constants of the relaxed structures are in good agreement with those reported experimentally for the monoclinic phase [2]: $a = 11.650$ Å, $b = 3.807$ Å, and $c = 4.945$ Å ($\beta = 101.1°$). The lattice parameters are also comparable with the parameters reported for FeGe [14]: $a = 11.838$ Å, $b = 3.937$ Å, and $c = 4.934$ Å ($\beta = 103.514°$).

The orthorhombic Pnma symmetry (space group No. 62): $a = 5.410$ Å, $b = 3.215$ Å, and $c = 6.112$ Å. The Wyckoff positions are 4c (-0.0045,1/4,0.2983) for Co, and 4c (0.8026,1/4,-0.0697) for Ge.

The orthorhombic Cmmm symmetry (space group No. 65): $a = 4.984$ Å, $b = 8.632$ Å, and $c = 3.884$ Å. The Wyckoff positions are 2b (1/2,0,0) and 4e (1/4,1/4,0) for Co, as well as 2a (0,0,0) and 4j (0,2/3,1/2) for Ge.

The hexagonal P$\bar{6}$2m symmetry (space group No. 189): $a = b = 5.009$ Å, and $c = 3.857$ Å. The Wyckoff positions are 3f (0.4665,0,0) for Co, and 1a (0,0,0) and 2d (1/3,2/3,0) for Ge.

The hexagonal P6/mmm symmetry (space group No. 191): $a = b = 4.987$ Å, and $c = 3.876$ Å. The Wyckoff positions are 3f (1/2,0,0) for Co, and 1a (0,0,0) and 2d (1/3,2/3,0) for Ge.

The cubic P2$_1$3 symmetry (space group No. 198): $a = b = c = 4.640$ Å. The Wyckoff positions are 4a (0.6360,0.6360,0.6360) for Co, and 4a (0.3394, 0.3394, 0.3394) for Ge. The lattice constant is in a good agreement with the experimental one, ~ 4.635 Å [2, 5, 53] and close to lattice constants of the similar monogermanides: 4.797 Å for MnGe [5] and 4.70 Å for FeGe [14, 54].

B. Zero pressure

To check the system's stability, we calculate the phonon dispersion relations for the symmetries mentioned above (Fig. 2). Since the number of degrees of freedom of the primitive unit cell determines an amount of dispersion relations, the phonon spectrum of C2/m [Fig. 2(a)] is the most complex. Similar crystal structures [containing the kagome-like net, cf. Fig. 1(a)–(c)] exhibit comparable phonon dispersion curves [cf. Fig. 2(c)–(e)]. The phonon frequency ranges for all presented structures are analogous.

Such similarities are also visible in the volume dependence of the ground state energy calculated for systems of different symmetries (Fig. 3). All structures have a comparable volume and nearly the same (within 0.5%) energy per one formula unit. Fitting the Birch–Murnaghan

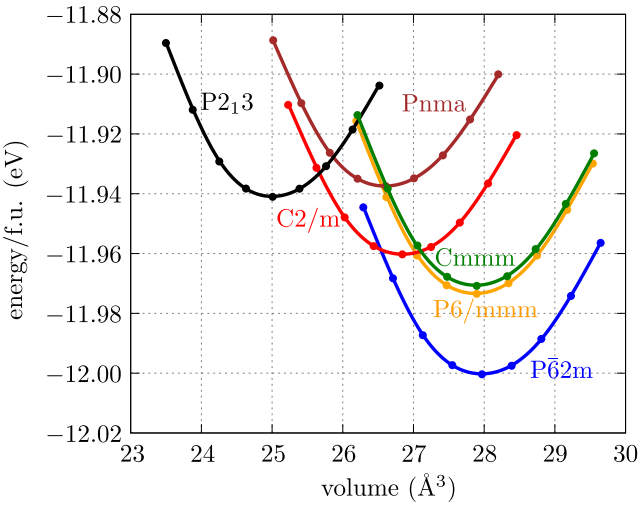

FIG. 3. Volume dependence of the ground-state energy calculated at zero pressure for different structures of CoGe.

equation of state [55]:

$$E(V) = E(V_0) + \frac{B_0 V}{B_0'}\left(\frac{(V_0/V)^{B_0'}}{B_0'-1}+1\right) - \frac{V_0 B_0}{B_0'-1}, \quad (1)$$

to energy versus volume data, we found a bulk modulus B_0 and its pressure derivative B_0' at the equilibrium volume V_0 (Tab. I). All symmetries are characterized by relatively large bulk modulus, which indicates a weak impact of external pressure on the system's mechanical properties.

Some of the structures discussed above can be eliminated at zero pressure due to instability of harmonic phonons. This applies especially to Cmmm and P6/mmm structures, which show imaginary soft modes at the Γ point. Interestingly, in both structures, this soft mode is associated with the same deformation of the kagome-net, i.e. mutually opposite rotation of the Co triangles forming this sublattice [cf. Figs 1(a) and 1(b) with Fig. 1(c)] around the c axis [27]. After optimization, the distorted kagome lattice in P$\bar{6}$2m is stable [Fig. 1(c)] without imaginary frequencies in the phonon spectrum [Fig. 2(d)]. In the final structure, with the P$\bar{6}$2m symmetry, the Co-triangles within the kagome-like structure are rotated by 4°, which is close to the rotation angle observed experimentally in RhPb [56], i.e. ∼ 4.5°.

The phonon dispersion curves of the cubic P2$_1$3 phase [Fig. 2(f)] are similar to those reported for RhGe [12]. Under zero pressure, the cubic P2$_1$3 (B20) phase has the highest energy among the reported structures (Fig. 3). However, as mentioned earlier, the transition from the hexagonal (P6/mmm) to cubic (P2$_1$3) symmetry occurs in FeGe also due to temperature increase [8, 26].

TABLE I. The ground-state energy and equilibrium volume calculated per formula unit, as well as bulk modulus B_0 and its pressure derivative B_0' fitted with the Birch–Murnaghan equation of state for different structures of CoGe.

Symmetry	B_0 (GPa)	B_0'	energy/f.u. (eV)	volume/f.u. (Å^3)
C2/m (SG:12)	147.40	3.90	−11.966	26.594
Pnma (SG:62)	142.59	5.76	−11.934	26.346
Cmmm (SG:65)	158.62	4.90	−11.973	27.655
P$\bar{6}$2m (SG:189)	157.01	4.82	−11.999	27.746
P6/mmm (SG:191)	158.62	4.82	−11.971	27.658
P2$_1$3 (SG:198)	153.81	6.65	−11.941	24.801

C. Role of external pressure

The stability of the system depends on external conditions. Below, we discuss the effect of the external pressure on the system's stability. The comparison of enthalpy (per formula unit) for the discussed symmetries is presented in Fig. 4(a). As the reference level of energy,

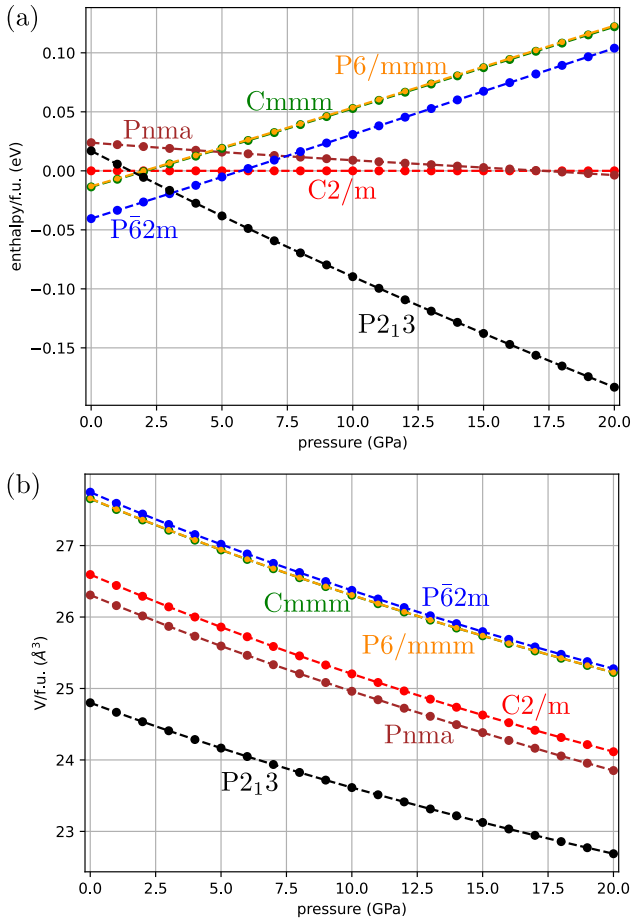

FIG. 4. Pressure dependence of enthalpy (a) and volume (b) calculated (per formula unit) for different CoGe structures (as labeled).

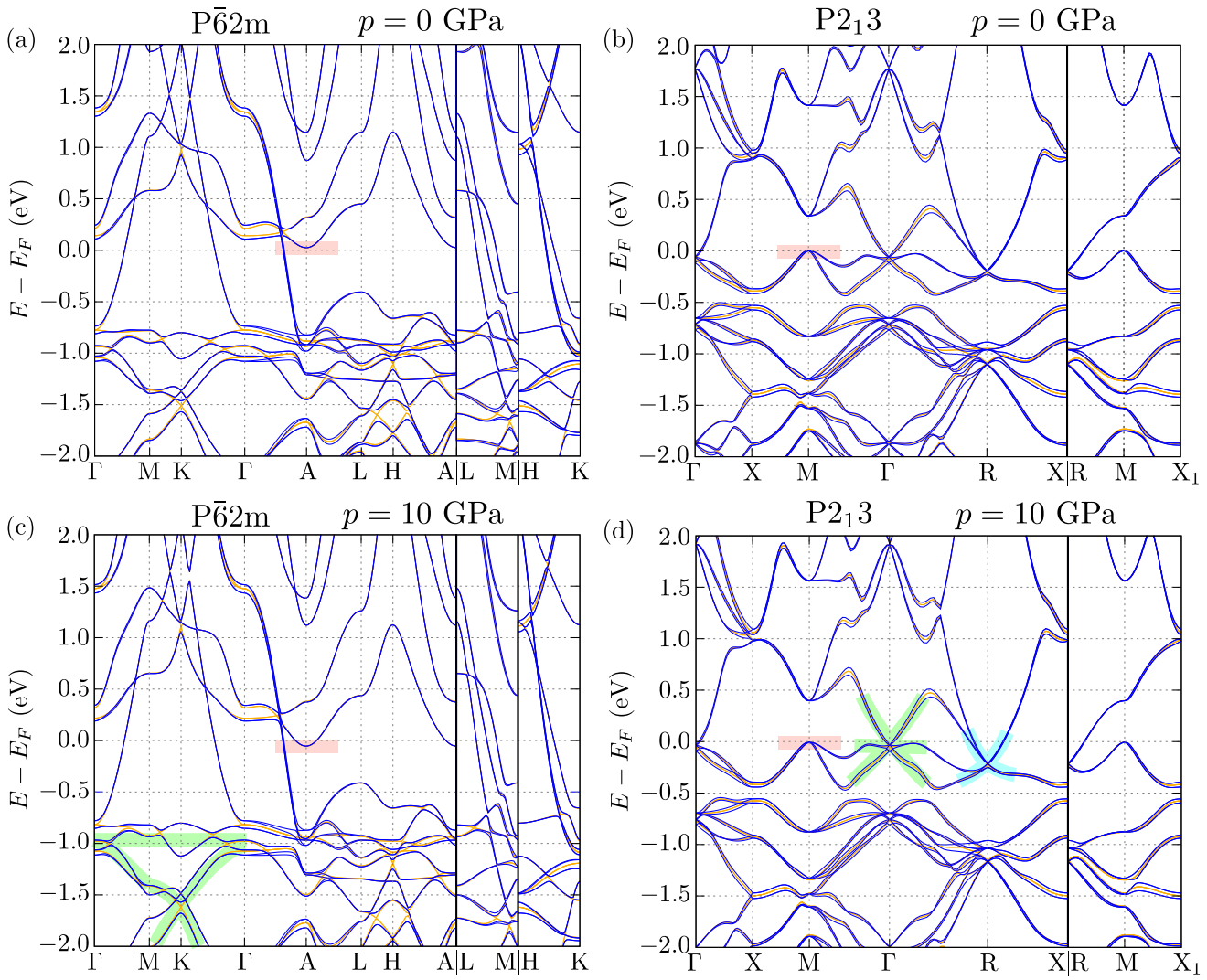

FIG. 5. The top and bottom panels present the electronic band structure in the absence and presence of the external pressure for the hexagonal Pē2m and cubic $P2_13$ phases (left and right column, respectively). Orange and blue lines correspond to the results obtained with and without spin–orbit coupling, respectively. The Pē2m band structure contains characteristic kagome-like features [marked by green background color on (c)], while the $P2_13$ exhibits typical spin-1 and double Weyl fermions features [marked by green and blue underground colors on (d), respectively]. Increasing pressure (cf. top and bottom panels) causes the Lifshitz transition [places marked by red background color, at the A point in Pē2m and the M point in $P2_13$ structure].

we choose the energy of the C2/m structure (red line). At low pressures, the Pē2m structure is the most favorable energetically. Then, above ~ 3 GPa, the cubic phase has the lowest energy and should be preferred, which is in agreement with the previous predictions [2, 14]. However, regardless of the mutual ground-state energy relations, under specific conditions, crystal can grow in some metastable structures mentioned earlier (i.e. C2/m, Pnma, or $P2_13$ structure). Based on this, we expect that the experimentally reported monoclinic C2/m phase [14] can come from the cubic $P2_13$ structure at low temperatures.

The unit cell of the unstable Cmmm phase can be constructed by doubling P6/mmm or Pē2m unit cells. For the Cmmm and P6/mmm symmetries, the ground-state energies and equilibrium volumes are mostly the same over the entire pressure range (cf. green and orange lines in Figs 3 and 4(a)). However, the imaginary soft mode in the phonon spectra indicates existence of a structure with lower energy. Indeed, our group-theoretical analysis of both soft modes points out at the dynamically stable structure of Pē2m symmetry with energy systematically lower than those of the Cmmm and P6/mmm phases. Even though all these structures have the same volume under pressure [cf. green, orange, and blue lines on Fig. 4(b)] only the Pē2m structure is stable over the entire pressure range [cf. blue line with green and orange

lines on Fig. 4(a)].

As expected, due to the relatively large value of bulk modulus, volume (per formula unit) does not strongly depend on pressure [see Fig. 4(b)]. Therefore, independently of the structure symmetry (i.e. arrangement of atoms), the atomic density of systems is approximately the same and inversely proportional to volume. Similarly, all structures exhibit similar compressibility, which is reflected in the relatively weak pressure dependence of volume (independently of the symmetry of the system). For example, the hexagonal P$\bar{6}$2m structure under external pressure of 10 GPa changes the lattice constants from $a = b = 5.009$ Å and $c = 3.857$ Å to $a = b = 4.914$ Å and $c = 3.790$ Å. Similarly, the cubic P2$_1$3 phase lattice constant shrinks from 4.640 Å to 4.556 Å. In both cases, the relative modification of the lattice constants induced by such pressure is around ~ 2 %.

Due to small compressibility and volume modification, the orbital overlap does not change much. Consequently, electronic band structures are unaffected by external pressure (see top and bottom panels in Fig. 5). Also, there is only small variation in corresponding phonon dispersion relations (not shown). For example, in the cubic P2$_1$3 structure only the frequency of the highest phonon mode at the Γ point is apparently changing from 8.54 THz to 9.29 THz, while the main features of the other phonon dispersion curves remain unchanged.

From the above analysis we can conclude that, under some "critical" pressure (estimated from theoretical calculations as $\sim$ 3 GPa), the studied system transforms from the P$\bar{6}$2m to P2$_1$3 symmetry – similarly to FeGe, which undergoes the phase transition from the hexagonal P6/mmm to cubic P2$_1$3 symmetry when temperature decreases [8, 26]. During the described transition, the volume of CoGe increases by about 2.75 Å^3 per formula unit.

III. ELECTRONIC PROPERTIES

For phases with the lowest energies on the enthalpy vs. pressure graph (Fig. 4), i.e. P$\bar{6}$2m and P2$_1$3, we investigate the electronic band structure. Their dispersion relations (Fig. 5) are characteristic for these symmetries and, generally, a whole class of similar materials. In the case of the hexagonal P$\bar{6}$2m phase, the electronic band structure exhibits the unique features of a system containing "kagome" net. For an ideal kagome lattice, the band structure contains a Dirac crossing at the K point, a strong van Hove singularity at the M point, and an almost flat band [37–45]. We should notice that, contrary to the ideal 2D kagome lattice, where a perfectly flat band is realized, in the three-dimensional (3D) multi-orbital systems the kagome-related "flat" band has a finite bandwidth. The nearly-flat band is mostly associated with the $d_{xz/yz}$ and d_{xy/x^2-y^2} orbitals of Co atoms [38, 39, 42] forming the distorted kagome net [bands marked with the green background line in Fig. 5(c)]. Analogously to CoSn-like compounds, the flat bands are located around -1 eV [38, 45, 56]. In case of the cubic P2$_1$3 phase, the electronic band structure exhibits characteristic features of TM monosilicide compounds [19, 20, 57–64], such as features of spin-1 fermions at the Γ point, and double degenerate Weyl points at the R point [marked by green and cyan background lines in Fig. 5(d)]. The spin-1 fermions are related to the crossing of three doubly-degenerate bands (in the absence of spin–orbit coupling). Similarly, one can observe the double Weyl point built by two Dirac-like cones centered at the same point. Both band structures of spin-1 fermions and double Weyl point are presented schematically in Fig. 6. As a consequence, a large Fermi arc is observed in the surface spectral function of CoGe with the cubic structure [53].

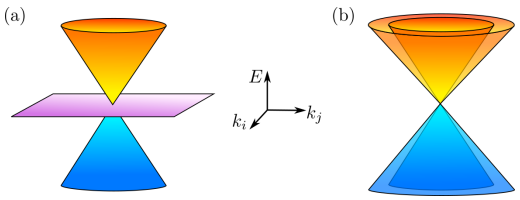

FIG. 6. Schematic band dispersions in 3D E-k space for the spin-1 fermion (a) and double Weyl fermion (b).

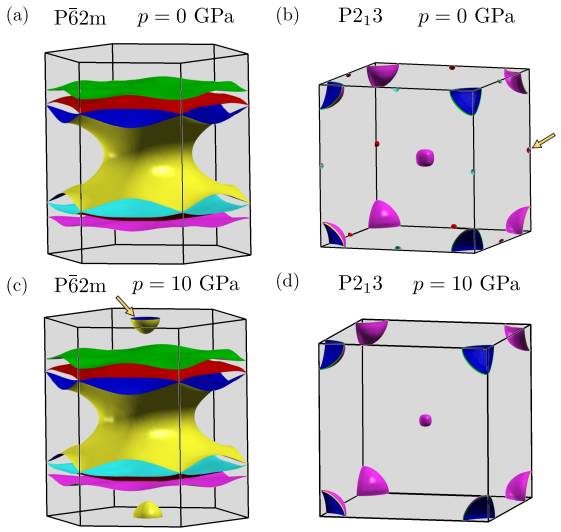

FIG. 7. Modification of the Fermi surface by the external pressure for the hexagonal P$\bar{6}$2m and cubic P2$_1$3 phases (as labeled).

The main features of the electronic band structure remain mostly unchanged under pressure. Nevertheless, in both cases, external hydrostatic pressure leads to the Lifshitz transition [65], i.e. change in the Fermi surface topology (see Fig. 7). In both structures, the compression shifts electronic bands and modifies the Fermi surface. In the case of hexagonal P$\bar{6}$2m structure, new Fermi pockets emerge around the A point [cf. Fig 7(a)

and 7(c)]. On the other hand, in the cubic $P2_13$ structure the small Fermi pocket at the M point disappears under pressure [cf. Fig 7(b) and 7(d)]. Such modifications of the Fermi surface under pressure are related to a relatively small modification of the electronic band structure under pressure. In the hexagonal structure, the bottom of the electron-like band at the A point is shifted to lower energies [cf. the electronic band structure at the A point, marked by a red background in Fig 5(a) and 5(c)]. Similarly, in the case of the cubic structure, the top of the hole-like band at the M point is also shifted to lower energies [cf. the electronic band structure at the M point, marked by the red background in Fig 5(b) and 5(d)].

IV. SUMMARY

In summary, we investigated the stability of several structures of cobalt monogermanide CoGe: monoclinic C2/m, orthorhombic Cmmm and Pnma, hexagonal P6/mmm and $P\bar{6}2m$, and cubic $P2_13$. From the study of lattice dynamics, we found that the monoclinic Cmmm and hexagonal P6/mmm structures are unstable and have the imaginary soft modes in the phonon spectra. Based on group-theoretical analysis, we reveal that both soft modes lead to the same stable $P\bar{6}2m$ structure, containing the distorted kagome lattice of Co atoms. Surprisingly, under ambient pressure, the $P\bar{6}2m$ structure has the lowest energy among studied phases. The cubic $P2_13$ structure is energetically favored under pressure above ~ 3 GPa.

We also discussed the electronic band structure of the most stable hexagonal $P\bar{6}2m$ and cubic $P2_13$ phases. We demonstrated that the former one shows characteristic features of the compounds containing the kagome net, while the latter exhibits traits of the chiral cubic structure, such as spin-1 fermions and double Weyl fermions. In fact, the $P\bar{6}2m$ structure contains the distorted kagome net of Co atoms, with two triangles forming the kagome-like net rotated in the opposite directions about 4° around the c axis. Furthermore, we show that external pressure weakly affects the main features of the electronic band structure. Nevertheless, the external hydrostatic pressure leads to the Lifshitz transition in both cases.

ACKNOWLEDGMENTS

Some figures in this work were rendered using VESTA [66] and XCRYSDEN [67] software. We kindly acknowledge support by National Science Centre (NCN, Poland) under Project No. 2021/43/B/ST3/02166.

Appendix A: Computational techniques

The first-principles density functional theory (DFT) calculations were performed using the Vienna Ab initio Simulation Package (VASP) code [68–70] with the projector augmented-wave (PAW) potentials [71]. For the exchange-correlation energy, the generalized gradient approximation (GGA) in the Perdew, Burke, and Ernzerhof for solids (PBEsol) parametrization was used [72]. The energy cutoff for the plane-wave expansion was set to 350 eV.

The optimization of the lattice constants and atom positions, including the spin–orbit coupling, was performed in the conventional unit cells. As a convergence condition of the optimization loop, we took the energy change below 10^{-6} eV and 10^{-8} eV for the ionic and electronic degrees of freedom, respectively. The following **k**–point grids within the Monkhorst–Pack [73] scheme were used for particular symmetries: $4 \times 12 \times 10$ for monoclinic C2/m, $6 \times 5 \times 3$ for orhoromic Pnma, $10 \times 6 \times 12$ for orhorombic Cmmm, $10 \times 10 \times 6$ for hexagonal P6/mmm and $P\bar{6}2m$, and $10 \times 10 \times 10$ for cubic $P2_13$. The symmetries of the system were analyzed using FINDSYM [74] and SPGLIB [75], while momentum space analysis was performed with SEEK-PATH [76].

The dynamical properties were calculated using the direct *Parlinski–Li–Kawazoe* method [77], implemented in PHONOPY package [78, 79]. Within this method, the interatomic force constants (IFC) are calculated from the Hellmann-Feynman (HF) forces generated by displacements of individual atoms inside the supercell. In our calculations, we used the following supercell sizes for different symmetries: $1\times3\times2$ for monoclinic C2/m, $2\times1\times3$ for orhoromic Pnma, $2 \times 3 \times 2$ for orhorombic Cmmm, $2\times2\times2$ for hexagonal P6/mmm and $P\bar{6}2m$, and $2\times2\times2$ for cubic $P2_13$. Phonon calculations were performed with the reduced $4 \times 4 \times 4$ **k**-points grid.

[1] V. Larchev and S. Popova, The polymorphism of transition metal monogermanides at high pressures and temperatures, J. Less-Common Met. **87**, 53 (1982).
[2] H. Takizawa, T. Sato, T. Endo, and M. Shimada, High-pressure synthesis and electrical and magnetic properties of MnGe and CoGe with the cubic B20 structure, J. Solid State Chem. **73**, 40 (1988).
[3] H. Wilhelm, M. Baenitz, M. Schmidt, U. K. Rößler, A. A. Leonov, and A. N. Bogdanov, Precursor phenomena at the magnetic ordering of the cubic helimagnet FeGe, Phys. Rev. Lett. **107**, 127203 (2011).
[4] S. V. Grigoriev, N. M. Potapova, S.-A. Siegfried, V. A. Dyadkin, E. V. Moskvin, V. Dmitriev, D. Menzel, C. D. Dewhurst, D. Chernyshov, R. A. Sadykov, L. N. Fomicheva, and A. V. Tsvyashchenko, Chiral properties of structure and magnetism in $Mn_{1-x}Fe_xGe$ compounds: When the left and the right are fighting, who wins?, Phys. Rev. Lett. **110**, 207201 (2013).
[5] J. F. DiTusa, S. B. Zhang, K. Yamaura, Y. Xiong, J. C. Prestigiacomo, B. W. Fulfer, P. W. Adams, M. I. Brick-

son, D. A. Browne, C. Capan, Z. Fisk, and J. Y. Chan, Magnetic, thermodynamic, and electrical transport properties of the noncentrosymmetric B20 germanides MnGe and CoGe, Phys. Rev. B **90**, 144404 (2014).
[6] V. A. Sidorov, A. E. Petrova, N. M. Chtchelkatchev, M. V. Magnitskaya, L. N. Fomicheva, D. A. Salamatin, A. V. Nikolaev, I. P. Zibrov, F. Wilhelm, A. Rogalev, and A. V. Tsvyashchenko, Magnetic, electronic, and transport properties of the high-pressure-synthesized chiral magnets $Mn_{1-x}Rh_xGe$, Phys. Rev. B **98**, 125121 (2018).
[7] F. Zheng, F. N. Rybakov, A. B. Borisov, D. Song, S. Wang, Z.-A. Li, H. Du, N. S. Kiselev, J. Caron, A. Kovács, M. Tian, Y. Zhang, S. Blügel, and R. E. Dunin-Borkowski, Experimental observation of chiral magnetic bobbers in B20-type FeGe, Nature Nanotech. **13**, 451 (2018).
[8] M. J. Stolt, X. Sigelko, N. Mathur, and S. Jin, Chemical pressure stabilization of the cubic B20 structure in skyrmion hosting $Fe_{1-x}Co_xGe$ alloys, Chem. Mater. **30**, 1146 (2018).
[9] S. Grytsiuk, M. Hoffmann, J.-P. Hanke, P. Mavropoulos, Y. Mokrousov, G. Bihlmayer, and S. Blügel, Ab initio analysis of magnetic properties of the prototype B20 chiral magnet FeGe, Phys. Rev. B **100**, 214406 (2019).
[10] L. V. Kamaeva, N. M. Chtchelkatchev, A. A. Suslov, M. V. Magnitskaya, and A. V. Tsvyashchenko, Structural and thermal stability of B20-type high-pressure phases FeGe and MnGe, J. Alloys Compd. **888**, 161565 (2021).
[11] S.-H. Baek, V. A. Sidorov, A. V. Nikolaev, T. Klimczuk, F. Ronning, and A. V. Tsvyashchenko, Possible quadrupole-order-driven commensurate-incommensurate phase transition in B20 CoGe, Phys. Rev. B **105**, 165132 (2022).
[12] N. M. Chtchelkatchev, M. V. Magnitskaya, and A. V. Tsvyashchenko, Ab initio study of noncentrosymmetric transition-metal monogermanide B20-RhGe synthesized at high temperature and pressure, Eur. Phys. J. Spec. Top **229**, 167 (2020).
[13] S. Bhan and K. Schubert, Zum aufbau der systeme kobalt-germanium, rhodium-silizium sowie einiger verwandter legierungen, International Journal of Materials Research **51**, 327 (1960).
[14] M. W. Richardson, Crystal structure refinements of the B 20 and monoclinic (CoGe-type) polymorphs of FeGe, Acta Chem. Scand. **21**, 753 (1967).
[15] A. Morozkin, Gd–Co–Ge system at 870/1070 K, Intermetallics **25**, 136 (2012).
[16] T. Jeong and W. E. Pickett, Implications of the B20 crystal structure for the magnetoelectronic structure of MnSi, Phys. Rev. B **70**, 075114 (2004).
[17] S. V. Grigoriev, D. Chernyshov, V. A. Dyadkin, V. Dmitriev, S. V. Maleyev, E. V. Moskvin, D. Menzel, J. Schoenes, and H. Eckerlebe, Crystal handedness and spin helix chirality in $Fe_{1-x}Co_xSi$, Phys. Rev. Lett. **102**, 037204 (2009).
[18] S. V. Grigoriev, D. Chernyshov, V. A. Dyadkin, V. Dmitriev, E. V. Moskvin, D. Lamago, T. Wolf, D. Menzel, J. Schoenes, S. V. Maleyev, and H. Eckerlebe, Interplay between crystalline chirality and magnetic structure in $Mn_{1-x}Fe_xSi$, Phys. Rev. B **81**, 012408 (2010).
[19] D. A. Pshenay-Severin, Y. V. Ivanov, A. A. Burkov, and A. T. Burkov, Band structure and unconventional electronic topology of CoSi, J. Phys.: Condens. Matter **30**, 135501 (2018).
[20] Z. Rao, H. Li, T. Zhang, S. Tian, C. Li, B. Fu, C. Tang, L. Wang, Z. Li, W. Fan, J. Li, Y. Huang, Z. Liu, Y. Long, C. Fang, H. Weng, Y. Shi, H. Lei, Y. Sun, T. Qian, and H. Ding, Observation of unconventional chiral fermions with long fermi arcs in CoSi, Nature **567**, 496 (2019).
[21] B. Balasubramanian, P. Manchanda, R. Pahari, Z. Chen, W. Zhang, S. R. Valloppilly, X. Li, A. Sarella, L. Yue, A. Ullah, P. Dev, D. A. Muller, R. Skomski, G. C. Hadjipanayis, and D. J. Sellmyer, Chiral magnetism and high-temperature skyrmions in B20-ordered Co-Si, Phys. Rev. Lett. **124**, 057201 (2020).
[22] O. L. Makarova, A. V. Tsvyashchenko, G. Andre, F. Porcher, L. N. Fomicheva, N. Rey, and I. Mirebeau, Neutron diffraction study of the chiral magnet MnGe, Phys. Rev. B **85**, 205205 (2012).
[23] N. Kanazawa, J.-H. Kim, D. S. Inosov, J. S. White, N. Egetenmeyer, J. L. Gavilano, S. Ishiwata, Y. Onose, T. Arima, B. Keimer, and Y. Tokura, Possible skyrmion-lattice ground state in the B20 chiral-lattice magnet MnGe as seen via small-angle neutron scattering, Phys. Rev. B **86**, 134425 (2012).
[24] T.-Y. Hsieh, B. B. Prasad, and G.-Y. Guo, Helicity-tunable spin hall and spin Nernst effects in unconventional chiral fermion semimetals XY (X = Co, Rh; Y = Si, Ge), Phys. Rev. B **106**, 165102 (2022).
[25] A. J. Pfau, J. Trey Diulus, S. He, G. H. Albuquerque, W. F. Stickle, and G. S. Herman, CoGe surface oxidation studied using X-ray photoelectron spectroscopy, Appl. Surf. Sci. **469**, 298 (2019).
[26] A. Kúkoľová, M. Dimitrievska, A. P. Litvinchuk, S. P. Ramanandan, N. Tappy, H. Menon, M. Borg, D. Grundler, and A. Fontcuberta i Morral, Cubic, hexagonal and tetragonal $FeGe_x$ phases ($x = 1, 1.5, 2$): Raman spectroscopy and magnetic properties, CrystEngComm **23**, 6506 (2021).
[27] A. Ptok, A. Kobiałka, M. Sternik, J. Łażewski, P. T. Jochym, A. M. Oleś, S. Stankov, and P. Piekarz, Chiral phonons in the honeycomb sublattice of layered CoSn-like compounds, Phys. Rev. B **104**, 054305 (2021).
[28] J. E. Saal, S. Kirklin, M. Aykol, B. Meredig, and C. Wolverton, Materials design and discovery with high-throughput density functional theory: The open quantum materials database (OQMD), JOM **65**, 1501 (2013).
[29] S. Kirklin, J. E. Saal, B. Meredig, A. Thompson, J. W. Doak, M. Aykol, S. Rühl, and C. Wolverton, The open quantum materials database (OQMD): assessing the accuracy of DFT formation energies, npj Comput. Mater. **1**, 15010 (2015).
[30] https://oqmd.org/materials/composition/CoGe.
[31] M. W. Richardson, The partial equilibrium diagram of the Fe-Ge system in the range 40-72 at. % Ge, and the crystallisation of some iron germanides by chemical transport reactions, Acta Chemica Scandinavica **21**, 2305 (1967).
[32] A. Larsson, M. Haeberlein, S. Lidin, and U. Schwarz, Single crystal structure refinement and high-pressure properties of CoSn, J. Alloys Compd. **240**, 79 (1996).
[33] J. Waerenborgh, L. Pereira, A. Gonçalves, and H. Noël, Crystal structure, ^{57}Fe Mössbauer spectroscopy and magnetization of $U_xFe_6Sn_6$ ($0 \leq x \leq 0.6$), Intermetallics **13**, 490 (2005).
[34] H. Pfisterer and K. Schubert, Neue phasen vom MnP

(B31)-typ, Naturwissenschaften **37**, 112 (1950).
[35] S. Geller, The rhodium–germanium system. I. the crystal structures of Rh_2Ge, Rh_5Ge_3 and RhGe, Acta Crystallographica **8**, 15 (1955).
[36] H.-C. Wang, S. Botti, and M. A. L. Marques, Predicting stable crystalline compounds using chemical similarity, npj Comput. Mater. **7**, 12 (2021).
[37] B. C. Sales, J. Yan, W. R. Meier, A. D. Christianson, S. Okamoto, and M. A. McGuire, Electronic, magnetic, and thermodynamic properties of the kagome layer compound FeSn, Phys. Rev. Materials **3**, 114203 (2019).
[38] W. R. Meier, M.-H. Du, S. Okamoto, N. Mohanta, A. F. May, M. A. McGuire, C. A. Bridges, G. D. Samolyuk, and B. C. Sales, Flat bands in the CoSn-type compounds, Phys. Rev. B **102**, 075148 (2020).
[39] M. Kang, S. Fang, L. Ye, H. C. Po, J. Denlinger, C. Jozwiak, A. Bostwick, E. Rotenberg, E. Kaxiras, J. G. Checkelsky, and R. Comin, Topological flat bands in frustrated kagome lattice CoSn, Nat. Commun. **11**, 4004 (2020).
[40] M. Kang, L. Ye, S. Fang, J.-S. You, A. Levitan, M. Han, J. I. Facio, C. Jozwiak, A. Bostwick, E. Rotenberg, M. K. Chan, R. D. McDonald, D. Graf, K. Kaznatcheev, E. Vescovo, D. C. Bell, E. Kaxiras, J. van den Brink, M. Richter, M. Prasad Ghimire, J. G. Checkelsky, and R. Comin, Dirac fermions and flat bands in the ideal kagome metal FeSn, Nat. Mater. **19**, 163 (2020).
[41] Z. Lin, C. Wang, P. Wang, S. Yi, L. Li, Q. Zhang, Y. Wang, Z. Wang, H. Huang, Y. Sun, Y. Huang, D. Shen, D. Feng, Z. Sun, J.-H. Cho, C. Zeng, and Z. Zhang, Dirac fermions in antiferromagnetic FeSn kagome lattices with combined space inversion and time-reversal symmetry, Phys. Rev. B **102**, 155103 (2020).
[42] H. Huang, L. Zheng, Z. Lin, X. Guo, S. Wang, S. Zhang, C. Zhang, Z. Sun, Z. Wang, H. Weng, L. Li, T. Wu, X. Chen, and C. Zeng, Flat-band-induced anomalous anisotropic charge transport and orbital magnetism in kagome metal CoSn, Phys. Rev. Lett. **128**, 096601 (2022).
[43] Z. Liu, M. Li, Q. Wang, G. Wang, C. Wen, K. Jiang, X. Lu, S. Yan, Y. Huang, D. Shen, J.-X. Yin, Z. Wang, Z. Yin, H. Lei, and S. Wang, Orbital-selective Dirac fermions and extremely flat bands in frustrated kagome-lattice metal CoSn, Nat. Commun. **11**, 4002 (2020).
[44] M. Han, H. Inoue, S. Fang, C. John, L. Ye, M. K. Chan, D. Graf, T. Suzuki, M. P. Ghimire, W. J. Cho, E. Kaxiras, and J. G. Checkelsky, Evidence of two-dimensional flat band at the surface of antiferromagnetic kagome metal FeSn, Nat. Commun. **12**, 5345 (2021).
[45] B. C. Sales, W. R. Meier, A. F. May, J. Xing, J.-Q. Yan, S. Gao, Y. H. Liu, M. B. Stone, A. D. Christianson, Q. Zhang, and M. A. McGuire, Tuning the flat bands of the kagome metal CoSn with Fe, In, or Ni doping, Phys. Rev. Materials **5**, 044202 (2021).
[46] X. Wu, F. Yang, C. Le, H. Fan, and J. Hu, Triplet p_z-wave pairing in quasi-one-dimensional $A_2Cr_3As_3$ superconductors (A =K, Rb, Cs), Phys. Rev. B **92**, 104511 (2015).
[47] X.-X. Wu, C.-C. Le, J. Yuan, H. Fan, and J.-P. Hu, Magnetism in quasi-one-dimensional $A_2Cr_3As_3$ (A =K, Rb) superconductors, Chinese Phys. Lett. **32**, 057401 (2015).
[48] H. Jiang, G. Cao, and C. Cao, Electronic structure of quasi-one-dimensional superconductor $K_2Cr_3As_3$ from first-principles calculations, Sci. Rep. **5**, 16054 (2015).
[49] C. Xu, N. Wu, G.-X. Zhi, B.-H. Lei, X. Duan, F. Ning, C. Cao, and Q. Chen, Coexistence of nontrivial topological properties and strong ferromagnetic fluctuations in quasi-one-dimensional $A_2Cr_3As_3$, npj Comput. Mater. **6**, 30 (2020).
[50] Y. Yang, S.-Q. Feng, H.-Y. Lu, W.-S. Wang, and Z.-P. Chen, Electronic structures of newly discovered quasi-one-dimensional superconductors $A_2Mo_3As_3$ (A =K, Rb, Cs), J. Supercond. Nov. Magn. **32**, 2421 (2019).
[51] K. Zhao, Q.-G. Mu, B.-B. Ruan, M.-H. Zhou, Q.-S. Yang, T. Liu, B.-J. Pan, S. Zhang, G.-F. Chen, and Z.-A. Ren, A new quasi-one-dimensional ternary molybdenum pnictide $Rb_2Mo_3As_3$ with superconducting transition at 10.5 K, Chinese Phys. Lett. **37**, 097401 (2020).
[52] B.-H. Lei and D. J. Singh, Multigap electron-phonon superconductivity in the quasi-one-dimensional pnictide $K_2Mo_3As_3$, Phys. Rev. B **103**, 094512 (2021).
[53] C. K. Barman, C. Mondal, S. Pujari, B. Pathak, and A. Alam, Symmetry protection and giant Fermi arcs from multifold fermions in binary, ternary, and quaternary compounds, Phys. Rev. B **102**, 155147 (2020).
[54] A. Tsvyashchenko, V. Sidorov, A. Petrova, L. Fomicheva, I. Zibrov, and V. Dmitrienko, Superconductivity and magnetism in noncentrosymmetric RhGe, J. Alloys Compd. **686**, 431 (2016).
[55] C. L. Fu and K. M. Ho, First-principles calculation of the equilibrium ground-state properties of transition metals: Applications to Nb and Mo, Phys. Rev. B **28**, 5480 (1983).
[56] A. Ptok, W. R. Meier, A. Kobiałka, S. Basak, M. Sternik, J. Łażewski, P. T. Jochym, M. A. McGuire, B. C. Sales, H. Miao, P. Piekarz, and A. M. Oleś, Phononic drumhead surface state in the distorted kagome compound RhPb, Phys. Rev. Res. **5**, 043231 (2023).
[57] P. Tang, Q. Zhou, and S.-C. Zhang, Multiple types of topological fermions in transition metal silicides, Phys. Rev. Lett. **119**, 206402 (2017).
[58] G. Chang, S.-Y. Xu, B. J. Wieder, D. S. Sanchez, S.-M. Huang, I. Belopolski, T.-R. Chang, S. Zhang, A. Bansil, H. Lin, and M. Z. Hasan, Unconventional chiral fermions and large topological Fermi arcs in RhSi, Phys. Rev. Lett. **119**, 206401 (2017).
[59] D. S. Sanchez, I. Belopolski, T. A. Cochran, X. Xu, J.-X. Yin, G. Chang, W. Xie, K. Manna, V. Süß, C.-Y. Huang, N. Alidoust, D. Multer, S. S. Zhang, N. Shumiya, X. Wang, G.-Q. Wang, T.-R. Chang, C. Felser, S.-Y. Xu, S. Jia, H. Lin, and M. Z. Hasan, Topological chiral crystals with helicoid-arc quantum states, Nature **567**, 500 (2019).
[60] D. Takane, Z. Wang, S. Souma, K. Nakayama, T. Nakamura, H. Oinuma, Y. Nakata, H. Iwasawa, C. Cacho, T. Kim, K. Horiba, H. Kumigashira, T. Takahashi, Y. Ando, and T. Sato, Observation of chiral fermions with a large topological charge and associated Fermi-arc surface states in CoSi, Phys. Rev. Lett. **122**, 076402 (2019).
[61] N. B. M. Schröter, D. Pei, M. G. Vergniory, Y. Sun, K. Manna, F. de Juan, J. A. Krieger, V. Süss, M. Schmidt, P. Dudin, B. Bradlyn, T. K. Kim, T. Schmitt, C. Cacho, C. Felser, V. N. Strocov, and Y. Chen, Chiral topological semimetal with multifold band crossings and long Fermi arcs, Nat. Phys. **15**, 759 (2019).
[62] H. Li, S. Xu, Z.-C. Rao, L.-Q. Zhou, Z.-J. Wang, S.-M.

Zhou, S.-J. Tian, S.-Y. Gao, J.-J. Li, Y.-B. Huang, H.-C. Lei, H.-M. Weng, Y.-J. Sun, T.-L. Xia, T. Qian, and H. Ding, Chiral fermion reversal in chiral crystals, Nat. Commun. **10**, 5505 (2019).

[63] M. Yao, K. Manna, Q. Yang, A. Fedorov, V. Voroshnin, B. Valentin Schwarze, J. Hornung, S. Chattopadhyay, Z. Sun, S. N. Guin, J. Wosnitza, H. Borrmann, C. Shekhar, N. Kumar, J. Fink, Y. Sun, and C. Felser, Observation of giant spin-split Fermi-arc with maximal chern number in the chiral topological semimetal PtGa, Nat. Commun. **11**, 2033 (2020).

[64] A. Bose and A. Narayan, Strain-induced topological charge control in multifold fermion systems, J. Phys.: Condens. Matter **33**, 375002 (2021).

[65] I. M. Lifshitz, Anomalies of electron characteristics of a metal in the high pressure region, Zh. Eksp. Teor. Fiz. **38**, 1569 (1960), [Sov. Phys. JETP **11**, 1130–1135 (1960)].

[66] K. Momma and F. Izumi, VESTA3 for three-dimensional visualization of crystal, volumetric and morphology data, J. Appl. Crystallogr. **44**, 1272 (2011).

[67] A. Kokalj, Xcrysden–a new program for displaying crystalline structures and electron densities, J. Mol. Graph. Model. **17**, 176 (1999).

[68] G. Kresse and J. Hafner, Ab initio molecular-dynamics simulation of the liquid-metal–amorphous-semiconductor transition in germanium, Phys. Rev. B **49**, 14251 (1994).

[69] G. Kresse and J. Furthmüller, Efficient iterative schemes for ab initio total-energy calculations using a plane-wave basis set, Phys. Rev. B **54**, 11169 (1996).

[70] G. Kresse and D. Joubert, From ultrasoft pseudopotentials to the projector augmented-wave method, Phys. Rev. B **59**, 1758 (1999).

[71] P. E. Blöchl, Projector augmented-wave method, Phys. Rev. B **50**, 17953 (1994).

[72] J. P. Perdew, A. Ruzsinszky, G. I. Csonka, O. A. Vydrov, G. E. Scuseria, L. A. Constantin, X. Zhou, and K. Burke, Restoring the density-gradient expansion for exchange in solids and surfaces, Phys. Rev. Lett. **100**, 136406 (2008).

[73] H. J. Monkhorst and J. D. Pack, Special points for Brillouin-zone integrations, Phys. Rev. B **13**, 5188 (1976).

[74] H. T. Stokes and D. M. Hatch, FINDSYM: program for identifying the space-group symmetry of a crystal, J. Appl. Cryst. **38**, 237 (2005).

[75] A. Togo and I. Tanaka, SPGLIB: a software library for crystal symmetry search (2018), arXiv:1808.01590.

[76] Y. Hinuma, G. Pizzi, Y. Kumagai, F. Oba, and I. Tanaka, Band structure diagram paths based on crystallography, Comput. Mater. Sci. **128**, 140 (2017).

[77] K. Parlinski, Z. Q. Li, and Y. Kawazoe, First-principles determination of the soft mode in cubic ZrO_2, Phys. Rev. Lett. **78**, 4063 (1997).

[78] A. Togo, L. Chaput, T. Tadano, and I. Tanaka, Implementation strategies in phonopy and phono3py, J. Phys. Condens. Matter **35**, 353001 (2023).

[79] A. Togo, First-principles phonon calculations with phonopy and phono3py, J. Phys. Soc. Jpn. **92**, 012001 (2023).

4.2.4 Lattice dynamics study of electron-correlation-induced charge density wave in antiferromagnetic kagome metal FeGe

A. Ptok, S. Basak, A. Kobiałka, M. Sternik, J. Łażewski, P. T. Jochym, A. M. Oleś, and P. Piekarz, arXiv:2403.0029, *submitted* to Phys. Rev. Materials as a Letter.

Charge density wave (CDW) is a periodic modulation of electron density that produces a standing wave pattern throughout the material. The formation of CDW usually is accompanied by a periodic distortion of the parent lattice, forming a superlattice. Although the most common mechanism behind the formation of CDW is Fermi surface nesting, in materials containing kagome lattice, the van Hove singularity can also drive a material towards CDW transition, as observed in AV_3Sb_5 (A=K, Rb, Cs) [25]. Recently, CDW was observed also in kagome metal FeGe. Interestingly, this phase was accompanied by an enhanced value magnetic moment of Fe. Theoretical analysis suggested that below the CDW temperature, a large dimerization among the Ge sites occurs in the kagome plane. This leads to a distortion of the other layers and an increased Fe-Fe correlation. This suggests that the CDW in FeGe may have its origin in the strong electron-electron correlation. To prove this hypothesis, in this paper, we perform a density functional theory (DFT) analysis of FeGe with different values of Hubbard U on the Fe-d orbital. We observe that after a critical value of U ($U_c \sim 3.5$ eV), the structure becomes unstable in P6/mmm symmetry. This instability is also followed by an increased value of magnetization of the Fe atoms (from 1.53 μ_B to 2.96 μ_B). Analysis of the soft mode leads us to conclude that the structures in P6/mmm symmetry stabilize in Immm symmetry, with a distortion in the hexagonal structure formed by the Ge atoms. We end the paper by theoretically generating the STM topography of FeGe of this new Immm symmetry and found that with the termination of the deformed hexagonal layer formed by the Ge atoms, the obtained STM topography has similarities with the experimentally observed STM image. An instability in the parent structure, increased value of magnetic moments, and similarities with experimentally observed STM images, all lead us to conclude that CDW in FeGe must be an enhanced electron-electron correlation-driven phenomenon.

Author's contribution: Numerical evaluations using VASP (phonon dispersion curves and density of states), analysis and discussion of obtained results, correspondence with other research groups during the prepublication period, partial preparation of figures.

Lattice dynamics study of electron-correlation-induced charge density wave in antiferromagnetic kagome metal FeGe

Andrzej Ptok,[1,*] Surajit Basak,[1] Aksel Kobiałka,[2] Małgorzata Sternik,[1]
Jan Łażewski,[1] Paweł T. Jochym,[1] Andrzej M. Oleś,[3] and Przemysław Piekarz[1]

[1] *Institute of Nuclear Physics, Polish Academy of Sciences, W. E. Radzikowskiego 152, PL-31342 Kraków, Poland*
[2] *Department of Physics and Astronomy, Uppsala University, Uppsala SE-75120, Sweden*
[3] *Institute of Theoretical Physics, Jagiellonian University, Prof. Stanisława Łojasiewicza 11, PL-30348 Kraków, Poland*

(Dated: March 4, 2024)

Electron-correlation-driven phonon soft modes have been recently reported in the antiferromagnetic kagome FeGe compound and associated with the observed charge density wave (CDW). In this paper, we present a systematic investigation of the CDW origin in the context of the *ab initio* lattice dynamics study. Performing the group theory analysis of the mentioned soft mode, we found that the stable structure has the Immm symmetry and can be achieved by the small shift of Ge atoms. Additionally, we show that the final structure realizes a distorted honeycomb Ge lattice as well as a non-flat kagome-like Fe net. For completeness, we present the electronic properties calculations. From the theoretical STM topography simulation, we indicate that the observed CDW occurs in the deformed honeycomb Ge sublattice.

I. INTRODUCTION

Kagome lattice materials attract significant attention due to their unique electronic properties [1], such as flat bands, van Hove singularities (VHSs) at the M point, and Dirac cone dispersion at the K point. From this, a wide range of exotic properties and behaviors emerge in the kagome lattice due to different degrees of electron filling [2–4]. For example, a strong correlation can induce magnetic order [5, 6], while a VHS close to the Fermi level can lead to the lattice instability and charge density wave (CDW) [7, 8]. The kagome lattices can also exhibit topological properties [1, 9–11], not only limited to the electronic structure [12–17]. Therefore, the kagome lattice materials provide an excellent platform to study new physical phenomena.

Recently, we have learned about several kagome lattice systems, which exhibit interesting properties. Here, we can mention Weyl semimetal $Co_3Sn_2S_2$, with ferromagnetic Co kagome net [18–23]. Topological properties and the break of the time reversal symmetry lead to the intrinsic giant anomalous Hall effect [18, 24, 25], while hosting of the exotic Weyl fermions [19] induces the appearance of the Fermi arc [20]. Another example, AV_3Sb_5 (A =K, Rb, and Cs) with a vanadium kagome net displays the CDW with the Star of David (SoD) pattern below $\sim$ 90 K [26–28]. Moreover, below $\sim$ 2 K the coexistence of CDW and superconducting state is observed [10, 29, 30]. Such compounds can also exhibit an unconventional anomalous Hall effect [31, 32]. Finally, also other well-studied kagome systems, such as FeSn [33–36], CoSn [36–38], Fe_3Sn_2 [39–41], $RETi_3Bi_4$ (RE = Yb, Pr, and Nd) [42–44], MMn_6Sn_6 (M =Y, Er, Tb) [45–52] and ScV_6Sn_6 [53, 54], or AV_6Sb_6 (A =K, Rb, Cs, or Gd) [11, 55–58] can be mentioned.

In this paper, we focus on FeGe, in which CDW was recently discovered [59, 60]. FeGe exhibits an antiferromagnetic (AFM) order below 410 K [61–65]. At room temperature, the Fe atoms are ferromagnetically coupled with the kagome sublattice plane and antiferromagnetically coupled between kagome sublattices, i.e. along c [so-called A-AFM order, see Fig. 1(d)]. At lower temperatures, a tilt of the Fe magnetic moments from the c axis was reported. The CDW phase is reported below 100 K [59]. The coexistence of these two ordered phases gives a great opportunity to study the interplay between them [59, 66]. The scanning tunneling microscopy (STM) of the surface charge distribution uncovers the 2×2 pattern [59, 67, 68].

In this context, it is important to recognize correctly the origin of the CDW. For example, in the case of vanadium kagome net systems (AV_3Sb_5) the CDW is associated with imaginary soft modes at the M and L points [69–72], which induce the structural phase transition [70, 73]. These soft modes lead to a stable structure with the C2/m [70] or Fmmm [71] symmetry. The phonon spectrum of FeGe, calculated without electron correlations, is similar to the other CoSn-like compounds [74], and no imaginary soft modes are observed. However, the introduction of the correlations leads to the softening of some optical phonons along the L–H direction [68, 75, 76]. Such soft modes generate the Ge-dimerization and were recognized as a source of CDW [77]. Nevertheless, a more thorough dynamical study of the CDW formation mechanism has not been performed so far. Here, using the *ab initio* techniques, we derive a critical value of the on-site Coulomb interaction, which induces imaginary soft modes in the phonon spectrum. Detailed analysis of the symmetry of these soft modes allow us to find a stable low-symmetry structure of FeGe.

The paper is organized as follows. Our results are presented and discussed in Sec. II. We start with a de-

* e-mail: aptok@mmj.pl

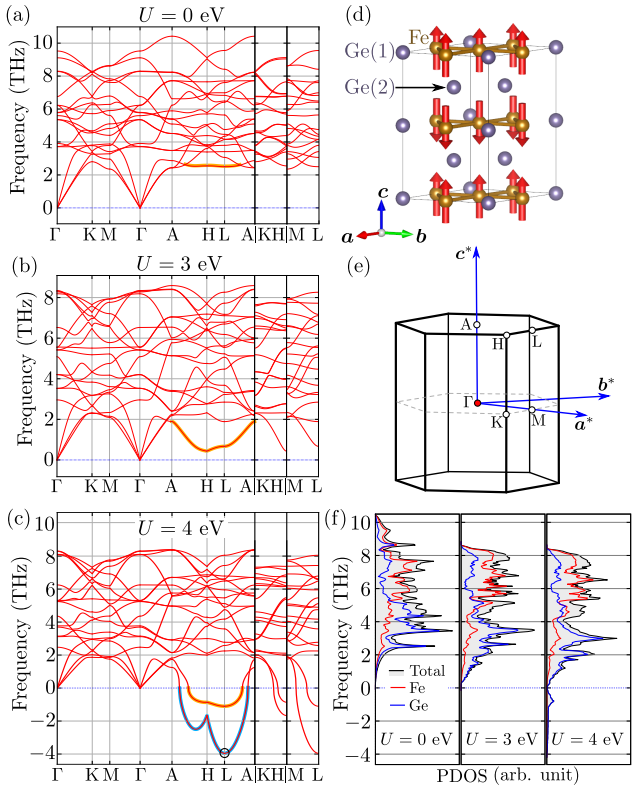

FIG. 1. (a)-(c) The effect of the local Coulomb interaction on the phonon dispersion curves along high symmetry directions for FeGe with the P6/mmm symmetry. Results for a different Hubbard U parameter (as labeled). (d) Magnetic unit cell of FeGe with the P6/mmm symmetry in the presence of the A-AFM order, and its Brillouin zone (e). (f) The phonon DOS as a function of the local Coulomb interaction value.

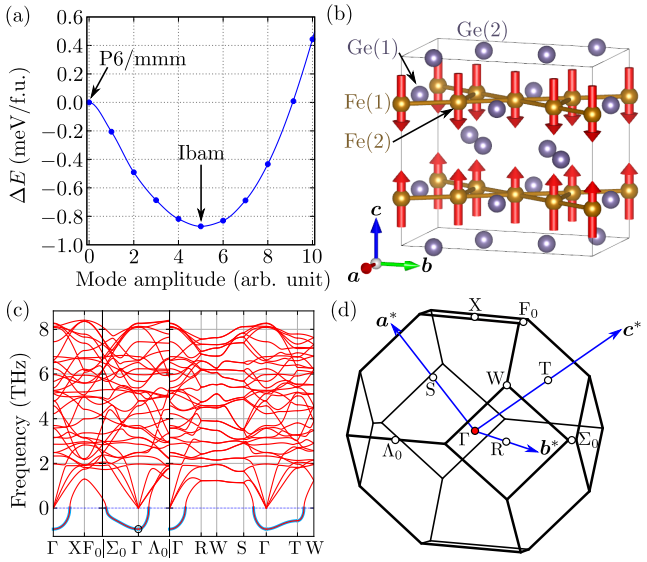

FIG. 2. (a) The soft mode amplitude dependence of the system's energy for structure induced by the soft mode at L point in P6/mmm structure. The zero of energy scale is set at the energy of the initial P6/mmm structure. The optimized system with the lowest energy has the Ibam symmetry and magnetic unit cell presented in panel (b). In (c), the phonon dispersion curves for FeGe with Ibam symmetry along high symmetry directions of the Brillouin zone are presented following the scheme displayed in (d).

scription of the dynamical properties of the FeGe system (Sec. II A). Using the electron-correlation-driven phonon soft mode analysis, we show that the stable structure has the Immm symmetry. Next, for this stable structure, we discuss the electronic properties (Sec. II B). Finally, we summarize and conclude our findings in Sec. III. Details of the numerical calculation can be found in the Appendix A.

II. RESULTS AND DISCUSSION

A. Dynamical properties and system stability

Let us start with a discussion of the lattice dynamics for the initial structure with the P6/mmm symmetry, in the presence of different values of Coulomb interaction on Fe d orbitals (Fig. 1). In the absence of the correlations ($U = 0$ eV), none of the phonon dispersion curves show any noticeable softening nor imaginary values [see Fig. 1(a)] [74]. The introduction of Hubbard U (within the DFT+U method) causes the softening of the lowest phonon mode along the H–L direction [68, 75, 76]. This is clearly visible when we compare that phonon branch for $U = 0$ eV and for $U = 3$ eV [cf. Fig. 1(a) and 1(b), where the soft mode is marked with an orange background]. However, further increase of U (e.g. to 4 eV) leads to the emergence of imaginary soft modes [presented as negative frequencies in Fig. 1(c)]. As we can see, there is some critical value of the Hubbard parameter (U_c) for which the soft modes become imaginary. At this higher U value, there are two imaginary soft branches [marked with orange and blue in Fig. 1(c)]. The branch marked with an orange background corresponds to the soft branch visible for $U < U_c$ in Fig. 1(b).

In Fig. 1(f) the phonon density of states spectra were compared for various values of the Hubbard U parameter. Increasing the local Coulomb potential (from 0 eV to 4 eV) causes an enhancement of both the magnetic moments of the iron atoms (from 1.53 μ_B to 2.96 μ_B) and the crystal cell volume (by about 12%). However, it is worth emphasizing that phonon softening is not connected with volume extension but only with correlation effects, which we verified by changing volume and U separately. What is more surprising, the increase in value of U on Fe results in a softening of phonon modes associated mainly with the vibrations of Ge atoms.

In the next parts of this manuscript, we assume that the Coulomb interaction on Fe d orbitals is $U = 4$ eV. Here, we should briefly discuss the value of U for Fe d

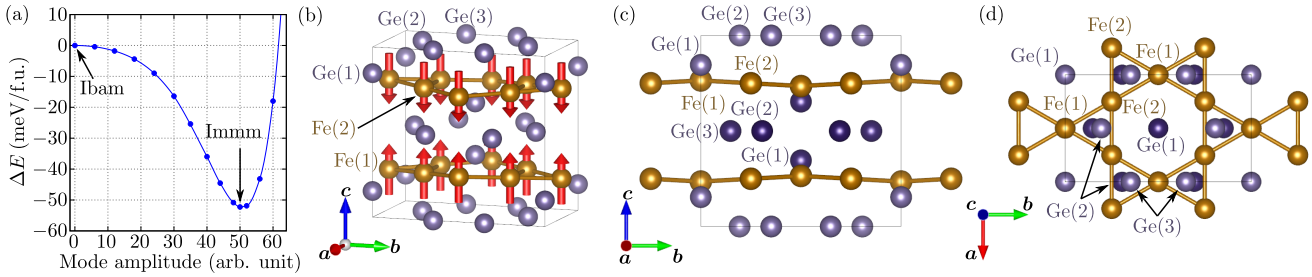

FIG. 3. (a) The soft mode amplitude dependence of system's energy, for the structure induced by the soft mode at the Γ point for the Ibam structure. The zero of energy scale is set at the energy of the Ibam structure. The system with minimum energy, after optimization, corresponds to the Immm structure, with magnetic unit cell presented in (b). The front and top view of the crystal with the Immm symmetry is presented in (c) and (d) panels, respectively.

orbitals. The value of the effective Hubbard U parameter of 4 eV is reasonable and was used in the study of other Fe-based compounds, such as FeO [78], Fe_2O_3 [78], Fe_3O_4 [79], or Fe_2SiO_4 [79]. However, in some cases a larger effective U is necessary (e.g. for iron-bearing sphalerite [80]). Nevertheless, as we mentioned earlier, for $U > U_c$ the phonon dispersion curves show imaginary soft modes. Since structural changes are defined by the polarization vector of the soft mode, our group symmetry analysis is independent on U.

Let us now analyze displacements induced by the lowest energy soft mode occurring at L=(0,1/2,1/2). Condensation of a such mode enforces doubling of the primitive unit cell along some directions. Additionally, freezing of displacements induced by its polarization vector lowers system energy because of the imaginary value of the soft mode frequency. In fact, the system's energy as a function of the displacement amplitude directly shows the existence of a structure with the lower energy [Fig. 2(a)]. This displaced and more stable structure will be the "base" of our further analysis.

The structure with the P6/mmm symmetry (space group No. 191) possesses the lattice parameters $a = b =$ 5.163 Å and c = 4.251 Å. The atoms are located at three nonequivalent Wyckoff positions: (*3f*) Fe (1/2,0,0), (*1a*) Ge(1) (0,0,0), and (*2d*) Ge(2) (1/3,2/3,1/2). The Fe atoms form an ideal kagome net, decorated by Ge(1) in the same plane. The Ge(2) atoms form the honeycomb lattice, located between the kagome layers. AFM magnetic order leads to doubling of the unit cell along the c direction [see Fig. 1(d)], i.e., magnetic unit cell containing 6 formula units. The L-point imaginary mode leads mainly to the displacement of Ge(2) atoms (along the $a + b$ direction of the P6/mmm structure) by about ±0.06 Å. We should also mention that the Fe atoms still form a kagome-like net with two different distances between atoms: Fe(1)–Fe(2) and Fe(2)–Fe(2) equal to 2.5860 Å and 2.5809 Å, respectively. The optimized structure has the Ibam symmetry (space group No. 72), with lattice constants a = 5.158 Å, b = 8.956 Å, and c = 8.501 Å, and four nonequivalent Wyckoff positions: (*4a*) Fe(1) (0,0,1/4), (*8e*) Fe(2) (1/4,1/4,1/4), (*4b*) Ge(1) (1/2,0,1/4), and (*8j*) Ge(2) (0.5142,0.6654,0). Just like before, Ge(1) atoms decorate the kagome net, while Ge(2) atoms form the deformed honeycomb-like lattice. The magnetic unit cell corresponds to the conventional cell and is presented in Fig. 2(b). The ground state energy of the system with the magnetic moment on Fe atoms along c and tilted from c axis are close to each other.

The phonon dispersion curves for the optimized Ibam structure are presented in Fig. 2(c). As we can see, the phonon spectrum still contains imaginary soft modes (marked with blue lines) and the most predominant soft mode occurs at the Γ point. In that case, the structure can be stabilized by shifts of atoms, mostly Ge(1), that do not modify the size of the unit cell. As a result, we can apply the same strategy as before to find the final crystal structure.

The dependence of the system's energy on the displacement amplitude of the polarization vector of the soft mode at the Γ point for the Ibam structure is presented in Fig. 3(a). The most important displacement is associated with the shift of the Ge(1) atoms along the c

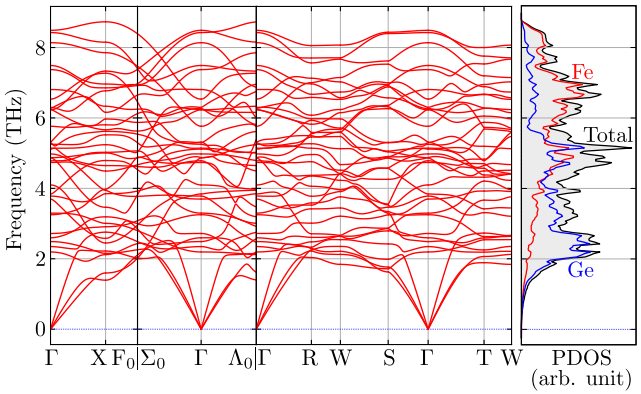

FIG. 4. The phonon dispersion curves along high symmetry directions and phonon density of states for FeGe with the Immm structure. The symbols of the high symmetry points are the same as in Fig. 2(d).

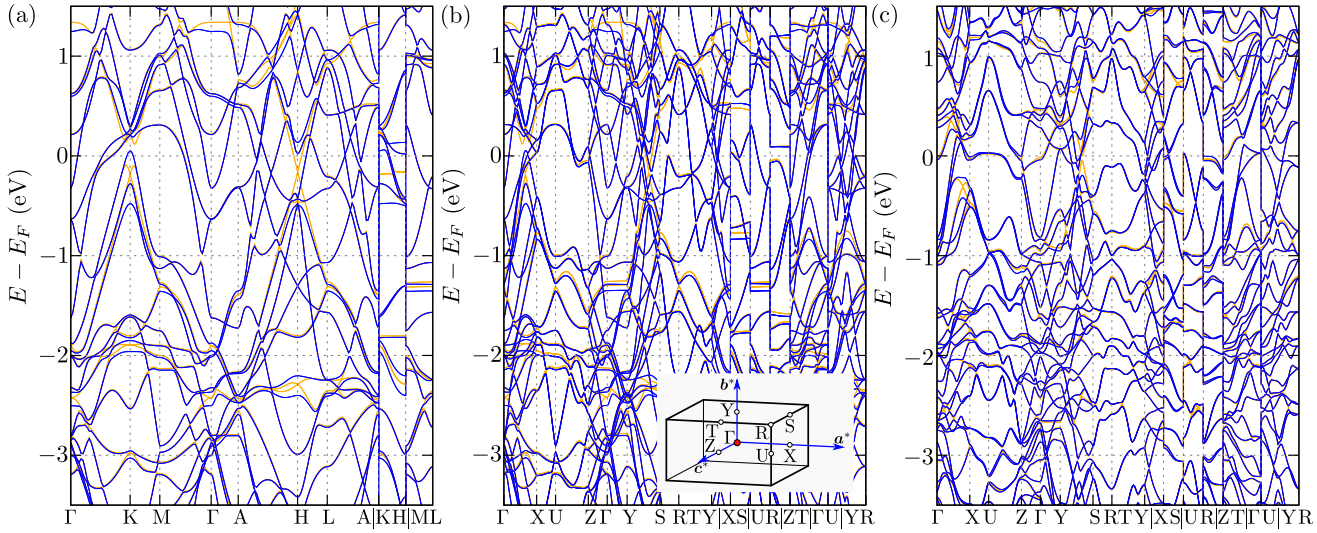

FIG. 5. The comparison of electronic band structures for the P6/mmm and Immm phases. (a) Electronic band structure for the P6/mmm magnetic unit cell. (b) Folded band structure for P6/mmm calculated using the unit cell in the shape of the magnetic unit cell for the Immm phase. (c) Electronic band structure for the Immm magnetic unit cell. The orange and blue lines correspond to the band structure in the absence and presence of the spin–orbit coupling, respectively. The inset in panel (b) shows the Brillouin zone for the Immm magnetic unit cell.

direction, which is in agreement with previous theoretical studies. The soft mode of Ibam structure leads to the Immm symmetry (space group No. 71). After optimization, the total energy decreases and lattice parameters read $a = 5.158$ Å, $b = 8.956$ Å, and $c = 8.501$ Å. The atoms are located in the Wyckoff positions: (*4j*) Fe(1) (1/2,0,0.2353), (*8k*) Fe(2) (1/4,1/4,1/4), (*4i*) Ge(1) (0,0,0.8462), (*4h*) Ge(2) (0,0.3063,1/2), and(*4g*) Ge(3) (0,0.3515,0). Similarly, the energies of the system with Fe magnetic moments along the c axis and tilted from the c direction are comparable. In this structure, the Ge(1) atoms are shifted from their initial positions by ±0.82 Å along the c direction. That large modification of the atomic position leads indirectly to large deformation of the Fe kagome-like net and the Ge honeycomb sublattice [see Fig. 3(c) and 3(d)]. The kagome-like lattice is not flat, while the deviation from the plane is around 0.13 Å. The distances between Fe atoms within the kagome-like net are 2.5791 Å and 2.5839 Å for Fe(2)–Fe(2) and Fe(2)–Fe(3), respectively. Similarly, the new distances between atoms in the deformed honeycomb sublattice are 2.94 Å and 2.66 Å for Ge(2)–Ge(3) and Ge(3)–Ge(3), respectively.

The phonon dispersion curves and phonon density of states for the final structure are presented in Fig. 4. As we can see, the structure with the Immm symmetry is dynamically stable. The vibrations associated with Fe atoms are mostly realized by the phonon modes in the higher frequency range, while the lowest modes correspond to the vibrations of Ge. Acoustic branches around the Γ point show well-visible linearity. The first nearly flat bands within the Brillouin zone are located above 2 THz (8.27 meV). Furthermore, a dense complex band structure is visible around 5 THz (20.68 meV), while phonon branches with the highest frequencies are around 9 THz (37.22 meV). These frequency ranges are in excellent agreement with the experimentally observed phonon spectrum [66].

B. Electronic properties

The electronic band structures for the P6/mmm and Immm magnetic unit cells are presented in Figs. 5(a) and 5(c), respectively. To facilitate comparison, we also present folded band structure for the P6/mmm phase [Fig. 5(b)], calculated using a cell of a shape similar to the magnetic unit cell of the Immm phase [presented in Fig. 3(b)]. As we can see, inclusion of the SOC opens band gaps in several points of the Brillouin zone (see orange and blue lines in Fig. 5, to compare the electronic band structure in the absence and presence of the SOC).

Moreover, we can simply find similarities between the electronic band structure for Immm [Fig. 5 (c)] and the folded band structure for P6/mmm [see Fig. 5(b)]. This suggests that the electronic spectra observed within angle-resolved photoemission spectroscopy (ARPES) measurements should be similar for the system before and after the transition to the CDW phase. The same behavior is also observed in vanadium-based kagome systems AV_3Sb_5 [81–84], where modification of the electronic ARPES spectra is mostly connected with transition to the CDW phase.

In the case of P6/mmm structure, all Fe atoms

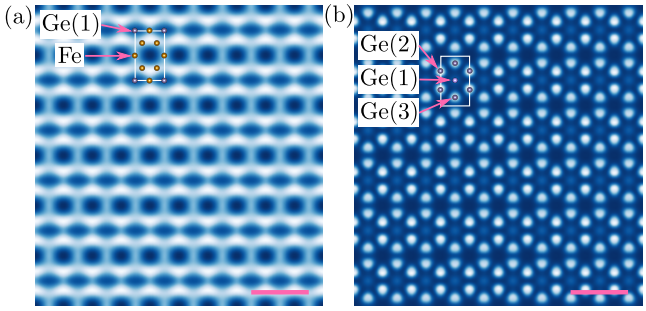

FIG. 6. Theoretically obtained STM topography of FeGe with the Immm symmetry, calculated ~ 1 Å above the surface. Results for termination on Fe kagome-like net (a), and deformed Ge honeycomb lattice (b). Inset presents the relative position and unit cell for the (001) surface. Scale bar, ~ 1 nm.

carry a magnetic moment of 2.96 μ_B. An additional magnetic moment is also induced on the Ge(1) atoms (0.165 μ_B). As we mentioned earlier, the transition from the P6/mmm to Imma phase leads to modification of the magnetic moments. The deformation of the kagome net causes a small increase of the Fe(1) magnetic moment (3.00 μ_B), while the Fe(2) magnetic moment remains unchanged (2.96 μ_B). Similarly, the shift of Ge(1) in the Immm structure, with respect to the position in the initial P6/mmm symmetry, leads to a small decrease of the magnetic moment on Ge(1) (0.125 μ_B). Additionally, the Ge(1) magnetic moment has an opposite direction to the nearest Fe kagome-like net.

For the Immm structure obtained here, we can simulate the STM topography for two different (001) surface terminations (see Fig. 6). The results presented are based on DFT slab calculations, while the STM topography comes from $E_F \pm 0.1$ eV energy window. In Figs 6(a) and 6(b) we present theoretically obtained STM topography for the FeGe terminated on the Fe kagome-like net and the deformed Ge honeycomb lattice, respectively. Comparison to the experimentally reported STM pattern [59] suggests that FeGe has termination on the deformed Ge honeycomb lattice. In the case of theoretically obtained results, both topographies are similar to the CDW stripe order. However, the Fourier transform of the experimental STM topography shows that the CDW peaks have a non-equal intensity [59]. In fact, one of the CDW peaks is much stronger than the other, which can suggest a stripe type of the CDW order. Moreover, from the theoretical point of view, the 2×2 CDW order in the P6/mmm structure due to the shift of Ge(1) out of the Fe kagome layer corresponds to the stripe order in the Immm structure, as presented in Fig. 6(b).

III. SUMMARY

Starting from the initial P6/mmm structure, which contains an ideal Fe kagome net, we found that there exists a critical value of the Hubbard U parameter (around ~ 3.5 eV), for which the softened phonon mode becomes imaginary. From analysis of the most predominant imaginary soft mode at the L point, we found a new structure with the Ibam symmetry. This structure comes from P6/mmm due to the shift of Ge atoms within the Fe kagome net layer. However, the lattice dynamics of Ibam structure reveals that the soft mode with imaginary frequency still exists at the Γ point. In this case, the displacement introduced by this soft mode associated with the shift of Ge atoms in a direction perpendicular to the Fe kagome net leads to a stable Immm structure.

Additionally, we performed calculations for the slab structure with the Immm symmetry to generate STM images for the Fe-kagome-like and Ge-deformed honeycomb surface terminations. The calculated STM topographies indicate the existence of charge ordering. The observed CDW phase is associated with a deformed Ge honeycomb-like lattice.

ACKNOWLEDGMENTS

Some figures in this work were rendered using VESTA [85] and XCRYSDEN [86] software. We kindly acknowledge support by National Science Centre (NCN, Poland) under Project No. 2021/43/B/ST3/02166.

Appendix A: Computational techniques

The first-principles density functional theory (DFT) calculations were performed using the projector augmented-wave (PAW) potentials [87] implemented in the Vienna Ab initio Simulation Package (VASP) code [88–90]. For the exchange-correlation energy, the generalized gradient approximation (GGA) in the Perdew–Burke–Ernzerhof (PBE) parametrization was used [91]. The energy cutoff for the plane-wave expansion was set to 350 eV. We introduced the correlation effect on Fe $3d$ orbitals using the DFT+U scheme proposed by Dudarev *et al.* [92].

The optimization of the lattice constants and atomic positions in the presence of the spin–orbit coupling (SOC) was performed for magnetic unit cells (with AFM order). The structures were optimized with different **k**-grids generated using the Monkhorst–Pack scheme [93] depending on the investigated symmetry. The initial structure with the P6/mmm symmetry was optimized using $8 \times 8 \times 5$ **k**–point grid. Structures with the Ibam and Immm symmetries were optimized with $15 \times 8 \times 8$ **k**–point grids. As a convergence criterion of the optimization loop, we took the energy change below 10^{-6} eV and 10^{-8} eV for ionic and electronic degrees of freedom, respectively. The symmetry of the structures after optimization was analyzed with FINDSYM [94] and SPGLIB [95], while momentum space analysis was performed within SEEK-PATH [96].

Dynamic properties were calculated using the direct *Parlinski–Li–Kawazoe* method [97], implemented in the PHONOPY package [98, 99]. Within this method, the interatomic force constants (IFC) are calculated from the Hellmann-Feynman (HF) forces acting on the atoms after displacements of individual atoms inside the supercell. We performed these calculations using the supercell with the shape corresponding to $2 \times 1 \times 2$ magnetic unit cells with the Ibam and Immm symmetries (approximately cubic shape, containing 24 formula units). During these calculations, reduced $5 \times 5 \times 5$ **k**-grid was used.

[1] J.-X. Yin, B. Lian, and M. Z. Hasan, Topological kagome magnets and superconductors, Nature **612**, 647 (2022).

[2] D. Guterding, H. O. Jeschke, and R. Valentí, Prospect of quantum anomalous Hall and quantum spin Hall effect in doped kagome lattice Mott insulators, Sci. Rep. **6**, 25988 (2016).

[3] S. Basak and A. Ptok, Shiba states in systems with density of states singularities, Phys. Rev. B **105**, 094204 (2022).

[4] Y. Wang, H. Wu, G. T. McCandless, J. Y. Chan, and M. N. Ali, Quantum states and intertwining phases in kagome materials, Nat. Rev. Phys. **5**, 635 (2023).

[5] A. Tanaka and H. Ueda, Stability of ferromagnetism in the hubbard model on the kagome lattice, Phys. Rev. Lett. **90**, 067204 (2003).

[6] F. Pollmann, P. Fulde, and K. Shtengel, Kinetic ferromagnetism on a kagome lattice, Phys. Rev. Lett. **100**, 136404 (2008).

[7] M. L. Kiesel, C. Platt, and R. Thomale, Unconventional Fermi surface instabilities in the kagome Hubbard model, Phys. Rev. Lett. **110**, 126405 (2013).

[8] W.-S. Wang, Z.-Z. Li, Y.-Y. Xiang, and Q.-H. Wang, Competing electronic orders on kagome lattices at van Hove filling, Phys. Rev. B **87**, 115135 (2013).

[9] H.-M. Guo and M. Franz, Topological insulator on the kagome lattice, Phys. Rev. B **80**, 113102 (2009).

[10] B. R. Ortiz, S. M. L. Teicher, Y. Hu, J. L. Zuo, P. M. Sarte, E. C. Schueller, A. M. M. Abeykoon, M. J. Krogstad, S. Rosenkranz, R. Osborn, R. Seshadri, L. Balents, J. He, and S. D. Wilson, CsV_3Sb_5: A $\mathbb{Z}_2$ topological kagome metal with a superconducting ground state, Phys. Rev. Lett. **125**, 247002 (2020).

[11] Y. Hu, X. Wu, Y. Yang, S. Gao, N. C. Plumb, A. P. Schnyder, W. Xie, J. Ma, and M. Shi, Tunable topological Dirac surface states and van Hove singularities in kagome metal GdV_6Sn_6, Sci. Adv. **8**, eadd2024 (2022).

[12] R. Chisnell, J. S. Helton, D. E. Freedman, D. K. Singh, R. I. Bewley, D. G. Nocera, and Y. S. Lee, Topological magnon bands in a kagome lattice ferromagnet, Phys. Rev. Lett. **115**, 147201 (2015).

[13] X. Ni, M. A. Gorlach, A. Alu, and A. B. Khanikaev, Topological edge states in acoustic kagome lattices, New J. Phys. **19**, 055002 (2017).

[14] H. Chen, H. Nassar, A. N. Norris, G. K. Hu, and G. L. Huang, Elastic quantum spin Hall effect in kagome lattices, Phys. Rev. B **98**, 094302 (2018).

[15] H. Xue, Y. Yang, F. Gao, Y. Chong, and B. Zhang, Acoustic higher-order topological insulator on a kagome lattice, Nature Mater. **18**, 108 (2019).

[16] Y. Xing, H. Chen, N. Xu, X. Li, and L. Zhang, Valley modulation and single-edge transport of magnons in breathing kagome ferromagnets, Phys. Rev. B **105**, 104409 (2022).

[17] Y.-H. He, Y.-F. Gao, Y. He, X.-F. Qi, J.-Q. Si, M. Yang, and S.-Y. Zhou, Realization of edge and corner states in photonic crystals with kagome lattices through topological insulator generators, Optics & Laser Technology **161**, 109196 (2023).

[18] E. Liu, Y. Sun, N. Kumar, L. Muechler, A. Sun, L. Jiao, S.-Y. Yang, D. Liu, A. Liang, Q. Xu, J. Kroder, V. Süß, H. Borrmann, C. Shekhar, Z. Wang, C. Xi, W. Wang, W. Schnelle, S. Wirth, Y. Chen, S. T. B. Goennenwein, and C. Felser, Giant anomalous hall effect in a ferromagnetic kagome-lattice semimetal, Nat. Phys. **14**, 1125 (2018).

[19] D. F. Liu, A. J. Liang, E. K. Liu, Q. N. Xu, Y. W. Li, C. Chen, D. Pei, W. J. Shi, S. K. Mo, P. Dudin, T. Kim, C. Cacho, G. Li, Y. Sun, L. X. Yang, Z. K. Liu, S. S. P. Parkin, C. Felser, and Y. L. Chen, Magnetic Weyl semimetal phase in a kagomé crystal, Science **365**, 1282 (2019).

[20] N. Morali, R. Batabyal, P. K. Nag, E. Liu, Q. Xu, Y. Sun, B. Yan, C. Felser, N. Avraham, and H. Beidenkopf, Fermi-arc diversity on surface terminations of the magnetic Weyl semimetal $Co_3Sn_2S_2$, Science **365**, 1286 (2019).

[21] J.-X. Yin, S. S. Zhang, G. Chang, Q. Wang, S. S. Tsirkin, Z. Guguchia, B. Lian, H. Zhou, K. Jiang, I. Belopolski, N. Shumiya, D. Multer, M. Litskevich, T. A. Cochran, H. Lin, Z. Wang, T. Neupert, S. Jia, H. Lei, and M. Z. Hasan, Negative flat band magnetism in a spin–orbit-coupled correlated kagome magnet, Nat. Phys. **15**, 443 (2019).

[22] Y. Xu, J. Zhao, C. Yi, Q. Wang, Q. Yin, Y. Wang, X. Hu, L. Wang, E. Liu, G. Xu, L. Lu, A. A. Soluyanov, H. Lei, Y. Shi, J. Luo, and Z.-G. Chen, Electronic correlations and flattened band in magnetic Weyl semimetal candidate $Co_3Sn_2S_2$, Nat. Commun. **11**, 3985 (2020).

[23] M. Kanagaraj, J. Ning, and L. He, Topological $Co_3Sn_2S_2$ magnetic Weyl semimetal: From fundamental understanding to diverse fields of study, Reviews in Physics **8**, 100072 (2022).

[24] Q. Wang, Y. Xu, R. Lou, Z. Liu, M. Li, Y. Huang, D. Shen, H. Weng, S. Wang, and H. Lei, Large intrinsic anomalous Hall effect in half-metallic ferromagnet $Co_3Sn_2S_2$ with magnetic Weyl fermions, Nat. Commun. **9**, 3681 (2018).

[25] S.-Y. Yang, J. Noky, J. Gayles, F. K. Dejene, Y. Sun, M. Dörr, Y. Skourski, C. Felser, M. N. Ali, E. Liu, and S. S. P. Parkin, Field-modulated anomalous Hall conductivity and planar hall effect in $Co_3Sn_2S_2$ nanoflakes, Nano Letters **20**, 7860 (2020).

[26] B. R. Ortiz, L. C. Gomes, J. R. Morey, M. Winiarski, M. Bordelon, J. S. Mangum, I. W. H. Oswald, J. A. Rodriguez-Rivera, J. R. Neilson, S. D. Wilson, E. Ertekin, T. M. McQueen, and E. S. Toberer,

New kagome prototype materials: discovery of KV_3Sb_5, RbV_3Sb_5, and CsV_3Sb_5, Phys. Rev. Mater. **3**, 094407 (2019).
[27] H. Li, T. T. Zhang, T. Yilmaz, Y. Y. Pai, C. E. Marvinney, A. Said, Q. W. Yin, C. S. Gong, Z. J. Tu, E. Vescovo, C. S. Nelson, R. G. Moore, S. Murakami, H. C. Lei, H. N. Lee, B. J. Lawrie, and H. Miao, Observation of unconventional charge density wave without acoustic phonon anomaly in kagome superconductors AV_3Sb_5 (A =Rb, Cs), Phys. Rev. X **11**, 031050 (2021).
[28] Z. Liang, X. Hou, F. Zhang, W. Ma, P. Wu, Z. Zhang, F. Yu, J.-J. Ying, K. Jiang, L. Shan, Z. Wang, and X.-H. Chen, Three-dimensional charge density wave and surface-dependent vortex-core states in a kagome superconductor CsV_3Sb_5, Phys. Rev. X **11**, 031026 (2021).
[29] B. R. Ortiz, P. M. Sarte, E. M. Kenney, M. J. Graf, S. M. L. Teicher, R. Seshadri, and S. D. Wilson, Superconductivity in the $\mathbb{Z}_2$ kagome metal KV_3Sb_5, Phys. Rev. Mater. **5**, 034801 (2021).
[30] R. Gupta, D. Das, C. H. Mielke III, Z. Guguchia, T. Shiroka, C. Baines, M. Bartkowiak, H. Luetkens, R. Khasanov, Q. Yin, Z. Tu, C. Gong, and H. Lei, Microscopic evidence for anisotropic multigap superconductivity in the CsV_3Sb_5 kagome superconductor, npj Quantum Materials **7**, 49 (2022).
[31] S.-Y. Yang, Y. Wang, B. R. Ortiz, D. Liu, J. Gayles, E. Derunova, R. Gonzalez-Hernandez, L. Šmejkal, Y. Chen, S. S. P. Parkin, S. D. Wilson, E. S. Toberer, T. McQueen, and M. N. Ali, Giant, unconventional anomalous hall effect in the metallic frustrated magnet candidate, KV_3Sb_5, Sci. Adv. **6**, eabb6003 (2020).
[32] F. H. Yu, T. Wu, Z. Y. Wang, B. Lei, W. Z. Zhuo, J. J. Ying, and X. H. Chen, Concurrence of anomalous Hall effect and charge density wave in a superconducting topological kagome metal, Phys. Rev. B **104**, L041103 (2021).
[33] M. Kang, L. Ye, S. Fang, J.-S. You, A. Levitan, M. Han, J. I. Facio, C. Jozwiak, A. Bostwick, E. Rotenberg, M. K. Chan, R. D. McDonald, D. Graf, K. Kaznatcheev, E. Vescovo, D. C. Bell, E. Kaxiras, J. van den Brink, M. Richter, M. Prasad Ghimire, J. G. Checkelsky, and R. Comin, Dirac fermions and flat bands in the ideal kagome metal FeSn, Nat. Mater. **19**, 163 (2020).
[34] M. Han, H. Inoue, S. Fang, C. John, L. Ye, M. K. Chan, D. Graf, T. Suzuki, M. P. Ghimire, W. J. Cho, E. Kaxiras, and J. G. Checkelsky, Evidence of two-dimensional flat band at the surface of antiferromagnetic kagome metal FeSn, Nat. Commun. **12**, 5345 (2021).
[35] H. Zhang, B. D. Oli, Q. Zou, X. Guo, Z. Wang, and L. Li, Visualizing symmetry-breaking electronic orders in epitaxial kagome magnet FeSn films, Nat. Commun. **14**, 6167 (2023).
[36] W. R. Meier, M.-H. Du, S. Okamoto, N. Mohanta, A. F. May, M. A. McGuire, C. A. Bridges, G. D. Samolyuk, and B. C. Sales, Flat bands in the CoSn-type compounds, Phys. Rev. B **102**, 075148 (2020).
[37] M. Kang, S. Fang, L. Ye, H. C. Po, J. Denlinger, C. Jozwiak, A. Bostwick, E. Rotenberg, E. Kaxiras, J. G. Checkelsky, and R. Comin, Topological flat bands in frustrated kagome lattice CoSn, Nat. Commun. **11**, 4004 (2020).
[38] Z. Liu, M. Li, Q. Wang, G. Wang, C. Wen, K. Jiang, X. Lu, S. Yan, Y. Huang, D. Shen, J.-X. Yin, Z. Wang, Z. Yin, H. Lei, and S. Wang, Orbital-selective Dirac fermions and extremely flat bands in frustrated kagome-lattice metal CoSn, Nat. Commun. **11**, 4002 (2020).
[39] L. Ye, M. Kang, J. Liu, F. von Cube, C. R. Wicker, T. Suzuki, C. Jozwiak, A. Bostwick, E. Rotenberg, D. C. Bell, L. Fu, R. Comin, and J. G. Checkelsky, Massive Dirac fermions in a ferromagnetic kagome metal, Nature **555**, 638 (2018).
[40] Z. Lin, J.-H. Choi, Q. Zhang, W. Qin, S. Yi, P. Wang, L. Li, Y. Wang, H. Zhang, Z. Sun, L. Wei, S. Zhang, T. Guo, Q. Lu, J.-H. Cho, C. Zeng, and Z. Zhang, Flatbands and emergent ferromagnetic ordering in Fe_3Sn_2 kagome lattices, Phys. Rev. Lett. **121**, 096401 (2018).
[41] J.-X. Yin, S. S. Zhang, H. Li, K. Jiang, G. Chang, B. Zhang, B. Lian, C. Xiang, I. Belopolski, H. Zheng, T. A. Cochran, S.-Y. Xu, G. Bian, K. Liu, T.-R. Chang, H. Lin, Z.-Y. Lu, Z. Wang, S. Jia, W. Wang, and M. Z. Hasan, Giant and anisotropic many-body spin–orbit tunability in a strongly correlated kagome magnet, Nature **562**, 91 (2018).
[42] L. Chen, Y. Zhou, H. Zhang, X. Ji, K. Liao, Y. Ji, Y. Li, Z. Guo, X. Shen, R. Yu, X. Yu, H. Weng, and G. Wang, Tunable magnetism and electron correlation in titanium-based kagome metals $RETi_3Bi_4$ (RE = Yb, Pr, and Nd) by rare-earth engineering (2023), arXiv:2307.02942.
[43] A. P. Sakhya, B. R. Ortiz, B. Ghosh, M. Sprague, M. I. Mondal, M. Matzelle, I. B. Elius, N. Valadez, D. G. Mandrus, A. Bansil, and M. Neupane, Observation of multiple flat bands and topological dirac states in a new titanium based slightly distorted kagome metal $YbTi_3Bi_4$ (2023), arXiv:2309.01176.
[44] M. I. Mondal, A. P. Sakhya, M. Sprague, B. R. Ortiz, M. Matzelle, B. Ghosh, N. Valadez, I. B. Elius, A. Bansil, and M. Neupane, Observation of multiple van hove singularities and correlated electronic states in a new topological ferromagnetic kagome metal $NdTi_3Bi_4$ (2023), arXiv:2311.11488.
[45] J.-X. Yin, W. Ma, T. A. Cochran, X. Xu, S. S. Zhang, H.-J. Tien, N. Shumiya, G. Cheng, K. Jiang, B. Lian, Z. Song, G. Chang, I. Belopolski, D. Multer, M. Litskevich, Z.-J. Cheng, X. P. Yang, B. Swidler, H. Zhou, H. Lin, T. Neupert, Z. Wang, N. Yao, T.-R. Chang, S. Jia, and M. Zahid Hasan, Quantum-limit Chern topological magnetism in $TbMn_6Sn_6$, Nature **583**, 533 (2020).
[46] N. J. Ghimire, R. L. Dally, L. Poudel, D. C. Jones, D. Michel, N. T. Magar, M. Bleuel, M. A. McGuire, J. S. Jiang, J. F. Mitchell, J. W. Lynn, and I. I. Mazin, Competing magnetic phases and fluctuation-driven scalar spin chirality in the kagome metal YMn_6Sn_6, Sci. Adv. **6**, eabe2680 (2020).
[47] M. Li, Q. Wang, G. Wang, Z. Yuan, W. Song, R. Lou, Z. Liu, Y. Huang, Z. Liu, H. Lei, Z. Yin, and S. Wang, Dirac cone, flat band and saddle point in kagome magnet YMn_6Sn_6, Nat. Commun. **12**, 3129 (2021).
[48] K. Fruhling, A. Streeter, S. Mardanya, X. Wang, P. Baral, O. Zaharko, I. I. Mazin, S. Chowdhury, W. D. Ratcliff, and F. Tafti, Topological Hall effect induced by chiral fluctuations in a kagome lattice (2024), arXiv:2401.17449.
[49] W. Ma, X. Xu, J.-X. Yin, H. Yang, H. Zhou, Z.-J. Cheng, Y. Huang, Z. Qu, F. Wang, M. Z. Hasan, and S. Jia, Rare earth engineering in RMn_6Sn_6 (R =Gd-Tm, Lu) topological kagome magnets, Phys. Rev. Lett. **126**, 246602 (2021).
[50] H. Zhang, J. Koo, C. Xu, M. Sretenovic, B. Yan, and X. Ke, Exchange-biased topological transverse thermo-

electric effects in a kagome ferrimagnet, Nat. Commun. **13**, 1091 (2022).
[51] C. Mielke III, W. L. Ma, V. Pomjakushin, O. Zaharko, S. Sturniolo, X. Liu, V. Ukleev, J. S. White, J.-X. Yin, S. S. Tsirkin, C. B. Larsen, T. A. Cochran, M. Medarde, V. Porée, D. Das, R. Gupta, C. N. Wang, J. Chang, Z. Q. Wang, R. Khasanov, T. Neupert, A. Amato, L. Liborio, S. Jia, M. Z. Hasan, H. Luetkens, and Z. Guguchia, Low-temperature magnetic crossover in the topological kagome magnet $TbMn_6Sn_6$, Commun. Phys. **5**, 107 (2022).
[52] S. X. M. Riberolles, T. J. Slade, D. L. Abernathy, G. E. Granroth, B. Li, Y. Lee, P. C. Canfield, B. G. Ueland, L. Ke, and R. J. McQueeney, Low-temperature competing magnetic energy scales in the topological ferrimagnet $TbMn_6Sn_6$, Phys. Rev. X **12**, 021043 (2022).
[53] H. W. S. Arachchige, W. R. Meier, M. Marshall, T. Matsuoka, R. Xue, M. A. McGuire, R. P. Hermann, H. Cao, and D. Mandrus, Charge density wave in kagome lattice intermetallic ScV_6Sn_6, Phys. Rev. Lett. **129**, 216402 (2022).
[54] S. Cao, C. Xu, H. Fukui, T. Manjo, Y. Dong, M. Shi, Y. Liu, C. Cao, and Y. Song, Competing charge-density wave instabilities in the kagome metal ScV_6Sn_6, Nat. Commun. **14**, 7671 (2023).
[55] Y. Yang, W. Fan, Q. Zhang, Z. Chen, X. Chen, T. Ying, X. Wu, X. Yang, F. Meng, G. Li, S. Li, L. Gu, T. Qian, A. P. Schnyder, J. gang Guo, and X. Chen, Discovery of two families of vsb-based compounds with v-kagome lattice, Chinese Phys. Lett. **38**, 127102 (2021).
[56] Q. Yin, Z. Tu, C. Gong, S. Tian, and H. Lei, Structures and physical properties of V-based kagome metals CsV_6Sb_6 and CsV_8Sb_{12}, Chinese Phys. Lett. **38**, 127401 (2021).
[57] M. Shi, F. Yu, Y. Yang, F. Meng, B. Lei, Y. Luo, Z. Sun, J. He, R. Wang, Z. Jiang, Z. Liu, D. Shen, T. Wu, Z. Wang, Z. Xiang, J. Ying, and X. Chen, A new class of bilayer kagome lattice compounds with dirac nodal lines and pressure-induced superconductivity, Nat. Commun. **13**, 2773 (2022).
[58] A. Mantravadi, V. Gvozdetskyi, A. Sarkar, Y. Mudryk, and J. V. Zaikina, Exploring the *A*-V-Sb landscape beyond AV_3Sb_5: A case study on the KV_6Sb_6 kagome compound, Phys. Rev. Mater. **7**, 115002 (2023).
[59] X. Teng, L. Chen, F. Ye, E. Rosenberg, Z. Liu, J.-X. Yin, Y.-X. Jiang, J. S. Oh, M. Z. Hasan, K. J. Neubauer, B. Gao, Y. Xie, M. Hashimoto, D. Lu, C. Jozwiak, A. Bostwick, E. Rotenberg, R. J. Birgeneau, J.-H. Chu, M. Yi, and P. Dai, Discovery of charge density wave in a kagome lattice antiferromagnet, Nature **609**, 490 (2022).
[60] J.-X. Yin, Y.-X. Jiang, X. Teng, M. S. Hossain, S. Mardanya, T.-R. Chang, Z. Ye, G. Xu, M. M. Denner, T. Neupert, B. Lienhard, H.-B. Deng, C. Setty, Q. Si, G. Chang, Z. Guguchia, B. Gao, N. Shumiya, Q. Zhang, T. A. Cochran, D. Multer, M. Yi, P. Dai, and M. Z. Hasan, Discovery of charge order and corresponding edge state in kagome magnet FeGe, Phys. Rev. Lett. **129**, 166401 (2022).
[61] O. Beckman, K. Carrander, L. Lundgren, and M. Richardson, Susceptibility measurements and magnetic ordering of hexagonal FeGe, Phys. Scr. **6**, 151 (1972).
[62] L. Häggström, T. Ericsson, R. Wäppling, and E. Karlsson, Mössbauer study of hexagonal FeGe, Phys. Scr. **11**, 55 (1975).
[63] J. B. Forsyth, C. Wilkinson, and P. Gardner, The low-temperature magnetic structure of hexagonal FeGe, J. Phys. F: Met. Phys. **8**, 2195 (1978).
[64] J. Bernhard, B. Lebech, and O. Beckman, Neutron diffraction studies of the low-temperature magnetic structure of hexagonal FeGe, J. Phys. F: Met. Phys. **14**, 2379 (1984).
[65] J. Bernhard, B. Lebech, and O. Beckman, Magnetic phase diagram of hexagonal FeGe determined by neutron diffraction, J. Phys. F: Met. Phys. **18**, 539 (1988).
[66] X. Teng, J. S. Oh, H. Tan, L. Chen, J. Huang, B. Gao, J.-X. Yin, J.-H. Chu, M. Hashimoto, D. Lu, C. Jozwiak, A. Bostwick, E. Rotenberg, G. E. Granroth, B. Yan, R. J. Birgeneau, P. Dai, and M. Yi, Magnetism and charge density wave order in kagome FeGe, Nat. Phys. **19**, 814 (2023).
[67] S. Shao, J.-X. Yin, I. Belopolski, J.-Y. You, T. Hou, H. Chen, Y. Jiang, M. S. Hossain, M. Yahyavi, C.-H. Hsu, Y. P. Feng, A. Bansil, M. Z. Hasan, and G. Chang, Intertwining of magnetism and charge ordering in kagome FeGe, ACS Nano **17**, 10164 (2023).
[68] Z. Chen, X. Wu, R. Yin, J. Zhang, S. Wang, Y. Li, M. Li, A. Wang, Y. Wang, Y.-J. Yan, and D.-L. Feng, Charge density wave with strong quantum phase fluctuations in kagome magnet FeGe (2023), arXiv:2302.04490.
[69] H. Tan, Y. Liu, Z. Wang, and B. Yan, Charge density waves and electronic properties of superconducting kagome metals, Phys. Rev. Lett. **127**, 046401 (2021).
[70] A. Ptok, A. Kobiałka, M. Sternik, J. Łażewski, P. T. Jochym, A. M. Oleś, and P. Piekarz, Dynamical study of the origin of the charge density wave in AV_3Sb_5 (A =K, Rb, Cs) compounds, Phys. Rev. B **105**, 235134 (2022).
[71] A. Subedi, Hexagonal-to-base-centered-orthorhombic $4Q$ charge density wave order in kagome metals KV_3Sb_5, RbV_3Sb_5, and CsV_3Sb_5, Phys. Rev. Mater. **6**, 015001 (2022).
[72] D. Subires, A. Korshunov, A. H. Said, L. Sánchez, B. R. Ortiz, S. D. Wilson, A. Bosak, and S. Blanco-Canosa, Order-disorder charge density wave instability in the kagome metal $(Cs,Rb)V_3Sb_5$, Nat. Commun. **14**, 1015 (2023).
[73] M. Gutierrez-Amigo, D. Dangić, C. Guo, C. Felser, P. J. W. Moll, M. G. Vergniory, and I. Errea, Phonon collapse and anharmonic melting of the 3D charge-density wave in kagome metals (2023), arXiv:2311.14112.
[74] A. Ptok, A. Kobiałka, M. Sternik, J. Łażewski, P. T. Jochym, A. M. Oleś, S. Stankov, and P. Piekarz, Chiral phonons in the honeycomb sublattice of layered CoSn-like compounds, Phys. Rev. B **104**, 054305 (2021).
[75] H. Miao, T. T. Zhang, H. X. Li, G. Fabbris, A. H. Said, R. Tartaglia, T. Yilmaz, E. Vescovo, J.-X. Yin, S. Murakami, X. L. Feng, K. Jiang, X. L. Wu, A. F. Wang, S. Okamoto, Y. L. Wang, and H. N. Lee, Signature of spin-phonon coupling driven charge density wave in a kagome magnet, Nat. Commun. **14**, 6183 (2023).
[76] H.-Y. Ma, J.-X. Yin, M. Z. Hasan, and J. Liu, Theory for charge density wave and orbital-flux state in antiferromagnetic kagome metal FeGe (2023), arXiv:2303.02824.
[77] Y. Wang, Enhanced spin-polarization via partial Ge-dimerization as the driving force of the charge density wave in FeGe, Phys. Rev. Mater. **7**, 104006 (2023).
[78] P. Liao and E. A. Carter, Ab initio DFT+U predictions of tensile properties of iron oxides, J. Mater. Chem. **20**,

6703 (2010).
[79] P. Piekarz, A. M. Oleś, and K. Parlinski, Comparative study of the electronic structures of Fe_3O_4 and Fe_2SiO_4, Acta Phys. Pol. A **118**, 307 (2010).
[80] Y. Feng, Z. Li, J. Chen, and Y. Chen, Effect of content and spin state of iron on electronic properties and floatability of iron-bearing sphalerite: A DFT+U study, International Journal of Mining Science and Technology **33**, 1563 (2023).
[81] H. Luo, Q. Gao, H. Liu, Y. Gu, D. Wu, C. Yi, J. Jia, S. Wu, X. Luo, Y. Xu, L. Zhao, Q. Wang, H. Mao, G. Liu, Z. Zhu, Y. Shi, K. Jiang, J. Hu, Z. Xu, and X. J. Zhou, Electronic nature of charge density wave and electron-phonon coupling in kagome superconductor KV_3Sb_5, Nat. Commun. **13**, 273 (2022).
[82] M. Kang, S. Fang, J.-K. Kim, B. R. Ortiz, S. H. Ryu, J. Kim, J. Yoo, G. Sangiovanni, D. Di Sante, B.-G. Park, C. Jozwiak, A. Bostwick, E. Rotenberg, E. Kaxiras, S. D. Wilson, J.-H. Park, and R. Comin, Twofold van hove singularity and origin of charge order in topological kagome superconductor CsV_3Sb_5, Nat. Phys. **18**, 301 (2022).
[83] T. Kato, Y. Li, T. Kawakami, M. Liu, K. Nakayama, Z. Wang, A. Moriya, K. Tanaka, T. Takahashi, Y. Yao, and T. Sato, Three-dimensional energy gap and origin of charge-density wave in kagome superconductor KV_3Sb_5, Commun. Mater. **3**, 30 (2022).
[84] Z. Jiang, H. Ma, W. Xia, Z. Liu, Q. Xiao, Z. Liu, Y. Yang, J. Ding, Z. Huang, J. Liu, Y. Qiao, J. Liu, Y. Peng, S. Cho, Y. Guo, J. Liu, and D. Shen, Observation of electronic nematicity driven by the three-dimensional charge density wave in kagome lattice KV_3Sb_5, Nano Lett. **23**, 5625 (2023).
[85] K. Momma and F. Izumi, VESTA3 for three-dimensional visualization of crystal, volumetric and morphology data, J. Appl. Crystallogr. **44**, 1272 (2011).
[86] A. Kokalj, Xcrysden–a new program for displaying crystalline structures and electron densities, J. Mol. Graph. Model. **17**, 176 (1999).
[87] P. E. Blöchl, Projector augmented-wave method, Phys. Rev. B **50**, 17953 (1994).
[88] G. Kresse and J. Hafner, Ab initio molecular-dynamics simulation of the liquid-metal–amorphous-semiconductor transition in germanium, Phys. Rev. B **49**, 14251 (1994).
[89] G. Kresse and J. Furthmüller, Efficient iterative schemes for ab initio total-energy calculations using a plane-wave basis set, Phys. Rev. B **54**, 11169 (1996).
[90] G. Kresse and D. Joubert, From ultrasoft pseudopotentials to the projector augmented-wave method, Phys. Rev. B **59**, 1758 (1999).
[91] J. P. Perdew, K. Burke, and M. Ernzerhof, Generalized gradient approximation made simple, Phys. Rev. Lett. **77**, 3865 (1996).
[92] S. L. Dudarev, G. A. Botton, S. Y. Savrasov, C. J. Humphreys, and A. P. Sutton, Electron-energy-loss spectra and the structural stability of nickel oxide: An LSDA+U study, Phys. Rev. B **57**, 1505 (1998).
[93] H. J. Monkhorst and J. D. Pack, Special points for Brillouin-zone integrations, Phys. Rev. B **13**, 5188 (1976).
[94] H. T. Stokes and D. M. Hatch, FINDSYM: program for identifying the space-group symmetry of a crystal, J. Appl. Cryst. **38**, 237 (2005).
[95] A. Togo and I. Tanaka, SPGLIB: a software library for crystal symmetry search (2018), arXiv:1808.01590.
[96] Y. Hinuma, G. Pizzi, Y. Kumagai, F. Oba, and I. Tanaka, Band structure diagram paths based on crystallography, Comput. Mater. Sci. **128**, 140 (2017).
[97] K. Parlinski, Z. Q. Li, and Y. Kawazoe, First-principles determination of the soft mode in cubic ZrO_2, Phys. Rev. Lett. **78**, 4063 (1997).
[98] A. Togo, L. Chaput, T. Tadano, and I. Tanaka, Implementation strategies in phonopy and phono3py, J. Phys. Condens. Matter **35**, 353001 (2023).
[99] A. Togo, First-principles phonon calculations with phonopy and phono3py, J. Phys. Soc. Jpn. **92**, 012001 (2023).

4.2.5 Dynamical Properties of $T_3Pb_2Ch_2$ (T =Pd,Pt and Ch =S,Se) with Transition Metal Kagome Net

S. Basak, A. Kobiałka, and A. Ptok, Adv. Phys. Res. **2**, 2300025 (2023).

$Pd_3Pb_2S_2$, with a similar crystal structure as the Shandite mineral $Ni_3Pb_2S_2$, was reported to be Dirac semimetal with higher order Fermi arcs. These special properties can be traced back to the presence of exact kagome layers in the symmetry group R$\bar{3}$m. Materials with a similar chemical formula such as $Pt_3Pb_2Ch_2$ (Ch=S, Se) are also known to exist in nature, but within symmetry group Cmcm. In this paper, we investigate the stability of compounds with the chemical formula $T_3Pb_2Ch_2$ (T=Pd, Pt and Ch=S, Se) in the Shandite-like crystal structure within the symmetry group R$\bar{3}$m. We observe that $Pt_3Pb_2S_2$ is the only compound that is not stable in this symmetry group and contains soft mode in the phonon band structure. After analyzing the soft mode at high symmetry point T, we found and plotted the atomic displacements that are required to make this compound stable. This leads us to the conclusion that the exact kagome structure formed by the Pt atoms needs to be distorted to stabilize the material in a group with lower symmetry (R$\bar{3}$c). One of the most promising characteristics of a topological semimetal is the presence of symmetry-protected degenerate points in the dispersion relation. In fact, in the cases we studied, we found the presence of degenerate lines (nodal lines), lines along which several branches have the same energy, in a phonon dispersion plot, protected by several rotational symmetry and time reversal symmetry. Moreover, the topological nature of the materials is further revealed by the presence of symmetry-protected surface states which arise due to the vibration of surface atoms and depend strongly on the type of surface termination. We ended this manuscript with the investigation of chiral phonons. It revealed that chiral phonons are not present in the kagome layers but they can arise due to the vibration of Pb atoms.

Author's contribution: Participation in the numerical calculation (phonons dispersion curves and density of states, chiral phonons, electronic band structure), discussion of obtained results, partial preparation of figures, partial preparation of the manuscript, participation in preparing the response for Referees.

RESEARCH ARTICLE

ADVANCED PHYSICS RESEARCH Open Access

www.advphysicsres.com

Dynamical Properties of $T_3Pb_2Ch_2$ (T=Pd,Pt and Ch=S,Se) with Transition Metal Kagome Net

Surajit Basak, Aksel Kobiałka,* and Andrzej Ptok**

Shandite with $Ni_3Pb_2S_2$ chemical formula and R$\bar{3}$m symmetry contains the kagome sublattice formed by transition metal atoms. Recent experimental results confirmed the possibility of successfully synthesizing $Pd_3Pb_2Ch_2$ (Ch=S,Se) with the same structure. This paper theoretically investigates the dynamical properties of such compounds. Furthermore, we study the possibility of realizing $Pt_3Pb_2Ch_2$ with the shandite structure. This study shows that the $Pd_3Pb_2Ch_2$ and $Pt_3Pb_2S_2$ are stable with R$\bar{3}$m symmetry. In the case of $Pt_3Pb_2S_2$, there is a soft mode, which is the source of the structural phase transition from R$\bar{3}$m to R$\bar{3}$c symmetry, related to the distortion within the kagome sublattice. This study discusses realized phonon nodal lines in bulk phonon dispersions in upper frequency modes. It shows that the shandite structure can host phonon surface states, with a strong dependence on the type of surface. Additionally, chiral phonons with circular motion of the Pb atoms around the equilibrium position are realized.

1. Introduction

The kagome lattice has the ideal electronic flat band.[1] Such features are observed in many compounds in which kagome sublattice is produced.[2–7] Furthermore, such lattices support the emergence of the edge states, which are observed not only in solid state systems (such as multilayer silicene,[2] GdV_6Sn_6 [8] or FeGe [9]), but also in acoustic[10–12] or photonic[13–15] lattices.

In condensed matter physics, the systems possessing the kagome structure attract a lot of attention because of the flat band and edge modes, as mentioned earlier. In addition, such systems are characterized by a multitude of unique properties. For example, recently discovered systems AV_3Sb_5 (A=K, Rb, Cs)[16] with vanadium kagome lattice, are characterized by the coexistence of superconductivity and charge density waves at low temperatures.[17] Magnetic systems containing the kagome lattice[18] exhibit Weyl behavior, which has been observed, for example, in the magnetic Mn_3Sn,[19] FeSn,[20–22] CoSn,[3,21–23] Fe_3Sn_2,[24] and $Co_3Sn_2S_2$.[25] Typically, such compounds are also characterized by an intrinsic anomalous Hall effect.[26–31]

In the context mentioned, compounds with the shandite structure ($Ni_3Pb_2S_2$),[32] which contain the transition metal kagome sublattice, have recently become very popular. Recently, from 930 shandite-like prototypical compounds only 34 were recognized as stable with magnetic order.[33] Currently, probably the most popular is the topological $Co_3Sn_2S_2$ magnetic Weyl semimetal.[34] The electronic band structure contains six nodal rings corresponding to three pairs of Weyl points in the Brillouin zone.[35] This allows the emergence of the Fermi arc surface state observed experimentally.[36] Moreover, the possibility of the existence of chiral edge states made this compound an excellent platform for the realization of the quantum anomalous Hall effect.[37]

1.1. Motivation

The mineral shandite, with the chemical formula $Ni_3Pb_2S_2$ and R$\bar{3}$m symmetry, can be successfully synthesized under controlled conditions.[32] Substitution of Se (under S) leads to stable $Ni_3Pb_2Se_2$ with the same structure.[38] Similarly, the substitution of Pb (with Ni) allows the realization of $Pd_3Pb_2Se_2$ with unchanged crystal structure,[39] and superconductivity under pressure.[40] Moreover, $Pd_3Pb_2S_2$ with shandite structure was reported,[41] as well as *laflammeite*, the "new" mineral $Pd_3Pb_2S_2$, with C2/m symmetry was reported.[42] Theoretical study suggests that $Pt_3Pb_2Ch_2$ (Ch = S, Se) should be Dirac semi-metals with higher-order Fermi arcs.[43] Lastly, $Pd_3Pb_2Se_2$ structure should also be stable under hydrostatic pressure.[44] This opens a new question: can the $Pt_3Pb_2Ch_2$ (Ch=S,Se) with the shandite crystal structure be realized? This is a very interesting problem, in the context of recent work showing the realization of $Pt_3Pb_2Ch_2$ (Ch=S,Se) with the Cmcm symmetry.[45,46] The possible formation of the structure different from shandite should not be unexpected in the context of ternary chalcogenides

S. Basak, A. Ptok
Institute of Nuclear Physics
Polish Academy of Sciences
W. E. Radzikowskiego 152, PL-31342 Kraków, Poland
E-mail: surajit.basak@ifj.edu.pl; aptok@mmj.pl

A. Kobiałka
Department of Physics
University of Basel
Klingelbergstrasse 82, CH-4056 Basel, Switzerland
E-mail: aksel.kobialka@unibas.ch

The ORCID identification number(s) for the author(s) of this article can be found under https://doi.org/10.1002/apxr.202300025

DOI: 10.1002/apxr.202300025

$M_3M'_2Ch_2$, for example $Ni_3Bi_2S_2$[47] and $Rh_3Bi_2S_2$[48] have C2/m symmetry, while $Pd_3Bi_2S_2$ possesses $I2_13$ symmetry.[49]

In this manuscript, based on the *ab initio* technique, we show that the $Pd_3Pb_2Ch_2$ (*Ch*=S,Se) and $Pt_3Pb_2Se_2$ are stable with shandite symmetry, while $Pt_3Pb_2S_2$ has imaginary phonon (soft) modes. As a result, $Pt_3Pb_2S_2$ is unstable with shandite symmetry, while the displacement of the atoms induced by the soft mode leads to a distorted kagome sublattice and stable $R\bar{3}c$ structure. The paper is organized as follows. Details of the computational methods are given in Section 2. Next, in Section 3, we present complex studies of $T_3Pb_2Ch_2$ (*T*=Pd,Pt, and *Ch*=S,Se) with shandite $R\bar{3}m$ symmetry. In particular, we discuss the crystal structure (Section 3.1), the main electronic properties (Section 3.2), the basic dynamical properties (Section 3.3), the realized phonon nodal lines (Section 3.4), the phonic surface states (Section 3.5), and the possible realization of the chiral phonons (Section 3.6). Furthermore, we present results for novel $Pt_3Pb_2S_2$ with $R\bar{3}c$ symmetry (Section 3.7). Finally, a brief summary is presented in Section 4.

2. Computational Details

First-principles (DFT) calculations were performed using the projector augmented-wave (PAW) potentials[50] implemented in the Vienna Ab initio Simulation Package (VASP) code.[51–53] Calculations were performed within the generalized gradient approximation (GGA) under the Perdew, Burke, and Ernzerhof (PBE) parameterization.[54] Wa had also included the spin–orbit coupling (SOC) and the van der Waals (vdW) corrections. The vdW correction was tested within two schemes: DFT-D2 [55] and DFT-D3.[56]

The conventional cell of the systems (containing three formula units) were optimized using 18×18×9 Γ-centered ***k***-grids in the Monkhorst–Pack scheme.[57] Calculations were carried out with an energy cutoff of 350 eV. The condition to break the optimization loop was set as the energy difference of 10^{-6} and 10^{-8} eV for successive steps for the ionic and electronic degrees of freedom, respectively. The symmetry of the system was analyzed by FINDSYM[58] and SPGLIB,[59] while momentum space analyzes were performed within SEEK-PATH.[60]

The dynamical properties were calculated using the direct *Parlinski–Li–Kawazoe* method.[61] In this calculation, the interatomic force constants (IFC) were found from the force acting on the atoms. The IFC were calculated using PHONOPY software[62] from the displacement of individual atoms. In these calculations, the supercell containing 2×2×1 conventional cells and reduced 5×5×5 Γ-centered ***k***-grids were used. Finally, the phononic surface states were calculated using the surface Green's function technique for a semi-infinite system,[63] implemented in WANNIERTOOLS.[64]

3. Results and Discussion

3.1. Crystal Structure

The $T_3Pb_2Ch_2$ compounds crystallized typically with shandite $Ni_3Pb_2S_2$ structure, with $R\bar{3}m$ symmetry (space group No. 166)[65] (shown in **Figure 1**). In such a structure, the positions of the atoms are characterized by a single free parameter z_{Ch}, which describes the position of the chalcogenide (S or Se) atom. The atoms occupy the respective highly symmetric Wyckoff positions: *T* transition metal atoms occupy the 9*e* (1/2,0,0) site, Pb occupies two nonequivalent 3*a* (0,0,0) and 3*b* (0,0,1/2) positions, while *Ch* chalcogenide atoms occupy the 6*c* (0,0,z_{Ch}) site. The transition metal atoms form the kagome sublattice, which is decorated by the Pb atom located in the same plane.

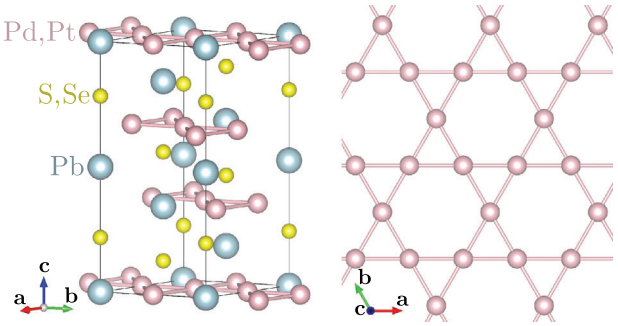

Figure 1. Conventional cell of $T_3Pb_2Ch_2$ (*T*=Pd,Pt and *Ch*=S,Se) compounds with shandite structure (left panel), where the transition metal atoms form a kagome sublattice (right panel).

Table 1. Lattice parameters for optimized $T_3Pb_2Ch_2$ compounds. To compare, data for $Ni_3Pb_2S_2$ and $Co_3Sn_2S_2$ is also presented.

system	$a = b$ (Å)	c (Å)	z_{Ch}
$Pd_3Pb_2S_2$	6.003	13.675	0.2174
$Pd_3Pb_2Se_2$	5.948	14.483	0.2104
$Pt_3Pb_2S_2$	6.216	13.363	0.2227
$Pt_3Pb_2Se_2$	6.124	14.230	0.2140
$Ni_3Pb_2S_2$ (Ref. [67])	5.576	13.658	0.285
$Co_3Sn_2S_2$ (Ref. [66])	5.375	13.176	0.216

The lattice parameters of the optimized structure of the discussed compounds with shandite are collected in **Table 1**. The obtained lattice parameters depend on the chemical formula of the compounds (i.e. the ionic radius of the substituted atoms). However, they are close to those of other ternary chalcogenides,[33] such as $Co_3Pb_2S_2$ with a = 5.495 Å and c = 13.719 Å, or $Mn_3Sb_2Te_2$ with a = 5.943 Å and c = 14.745 Å. Similarly, the free parameter z_{Ch} is closer to that reported in the $Co_3Sn_2S_2$,[66] than in clean shandite $Ni_3Pb_2S_2$.[67]

Role of the vdW Correction

During calculation, we test role of the vdW correction within the DFT-D2 [55] and DFT-D3 [56] schemes. Lattice parameters, as well as the results presented in the next part of this manuscript, obtain negligible differences. We conclude that the vdW correction plays a relatively small role in the case of the discussed compounds.

3.2. Electronic Band Structure

The electronic band structure of the investigated compounds with $R\bar{3}m$ shandite structure is shown in **Figure 2**. Theoretical results do not reveal any magnetic order in such compounds. The electronic band structure is similar to the previously reported $Pd_3Pb_2Ch_2$ (*Ch*=S,Se) by Nie *et al.* in Ref. [43]. In each compound,

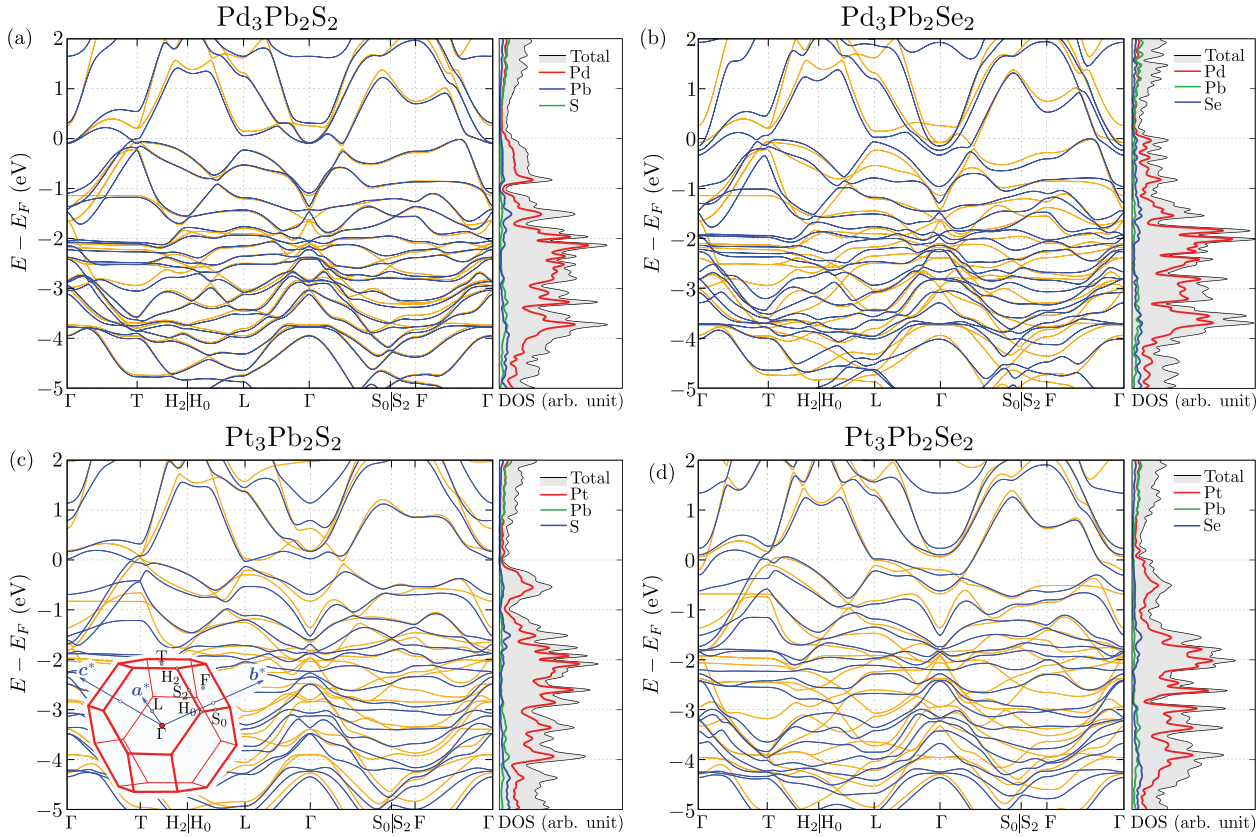

Figure 2. The electronic band structure and density of states for discussed compounds (as labeled). The orange and blue lines on the left panels correspond to the electronic band structure in the absence and presence of spin–orbit coupling, respectively. Circles mark the high symmetry points, while the inset presents the Brillouin zone and its high symmetry points.

we observed a strong role of the SOC on the band structure (cf. the orange and blue lines in Figure 2, for results without and with SOC, respectively). This is crucial around the Γ point, where SOC leads to a strong decoupling of the bands. Along the Γ–T direction, the type-I Dirac point and the band inversion around the T point are realized.[43] Theoretical investigations of the electronic band structure,[43] based on the calculation of symmetry-based indicators $Z_{2,2,2,4} = (111; 0)$[68–71] suggest possible electronic edge states. However, the absence of magnetic order does not allow for the emergence of the Weyl behavior reported in $Co_3Sn_2S_2$.[25] However, further research is necessary on the topological properties of such compounds.

Several flat bands originating from the kagome sublayers are visible in the electronic band structures (right part of the panels in Figure 2). This is reflected in the electronic density of states (DOS), in the form of distinct peaks. Indeed, partial DOS analyses show that the peaks are related to the Pt atoms forming the kagome net. All peaks are well below the Fermi level, below −1 eV.

3.3. Dynamical Stability

3.3.1. Phonon Dispersions

The phonon dispersion curves are presented in **Figure 3**. All of the discussed compounds possess phonon dispersions with similar features. First, independently of the chemical formula, the phonon branches form several groups, separated by the band gaps (marked by a gray area in Figure 3). The analyzes of the phonon DOS (**Figure 4**) show that the branches with the lowest frequencies (below 4 THz) are related to the vibration of all modes. Only in this range of frequencies Pb atoms participate in the phonon vibrations, while for higher frequencies the Pb contribution is negligible. The modes above 4 THz are related to the collective vibration modes of the transition metal and chalcogenide atoms.

IR and Raman active modes. The phonon modes at the Γ point can be decomposed into irreducible representations of the space group $R\bar{3}m$ as follows:

$$\Gamma_{\text{acoustic}} = A_{2u} + E_u, \tag{1}$$

$$\Gamma_{\text{optic}} = A_{1g} + A_{1u} + 4A_{2u} + 5E_u + E_g$$

In total, there are 21 vibrational modes, seven nodegenerate (A_{1u}, A_{1g}, and A_{2u}) and seven doubly degenerate (E_u and E_g). From this, the A_{2u} and E_u modes are infrared (IR) active, while A_{1g} and E_g are Raman active. The selective rules for these Raman active modes were described in earlier studies of TBi_2Te_4 (T=Mn,Fe).[72] From this, the Raman modes A_{1g} and E_g can be easily distinguished during Raman scattering measurements (with linear or circular polarized light), because of the different intensity.

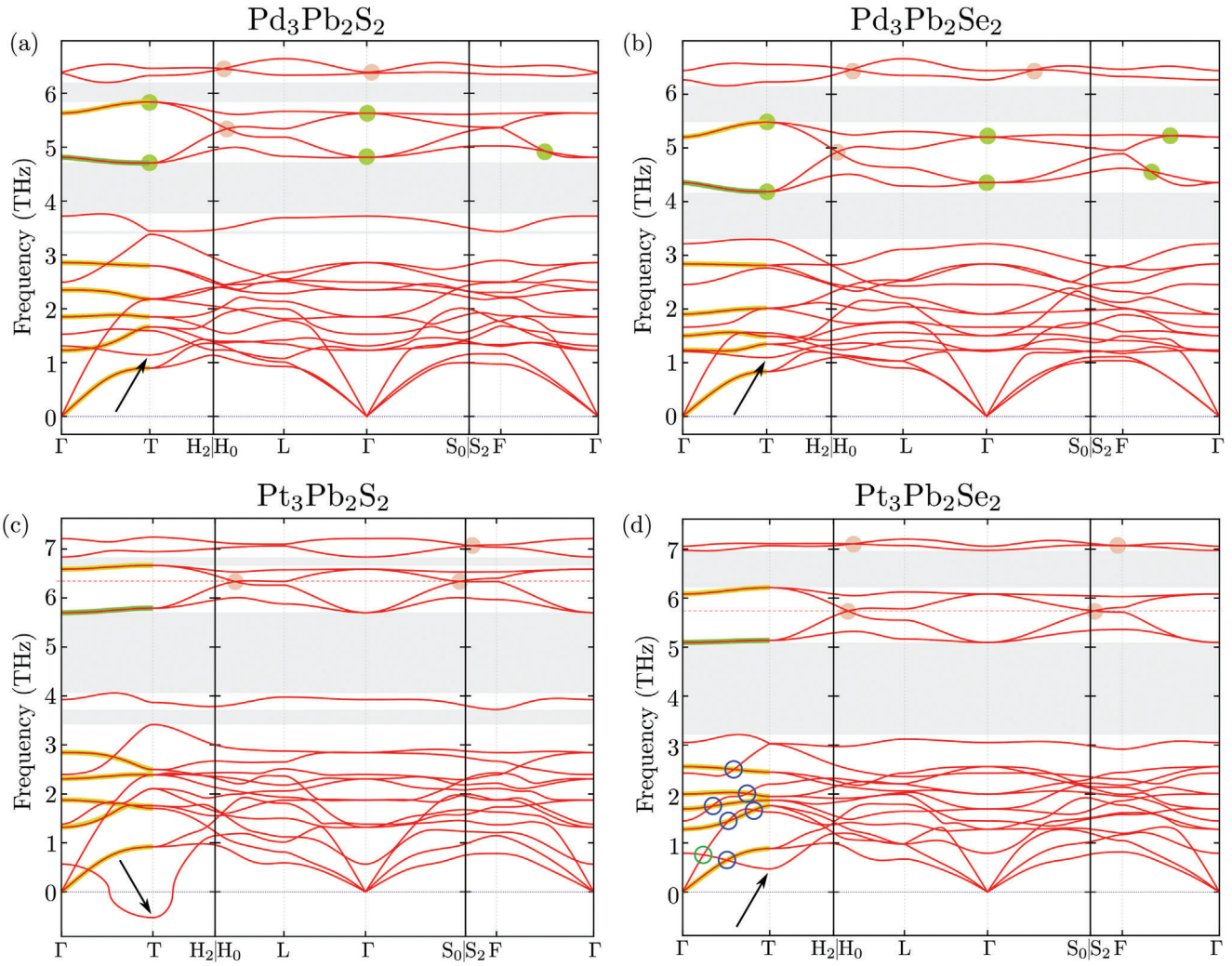

Figure 3. The phonon dispersions for the discussed compounds (as labeled). Highlighted modes at Γ–T pat denote doubly degenerate modes with initial irreducible representations E_u and E_g at the Γ point (solid yellow and green line, respectively). Gray areas denote the band gaps, and circles denote phonon degenerate Dirac points.

The observed characteristic frequencies of the modes at Γ points and their irreducible representations for discussed compounds with $R\bar{3}$ symmetry are collected in **Table 2**, while the schematic illustration of the IR and Raman active modes are presented in **Figure 5**. Raman active modes are realized only by chalcogenide atoms. In contrast to this, all atoms contribute in the IR active modes.

3.3.2. Mode Softening and System Stability

From the comparison of the phonon dispersion curves of all compounds, we can find softening of some branches at the T point (shown by black arrows in Figure 3). In the case of $Pd_3Pb_2Ch_2$ (*Ch* = S, Se), the modes described at the T point are located around 1 THz. For $Pt_3Pb_2Se_2$ [Figure 3d], this mode is clearly shifted to the lower frequencies (between 0.5 THz, below the acoustic branches). However, this mode plays the most important role in the case of $Pt_3Pb_2S_2$, where we have an imaginary frequency presented in Figure 3c as a negative value. This means that only $Pt_3Pb_2S_2$ cannot be stable with $R\bar{3}m$ symmetry. The exact analysis of this mode will be presented in Section 3.7. Here, we should also note that the softening branch is related to the lowest nondegenerate A_{1u} mode at the Γ point.

3.4. Phonon Nodal Lines

Realization of the degenerated points in the electronic band structure is a key point in the topological systems. An excellent example of such behavior is the realization of Dirac or Weyl points in an electronic band structure.[73] In some situations (typically guarantee by the space group symmetries), the band crossing can be realized along a line or within some plane, forming a nodal line or nodal plane, respectively. Such phenomena are well known from the study of the electronic band structure of topological semimetals.[73–76] Similar behavior can also be realized in phononic systems.[77,78] In this section, we discuss

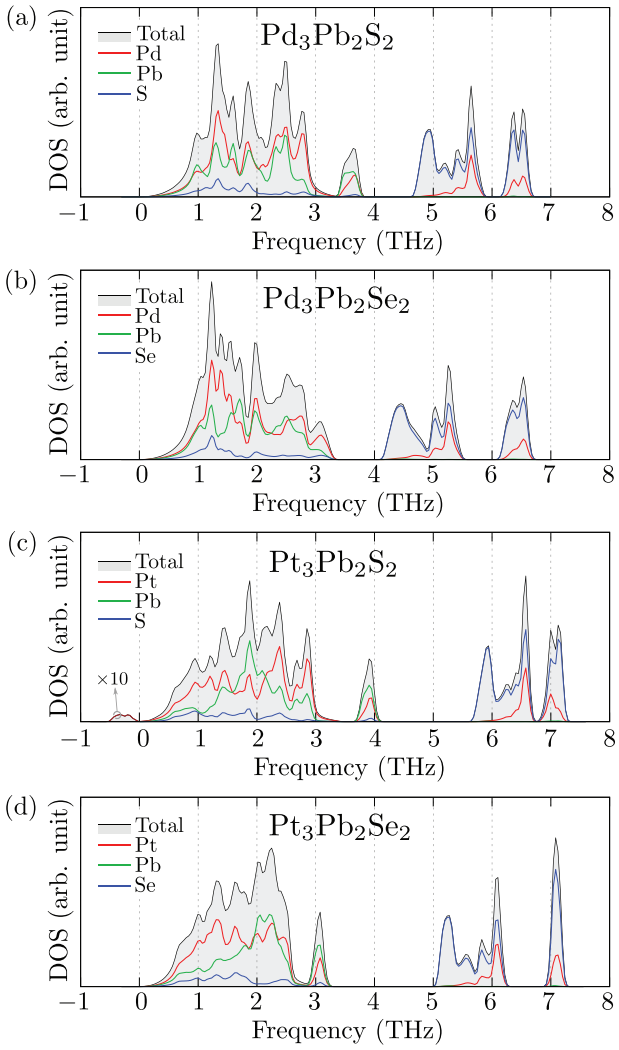

Figure 4. The phonon density of states for discuss compounds (as labeled). For $Pt_3Pb_2S_2$, to guide the eye, the magnitude for softmodes was increased ten times.

Table 2. Characteristic frequencies (THz) and symmetries of the modes at the Γ point for discuss compounds with with R$\bar{3}$m symmetry.

$Pd_3Pb_2S_2$		$Pd_3Pb_2Se_2$		$Pt_3Pb_2S_2$		$Pt_3Pb_2Se_2$	
1.23	(E_u)	1.21	(A_{1u})	0.57	(A_{1u})	0.79	(A_{1u})
1.31	(A_{1u})	1.24	(E_u)	1.32	(E_u)	1.28	(E_u)
1.53	(A_{2u})	1.50	(E_u)	1.38	(A_{2u})	1.45	(A_{2u})
1.85	(E_u)	1.66	(A_{2u})	1.87	(E_u)	1.69	(E_u)
2.35	(E_u)	1.90	(E_u)	2.31	(E_u)	2.00	(E_u)
2.49	(A_{2u})	2.45	(A_{2u})	2.40	(A_{2u})	2.43	(A_{2u})
2.85	(E_u)	2.84	(E_u)	2.85	(E_u)	2.56	(E_u)
3.72	(A_{2u})	3.21	(A_{2u})	3.93	(A_{2u})	3.05	(A_{2u})
4.81	(E_g)	4.35	(E_g)	5.70	(E_g)	5.09	(E_g)
5.63	(E_u)	5.20	(E_u)	6.59	(E_u)	6.08	(E_u)
6.38	(A_{2u})	6.27	(A_{1g})	6.84	(A_{2u})	6.98	(A_{2u})
6.39	(A_{1g})	6.44	(A_{2u})	7.21	(A_{1g})	7.06	(A_{1g})

the realization of the phonon nodal lines (i.e., crossing of the branches of phonon dispersion in the momentum space) in the discussed compounds.

The space group R$\bar{3}$m symmetry is characterized by space inversion $\mathcal{I}$, three-fold rotation axis $3_{(111)}$, two-fold rotation axes $2_{(1\bar{1}0)}$, $2_{(10\bar{1})}$, $2_{(01\bar{1})}$, and mirror planes $\mathcal{M}_{(1\bar{1}0)}$, $\mathcal{M}_{(10\bar{1})}$, $\mathcal{M}_{(01\bar{1})}$ (in the primitive unit cell basis). The three-fold rotation axis $3_{(111)}$ [along $\boldsymbol{c}$ direction in Figure 1a] leads to preservation of the degeneration of the branches along the rotation axis. As a result, the degeneracy at the Γ point is the same as the branches along the Γ–T direction (to guide the eye, the double generated branches are marked by yellow and gray lines in Figure 2). This leads to the emergence of typical symmetry that enforces the phonon nodal line along the Γ–T direction.

Time-reversal invaraint momentum points include one Γ, one T, three L, and three F symmetry points. The little group analyzes are allowed for six irreducible representations at Γ and T points. This is in agreement with Equation (1) describing irreducible representations at Γ (four possible nondegenerate representations and two possible double-degenerate representations). In the case of L and F points, only four nondegenerate representations are allowed. Due to the arguments from the previous paragraph, there are no other degenerate branches in the phonon dispersion other than the one along the Γ–T direction (according to Table 1).

However, the presence of inversion symmetry and time-reversal symmetry allows for the realization of other nodal lines. For example, in the case of MoB_2 with R$\bar{3}$m symmetry, a helical topological nodal line protected by $\mathcal{PT}$ symmetry (i.e., a combination of time-reversal symmetry $\mathcal{T}$ and inversion symmetry $\mathcal{P}$) is realized by the phonon branches in "higher" frequency mode.[79] A similar situation is realized in our case, while the nodal line has another character. Few examples of nodal lines realized in $Pt_3Pb_2Se_2$ are presented in **Figure 6**. In the case of the highest modes (bands No. 20 & 21) the nodal lines form a closed contour through the Brillouin zone in the *xy* plane. Contrary to this, the nodal lines coming from crossing band No. 17 & 18 form open lines mostly along the *z* direction. In both cases, the nodal lines are related to mostly constant frequencies — in range 7.07 THz – 7.11 THz for No. 20 & 21, and in range 5.73 THz – 5.74 Thz for No. 17 & 18. Both band crossing points are marked by green and red filled circles in Figure 3. The degeneracy of the bands along the Γ –T direction is reflected in the shape of the nodal lines between bands No. 16 & 17, and No. 18 & 19. Degenerate bands form the nodal lines along this direction (vertical line along the Brillouin zone). However, additional bands crossing out of the Γ–T direction create a star-like shape of the nodal line (visible on top of the view panel). Two fold rotational symmetries lead to the additional rotation of these nodal lines in the lower half of the Brillouin zone, with respect to the upper half. Finally, the total shape of the nodal lines takes the form of a shifted hourglass. In these cases, nodal lines are realized for frequencies 6.07 THz – 6.21 THz for band No. 18 & 19, and 5.03 – 5.22 THz for band No. 16 & 17. Similarly to the case of MoB_2 with R$\bar{3}$m symmetry,[79] the described nodal lines are protected by $\mathcal{PT}$ symmetry.

The nodal lines can also be found in the lower frequencies range. Here, the situation is more complicated. In the case of lower frequencies, many crossings of the nondegenerate and

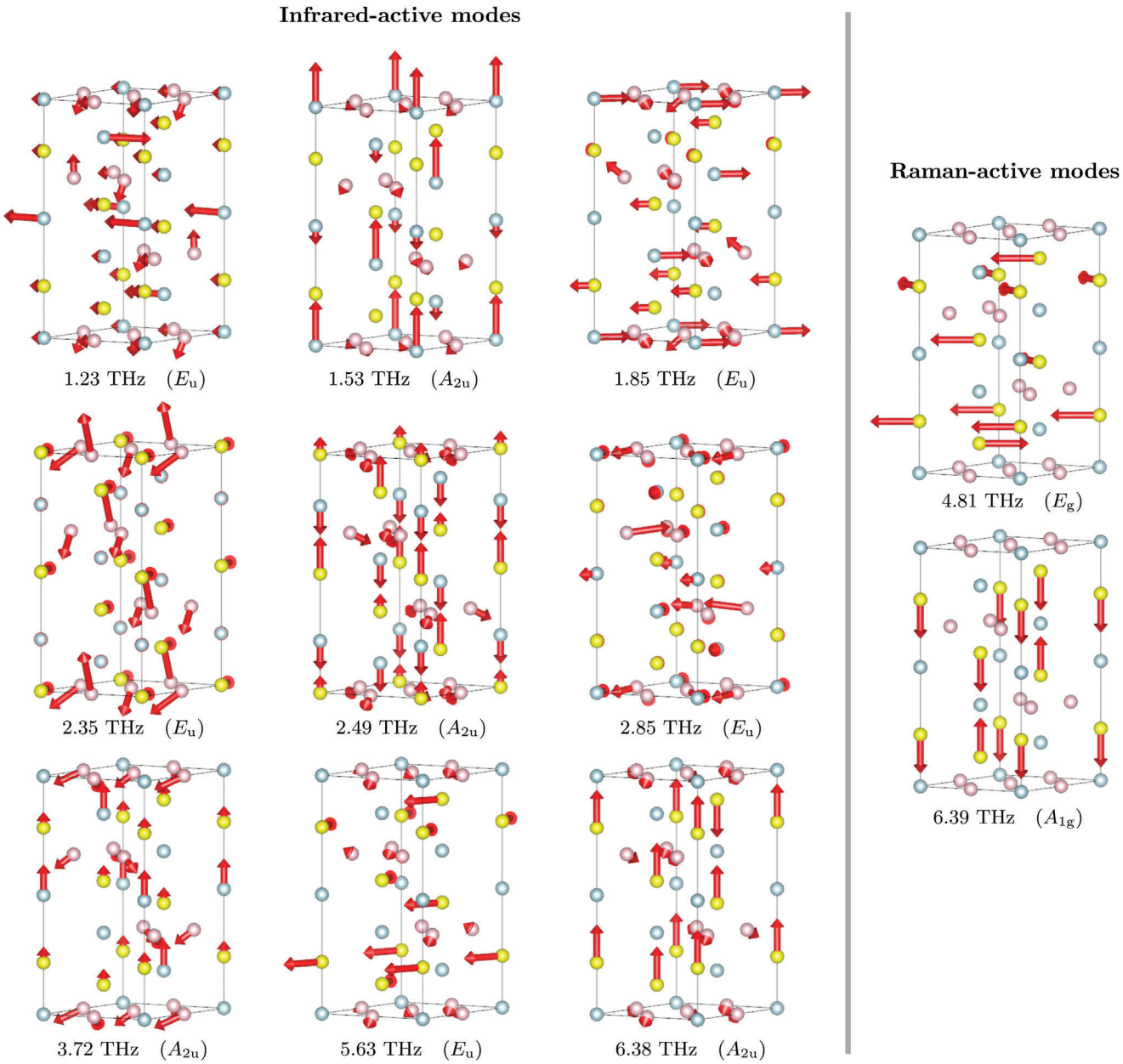

Figure 5. Schematic illustration of infrared and Raman active modes in $Pd_3Pb_2S_2$.

double-degenerate branches can be found [few examples are marked by blue circles in Figure 3d], which allow the realization of higher degenerate points. For example, the nodal line between band No. 1 & 2 is in the range of 0–1.1 THz and is related to a very complex structure containing lines and rings. However, a comparison of the phonon dispersion curves for all the discussed compounds with R$\bar{3}$m symmetry (Figure 3) suggests an incidental source of these nodal lines. On the other hand, this opens up a new possibility for nodal lines engineering via atom substitution.[80]

From an experimental point of view, the realization of the described nodal lines can be confirmed using meV-resolution inelastic x-ray scattering (IXS)[79]

3.5. Phononic Surface States

In this section, we focus on the phonon surface states in the high-frequency range. We discuss here the surface states for $Pt_3Pb_2Se_2$, however, conclusions should be similar to those for other compounds as well. In our investigation, we calculated the phonon spectral function using the Green function technique for different surfaces presented in **Figure 7**. Additionally, in this range of frequencies, the (bulk) phonon modes are related to the vibrations of the Pt and Se atoms [see Figure 4d]. This allows for the study of the surface modes associated with the kagome lattice of the transition metal atoms, i.e., Pt in our case. Here, we chose a few different surfaces realizing three types of terminations:

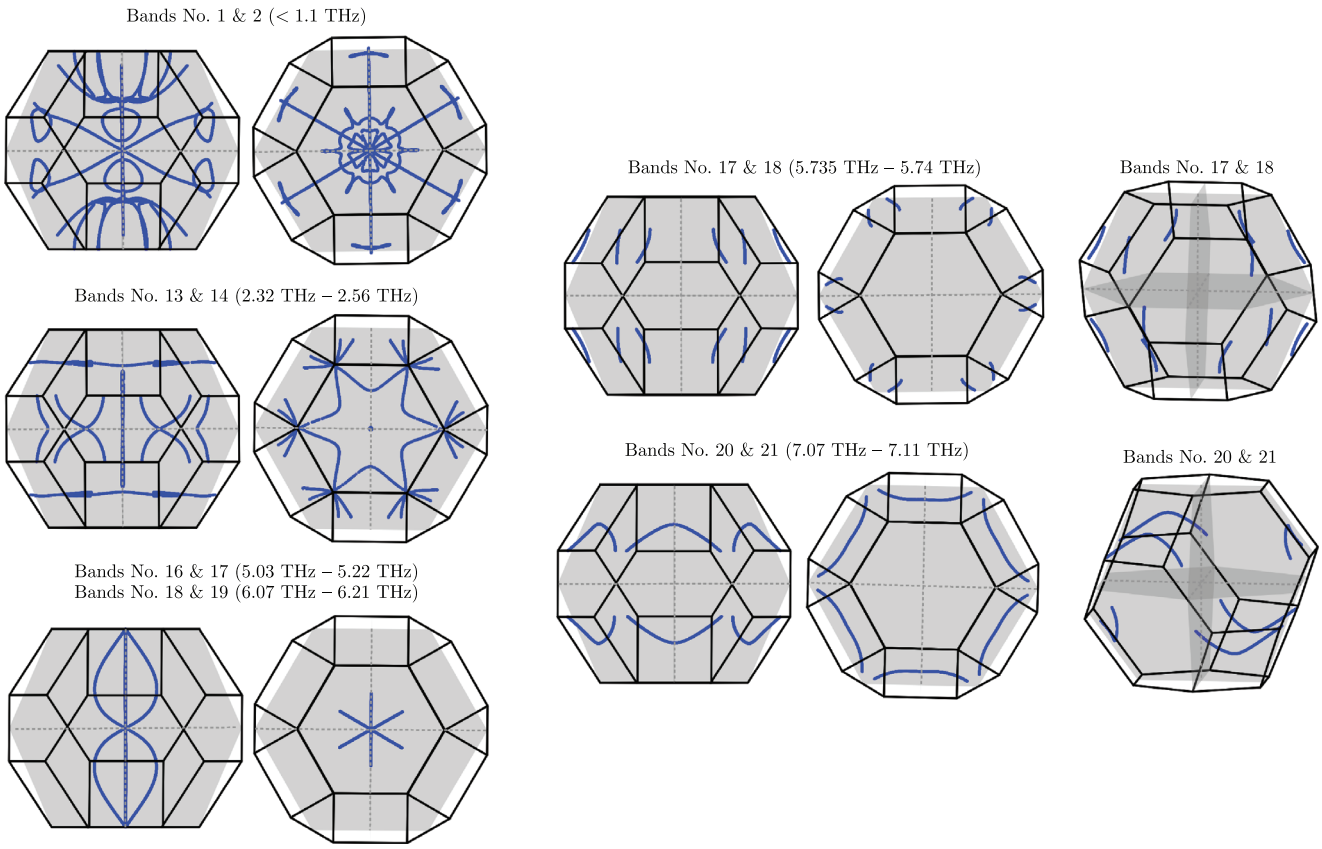

Figure 6. Example of the phonon nodal lines between different bands (as labeled) realized in $Pt_3Pb_2Se_2$. Left and right panels show the top and front view on the Brillouin zone. For nodal lines coming from bands No. 17 and 18 (20 and 21) a general view is also presented (right column). The nodal lines are realized in the range of frequencies shown above the Brillouin zones.

- surface (001) in the conventional cell basis [surface (111) in the primitive unit cell basis] — realizes the surface perpendicular to the kagome net [Figure 7b, with normal vector parallel to $\boldsymbol{c}$ in Figure 1].
- surface (100) in the conventional cell basis [surface $(\bar{1}01)$ in the primitive unit cell basis] — realizes the surface perpendicular to the kagome net terminated by the triangular lattice [Figure 7c, with normal vector parallel to $\boldsymbol{a}$ in Figure 1].
- surface $(\bar{1}10)$ in the conventional cell basis [surface $(2\bar{1}\bar{1})$ in the primitive unit cell basis] — realizes the surface parallel to the kagome net terminated by the chain of Pt atoms [Figure 7d, with normal vector parallel to $\boldsymbol{b} - \boldsymbol{a}$ in Figure 1].

The spectra for different surfaces are presented in Figure 7e–j). As we can see, the spectra are more complex than those observed in monoatomic systems such as graphene.[81] To extract the surface states more straightforwardly, we present spectra of bulk modes (upper panels), and spectra containing all modes (lower panels). In the case of (001) surface [Figure 7b,e,f] there is one edge mode in the range of bulk states (green arrow). However, out of this range, several groups of edge modes are well visible (yellow arrow). This is true for frequencies below 5.1 THz, as weel above 6.3 THz. These modes can be related to the vibrations of the "free standing" Pt–Se molecule at the (001) surface termination [Figure 7b]. In the case of (100) and $(\bar{1}10)$ surfaces, the spectra are more complex, and many surface states are realized [arrows in Figure 7h,j].

The realized phonon surface states are associated with the vibrations of the atoms at the edge of the slab. Similar results have been reported for the 2D graphene stripe.[81] In this situation, the surface states separated from the bulk modes spectra[82] denote propagation of the phonon mode along the surface.[83] However, for the (100) surface terminated by the triangle lattice, the edge mode can be associated with a strong localized mode due to the geometry of the lattice.[83,84] In the case of the $(\bar{1}10)$ surface, the dispersionless edge modes along $\bar{\Gamma}$–$\bar{X}$ can be similar to the 1D topological hinge electronic states protected by three-fold rotational and inversion symmetries in bismuth.[85] Similarly to the other systems, the phonon edge mode strongly depends on surface termination.[82] Nevertheless, the topological nature of such surface states should be the source of further phonon surface states in shandite-like systems.

3.6. Chiral Phonons

The existence of three-fold rotational symmetry in the shandite-like structure allows the emergence of the chiral phonons,[86–89] which are related to the circular motion of the atoms around the equilibrium positions. Indeed, the analyzes presented in

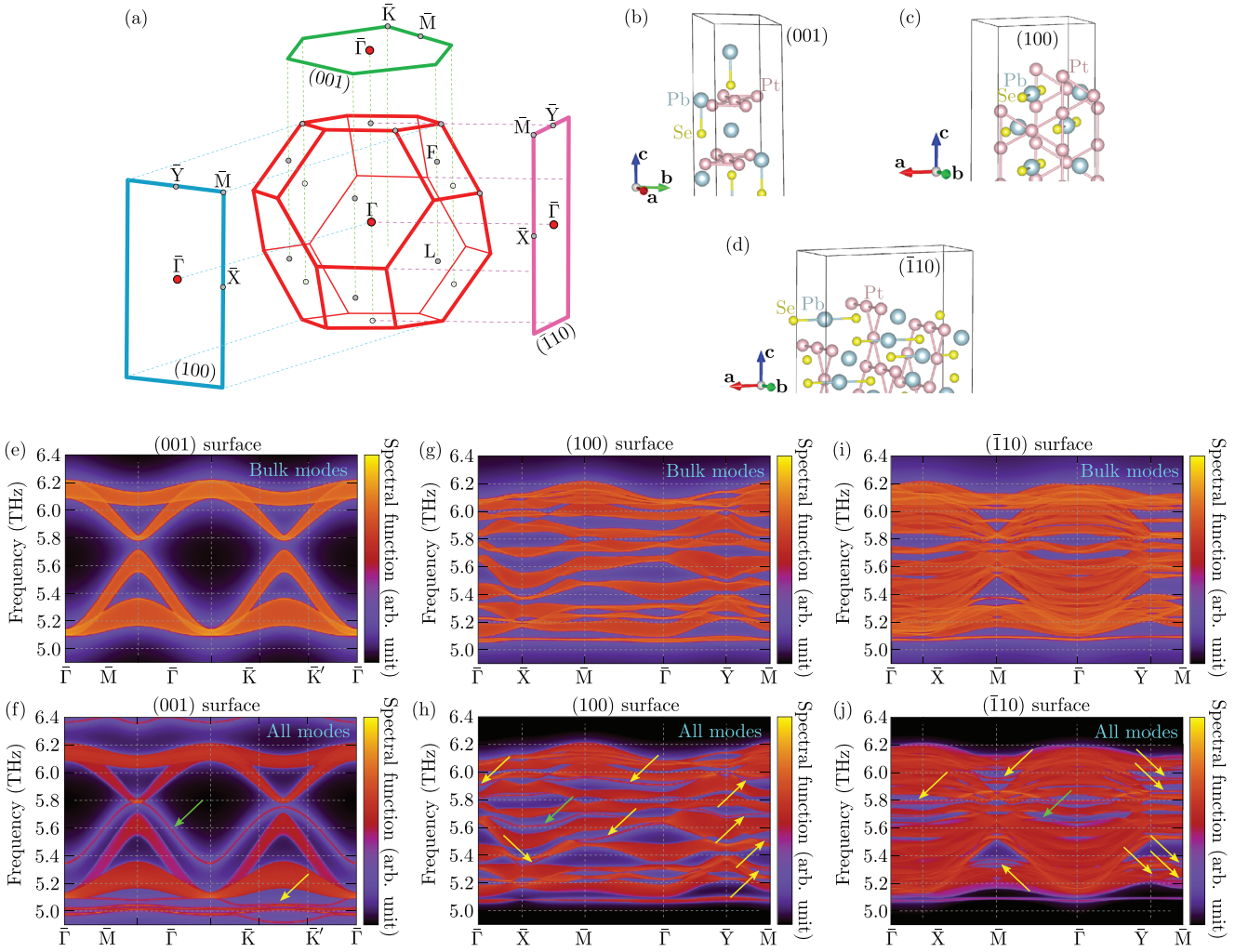

Figure 7. a) Projection of the 3D bulk Brillouin zone into the 2D surface Brillouin zone (for different surfaces, as labeled). b–d) Termination for the discussed surfaces (as labeled). e–f) Spectral function for different surfaces (as labeled). To compare the above, we present bulk state spectra (upper panels) and spectra containing all modes (lower panels). The yellow and green arrows indicate surface states.

the following show that chiral phonons can occur and are associated with Pd atoms. However, due to the presence of inversion symmetry, the total angular momentum is equal to zero.[90] Similarly to CoSn-like compounds [91] or layered magnetic topological insulator $T\mathrm{Bi}_2\mathrm{Te}_4$ (T=Mn,Fe).[72] Nevertheless, the translational symmetry break due to doping can lead to the emergence of states with non-zero total angular momentum.[92–94]

To study the possible realization of the phonon circular polarization, let us first define the phonon chirality. To do this, first we should re-express the phonon polarization vectors e_q describing vibrations of atoms induced by each phonon mode at given wavevector $\boldsymbol{k}$, in the new basis: $|R_1\rangle = \frac{1}{\sqrt{2}}(1\ i\ 0\ \cdots)$; $|L_1\rangle = \frac{1}{\sqrt{2}}(1\ -i\ 0\ \cdots)$; $|Z_1\rangle = (0\,0\,1\cdots)$; $\cdots$; $|R_j\rangle = \frac{1}{\sqrt{2}}(\cdots\ 1\ i\ 0\ \cdots)$; and $|L_j\rangle = \frac{1}{\sqrt{2}}(\cdots\ 1\ -i\ 0\ \cdots)$; $|Z_j\rangle = (\cdots 0\,0\,1\cdots)$. Here, each component of the polarization vector described the motion of the atoms along x, y, and z directions, while the polarization vector contains $3N$ components (where N is the total number of atoms in the primitive unit cell). Our new basis denotes right-handed and left-handed circulation ($|R_j\rangle$ and $|L_j\rangle$, respectively) of the j-th atom. In this case, we investigate the chiral modes realized in the xy plane (perpendicular to the $\boldsymbol{c}$ direction). Now, each polarization vector e can be given in the form:

$$\mathrm{e} = \sum_j \left(\alpha_j^R |R_j\rangle + \alpha_L^j |L_j\rangle + \alpha_j^Z |Z_j\rangle\right) \tag{2}$$

where $\alpha_j^V = \langle V_j|\mathrm{e}\rangle$, for $V \in \{R, L, Z\}$.

The operator for phonon circular polarization along the z-axis can be defined as:

$$\hat{S}^z \equiv \sum_{j=1}^{N} s_j^z = \sum_{j=1}^{N} \left(|R_j\rangle\langle R_j| + |L_j\rangle\langle L_j|\right) \tag{3}$$

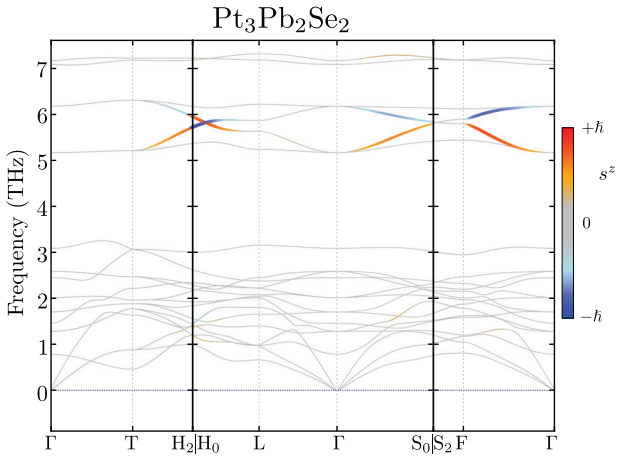

Figure 8. Chirality of the phonon modes for $Pt_3Pb_2Se_2$. Color and size of the lines correspond to the phonon polarization calculated for one Pb atom.

and the phonon circular polarization is equal to:

$$s^z_{\text{ph}} = \mathrm{e}^{\dagger}\hat{S}^z\mathrm{e} = \sum_{j=1}^{N} s^z_j\hbar = \sum_{j=1}^{N}\left(|\alpha^R_j|^2 - |\alpha^L_j|^2\right)\hbar \tag{4}$$

with $|s^y_{\text{ph}}| \leq 1$, since $\sum_j(|\alpha^R_j|^2 + |\alpha^L_j|^2) = 1$. Here, we introduce s^z_j, which denotes the contribution of each atom to the circular polarization of phonons. In the case of $|s^z_j| = 1$, the jth atom realizes motion along an ideal circle around the equilibrium position; for $|s^z_j| = 0$, ordinary vibrations are realized, and for $0 < |s^z_j| < 1$, elliptic orbits are realized.

The calculated circular phonon polarization for $Pt_3Pb_2Se_2$ is presented in **Figure 8**. As we can see, at the higher frequencies branch out (from 5 to 6 THz) and the chiral phonon modes can be realized. The exact analyzes of the phonon polarization vectors show that the chiral modes are realized by Pb atoms. Here, we should note that the chiral modes are realized in nondegenerate branches, coming from the decoupling of two doubly degenerate branches with E_g and E_u symmetry at Γ point.

3.7. Stable $Pt_3Pb_2S_2$ with R$\bar{3}$c Symmetry

The existence of a soft mode in the $Pt_3Pb_2S_2$ phonon dispersion, mentioned earlier in Section 3, indicates the existence of a collective movement of atoms that transforms a higher-symmetry crystal structure into a lower-symmetry crystal structure. Careful investigation of the atom displacement induced by the soft mode in the initial (unstable) structure can provide information about the final (stable) symmetry of the system.[61,95] In our case, the soft modes emerging at $T = (1/2, 1/2, 1/2)$ wave vector lead not only to atom displacement but also to an increase in the size of the primitive unit cell,[96] which is related to the periodicity of the induced displacement pattern.

The soft mode leads in a natural way to the symmetry breaking of the system. **Figure 9**a presents schematic representation of the atomic displacement pattern realized in the soft mode in $Pt_3Pb_2S_2$ with initial R$\bar{3}$m symmetry. The soft mode resulted in the displacement of only the Pt atoms instead of the kagome lattice. As a result, the symmetry breaking is related to the distortion of the kagome lattice.

The dependence of the system energy on the mode amplitude is shown in Figure 9b. As we can see, the atomic displacements induced by the soft mode leads to the minimization of the energy. Exact system optimization leads to the system with R$\bar{3}$c symmetry (space group No. 167). The optimized structure has lattice constants $a = 6.245$ and $c = 26.631$ Å. The Pt atoms are located at the Wyckoff position 18e (0.4812,0,1/4), the Pb atoms at two nonequivalent Wyckoff positions 6b (0,0,0) and 6a (0,0,1/2), while the S atom is located at the Wyckoff position 12c (0,0,0.3618). Note that the (conventional) unit cell with R$\bar{3}$c is twice as high as the initial R$\bar{3}$m system. Furthermore, by comparing both structures, we can see that the displacement of the Pt atoms is around 0.12 Å from the atomic positions in the ideal kagome sublattice.

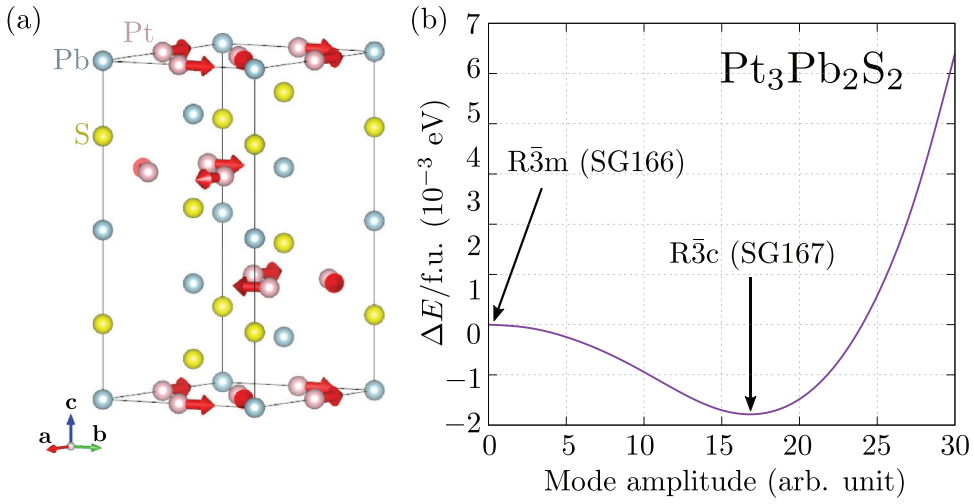

Figure 9. a) Schematic representation of the atomic displacement pattern realized in $Pt_3Pb_2S_2$ with R$\bar{3}m$ symmetry. b) Total energy of $Pt_3Pb_2S_2$ as a function of the soft mode amplitude. The relative energies of the initial R$\bar{3}$m and final R$\bar{3}$c structures are indicated by arrows.

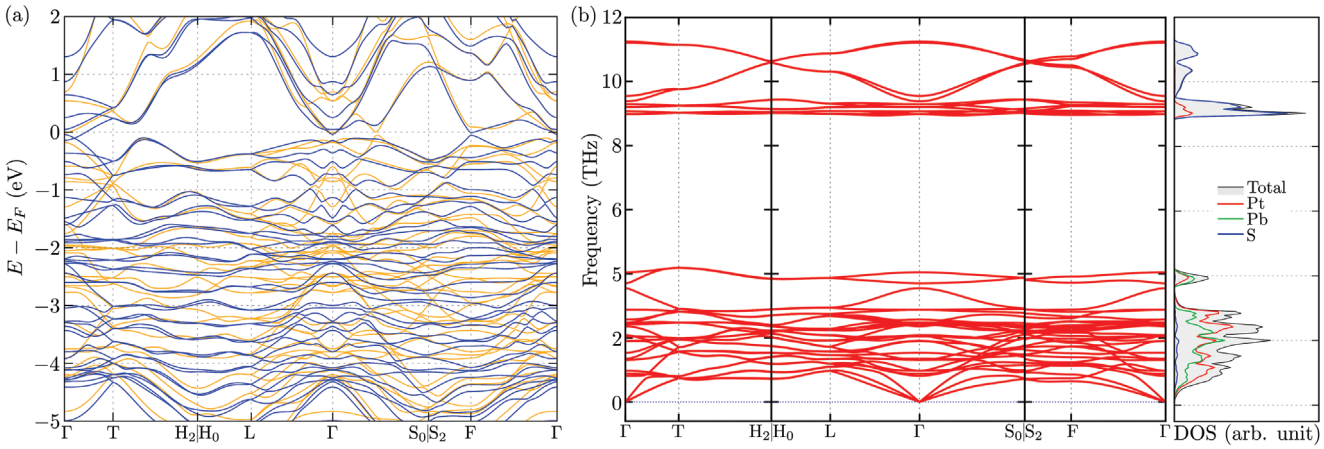

Figure 10. a) The electronic band structure of $Pt_3Pb_2S_2$ with R$\bar{3}$c symmetry. The orange and blue lines on the left panels correspond to the electronic band structure in the absence and presence of spin–orbit coupling, respectively. b) The phonon dispersion and phonon density of states for $Pt_3Pb_2S_2$ with R$\bar{3}$c symmetry.

Table 3. Characteristic frequencies (THz) and symmetries of the modes at the Γ point for $Pt_3Pb_2S_2$ with R$\bar{3}$c symmetry.

0.82	(A_{2u})	0.88	(A_{1u})	0.97	(E_g)	1.31	(E_u)
1.35	(A_{2g})	1.54	(A_{2g})	1.90	(E_g)	2.04	(E_u)
2.08	(E_u)	2.36	(A_{2u})	2.42	(A_{2u})	2.42	(A_{2u})
2.42	(E_u)	2.42	(A_{2u})	2.48	(E_u)	2.57	(E_u)
2.57	(E_u)	2.87	(E_u)	3.55	(A_{2g})	3.70	(A_{1u})
4.05	(A_{2u})	8.98	(E_g)	9.06	(E_u)	9.06	(E_u)
9.20	(E_u)	9.29	(E_u)	9.38	(A_{2u})	9.54	(A_{2g})
11.21	(A_{1u})	11.24	(A_{1g})				

The electronic character of $Pt_3Pb_2S_2$ remains unchanged, and the system exhibits metallic features. The electronic band structure is more complex than for R$\bar{3}$m [**Figure 10**a], due to the folding of the Brillouin zone along the (111) direction. However, several nearly flat bands are visible. Also, around the Fermi level, there exist a few Dirac points along the Γ–T direction. The topological properties can still be expected in this case, and thus this topic warrants future studies in this direction.

The phonon dispersion curve does not show soft modes [Figure 10b], and $Pt_3Pb_2S_2$ should be stable with R$\bar{3}$c symmetry. In this case, the phonon modes at the Γ point can be decomposed into irreducible representations as follows:

$$\Gamma_{\text{acoustic}} = A_{2u} + E_u, \tag{5}$$

$$\Gamma_{\text{optic}} = 2A_{1g} + 3A_{1u} + 4A_{2g} + 4A_{2u} + 7E_u + 6E_g$$

The increasing number of irreducible representations is related to the doubled number of the atoms in the (primitive) unit cell. The activity of the mode is unchanged [cf. Equation 1], i.e., modes A_{2u} and E_u are IR active, while A_{1g} and E_g are Raman active. The characteristic frequencies and symmetries of the modes at the Γ point for $Pt_3Pb_2S_2$ with R$\bar{3}$c symmetry are collected in **Table 3**, and can be used in the experimental classification of the real system.

4. Conclusion

In this paper, we present a comprehensive study of the dynamical properties of the $T_3Pb_2Ch_2$ (T=Pd,Pt and Ch=S,Se) with shandite-like structure (R$\bar{3}$m symmetry). We show that $Pd_3Pb_2Ch_2$ and $Pt_3Pb_2Se_2$ should crystallize with shandite structure. Contrary to this, $Pt_3Pb_2S_2$ is unstable dynamically, and phonon spectra exhibits the imaginary soft mode. Analysis of this soft mode leads to the stable structure of $Pt_3Pb_2S_2$ with R$\bar{3}$c symmetry (without soft modes).

Furthermore, we present theoretically obtained characteristic frequencies and symmetries of the modes at the Γ point for each compound, which should help to confirm our findings experimentally, within infrared or Raman spectroscopy measurements. From the partial phonon DOS we show that the higher frequencies vibrations are associated only with transition metal and lead atoms. Moreover, the branches in the higher frequencies give rise to the symmetry enforcing phonon nodal line.

The most interesting phonon properties of shandie-like compounds are associated with the emergence of phonon surface states and chiral phonons. We show that the phonon surface states can be realized independently of the surface termination and are mostly related to the kagome sublattice of transition metal atoms. The existence of three-fold rotational symmetry allows the occurrence of chiral phonons in the system. We show that the chiral phonons are realized by the circular motion of the Pb atoms. Our findings can also be applied to other compounds with the shandite R$\bar{3}$m structure.

Acknowledgments

Some figures in this work were rendered using VESTA[97] software. This work was supported by the Polish National Agency for Academic Exchange (NAWA, Poland) under the grant BPN/BEK/2021/1/00474 (AK). This work was supported by the National Science Centre (NCN, Poland) under Project no. 2021/43/B/ST3/02166.

Conflict of Interest

The authors declare no conflict of interest.

Data Availability Statement

The data that support the findings of this study are available from the corresponding author upon reasonable request.

Keywords

chiral modes, nodal lines, phonons, surface states

Received: February 25, 2023
Revised: May 13, 2023
Published online:

[1] W. Jiang, M. Kang, H. Huang, H. Xu, T. Low, F. Liu, *Phys. Rev. B* **2019**, *99*, 125131.
[2] Z. Li, J. Zhuang, L. Wang, H. Feng, Q. Gao, X. Xu, W. Hao, X. Wang, C. Zhang, K. Wu, S. X. Dou, L. Chen, Z. Hu, Y. Du, *Sci. Adv.* **2018**, *4*, eaau4511.
[3] W. R. Meier, M.-H. Du, S. Okamoto, N. Mohanta, A. F. May, M. A. McGuire, C. A. Bridges, G. D. Samolyuk, B. C. Sales, *Phys. Rev. B* **2020**, *102*, 075148.
[4] Z. Liu, M. Li, Q. Wang, G. Wang, C. Wen, K. Jiang, X. Lu, S. Yan, Y. Huang, D. Shen, J.-X. Yin, Z. Wang, Z. Yin, H. Lei, S. Wang, *Nat. Commun.* **2020**, *11*, 4002.
[5] M. Li, Q. Wang, G. Wang, Z. Yuan, W. Song, R. Lou, Z. Liu, Y. Huang, Z. Liu, H. Lei, Z. Yin, S. Wang, *Nat. Commun.* **2021**, *12*, 3129.
[6] T. Nguyen, M. Li, *J. Appl. Phys.* **2022**, *131*, 060901.
[7] Z. Sun, H. Zhou, C. Wang, S. Kumar, D. Geng, S. Yue, X. Han, Y. Haraguchi, K. Shimada, P. Cheng, L. Chen, Y. Shi, K. Wu, S. Meng, B. Feng, *Nano Lett.* **2022**, *22*, 4596.
[8] Y. Hu, X. Wu, Y. Yang, S. Gao, N. C. Plumb, A. P. Schnyder, W. Xie, J. Ma, M. Shi, *Sci. Adv.* **2022**, *8*, 38eadd2024.
[9] J.-X. Yin, Y.-X. Jiang, X. Teng, M. S. Hossain, S. Mardanya, T.-R. Chang, Z. Ye, G. Xu, M. M. Denner, T. Neupert, B. Lienhard, H.-B. Deng, C. Setty, Q. Si, G. Chang, Z. Guguchia, B. Gao, N. Shumiya, Q. Zhang, T. A. Cochran, D. Multer, M. Yi, P. Dai, M. Z. Hasan, *Phys. Rev. Lett.* **2022**, *129*, 166401.
[10] X. Ni, M. A. Gorlach, A. Alu, A. B. Khanikaev, *New J. Phys.* **2017**, *19*, 055002.
[11] H. Xue, Y. Yang, F. Gao, Y. Chong, B. Zhang, *Nat. Mater.* **2019**, *18*, 108.
[12] Q. Wu, H. Chen, X. Li, G. Huang, *Phys. Rev. Appl.* **2020**, *14*, 014084.
[13] H. Zhong, R. Wang, F. Ye, J. Zhang, L. Zhang, Y. Zhang, M. R. Belić, Y. Zhang, *Results in Physics* **2019**, *12*, 996.
[14] Y. Chen, X. Lu, H. Chen, *Opt. Lett.* **2019**, *44*, 4251.
[15] M. Li, D. Zhirihin, M. Gorlach, X. Ni, D. Filonov, A. Slobozhanyuk, A. Alù, A. B. Khanikaev, *Nat. Photonics* **2020**, *14*, 89.
[16] B. R. Ortiz, L. C. Gomes, J. R. Morey, M. Winiarski, M. Bordelon, J. S. Mangum, I. W. H. Oswald, J. A. Rodriguez-Rivera, J. R. Neilson, S. D. Wilson, E. Ertekin, T. M. McQueen, E. S. Toberer, *Phys. Rev. Mater.* **2019**, *3*, 094407.
[17] T. Neupert, M. M. Denner, J.-X. Yin, R. Thomale, M. Z. Hasan, *Nat. Phys.* **2022**, *18*, 137.
[18] V. Meschke, P. Gorai, V. Stevanović, E. S. Toberer, *Chem. Mater.* **2021**, *33*, 4373.
[19] K. Kuroda, T. Tomita, M.-T. Suzuki, C. Bareille, A. A. Nugroho, P. Goswami, M. Ochi, M. Ikhlas, M. Nakayama, S. Akebi, R. Noguchi, R. Ishii, N. Inami, K. Ono, H. Kumigashira, A. Varykhalov, T. Muro, T. Koretsune, R. Arita, S. Shin, T. Kondo, S. Nakatsuji, *Nature Mater.* **2017**, *16*, 1090.
[20] M. Kang, L. Ye, S. Fang, J.-S. You, A. Levitan, M. Han, J. I. Facio, C. Jozwiak, A. Bostwick, E. Rotenberg, M. K. Chan, R. D. McDonald, D. Graf, K. Kaznatcheev, E. Vescovo, D. C. Bell, E. Kaxiras, J. van den Brink, M. Richter, M. Prasad Ghimire, J. G. Checkelsky, R. Comin, *Nat. Mater.* **2020**, *19*, 163.
[21] Y. Xie, L. Chen, T. Chen, Q. Wang, Q. Yin, J. R. Stewart, M. B. Stone, L. L. Daemen, E. Feng, H. Cao, H. Lei, Z. Yin, A. H. MacDonald, P. Dai, *Commun. Phys.* **2021**, *4*, 240.
[22] M. A. Kassem, Y. Tabata, T. Waki, H. Nakamura, *J. Solid State Chem.* **2016**, *233*, 8.
[23] M. Kang, S. Fang, L. Ye, H. C. Po, J. Denlinger, C. Jozwiak, A. Bostwick, E. Rotenberg, E. Kaxiras, J. G. Checkelsky, R. Comin, *Nat. Commun.* **2020**, *11*, 4004.
[24] L. Ye, M. Kang, J. Liu, F. von Cube, C. R. Wicker, T. Suzuki, C. Jozwiak, A. Bostwick, E. Rotenberg, D. C. Bell, L. Fu, R. Comin, J. G. Checkelsky, *Nature* **2018**, *555*, 638.
[25] Y. Xu, J. Zhao, C. Yi, Q. Wang, Q. Yin, Y. Wang, X. Hu, L. Wang, E. Liu, G. Xu, L. Lu, A. A. Soluyanov, H. Lei, Y. Shi, J. Luo, Z.-G. Chen, *Nat. Commun.* **2020**, *11*, 3985.
[26] T. Kida, L. A. Fenner, A. A. Dee, I. Terasaki, M. Hagiwara, A. S. Wills, *J. Phys.: Condens. Matter* **2011**, *23*, 112205.
[27] Q. Wang, Y. Xu, R. Lou, Z. Liu, M. Li, Y. Huang, D. Shen, H. Weng, S. Wang, H. Lei, *Nat. Commun.* **2018**, *9*, 3681.
[28] E. Liu, Y. Sun, N. Kumar, L. Muechler, A. Sun, L. Jiao, S.-Y. Yang, D. Liu, A. Liang, Q. Xu, J. Kroder, V. Süß, H. Borrmann, C. Shekhar, Z. Wang, C. Xi, W. Wang, W. Schnelle, S. Wirth, Y. Chen, S. T. B. Goennenwein, C. Felser, *Nat. Phys.* **2018**, *14*, 1125.
[29] G. S. Thakur, P. Vir, S. N. Guin, C. Shekhar, R. Weihrich, Y. Sun, N. Kumar, C. Felser, *Chem. Mater.* **2020**, *32*, 1612.
[30] D. Zhang, Z. Hou, W. Mi, *Appl. Phys. Lett.* **2022**, *120*, 232401.
[31] K. I. A. Khan, R. S. Yadav, H. Bangar, A. Kumar, N. Chowdhury, P. K. Muduli, P. K. Muduli, *Nanoscale* **2022**, *14*, 8484.
[32] W. M. Skinner, G. Qian, A. N. Buckley, *J. Solid State Chem.* **2013**, *206*, 32.
[33] H. K. Singh, A. Sehrawat, C. Shen, I. Samathrakis, I. Opahle, H. Zhang, R. Xie, *Acta Mater.* **2023**, *242*, 118474.
[34] M. Kanagaraj, J. Ning, L. He, *Reviews in Physics* **2022**, *8*, 100072.
[35] Q. Xu, E. Liu, W. Shi, L. Muechler, J. Gayles, C. Felser, Y. Sun, *Phys. Rev. B* **2018**, *97*, 235416.
[36] D. F. Liu, A. J. Liang, E. K. Liu, Q. N. Xu, Y. W. Li, C. Chen, D. Pei, W. J. Shi, S. K. Mo, P. Dudin, T. Kim, C. Cacho, G. Li, Y. Sun, L. X. Yang, Z. K. Liu, S. S. P. Parkin, C. Felser, Y. L. Chen, *Science* **2019**, *365*, 1282.
[37] L. Muechler, E. Liu, J. Gayles, Q. Xu, C. Felser, Y. Sun, *Phys. Rev. B* **2020**, *101*, 115106.
[38] *Z. Kristallogr. Cryst. Mater.* **1997**, *212*, 136.
[39] S. Seidlmayer, F. Bachhuber, I. Anusca, J. Rothballer, M. Bräu, P. Peter, R. Weihrich, *Z. Kristallogr.* **2010**, *225*, 371.
[40] F. H. Yu, X. Y. Hua, T. Chen, J. Sun, M. Z. Shi, W. Z. Zhuo, D. H. Ma, H. H. Wang, J. J. Ying, X. H. Chen, *New J. Phys.* **2020**, *22*, 123013.
[41] M. Zabel, S. Wandinger, K.-J. Range, *Z. Naturforsch. B* **1979**, *34*, 238.
[42] A. Y. Barkov, R. F. Martin, T. A. A. Halkoaho, A. J. Criddle, *Can. Mineral.* **2002**, *40*, 671.
[43] S. Nie, J. Chen, C. Yue, C. Le, D. Yuan, Z. Wang, W. Zhang, H. Weng, *Science Bulletin* **2022**, *67*, 1958.
[44] K. Hossain, R. A. Rabu, M. S. Khanom, M. K. Hossain, F. Ahmed, *Phys. B* **2022**, *637*, 413920.
[45] Y. Fang, S. Wang, X. Zhang, G. Lin, W. Zhao, X. Wang, W. Wang, F. Huang, *Inorg. Chem.* **2021**, *60*, 16538.
[46] S. Wang, K. Bu, D. Wang, C. Zheng, X. Che, Z. Han, F. Huang, *J. Alloys Compd.* **2021**, *853*, 157092.
[47] T. Sakamoto, M. Wakeshima, Y. Hinatsu, *J. Phys.: Condens. Matter* **2006**, *18*, 4417.
[48] U. S. Kaluarachchi, W. Xie, Q. Lin, V. Taufour, S. L. Bud'ko, G. J. Miller, P. C. Canfield, *Phys. Rev. B* **2015**, *91*, 174513.

[49] R. Weihrich, S. F. Matar, V. Eyert, F. Rau, M. Zabel, M. Andratschke, I. Anusca, T. Bernert, *Progress in Solid State Chemistry* **2007**, *35*, 309.
[50] P. E. Blöchl, *Phys. Rev. B* **1994**, *50*, 17953.
[51] G. Kresse, J. Hafner, *Phys. Rev. B* **1994**, *49*, 14251.
[52] G. Kresse, J. Furthmüller, *Phys. Rev. B* **1996**, *54*, 11169.
[53] G. Kresse, D. Joubert, *Phys. Rev. B* **1999**, *59*, 1758.
[54] J. P. Perdew, K. Burke, M. Ernzerhof, *Phys. Rev. Lett.* **1996**, *77*, 3865.
[55] S. Grimme, *J. Comput. Chem.* **2006**, *27*, 1787.
[56] S. Grimme, J. Antony, S. Ehrlich, H. Krieg, *J. Chem. Phys.* **2010**, *132*, 154104.
[57] H. J. Monkhorst, J. D. Pack, *Phys. Rev. B* **1976**, *13*, 5188.
[58] H. T. Stokes, D. M. Hatch, *J. Appl. Cryst.* **2005**, *38*, 237.
[59] A. Togo, I. Tanaka, Spglib: a software library for crystal symmetry search, arXiv:1808.01590, **2018**.
[60] Y. Hinuma, G. Pizzi, Y. Kumagai, F. Oba, I. Tanaka, *Comput. Mater. Sci.* **2017**, *128*, 140.
[61] K. Parlinski, Z. Q. Li, Y. Kawazoe, *Phys. Rev. Lett.* **1997**, *78*, 4063.
[62] A. Togo, I. Tanaka, *Scr. Mater.* **2015**, *108*, 1.
[63] M. P. L. Sancho, J. M. L. Sancho, J. M. L. Sancho, J. Rubio, *J. Phys. F: Met. Phys.* **1985**, *15*, 851.
[64] Q. S. Wu, S. N. Zhang, H.-F. Song, M. Troyer, A. A. Soluyanov, *Comput. Phys. Commun.* **2018**, *224*, 405.
[65] P. Vaqueiro, G. G. Sobany, *Solid State Sciences* **2009**, *11*, 513.
[66] M. Holder, Y. S. Dedkov, A. Kade, H. Rosner, W. Schnelle, A. Leithe-Jasper, R. Weihrich, S. L. Molodtsov, *Phys. Rev. B* **2009**, *79*, 205116.
[67] M. A. Peacock, J. McAndrew, *Am. Mineral.* **1950**, *35*, 425.
[68] L. Fu, C. L. Kane, *Phys. Rev. B* **2007**, *76*, 045302.
[69] H. C. Po, A. Vishwanath, H. Watanabe, *Nat. Commun.* **2017**, *8*, 50.
[70] Z. Song, T. Zhang, Z. Fang, C. Fang, *Nat. Commun.* **2018**, *9*, 3530.
[71] E. Khalaf, H. C. Po, A. Vishwanath, H. Watanabe, *Phys. Rev. X* **2018**, *8*, 031070.
[72] A. Kobiałka, M. Sternik, A. Ptok, *Phys. Rev. B* **2022**, *105*, 214304.
[73] N. P. Armitage, E. J. Mele, A. Vishwanath, *Rev. Mod. Phys.* **2018**, *90*, 015001.
[74] C. Fang, H. Weng, X. Dai, Z. Fang, *Chinese Phys. B* **2016**, *25*, 117106.
[75] H. Gao, J. W. Venderbos, Y. Kim, A. M. Rappe, *Annu. Rev. Mater. Res.* **2019**, *49*, 153.
[76] B. Q. Lv, T. Qian, H. Ding, *Rev. Mod. Phys.* **2021**, *93*, 025002.
[77] Y. Yang, *Front. Phys.* **2022**, *10*, 1057520.
[78] X. Wang, T. Yang, Z. Cheng, G. Surucu, J. Wang, F. Zhou, Z. Zhang, G. Zhang, *Appl. Phys. Rev.* **2022**, *9*, 041304.
[79] T. T. Zhang, H. Miao, Q. Wang, J. Q. Lin, Y. Cao, G. Fabbris, A. H. Said, X. Liu, H. C. Lei, Z. Fang, H. M. Weng, M. P. M. Dean, *Phys. Rev. Lett.* **2019**, *123*, 245302.
[80] N. Li, J. Ren, L. Wang, G. Zhang, P. Hänggi, B. Li, *Rev. Mod. Phys.* **2012**, *84*, 1045.
[81] J. Li, L. Wang, J. Liu, R. Li, Z. Zhang, X.-Q. Chen, *Phys. Rev. B* **2020**, *101*, 081403.
[82] S. Basak, A. Ptok, *Materials* **2023**, *16*, 78.
[83] M. A. J. Herrera, S. N. Kempkes, M. B. de Paz, A. García-Etxarri, I. Swart, C. M. Smith, D. Bercioux, *Phys. Rev. B* **2022**, *105*, 085411.
[84] B.-J. Yang, N. Nagaosa, *Phys. Rev. Lett.* **2014**, *112*, 246402.
[85] C.-H. Hsu, X. Zhou, T.-R. Chang, Q. Ma, N. Gedik, A. Bansil, S.-Y. Xu, H. Lin, L. Fu, *PNAS* **2019**, *116*, 13255.
[86] L. Zhang, J. Ren, J.-S. Wang, B. Li, *Phys. Rev. Lett.* **2010**, *105*, 225901.
[87] L. Zhang, Q. Niu, *Phys. Rev. Lett.* **2015**, *115*, 115502.
[88] Y. Liu, C.-S. Lian, Y. Li, Y. Xu, W. Duan, *Phys. Rev. Lett.* **2017**, *119*, 255901.
[89] H. Chen, W. Wu, S. A. Yang, X. Li, L. Zhang, *Phys. Rev. B* **2019**, *100*, 094303.
[90] S. Coh, Classification of materials with phonon angular momentum and microscopic origin of angular momentum, arXiv:1911.05064, **2019**.
[91] A. Ptok, A. Kobiałka, M. Sternik, J. Łażewski, P. T. Jochym, A. M. Oleś, S. Stankov, P. Piekarz, *Phys. Rev. B* **2021**, *104*, 054305.
[92] S. Basak, P. Piekarz, A. Ptok, Chiral phonon in the cubic system based on the Laves phase of ABi_2 (A =K, Rb, Cs), arXiv:2208.14041, **2022**.
[93] S. Basak, A. Ptok, *Crystals* **2022**, *12*, 436.
[94] J. Skórka, K. J. Kapcia, P. T. Jochym, A. Ptok, *Mater. Today Commun.* **2023**, *35*, 105888.
[95] M. Sternik, K. Parlinski, *J. Chem. Phys.* **2005**, *123*, 204708.
[96] O. Sikora, D. Gotfryd, A. Ptok, M. Sternik, K. Wohlfeld, A. M. Oleś, P. Piekarz, *Phys. Rev. B* **2020**, *102*, 085129.
[97] K. Momma, F. Izumi, *J. Appl. Crystallogr.* **2011**, *44*, 1272.

4.2.6 Chiral phonon in the cubic system based on the Laves phase of $A\mathbf{Bi}_2$ (A = **K, Rb, Cs**)

S. Basak, P. Piekarz, and A. Ptok, Comput. Mater. Sci. **230**, 112545 (2023).

The vibration of atoms in a circular or elliptical orbit around their equilibrium position can give rise to phonons with non-zero pseudo-angular momentum (PAM), named chiral phonons. We start this manuscript by looking for the presence of chiral phonons in the Laves phase of $A\mathrm{Bi}_2$ (A = K, Rb, Cs). To begin with, we observe that the kagome layer formed by Bi atoms do not host chiral phonons. They are only found in the layers of alkali atoms A. The band structure and density of states analysis leads us to the conclusion that the band structure contains phonon flat bands, which can be interesting to generate strong electron-phonon interaction in this system. Moreover, as the electrons in the presence of a transverse magnetic field can gather at two opposite edges of a sample (electron Hall effect), phonons can give rise to the phonon Hall effect in the presence of the transverse magnetic field. In fact, phonons with intrinsic angular momentum like chiral phonons can produce the phonon Hall effect even in the absence of any external magnetic field, giving rise to a thermal current in the sample. For these to happen one important criterion is broken inversion symmetry. In the second part of this article, we break the inversion symmetry of the materials by doping and predict two new materials that can be used as a platform to study the phonon Hall effect. We also show their dynamical stability to assert that these materials can be synthesized in the lab.

Author's contribution: Performing the numerical calculation (phonon dispersion curves and phonon chirality), analysis and discussion of obtained results, partial preparation of figures, partial preparation of the manuscript, participation in preparing the response for Referees.

Computational Materials Science 230 (2023) 112545

Contents lists available at ScienceDirect

Computational Materials Science

journal homepage: www.elsevier.com/locate/commatsci

Full length article

Chiral phonon in the cubic system based on the Laves phase of ABi_2 (A = K, Rb, Cs)

Surajit Basak, Przemysław Piekarz, Andrzej Ptok *

Institute of Nuclear Physics, Polish Academy of Sciences, ul. W.E. Radzikowskiego 152, 31-342 Kraków, Poland

ARTICLE INFO

Keywords:
DFT calculations
Lattice dynamics
Chiral phonons

ABSTRACT

AB_2 (A = K, Rb, Cs) compounds crystallize in the cubic Laves phase (symmetry $Fd\bar{3}m$). The geometry of the crystal structure allows the realization of chiral phonons, which are associated with the circulation of atoms around their equilibrium positions. Due to the inversion symmetry and time reversal symmetry, total pseudo-angular momentum (PAM) of the system vanishes. We show that the doping of these system can lead to a new phase with symmetry $F\bar{4}3m$. New systems ($KRbBi_4$ and $RbCsBi_4$) do not exhibit soft modes (are stable dynamically). Due to the inversion symmetry breaking, realized chiral phonon modes possess a non-zero total PAM. In both type of systems the chiral phonons are realized for the wavevectors at the edge of the Brillouin zone. This study explores the possibility of chiral phonon engineering via doping, and predicts two new materials. Discussing the problem opens a new way to study the phonon Hall effect.

1. Introduction

Chirality, a property, which distinguishes a system from its mirror image, plays an important role in physics. In lattice dynamics, chirality can be discuss in context of the chiral phonons, i.e., vibration modes associated with the circular motion of the atoms around the equilibrium position [1]. Chiral phonons were studied in many two dimensional (2D) lattices, e.g., honeycomb lattice [1,2], kagome lattice [3], or moiré superlattices [4]. Recently, chiral phonons were also reported in many three dimensional (3D) materials, e.g.: transition metal dichalcogenides [5–8] and their heterostructures [9–11], pervoskites [12–15], graphene/hexagonal boron nitride heterostructure [16], 2D magnets ($CrBr_3$ [17] or Fe_3GeTe_2 [18]), cuprates [19], CoSn-like systems [20], ternary YAlSi compound [21], chiral systems (ABi-like compounds [22], α-HgS [23] or SiO_4 [24]), and magnetic topological insulators TBi_2Te_4 [25]. Due to their extraordinary properties (e.g., realization of the phonon Hall effect [26–33]), it has attracted a lot of theoretical and experimental attentions.

Motivation.— Chiral phonons can be characterized by the phonon circular polarization (PCP), or equivalently by the pseudo-angular momentum (PAM) [1]. Non-zero value of PCP (PAM) gives information about the presence of the chiral phonons in the system [detailed discussion can be found in Supplementary Material (SM) [34]]. However, from experimental point of view, most interesting are materials, which in natural way possess a non-zero total PCP (PAM). In such cases, the strain gradient [1] or the temperature gradient [35] can be source of phonon Hall effect. The main condition to realize such systems is a broken inversion symmetry or/and time reversal symmetry [36].

In this paper we discuss realization of the chiral phonon in the ABi_2 (A = K, Rb, Cs) compounds [37,38], crystallized in the Laves phase (Fig. 1). Clean system, due to the presence of both inversion and time reversal symmetry, hosts chiral phonons with vanishing total PCP (PAM). We will show that the doped system can host chiral phonons with a non-zero total PCP (PAM), what that opens a new way to chiral phonon engineering and their experimental exploration.

In our study we used the *ab initio* techniques to study the dynamical properties of the (based and modified) systems. During the study, we theoretically calculated and analyzed the phonon dispersions. Firstly, this allows us to discuss the system stability in context of lattice dynamics. Next, study of the phonon polarization vectors allow us to explore the behavior of chiral phonons, through the calculation of PCP (detailed can be found in the SM [34]).

2. Calculations details

The first-principle calculations were performed within density-functional theory (DFT) within the projector augmented-wave (PAW) method [39] implemented in the Vienna *Ab initio* Simulation

* Corresponding author.
E-mail addresses: surajit.basak@ifj.edu.pl (S. Basak), piekarz@wolf.ifj.edu.pl (P. Piekarz), aptok@mmj.pl (A. Ptok).
URL: https://www.mmj.pl/~aptok/ (A. Ptok).

https://doi.org/10.1016/j.commatsci.2023.112545
Received 14 April 2023; Received in revised form 27 September 2023; Accepted 28 September 2023
Available online 5 October 2023

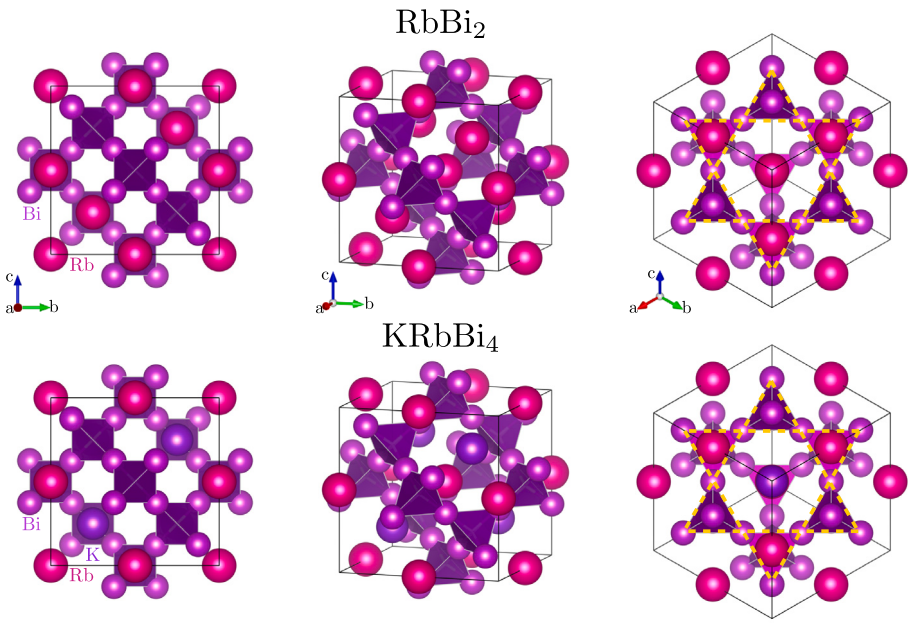

Fig. 1. Conventional cell of $RhBi_2$ in cubic Laves phase (top panels). Rightmost column presents crystal structure along (111) direction showing kagome net (dashed orange line) of corner-sharing tetrahedra of Bi atoms. Conventional cell of $KRhBi_4$ (bottom panels) obtained from $RhBi_2$ by K doping (or KBi_2 by Rb doping).

Package (VASP) [40–42]. The exchange–correlation potential was obtained by the generalized gradient approximation (GGA) in the form proposed by Perdew, Burke, and Ernzerhof (PBE) [43]. We also investigated the impact of the spin–orbit coupling (SOC) [44] on the electronic structure. The energy cut-off for the plane-wave expansion was equal to 350 eV. The optimization of the conventional cell was performed using a 10 × 10 × 10 Monkhorst–Pack **k**-grid [45]. The structures were relaxed using the conjugate gradient technique with the energy convergence criteria set at 10^{-8} eV and 10^{-6} eV for the electronic and ionic iterations, respectively (the optimized lattice constant are in excellent agreement with the experimental values [38], and are collected in Tab. S1 in the SM [34]). Symmetry of the structures were analyzed with FINDSYM [46] and SEEK-PATH [47,48] packages.

The dynamical properties were calculated using the direct *Parlinski–Li–Kawazoe* method [49]. Under this calculation, the interatomic force constants (IFC) are found from the forces acting on atoms when an individual atom is displaced. The forces were obtained by the first-principle calculations with VASP using conventional cell, and reduced 4 × 4 × 4 **k**-grid. The phonon dispersion and polarization vectors analyses were performed using the ALAMODE software [50,51]. The mode symmetries at the Γ point were found by the PHONOPY software [52]. Finally, the chiral phonons were studies by calculation of the PCP (for more details, see Sec. SII in the SM [34]).

3. Results and discussion

3.1. Systems characterization

Base compounds ABi_2 (A = K, Rb, Cs) crystallize in the cubic Laves phase (space group $Fd\bar{3}m$, No. 227), with a pyrochlore lattice [37,38] (left panel in Fig. 1). Alkali metals A atom and Bi atom are in high symmetric Wyckoff position 8*b* (3/8, 3/8, 3/8) and 16*c* (0, 0, 0), respectively. The Bi atoms form corner sharing tetrahedrons, which are intertwined with the diamond structures formed by the Rb atoms. Alternatively, the structure an be described as stacking of 3D kagome nets of Bi atoms. The Rb atoms are located above the four hexagon faces of the capped tetrahedron of the 12 Bi atoms (right panel in Fig. 1). ABi_2, similar to the related Bi compounds (ABi or ABi_3 [53–56]), exhibits the superconducting properties [57–61].

In our study, we are focused on $KRbBi_4$ and $RbCsBi_4$, which can be realized when the one alkali atom (in primitive unit cell of the base ABi_2) is replaced by one of another type. Group analyses of these systems, after the DFT optimization procedure, show that both compounds have $F\bar{4}3m$ symmetry (space group No. 216). In this case, the alkali atoms are located at (non-equivalent) high symmetry Wyckoff position 4*a* (0, 0, 0) and 4*c* (1/4, 1/4, 1/4), while Bi atom in position 16*c* (x_{Bi}, x_{Bi}, x_{Bi}), where x_{Bi} is a free parameter (we found x_{Bi} equal to approximately $\sim 3/8$ for both compounds).

3.2. Phonon spectrum and flat band

Let us start by giving a short description of the phonon spectrum. All of the described compounds are stable, i.e. the phonon spectrum do not exhibit imaginary frequencies. Exact analyses of the partial phonon density of states (Fig. S1 in the SM [34]) clearly show a decrease in the frequencies of vibrations related to the alkali metal, during substitution K→Rb→Cs, due to the increasing masses of the atoms. Similar property is observed for the breathing mode of the Bi atoms tetrahedra. This non-degenerate mode (with symmetry A_{2u} for $Fd\bar{3}m$ phase, and symmetry A_1 for $F\bar{4}3m$ phase) shows an unusual decrease in frequency from ~2.5 THz for KBi_2 to ~1.2 THz for $CsBi_2$ (see Tab. S2 in the SM [34]). At the same time, oscillations of the heavy Bi atoms are mostly realized in the intermediate range of frequencies (approximately, between 1 THz and 1.75 THz).

For the compounds with "light" alkali atoms (KBi_2 and $KRbBi_4$), the separation of the modes in the frequency domain is observed – the modes related to the alkali atoms are mostly observed at the higher frequencies. Contrary to this, in the compounds containing the "heavy" alkali atoms ($RbCsBi_4$ and $CsBi_2$), the vibrational modes are strongly mixed between alkali and Bi atoms. This type of the separation allow realized the phonon flat bands for KBi_2, at frequencies around 1.4 THz [Fig. 2(a)]. Formation of the phonon flat band is allowed due to the realization of the 3D kagome lattice of Bi atoms. Indeed, the flat bands correspond to the strong peaks in the phonon density of states in the range of frequencies related to the Bi atoms [Fig. S1(a) in the SM [34]].

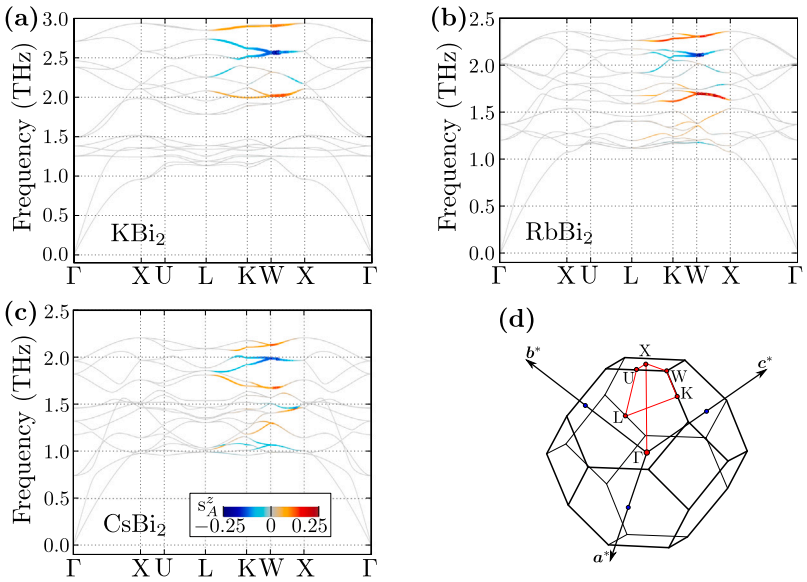

Fig. 2. Phonon dispersion for the base systems $A\mathrm{Bi}_2$ (as labeled), along high symmetry directions (a)–(c). Color code and linewidth correspond to the phonon circular polarization [for vibration in the plane perpendicular to the (111) direction] for one from the alkali atoms. Panel (c) presents the discussed Brillouin zone and high symmetry points.

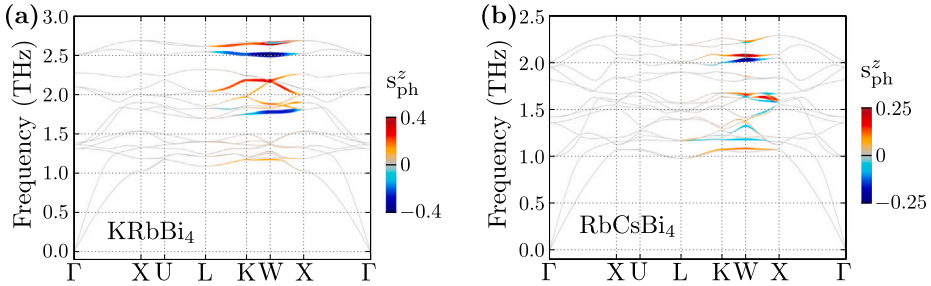

Fig. 3. Phonon dispersion for the modified systems (as labeled), along the high symmetry directions [with the same marking as at Fig. 3(d)]. Color code and linewidth correspond to the total phonon circular polarization [for vibration in the plane perpendicular to the (111) direction].

Chiral phonons and their properties. Substitution of external atoms decrease the symmetry of the system but preserves the two- and three-fold rotational symmetry. From this, the circular vibration of the atoms in both structures can be expected. Indeed, the PCP calculations (Figs. 2 and 3) directly show the existence of chiral phonons.

In the case of $\mathrm{Fd}\bar{3}\mathrm{m}$ phase, the chiral modes are realized by (opposite) circular vibrations of alkali atoms (located in two non-equivalent positions, let say $\mathcal{A}$ and $\mathcal{B}$, in primitive unit cell). When atom in position $\mathcal{A}$ has positive circulation, the atom in position $\mathcal{B}$ has negative circulation, and *vice versa*. Due to the equal masses of both the atoms, chiral modes are realized along the circles with the same radius in both positions. However, due to the inversion symmetry and time reversal symmetry, the chiral modes have zero total PCP. In a natural way, the inversion symmetry can be broken by the introduction of external atoms in the base system $A\mathrm{Bi}_2$, and that should lead to chiral phonons with non-zero PCP (or equivalently PAM) [36]. This phenomena can be realized in KRbBi_4 and RbCsBi_4, which can be made from KBi_2, RbBi_2, or CsBi_2, by the substitution of other alkali atoms. Substitution of this type leads to a situation when diamond-like sublattice of the alkali atoms contains two different atoms (with different masses). Then, contrary to the base compounds, the non-vanishing total PCP can be observed for several branches. The related phonon dispersion are presented in Fig. 3.

Here, we should also comment briefly on the chiral modes in the 3D kagome sublattice of Bi atoms. In the 2D kagome lattice, the chiral modes can be realized by the breaking of spatial inversion symmetry [3]. Thus, in the base $A\mathrm{Bi}_2$ system the chiral modes are not realized in the Bi sublattice. However, breaking the inversion symmetry in the modified compounds KRbBi_4 and RbCsBi_4 affects also the Bi sublattice (see Fig. S2 in the SM [34]). Contrary to the vibrations of the alkali atoms, the Bi atoms within the chiral modes circulate along an ellipse (with small semi-minor axis).

In case of the modified systems, the non-zero PCP (PAM) arises as a consequence of the difference in the circular motion of the atoms (mostly, in two non-equivalent positions of the alkali atoms). However, main properties of the circular motion of the alkali atoms in the system is preserved. When the atom in position $\mathcal{A}$ has positive circulation and realize the motion along circle with some radius, the atoms in position $\mathcal{B}$ has negative circulation, and *vice versa*.

In Fig. 4 we present examples of the chiral modes realized for two non-equivalent W points. Both wavevectors are associated with the same square face of the Brillouin zone and possess 2-fold rotational symmetry [Fig. 4(a)]. Due to the C_2 symmetry, the direction of circulation at one W point is a mirror reflection of its pair – applying the C_2 symmetry leads to a change in the direction of circulation [cf. W_1 and W_3 presented in Fig. 4(c) and Fig. 4(e), or W_2 and W_4 presented in Fig. 4(d) and Fig. 4(f)]. This situation is similar to the simple 2D system with hexagonal symmetry [1], where the change of wavevector (from K to K') leads to the inversion of circulation. However, contrary to the 2D hexagonal system, the chiral phonons do not vanish at the edge of the square face of the Brillouin zone (see Fig. S2 in the SM [34]). This is associated with the additional properties of the system not observed in the 2D hexagonal system, i.e., change of the wavevector along the edge of the square face of the Brillouin zone leads also to the rotation of the

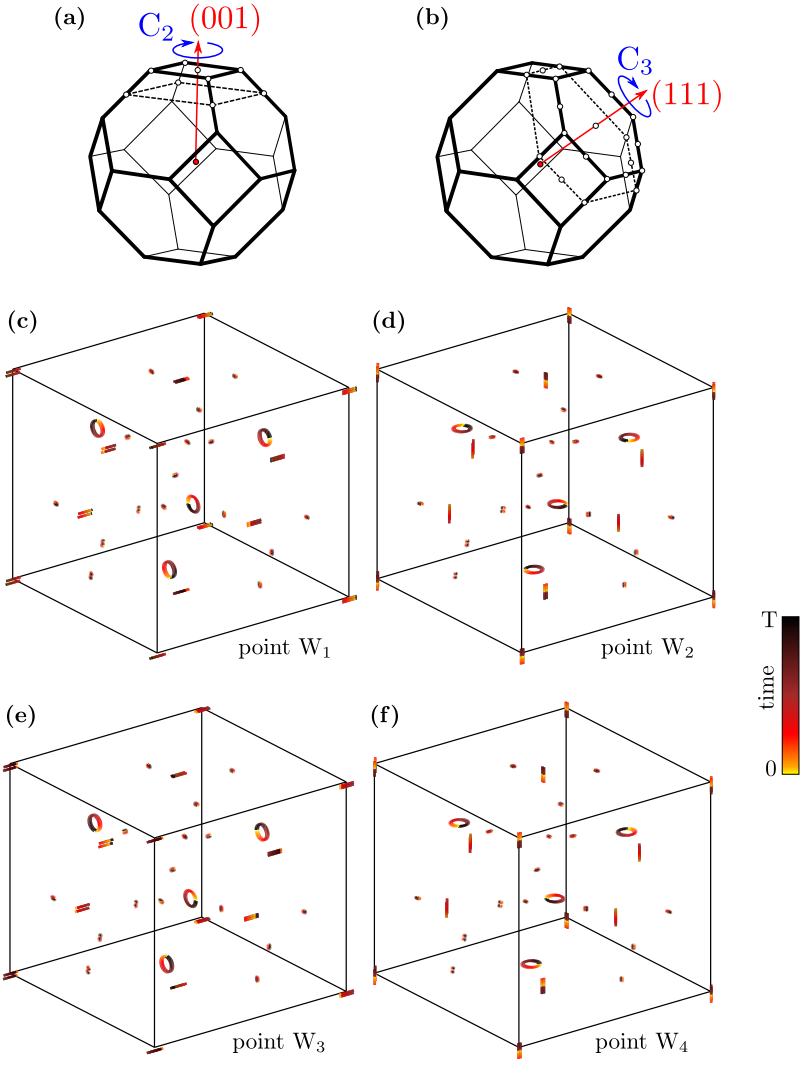

Fig. 4. C_2 (a) and C_3 (b) rotation in the reciprocal space. Visualization of the chiral mode in the conventional cell for W type wavevectors (c)–(f). Color of line correspond to the time, during one period T of the oscillation. Results for 9th phonon mode realized by the Rb atom in $KRbCs_4$.

plane within the chiral modes are realized. This is well visible, when we compare the panels from (c) to (f) in Fig. 4. Similar behavior can be observed in case of the non-equivalent L points which are present in the hexagonal face of the Brillouin zone and possess a three-fold rotational symmetry [Fig. 4(b)].

The described behavior of the non-vanishing chiral modes at the edge of the Brillouin zone can be explained in a simple way. In the 2D hexagonal system, change of phase of the phonon wavefunction must be realized along paths connecting Γ points of neighboring Brillouin zones (e.g. Γ–K–M–K'–Γ, where at the M point the chiral phonons are not realized). This property is intrinsic, and in our case realized along paths Γ–X–Γ, or Γ–L–Γ, while X and L points are located exactly at the rotational symmetry axis. As a consequence, at these points the chiral modes are not realized. Indeed, in our case, on the square and hexagonal faces of Brillouin zone of the discussed systems, the chiral phonons are not realized only at the central X and L points.

Discussed changes of the phonon wavefunction phase (e.g. at the edge of the square face of the Brillouin zone, along W_1–W_2–W_3–W_4 path), is related only to the mentioned modification of the plane in which the chiral phonon modes are realized. At the same time, magnitudes of the circulations do not changed value – this can be observed on the PCP plot (see Fig. S2 in the SM [34]). The PCP changes value when we change one W point to another one (depending on the plane of the projection).

3.3. Raman active modes

In both type of symmetries, the modes at the Γ point can be decomposed to seven irreducible representations: one non-degenerate A-type mode, one double-degenerate E-type mode, and five triple-degenerated T-type modes (see Sec. SIII in the SM [34]). Three of these modes are the Raman active (see Sec. SIV in the SM [34]). Using the Raman selective rules [62], it is possible to distinguish the active modes, using the different backscattering configurations. The same holds for both linear polarized (parallel and perpendicular configuration) and circular polarized (co-circular and cross-circular configuration) Raman spectra measurements.

Typically, in case of systems with hexagonal symmetry, the circular polarized Raman spectroscopy can be used to study the chiral modes [17,18]. However, the method is limited only to the wavevectors in vicinity of the Γ point. Our analyses of the realized chiral phonons (within the PCP calculations – presented in Figs. 2 and 3) clearly show that the chiral modes in discussed compounds are realized around the edges of the Brillouin zone (e.g. along the L–K–W–X path). From another site, the role of the external magnetic field in realization of the chiral modes is well known [14,63,64]. The chiral modes can emerge in the presence of the magnetic field at the Γ point, as a consequence of the decoupled doubly degenerate (Raman active) E

type modes, into two non-degenerated chiral modes with opposite circulation. Frequencies of the E type modes are collected in Tab. S2 in the SM [34].

4. Summary and outlook

We discuss the realization of the chiral phonon modes in the cubic system $KRbBi_4$ and $RbCsBi_4$, based on the Laves phase of ABi_2 (A = K, Rb, Cs). Using the lattice dynamics, we show that the two new compounds ($KRbBi_4$ and $RbCsBi_4$) can be stable, and crystallize with the $F\bar{4}3m$ symmetry. The initial ABi_2 systems possess both inversion symmetry and time reversal symmetry and as a consequence the chiral phonons with total zero phonon circular polarization (pseudo angular momentum) can be realized. In this case the alkali atoms undergo circular motions with opposite circulations. Contrary to this, in the proposed $KRbBi_4$ and $RbCsBi_4$ compounds, the inversion symmetry is broken, and the chiral phonon modes with non-zero phonon circular polarization (pseudo angular momentum) emerge. Additionally, the chiral modes are realized for the wavevectors at the edge of the Brillouin zone, which possess two- and three-fold rotational symmetry. The vanishing of the chiral modes is observed only for X and L points, which are located at the rotational symmetry axis. Realization of chiral phonons with a non-zero PAM in the reported compounds opens up a new way to engineering materials for phonon Hall effect.

CRediT authorship contribution statement

Surajit Basak: Validation, Formal analysis, Investigation, Writing – review & editing. **Przemysław Piekarz:** Validation, Formal analysis, Investigation, Writing – review & editing. **Andrzej Ptok:** Conceptualization, Methodology, Validation, Formal analysis, Investigation, Writing – original draft, Writing – review & editing, Visualization, Supervision.

Data availability

Data will be made available on request.

Acknowledgments

Some figures and movies in this work were rendered using Vesta [65] and VMD [66] software. We thank Sylwia Gutowska and Bartłłomiej Wiendlocha for valuable comments and discussions. S.B. is grateful to IT4Innovations (VŠB-TU Ostrava) for hospitality during a part of the work on this project. This work was supported by the National Science Centre (NCN, Poland) under grants No. 2017/25/B/ST3/02586 (S.B.) and 2021/43/B/ST3/02166 (A.P.). A.P. appreciates funding in the frame of scholarships of the Minister of Science and Higher Education (Poland) for outstanding young scientists (2019 edition, no. 818/STYP/14/2019).

Declaration of competing interest

The authors declare that they have no known competing financial interests or personal relationships that could have appeared to influence the work reported in this paper.

Appendix A. Supplementary data

Supplementary material related to this article can be found online at https://doi.org/10.1016/j.commatsci.2023.112545.

References

[1] L. Zhang, Q. Niu, Phys. Rev. Lett. 115 (2015) 115502, http://dx.doi.org/10.1103/PhysRevLett.115.115502, URL DOI:10.1103/PhysRevLett.115.115502.
[2] Y. Liu, C.-S. Lian, Y. Li, Y. Xu, W. Duan, Phys. Rev. Lett. 119 (2017) 255901, http://dx.doi.org/10.1103/PhysRevLett.119.255901, URL https://link.aps.org/doi/10.1103/PhysRevLett.119.255901.
[3] H. Chen, W. Wu, S.A. Yang, X. Li, L. Zhang, Phys. Rev. B 100 (2019) 094303, http://dx.doi.org/10.1103/PhysRevB.100.094303, URL DOI:10.1103/PhysRevB.100.094303.
[4] N. Suri, C. Wang, Y. Zhang, D. Xiao, Nano Lett. 21 (2021) 10026, http://dx.doi.org/10.1021/acs.nanolett.1c03692, URL DOI:10.1021/acs.nanolett.1c03692.
[5] S.-Y. Chen, C. Zheng, M.S. Fuhrer, J. Yan, Nano Lett. 15 (2015) 2526, http://dx.doi.org/10.1021/acs.nanolett.5b00092, URL DOI:10.1021/acs.nanolett.5b00092.
[6] H. Zhu, J. Yi, M.-Y. Li, J. Xiao, L. Zhang, C.-W. Yang, R.A. Kaindl, L.-J. Li, Y. Wang, X. Zhang, Science 359 (2018) 579, http://dx.doi.org/10.1126/science.aar2711, URL DOI:10.1126/science.aar2711.
[7] E. Liu, J. van Baren, T. Taniguchi, K. Watanabe, Y.-C. Chang, C.H. Lui, Phys. Rev. Res. 1 (2019) 032007(R), http://dx.doi.org/10.1103/PhysRevResearch.1.032007, URL DOI:10.1103/PhysRevResearch.1.032007.
[8] X. Chen, X. Lu, S. Dubey, Q. Yao, S. Liu, X. Wang, Q. Xiong, L. Zhang, A. Srivastava, Nat. Phys. 15 (2019) 221, http://dx.doi.org/10.1038/s41567-018-0366-7, URL DOI:10.1038/s41567-018-0366-7.
[9] A. Delhomme, D. Vaclavkova, A. Slobodeniuk, M. Orlita, M. Potemski, D.M. Basko, K. Watanabe, T. Taniguchi, D. Mauro, C. Barreteau, E. Giannini, A.F. Morpurgo, N. Ubrig, C. Faugeras, 2D Mater. 7 (2020) 041002, http://dx.doi.org/10.1088/2053-1583/aba567, URL DOI:10.1088/2053-1583/aba567.
[10] W. Zhang, A. Srivastava, X. Li, L. Zhang, Phys. Rev. B 102 (2020) 174301, http://dx.doi.org/10.1103/PhysRevB.102.174301, URL DOI:10.1103/PhysRevB.102.174301.
[11] I. Maity, A.A. Mostofi, J. Lischner, Phys. Rev. B 105 (2022) L041408, http://dx.doi.org/10.1103/PhysRevB.105.L041408, URL DOI:10.1103/PhysRevB.105.L041408.
[12] T.F. Nova, A. Cartella, A. Cantaluppi, M. Först, D. Bossini, R.V. Mikhaylovskiy, A.V. Kimel, R. Merlin, A. Cavalleri, Nat. Phys. 13 (2017) 132, http://dx.doi.org/10.1038/nphys3925, URL DOI:10.1038/nphys3925.
[13] D.M. Juraschek, M. Fechner, A.V. Balatsky, N.A. Spaldin, Phys. Rev. Mater. 1 (2017) 014401, http://dx.doi.org/10.1103/PhysRevMaterials.1.014401, URL DOI:10.1103/PhysRevMaterials.1.014401.
[14] D.M. Juraschek, N.A. Spaldin, Phys. Rev. Mater. 3 (2019) 064405, http://dx.doi.org/10.1103/PhysRevMaterials.3.064405, URL https://link.aps.org/doi/10.1103/PhysRevMaterials.3.064405.
[15] X. Li, B. Fauqué, Z. Zhu, K. Behnia, Phys. Rev. Lett. 124 (2020) 105901, http://dx.doi.org/10.1103/PhysRevLett.124.105901, URL DOI:10.1103/PhysRevLett.124.105901.
[16] M. Gao, W. Zhang, L. Zhang, Nano Lett. 18 (2018) 4424, http://dx.doi.org/10.1021/acs.nanolett.8b01487, URL DOI:10.1021/acs.nanolett.8b01487.
[17] T. Yin, K.A. Ulman, S. Liu, A. Granados del Águila, Y. Huang, L. Zhang, M. Serra, D. Sedmidubsky, Z. Sofer, S.Y. Quek, Q. Xiong, Adv. Mater. 33 (2021) 2101618, http://dx.doi.org/10.1002/adma.202101618, URL DOI:10.1002/adma.202101618.
[18] L. Du, J. Tang, Y. Zhao, X. Li, R. Yang, X. Hu, X. Bai, X. Wang, K. Watanabe, T. Taniguchi, D. Shi, G. Yu, X. Bai, T. Hasan, G. Zhang, Z. Sun, Adv. Funct. Mater. 29 (2019) 1904734, http://dx.doi.org/10.1002/adfm.201904734, URL DOI:10.1002/adfm.201904734.
[19] G. Grissonnanche, S. Thériault, A. Gourgout, M.-E. Boulanger, E. Lefrançois, A. Ataei, F. Laliberté, M. Dion, J.-S. Zhou, S. Pyon, T. Takayama, H. Takagi, N. Doiron-Leyraud, L. Taillefer, Nat. Phys. 16 (2020) 1108, http://dx.doi.org/10.1038/s41567-020-0965-y, URL DOI:10.1038/s41567-020-0965-y.
[20] A. Ptok, A. Kobiałka, M. Sternik, J. Łażewski, P.T. Jochym, A.M. Oleś, S. Stankov, P. Piekarz, Phys. Rev. B 104 (2021) 054305, http://dx.doi.org/10.1103/PhysRevB.104.054305, URL DOI:10.1103/PhysRevB.104.054305.
[21] S. Basak, A. Ptok, Crystals 12 (2022) 436, http://dx.doi.org/10.3390/cryst12030436, URL DOI:10.3390/cryst12030436.
[22] J. Skórka, K.J. Kapcia, P.T. Jochym, A. Ptok, Mater. Today Commun. 35 (2023) 105888, http://dx.doi.org/10.1016/j.mtcomm.2023.105888, URL DOI:10.1016/j.mtcomm.2023.105888.
[23] K. Ishito, H. Mao, Y. Kousaka, Y. Togawa, S. Iwasaki, T. Zhang, S. Murakami, J.-i. Kishine, T. Satoh, Nat. Phys. 19 (2023) 35, http://dx.doi.org/10.1038/s41567-022-01790-x, URL DOI:10.1038/s41567-022-01790-x.
[24] Q. Wang, S. Li, J. Zhu, H. Chen, W. Wu, W. Gao, L. Zhang, S.A. Yang, Phys. Rev. B 105 (2022) 104301, http://dx.doi.org/10.1103/PhysRevB.105.104301, URL DOI:10.1103/PhysRevB.105.104301.
[25] A. Kobiałka, M. Sternik, A. Ptok, Phys. Rev. B 105 (2022) 214304, http://dx.doi.org/10.1103/PhysRevB.105.214304, URL DOI:10.1103/PhysRevB.105.214304.
[26] C. Strohm, G.L.J.A. Rikken, P. Wyder, Phys. Rev. Lett. 95 (2005) 155901, http://dx.doi.org/10.1103/PhysRevLett.95.155901, URL DOI:10.1103/PhysRevLett.95.155901.
[27] L. Zhang, J. Ren, J.-S. Wang, B. Li, J. Phys.: Condens. Matter 23 (2011) 305402, http://dx.doi.org/10.1088/0953-8984/23/30/305402, URL DOI:10.1088/0953-8984/23/30/305402.

[28] K. Sugii, M. Shimozawa, D. Watanabe, Y. Suzuki, M. Halim, M. Kimata, Y. Matsumoto, S. Nakatsuji, M. Yamashita, Phys. Rev. Lett. 118 (2017) 145902, http://dx.doi.org/10.1103/PhysRevLett.118.145902, URL DOI:10.1103/PhysRevLett.118.145902.

[29] Y. Kasahara, K. Sugii, T. Ohnishi, M. Shimozawa, M. Yamashita, N. Kurita, H. Tanaka, J. Nasu, Y. Motome, T. Shibauchi, Y. Matsuda, Phys. Rev. Lett. 120 (2018) 217205, http://dx.doi.org/10.1103/PhysRevLett.120.217205, URL DOI:10.1103/PhysRevLett.120.217205.

[30] X. Zhang, Y. Zhang, S. Okamoto, D. Xiao, Phys. Rev. Lett. 123 (2019) 167202, http://dx.doi.org/10.1103/PhysRevLett.123.167202, URL DOI:10.1103/PhysRevLett.123.167202.

[31] M.-E. Boulanger, G. Grissonnanche, S. Badoux, A. Allaire, É. Lefrançois, A. Legros, A. Gourgout, M. Dion, C.H. Wang, X.H. Chen, R. Liang, W.N. Hardy, D.A. Bonn, L. Taillefer, Nature Commun. 11 (2020) 5325, http://dx.doi.org/10.1038/s41467-020-18881-z, URL DOI:10.1038/s41467-020-18881-z.

[32] T. Yokoi, S. Ma, Y. Kasahara, S. Kasahara, T. Shibauchi, N. Kurita, H. Tanaka, J. Nasu, Y. Motome, C. Hickey, S. Trebst, Y. Matsuda, Science 373 (2021) 568, http://dx.doi.org/10.1126/science.aay5551, URL DOI:10.1126/science.aay5551.

[33] H. Zhang, C. Xu, C. Carnahan, M. Sretenovic, N. Suri, D. Xiao, X. Ke, Phys. Rev. Lett. 127 (2021) 247202, http://dx.doi.org/10.1103/PhysRevLett.127.247202, URL DOI:10.1103/PhysRevLett.127.247202.

[34] See Supplementary Material for the computational details and the additional numerical results.

[35] S. Park, B.-J. Yang, Nano Lett. 20 (2020) 7694, http://dx.doi.org/10.1021/acs.nanolett.0c03220, URL DOI:10.1021/acs.nanolett.0c03220.

[36] S. Coh, Classification of materials with phonon angular momentum and microscopic origin of angular momentum, 2019, arXiv:arXiv:1911.05064.

[37] G. Gnutzmann, F.W. Dorn, W. Klemm, Z. Anorg. Allgem. Chem. 309 (1961) 210, http://dx.doi.org/10.1002/zaac.19613090308, URL DOI:10.1002/zaac.19613090308.

[38] F. Emmerling, N. Längin, D. Petri, M. Kroeker, C. Röhr, Z. Anorg. Allgem. Chem. 630 (2004) 171, http://dx.doi.org/10.1002/zaac.200300312, URL DOI:10.1002/zaac.200300312.

[39] P.E. Blöchl, Phys. Rev. B 50 (1994) 17953, http://dx.doi.org/10.1103/PhysRevB.50.17953, URL DOI:10.1103/PhysRevB.50.17953.

[40] G. Kresse, J. Hafner, Phys. Rev. B 49 (1994) 14251, http://dx.doi.org/10.1103/PhysRevB.49.14251, URL DOI:10.1103/PhysRevB.49.14251.

[41] G. Kresse, J. Furthmüller, Phys. Rev. B 54 (1996) 11169, http://dx.doi.org/10.1103/PhysRevB.54.11169, URL DOI:10.1103/PhysRevB.54.11169.

[42] G. Kresse, D. Joubert, Phys. Rev. B 59 (1999) 1758, http://dx.doi.org/10.1103/PhysRevB.59.1758, URL DOI:10.1103/PhysRevB.59.1758.

[43] J.P. Perdew, K. Burke, M. Ernzerhof, Phys. Rev. Lett. 77 (1996) 3865, http://dx.doi.org/10.1103/PhysRevLett.77.3865, URL DOI:10.1103/PhysRevLett.77.3865.

[44] S. Steiner, S. Khmelevskyi, M. Marsmann, G. Kresse, Phys. Rev. B 93 (2016) 224425, http://dx.doi.org/10.1103/PhysRevB.93.224425, URL DOI:10.1103/PhysRevB.93.224425.

[45] H.J. Monkhorst, J.D. Pack, Phys. Rev. B 13 (1976) 5188, http://dx.doi.org/10.1103/PhysRevB.13.5188, URL DOI:10.1103/PhysRevB.13.5188.

[46] H.T. Stokes, D.M. Hatch, J. Appl. Crystallogr. 38 (2005) 237, http://dx.doi.org/10.1107/S0021889804031528, URL DOI:10.1107/S0021889804031528.

[47] Y. Hinuma, G. Pizzi, Y. Kumagai, F. Oba, I. Tanaka, Comput. Mater. Sci. 128 (2017) 140, http://dx.doi.org/10.1016/j.commatsci.2016.10.015, URL DOI:10.1016/j.commatsci.2016.10.015.

[48] A. Togo, I. Tanaka, *Spglib*: A software library for crystal symmetry search, 2018, arXiv:arXiv:1808.01590.

[49] K. Parlinski, Z.Q. Li, Y. Kawazoe, Phys. Rev. Lett. 78 (1997) 4063, http://dx.doi.org/10.1103/PhysRevLett.78.4063, URL DOI:10.1103/PhysRevLett.78.4063.

[50] T. Tadano, Y. Gohda, S. Tsuneyuki, J. Phys.: Condens. Matter 26 (2014) 225402, http://dx.doi.org/10.1088/0953-8984/26/22/225402, URL DOI:10.1088/0953-8984/26/22/225402.

[51] T. Tadano, S. Tsuneyuki, J. Phys. Soc. Japan 87 (2018) 041015, http://dx.doi.org/10.7566/JPSJ.87.041015, URL DOI:10.7566/JPSJ.87.041015.

[52] A. Togo, I. Tanaka, Scr. Mater. 108 (2015) 1, http://dx.doi.org/10.1016/j.scriptamat.2015.07.021, URL DOI:10.1016/j.scriptamat.2015.07.021.

[53] T. Sambongi, J. Phys. Soc. Japan 30 (1971) 294, http://dx.doi.org/10.1143/JPSJ.30.294, URL DOI:10.1143/JPSJ.30.294.

[54] S.K. Kushwaha, J.W. Krizan, J. Xiong, T. Klimczuk, Q.D. Gibson, T. Liang, N.P. Ong, R.J. Cava, J. Phys.: Condens. Matter 26 (2014) 212201, http://dx.doi.org/10.1088/0953-8984/26/21/212201, URL DOI:10.1088/0953-8984/26/21/212201.

[55] K. Górnicka, S. Gutowska, M.J. Winiarski, B. Wiendlocha, W. Xie, R.J. Cava, T. Klimczuk, Chem. Mater. 32 (2020) 3150, http://dx.doi.org/10.1021/acs.chemmater.0c00179, URL DOI:10.1021/acs.chemmater.0c00179.

[56] T. Kinjo, S. Kajino, T. Nishio, K. Kawashima, Y. Yanagi, I. Hase, T. Yanagisawa, S. Ishida, H. Kito, N. Takeshita, K. Oka, H. Eisaki, Y. Yoshida, A. Iyo, Supercond. Sci. Technol. 29 (2016) 03LT02, http://dx.doi.org/10.1088/0953-2048/29/3/03lt02, URL DOI:10.1088/0953-2048/29/3/03lt02.

[57] S. Sun, K. Liu, H. Lei, J. Phys.: Condens. Matter 28 (2016) 085701, http://dx.doi.org/10.1088/0953-8984/28/8/085701, URL DOI:10.1088/0953-8984/28/8/085701.

[58] M.J. Winiarski, B. Wiendlocha, S. Gołąb, S.K. Kushwaha, P. Wiśniewski, D. Kaczorowski, J.D. Thompson, R.J. Cava, T. Klimczuk, Phys. Chem. Chem. Phys. 18 (2016) 21737, http://dx.doi.org/10.1039/C6CP02856J, URL DOI:10.1039/C6CP02856J.

[59] S. Gołąb, B. Wiendlocha, Phys. Rev. B 99 (2019) 104520, http://dx.doi.org/10.1103/PhysRevB.99.104520, URL DOI:10.1103/PhysRevB.99.104520.

[60] H. Li, M. Ikeda, A. Suzuki, T. Taguchi, Y. Zhang, H. Goto, R. Eguchi, Y.-F. Liao, H. Ishii, Y. Kubozono, Phys. Chem. Chem. Phys. 24 (2022) 7185, http://dx.doi.org/10.1039/D2CP00679K, URL DOI:10.1039/D2CP00679K.

[61] S. Gutowska, B. Wiendlocha, T. Klimczuk, M.J. Winiarski, J. Phys. Chem. C 127 (2022) 14402, http://dx.doi.org/10.1021/acs.jpcc.3c02176, URL DOI:10.1021/acs.jpcc.3c02176.

[62] R. Loudon, Adv. Phys. 50 (2001) 813, http://dx.doi.org/10.1080/00018730110101395, URL DOI:10.1080/00018730110101395.

[63] G. Schaack, J. Phys. C: Solid State Phys. 9 (1976) L297, http://dx.doi.org/10.1088/0022-3719/9/11/009, URL DOI:10.1088/0022-3719/9/11/009.

[64] D.M. Juraschek, T. Neuman, P. Narang, Phys. Rev. Res. 4 (2022) 013129, http://dx.doi.org/10.1103/PhysRevResearch.4.013129, URL DOI:10.1103/PhysRevResearch.4.013129.

[65] K. Momma, F. Izumi, J. Appl. Crystallogr. 44 (2011) 1272, http://dx.doi.org/10.1107/S0021889811038970, URL DOI:10.1107/S0021889811038970.

[66] W. Humphrey, A. Dalke, K. Schulten, J. Mol. Graph. 14 (1996) 33, http://dx.doi.org/10.1016/0263-7855(96)00018-5, URL DOI:10.1016/0263-7855(96)00018-5.

Chapter 5

Final thoughts

This thesis contains a collection of my works done during the years of my PhD studies. The works culminated into a series of seven papers, focusing on the electronic and lattice dynamical properties of materials containing kagome lattice. My contributions to those papers were mostly about performing several numerical calculations, analyzing them, and communicating them with the other co-authors. For the electronic part, the work was mostly related to the effects of a magnetic impurity on a s-wave superconductor. We showed how the presence of van Hove singularity (VHS) and flat band singularity (coming from the flat band in the band structure) can drastically affect the coupling strength of the impurity to the superconductor and the localization of the in-gap bound states (Shiba states). This knowledge can be used to harness the Shiba states for application purposes, since for application those Shiba states are more important which are strongly correlated to the substance and have long localization lengths. For the lattice dynamics side, I studied a diverse array of properties in systems with kagome or kagome-like lattices. This involves the study of the dynamical stability of different phases for RhPb, FeGe, CoGe, and NbReSi. Studies of this kind have several implications. For one, they can provide important information about the structure realized in the experiment (RhPb, NbReSi, CoGe). In some cases, it can be used as a tool to track the onset of exotic quantum phases like charge density wave (FeGe). I also looked for the presence of flat bands and symmetry-protected degenerate points and degenerate lines in the phonon band structures of those materials. While the presence of almost dispersion-less phonon may help a strong electron-phonon interaction, the symmetry-protected degenerate points are of topological significance. A part of the work involved investigation of the presence of chiral phonons in some materials containing kagome lattice [$T_3\mathrm{Pb}_2Ch_2$ (T = Pd, Pt and Ch = S, Se), $A\mathrm{Bi}_2$ (A = K, Rb, Cs)], while theoretically proposing two new dynamically-stable systems which contain phonons with non-zero total pseudo-angular momentum. In the end, systems containing kagome lattice have been explored intensively in recent years for their promising proposed applications. However, the effect of the flat band on the properties of the parent system is still a very much open area and hopefully will reveal more and more new fundamentally interesting properties driven by the potential for technological applications in the days to come.

Bibliography

[1]B. Sutherland, "Localization of electronic wave functions due to local topology", Phys. Rev. B **34**, 5208 (1986).

[2]E. H. Lieb, "Two theorems on the Hubbard model", Phys. Rev. Lett. **62**, 1201 (1989).

[3]A. A. Daniel Leykam and S. Flach, "Artificial flat band systems: from lattice models to experiments", Advances in Physics: X **3**, 1473052 (2018).

[4]M. Kang, S. Fang, L. Ye, H. C. Po, J. Denlinger, C. Jozwiak, A. Bostwick, E. Rotenberg, E. Kaxiras, J. G. Checkelsky, and R. Comin, "Topological flat bands in frustrated kagome lattice CoSn", Nat. Commun. **11**, 4004 (2020).

[5]M. Kang, L. Ye, S. Fang, J.-S. You, A. Levitan, M. Han, J. I. Facio, C. Jozwiak, A. Bostwick, E. Rotenberg, M. K. Chan, R. D. McDonald, D. Graf, K. Kaznatcheev, E. Vescovo, D. C. Bell, E. Kaxiras, J. van den Brink, M. Richter, M. Prasad Ghimire, J. G. Checkelsky, and R. Comin, "Dirac fermions and flat bands in the ideal kagome metal FeSn", Nature Materials **19**, 163–169 (2020).

[6]Z. Lin, J.-H. Choi, Q. Zhang, W. Qin, S. Yi, P. Wang, L. Li, Y. Wang, H. Zhang, Z. Sun, L. Wei, S. Zhang, T. Guo, Q. Lu, J.-H. Cho, C. Zeng, and Z. Zhang, "Flatbands and emergent ferromagnetic ordering in Fe_3Sn_2 kagome lattices", Phys. Rev. Lett. **121**, 096401 (2018).

[7]Z. Sun, H. Zhou, C. Wang, S. Kumar, D. Geng, S. Yue, X. Han, Y. Haraguchi, K. Shimada, P. Cheng, L. Chen, Y. Shi, K. Wu, S. Meng, and B. Feng, "Observation of topological flat bands in the kagome semiconductor Nb_3Cl_8", Nano Letters **22**, 4596 (2022).

[8]S. Mukherjee, A. Spracklen, D. Choudhury, N. Goldman, P. Öhberg, E. Andersson, and R. R. Thomson, "Observation of a localized flat-band state in a photonic Lieb lattice", Phys. Rev. Lett. **114**, 245504 (2015).

[9]M. L. Kiesel, C. Platt, and R. Thomale, "Unconventional fermi surface instabilities in the kagome Hubbard model", Phys. Rev. Lett. **110**, 126405 (2013).

[10]W.-S. Wang, Z.-Z. Li, Y.-Y. Xiang, and Q.-H. Wang, "Competing electronic orders on kagome lattices at van hove filling", Phys. Rev. B **87**, 115135 (2013).

[11]J.-X. Yin, S. S. Zhang, H. Li, K. Jiang, G. Chang, B. Zhang, B. Lian, C. Xiang, I. Belopolski, H. Zheng, T. A. Cochran, S.-Y. Xu, G. Bian, K. Liu, T.-R. Chang, H. Lin, Z.-Y. Lu, Z. Wang, S. Jia, W. Wang, and M. Z. Hasan, "Giant and anisotropic many-body spin–orbit tunability in a strongly correlated kagome magnet", Nature **562**, 91 (2018).

[12]N. J. Ghimire and I. I. Mazin, "Topology and correlations on the kagome lattice", Nature Materials **19**, 137–138 (2020).

[13]E. Tang, J.-W. Mei, and X.-G. Wen, "High-temperature fractional quantum Hall states", Phys. Rev. Lett. **106**, 236802 (2011).

[14]T. Kida, L. A. Fenner, A. A. Dee, I. Terasaki, M. Hagiwara, and A. S. Wills, "The giant anomalous Hall effect in the ferromagnet Fe_3Sn_2–a frustrated kagome metal", J. Phys.: Condens. Matter. **23**, 112205 (2011).

[15]S. Baidya, A. V. Mallik, S. Bhattacharjee, and T. Saha-Dasgupta, "Interplay of magnetism and topological superconductivity in bilayer kagome metals", Phys. Rev. Lett. **125**, 026401 (2020).

[16]R. Chisnell, J. S. Helton, D. E. Freedman, D. K. Singh, R. I. Bewley, D. G. Nocera, and Y. S. Lee, "Topological magnon bands in a kagome lattice ferromagnet", Phys. Rev. Lett. **115**, 147201 (2015).

[17]Y.-H. He, Y.-F. Gao, Y. He, X.-F. Qi, J.-Q. Si, M. Yang, and S.-Y. Zhou, "Realization of edge and corner states in photonic crystals with kagome lattices through topological insulator generators", Optics & Laser Technology **161**, 109196 (2023).

[18]S. V. Isakov, S. Wessel, R. G. Melko, K. Sengupta, and Y. B. Kim, "Hard-core bosons on the kagome lattice: valence-bond solids and their quantum melting", Phys. Rev. Lett. **97**, 147202 (2006).

[19]J. M. B. Lopes dos Santos, N. M. R. Peres, and A. H. Castro Neto, "Graphene bilayer with a twist: electronic structure", Phys. Rev. Lett. **99**, 256802 (2007).

[20]Y. Choi, H. Kim, Y. Peng, A. Thomson, C. Lewandowski, R. Polski, Y. Zhang, H. S. Arora, K. Watanabe, T. Taniguchi, J. Alicea, and S. Nadj-Perge, "Correlation-driven topological phases in magic-angle twisted bilayer graphene", Nature **589**, 536 (2021).

[21]S. Lisi, X. Lu, T. Benschop, T. A. de Jong, P. Stepanov, J. R. Duran, F. Margot, I. Cucchi, E. Cappelli, A. Hunter, A. Tamai, V. Kandyba, A. Giampietri, A. Barinov, J. Jobst, V. Stalman, M. Leeuwenhoek, K. Watanabe, T. Taniguchi, L. Rademaker, S. J. van der Molen, M. P. Allan, D. K. Efetov, and F. Baumberger, "Observation of flat bands in twisted bilayer graphene", Nat. Phys. **17**, 189 (2021).

[22]M. Uldemolins, A. Mesaros, and P. Simon, "Effect of van hove singularities on shiba states in two-dimensional *s*-wave superconductors", Phys. Rev. B **103**, 214514 (2021).

[23]W. R. Meier, M.-H. Du, S. Okamoto, N. Mohanta, A. F. May, M. A. McGuire, C. A. Bridges, G. D. Samolyuk, and B. C. Sales, "Flat bands in the cosn-type compounds", Phys. Rev. B **102**, 075148 (2020).

[24]E. Liu, Y. Sun, N. Kumar, L. Muechler, A. Sun, L. Jiao, S.-Y. Yang, D. Liu, A. Liang, Q. Xu, J. Kroder, V. Süß, H. Borrmann, C. Shekhar, Z. Wang, C. Xi, W. Wang, W. Schnelle, S. Wirth, Y. Chen, S. T. B. Goennenwein, and C. Felser, "Giant anomalous Hall effect in a ferromagnetic kagome-lattice semimetal", Nat. Phys. **14**, 1125 (2018).

[25]Y.-X. Jiang, J.-X. Yin, M. M. Denner, N. Shumiya, B. R. Ortiz, G. Xu, Z. Guguchia, J. He, M. S. Hossain, X. Liu, J. Ruff, L. Kautzsch, S. S. Zhang, G. Chang, I. Belopolski, Q. Zhang, T. A. Cochran, D. Multer, M. Litskevich, Z.-J. Cheng, X. P. Yang, Z. Wang, R. Thomale, T. Neupert, S. D. Wilson, and M. Z. Hasan, "Unconventional chiral charge order in kagome superconductor KV_3Sb_5", Nature Materials **20**, 1353 (2021).

[26]A. Ptok, A. Kobiałka, M. Sternik, J. Ła żewski, P. T. Jochym, A. M. Ole ś, and P. Piekarz, "Dynamical study of the origin of the charge density wave in AV_3Sb_5 ($A = K$, Rb, Cs) compounds", Phys. Rev. B **105**, 235134 (2022).

[27]N. Shumiya, M. S. Hossain, J.-X. Yin, Y.-X. Jiang, B. R. Ortiz, H. Liu, Y. Shi, Q. Yin, H. Lei, S. S. Zhang, G. Chang, Q. Zhang, T. A. Cochran, D. Multer, M. Litskevich, Z.-J. Cheng, X. P. Yang, Z. Guguchia, S. D. Wilson, and M. Z. Hasan, "Intrinsic nature of chiral charge order in the kagome superconductor RbV_3Sb_5", Phys. Rev. B **104**, 035131 (2021).

[28]Z. Wang, Y.-X. Jiang, J.-X. Yin, Y. Li, G.-Y. Wang, H.-L. Huang, S. Shao, J. Liu, P. Zhu, N. Shumiya, M. S. Hossain, H. Liu, Y. Shi, J. Duan, X. Li, G. Chang, P. Dai, Z. Ye, G. Xu, Y. Wang, H. Zheng, J. Jia, M. Z. Hasan, and Y. Yao, "Electronic nature of chiral charge order in the kagome superconductor CsV_3Sb_5", Phys. Rev. B **104**, 075148 (2021).

[29]T. Soda, T. Matsuura, and Y. Nagaoka, "s-d Exchange Interaction in a Superconductor", Progress of Theoretical Physics **38**, 551–567 (1967).

[30]M. Fowler and K. Maki, "Conditions for bound states in a superconductor with a magnetic impurity. ii", Phys. Rev. B **1**, 181–188 (1970).

[31]E. Müller-Hartmann and J. Zittartz, "Specific heat of superconductors with magnetic impurities", Solid State Communications **11**, 401–404 (1972).

[32]H. Shiba, "Classical spins in superconductors", Progress of Theoretical Physics **40**, 435–451 (1968).

[33]A. Sakurai, "Comments on superconductors with magnetic impurities", Progress of Theoretical Physics **44**, 1472–1476 (1970).

[34]M. I. Salkola, A. V. Balatsky, and J. R. Schrieffer, "Spectral properties of quasiparticle excitations induced by magnetic moments in superconductors", Phys. Rev. B **55**, 12648–12661 (1997).

[35]B. W. Heinrich, J. I. Pascual, and K. J. Franke, "Single magnetic adsorbates on s-wave superconductors", Progress in Surface Science **93**, 1–19 (2018).

[36]H. Huang, C. Padurariu, J. Senkpiel, R. Drost, A. L. Yeyati, J. C. Cuevas, B. Kubala, J. Ankerhold, K. Kern, and C. R. Ast, "Tunnelling dynamics between superconducting bound states at the atomic limit", Nature Physics **16**, 1227–1231 (2020).

[37]H. Huang, J. Senkpiel, C. Padurariu, R. Drost, A. Villas, R. L. Klees, A. L. Yeyati, J. C. Cuevas, B. Kubala, J. Ankerhold, K. Kern, and C. R. Ast, "Spin-dependent tunneling between individual superconducting bound states", Phys. Rev. Res. **3**, L032008 (2021).

[38]L. Schneider, P. Beck, J. Wiebe, and R. Wiesendanger, "Atomic-scale spin-polarization maps using functionalized superconducting probes", Science Advances **7**, eabd7302 (2021).

[39]A. Villas, R. L. Klees, G. Morrás, H. Huang, C. R. Ast, G. Rastelli, W. Belzig, and J. C. Cuevas, "Tunneling processes between Yu–Shiba–Rusinov bound states", Phys. Rev. B **103**, 155407 (2021).

[40]S. Nakosai, Y. Tanaka, and N. Nagaosa, "Two-dimensional p-wave superconducting states with magnetic moments on a conventional s-wave superconductor", Phys. Rev. B **88**, 180503 (2013).

[41]F. Pientka, L. I. Glazman, and F. von Oppen, "Topological superconducting phase in helical shiba chains", Phys. Rev. B **88**, 155420 (2013).

[42]J. Klinovaja, P. Stano, A. Yazdani, and D. Loss, "Topological superconductivity and majorana fermions in RKKY systems", Phys. Rev. Lett. **111**, 186805 (2013).

[43]Y. Kim, M. Cheng, B. Bauer, R. M. Lutchyn, and S. Das Sarma, "Helical order in one-dimensional magnetic atom chains and possible emergence of Majorana bound states", Phys. Rev. B **90**, 060401 (2014).

[44]J. Li, H. Chen, I. K. Drozdov, A. Yazdani, B. A. Bernevig, and A. H. MacDonald, "Topological superconductivity induced by ferromagnetic metal chains", Phys. Rev. B **90**, 235433 (2014).

[45]J. Röntynen and T. Ojanen, "Topological superconductivity and high chern numbers in 2d ferromagnetic shiba lattices", Phys. Rev. Lett. **114**, 236803 (2015).

[46]B. Braunecker and P. Simon, "Self-stabilizing temperature-driven crossover between topological and nontopological ordered phases in one-dimensional conductors", Phys. Rev. B **92**, 241410 (2015).

[47]J. Li, T. Neupert, Z. Wang, A. H. MacDonald, A. Yazdani, and B. A. Bernevig, "Two-dimensional chiral topological superconductivity in Shiba lattices", Nat. Commun. **7**, 12297 (2016).

[48]M. Schecter, K. Flensberg, M. H. Christensen, B. M. Andersen, and J. Paaske, "Self-organized topological superconductivity in a yu-shiba-rusinov chain", Phys. Rev. B **93**, 140503 (2016).

[49]M. H. Christensen, M. Schecter, K. Flensberg, B. M. Andersen, and J. Paaske, "Spiral magnetic order and topological superconductivity in a chain of magnetic adatoms on a two-dimensional superconductor", Phys. Rev. B **94**, 144509 (2016).

[50]S. Hoffman, J. Klinovaja, and D. Loss, "Topological phases of inhomogeneous superconductivity", Phys. Rev. B **93**, 165418 (2016).

[51]B. Braunecker and P. Simon, "Interplay between classical magnetic moments and superconductivity in quantum one-dimensional conductors: toward a self-sustained topological majorana phase", Phys. Rev. Lett. **111**, 147202 (2013).

[52]M. M. Vazifeh and M. Franz, "Self-organized topological state with majorana fermions", Phys. Rev. Lett. **111**, 206802 (2013).

[53]A. Heimes, P. Kotetes, and G. Schön, "Majorana fermions from Shiba states in an antiferromagnetic chain on top of a superconductor", Phys. Rev. B **90**, 060507 (2014).

[54]P. M. R. Brydon, S. Das Sarma, H.-Y. Hui, and J. D. Sau, "Topological yu-shiba-rusinov chain from spin-orbit coupling", Phys. Rev. B **91**, 064505 (2015).

[55]S. Nadj-Perge, I. K. Drozdov, J. Li, H. Chen, S. Jeon, J. Seo, A. H. MacDonald, B. A. Bernevig, and A. Yazdani, "Observation of majorana fermions in ferromagnetic atomic chains on a superconductor", Science **346**, 602–607 (2014).

[56]R. Pawlak, M. Kisiel, J. Klinovaja, T. Meier, S. Kawai, T. Glatzel, D. Loss, and E. Meyer, "Probing atomic structure and majorana wavefunctions in mono-atomic fe chains on superconducting pb surface", npj Quantum. Inf. **2**, 16035 (2016).

[57]B. E. Feldman, M. T. Randeria, J. Li, S. Jeon, Y. Xie, Z. Wang, I. K. Drozdov, B. Andrei Bernevig, and A. Yazdani, "High-resolution studies of the Majorana atomic chain platform", Nat. Phys. **13**, 286 (2017).

[58]S. Jeon, Y. Xie, J. Li, Z. Wang, B. A. Bernevig, and A. Yazdani, "Distinguishing a majorana zero mode using spin-resolved measurements", Science **358**, 772 (2017).

[59]H. Kim, A. Palacio-Morales, T. Posske, L. Rózsa, K. Palotás, L. Szunyogh, M. Thorwart, and R. Wiesendanger, "Toward tailoring majorana bound states in artificially constructed magnetic atom chains on elemental superconductors", Sci. Adv. **4**, eaar5251 (2018).

[60]M. Ruby, F. Pientka, Y. Peng, F. von Oppen, B. W. Heinrich, and K. J. Franke, "End states and subgap structure in proximity-coupled chains of magnetic adatoms", Phys. Rev. Lett. **115**, 197204 (2015).

[61]G. C. Ménard, S. Guissart, C. Brun, S. Pons, V. S. Stolyarov, F. Debontridder, M. V. Leclerc, E. Janod, L. Cario, D. Roditchev, P. Simon, and T. Cren, "Coherent long-range magnetic bound states in a superconductor", Nature Physics **11**, 1013 (2015).

[62]A. Ptok, A. Kobiałka, M. Sternik, J. Łażewski, P. T. Jochym, A. M. Oleś, S. Stankov, and P. Piekarz, "Chiral phonons in the honeycomb sublattice of layered CoSn-like compounds", Phys. Rev. B **104**, 054305 (2021).

[63]S. Raghu and F. D. M. Haldane, "Analogs of quantum-hall-effect edge states in photonic crystals", Phys. Rev. A **78**, 033834 (2008).

[64]T. Ozawa, H. M. Price, A. Amo, N. Goldman, M. Hafezi, L. Lu, M. C. Rechtsman, D. Schuster, J. Simon, O. Zilberberg, and I. Carusotto, "Topological photonics", Rev. Mod. Phys. **91**, 015006 (2019).

[65]J.-X. Yin, N. Shumiya, S. Mardanya, Q. Wang, S. S. Zhang, H.-J. Tien, D. Multer, Y. Jiang, G. Cheng, N. Yao, S. Wu, D. Wu, L. Deng, Z. Ye, R. He, G. Chang, Z. Liu, K. Jiang, Z. Wang, T. Neupert, A. Agarwal, T.-R. Chang, C.-W. Chu, H. Lei, and M. Z. Hasan, "Fermion–boson many-body interplay in a frustrated kagome paramagnet", Nat. Commun. **11**, 4003 (2020).

[66]J. Lee, K. Fujita, K. McElroy, J. A. Slezak, M. Wang, Y. Aiura, H. Bando, M. Ishikado, T. Masui, J.-X. Zhu, A. V. Balatsky, H. Eisaki, S. Uchida, and J. C. Davis, "Interplay of electron–lattice interactions and superconductivity in $Bi_2Sr_2CaCu2O_{8+\delta}$", Nature **442**, 546 (2006).

[67]L. Shan, J. Gong, Y.-L. Wang, B. Shen, X. Hou, C. Ren, C. Li, H. Yang, H.-H. Wen, S. Li, and P. Dai, "Evidence of a spin resonance mode in the iron-based superconductor $Ba_{0.6}K_{0.4}Fe_2As_2$ from scanning tunneling spectroscopy", Phys. Rev. Lett. **108**, 227002 (2012).

[68]L. Zhang and Q. Niu, "Chiral phonons at high-symmetry points in monolayer hexagonal lattices", Phys. Rev. Lett. **115**, 115502 (2015).

[69]H. Chen, W. Wu, S. A. Yang, X. Li, and L. Zhang, "Chiral phonons in kagome lattices", Phys. Rev. B **100**, 094303 (2019).

[70]Y. Liu, C.-S. Lian, Y. Li, Y. Xu, and W. Duan, "Pseudospins and topological effects of phonons in a kekulé lattice", Phys. Rev. Lett. **119**, 255901 (2017).

[71]Q. Wang, S. Li, J. Zhu, H. Chen, W. Wu, W. Gao, L. Zhang, and S. A. Yang, "Chiral phonons in lattices with c_4 symmetry", Phys. Rev. B **105**, 104301 (2022).

[72]N. Suri, C. Wang, Y. Zhang, and D. Xiao, "Chiral phonons in moiré superlattices", Nano Letters **21**, 10026–10031 (2021).

[73]D. Liu and J. Shi, "Circular phonon dichroism in weyl semimetals", Phys. Rev. Lett. **119**, 075301 (2017).

[74]G. Grissonnanche, A. Legros, S. Badoux, E. Lefrançois, V. Zatko, M. Lizaire, F. Laliberté, A. Gourgout, J.-S. Zhou, S. Pyon, T. Takayama, H. Takagi, S. Ono, N. Doiron-Leyraud, and L. Taillefer, "Giant thermal hall conductivity in the pseudogap phase of cuprate superconductors", Nature **571**, 376 (2019).

[75]G. Grissonnanche, S. Thériault, A. Gourgout, M.-E. Boulanger, E. Lefrançois, A. Ataei, F. Laliberté, M. Dion, J.-S. Zhou, S. Pyon, T. Takayama, H. Takagi, N. Doiron-Leyraud, and L. Taillefer, "Chiral phonons in the pseudogap phase of cuprates", Nat. Phys. **16**, 1108 (2020).

[76]S.-Y. Chen, C. Zheng, M. S. Fuhrer, and J. Yan, "Helicity-resolved raman scattering of mos2, mose2, ws2, and wse2 atomic layers", Nano Letters **15**, 2526 (2015).

[77]H. Zhu, J. Yi, M.-Y. Li, J. Xiao, L. Zhang, C.-W. Yang, R. A. Kaindl, L.-J. Li, Y. Wang, and X. Zhang, "Observation of chiral phonons", Science **359**, 579 (2018).

[78]C. Dornes, Y. Acremann, M. Savoini, M. Kubli, M. J. Neugebauer, E. Abreu, L. Huber, G. Lantz, C. A. F. Vaz, H. Lemke, E. M. Bothschafter, M. Porer, V. Esposito, L. Rettig, M. Buzzi, A. Alberca, Y. W. Windsor, P. Beaud, U. Staub, D. Zhu, S. Song, J. M. Glownia, and S. L. Johnson, "The ultrafast einstein–de haas effect", Nature **565**, 209 (2019).

[79]S. R. Tauchert, M. Volkov, D. Ehberger, D. Kazenwadel, M. Evers, H. Lange, A. Donges, A. Book, W. Kreuzpaintner, U. Nowak, and P. Baum, "Polarized phonons carry angular momentum in ultrafast demagnetization", Nature **602**, 73 (2022).

[80]C. Strohm, G. L. J. A. Rikken, and P. Wyder, "Phenomenological evidence for the phonon hall effect", Phys. Rev. Lett. **95**, 155901 (2005).

[81]S. Basak and A. Ptok, "Shiba states in systems with density of states singularities", Phys. Rev. B **105**, 094204 (2022).

[82]A. Ptok, W. R. Meier, A. Kobiałka, S. Basak, M. Sternik, J. Łażewski, P. T. Jochym, M. A. McGuire, B. C. Sales, H. Miao, P. Piekarz, and A. M. Oleś, "Phononic drumhead surface state in the distorted kagome compound RhPb", Phys. Rev. Res. **5**, 043231 (2023).

[83]S. Basak, Aksel Kobiałka, Małgorzata Sternik, Jan Łażewski, Paweł T. Jochym, Andrzej M. Oleś, Przemysław Piekarz, and A. Ptok, "Pressure dependence of electronic and dynamical properties of CoGe with different symmetries", arXiv:2403.0758 (2024).

[84]A. Ptok, S. Basak, Aksel Kobiałka, Małgorzata Sternik, Jan Łażewski, Paweł T. Jochym, Andrzej M. Oleś, and Przemysław Piekarz, "Lattice dynamics study of electron-correlation-induced charge density wave in antiferromagnetic kagome metal FeGe", arXiv: **2403.00297** (2024).

[85]S. Basak, A. Kobiałka, and A. Ptok, "Dynamical properties of $T_3Pb_2Ch_2$ (T =Pd,Pt and Ch =S,Se) with transition metal kagome net", Adv. Phys. Res. **2**, 2300025 (2022).

[86]S. Basak, P. Piekarz, and A. Ptok, "Chiral phonon in the cubic system based on the laves phase of ABi_2 (A = K, Rb, Cs)", Comput. Mater. Sci. **230**, 112545 (2023).

[87]S. A. Parameswaran, R. Roy, and S. L. Sondhi, "Fractional quantum Hall physics in topological flat bands", Comptes Rendus. Physique **14**, 816 (2013).

[88]W. Beugeling, J. C. Everts, and C. Morais Smith, "Topological phase transitions driven by next-nearest-neighbor hopping in two-dimensional lattices", Phys. Rev. B **86**, 195129 (2012).

[89]P. Hohenberg and W. Kohn, "Inhomogeneous electron gas", Phys. Rev. **136**, B864 (1964).

[90]W. Kohn and L. J. Sham, "Self-consistent equations including exchange and correlation effects", Phys. Rev. **140**, A1133 (1965).

[91]J. P. Perdew, K. Burke, and M. Ernzerhof, "Generalized gradient approximation made simple", Phys. Rev. Lett. **77**, 3865 (1996).

[92]P. E. Blöchl, "Projector augmented-wave method", Phys. Rev. B **50**, 17953 (1994).

[93]A. A. Mostofi, J. R. Yates, Y.-S. Lee, I. Souza, D. Vanderbilt, and N. Marzari, "Wannier90: a tool for obtaining maximally-localised Wannier functions", Comput. Phys. Commun. **178**, 685 (2008).

[94]Q. S. Wu, S. N. Zhang, H.-F. Song, M. Troyer, and A. A. Soluyanov, "WannierTools: an open-source software package for novel topological materials", Comput. Phys. Commun. **224**, 405 (2018).

[95]D. H. Lee and J. D. Joannopoulos, "Simple scheme for surface-band calculations. I", Phys. Rev. B **23**, 4988 (1981).

[96]M. P. L. Sancho, J. M. L. Sancho, J. M. L. Sancho, and J. Rubio, "Highly convergent schemes for the calculation of bulk and surface green functions", J. Phys. F: Met. Phys. **15**, 851 (1985).

[97]H. Hellmann, "Einführung in die quantenchemie", Leipzig: Franz Deuticke., 285 (1937).

[98]R. P. Feynman, "Forces in molecules", Phys. Rev. **56**, 340 (1939).

[99]T. Tadano, Y. Gohda, and S. Tsuneyuki, "Anharmonic force constants extracted from first-principles molecular dynamics: applications to heat transfer simulations", J. Phys.: Condens. Matter **26**, 225402 (2014).

[100]A. Togo and I. Tanaka, "First principles phonon calculations in materials science", Scr. Mater. **108**, 1 (2015).

[101]K. Kunc and R. M. Martin, "Ab initio force constants of gaas: a new approach to calculation of phonons and dielectric properties", Phys. Rev. Lett. **48**, 406–409 (1982).

[102]W. Frank, C. Elsässer, and M. Fähnle, "Ab initio force-constant method for phonon dispersions in alkali metals", Phys. Rev. Lett. **74**, 1791–1794 (1995).

[103]K. Parlinski, Z. Q. Li, and Y. Kawazoe, "First-principles determination of the soft mode in cubic zro_2", Phys. Rev. Lett. **78**, 4063–4066 (1997).

[104]S. Basak and A. Ptok, "Theoretical study of dynamical and electronic properties of noncentrosymmetric superconductor NbReSi", Materials **16**, 78 (2023).